Forschungszentrum Karlsruhe
in der Helmholtz-Gemeinschaft

Wissenschaftliche Berichte
FZKA 7247
SAM-LACOMERA-D18

Results of Boil-off Experiment QUENCH-11

**W. Hering, P. Groudev, M. Heck,
C. Homann, G. Schanz, L. Sepold,
A. Stefanova, U. Stegmaier, M. Steinbrück,
H. Steiner, J. Stuckert**

**Institut für Materialforschung
Institut für Reaktorsicherheit
Programm Nukleare Sicherheitsforschung**

Juni 2007

Forschungszentrum Karlsruhe

in der Helmholtz-Gemeinschaft

Wissenschaftliche Berichte

FZKA 7247

SAM-LACOMERA-D18

Results of Boil-off Experiment QUENCH-11

W. Hering, P. Groudev*, M. Heck, Ch. Homann, G. Schanz, L. Sepold, A. Stefanova*, U. Stegmaier, M. Steinbrück, H. Steiner, J. Stuckert

Institut für Materialforschung

Institut für Reaktorsicherheit

Programm Nukleare Sicherheitsforschung

* Bulgarian Academy of Sciences, Institute for Nuclear Research and Nuclear Energy, Sofia

Forschungszentrum Karlsruhe GmbH, Karlsruhe

2007

Forschungszentrum Karlsruhe GmbH
Postfach 3640, 76021 Karlsruhe

Mitglied der Hermann von Helmholtz-Gemeinschaft
Deutscher Forschungszentren (HGF)

ISSN 0947-8620

urn:nbn:de:0005-072478

Zusammenfassung

Ergebnisse des Ausdampf-Experiments QUENCH-11

In den QUENCH-Versuchen wird der Wasserstoffquellterm bei der Einspeisung von Notkühlwasser in einen trockenen, überhitzten Reaktorkern eines Leichtwasserreaktors (LWR) untersucht. Die Standard-Testbündel bestehen aus 21 Brennstabsimulatoren mit einer Gesamtlänge von ca. 2,50 m.

Der Ausdampf-Versuch QUENCH-11 wurde am 8. Dezember 2005 im Forschungszentrum Karlsruhe durchgeführt. Es war das zweite Experiment im Rahmen des EU-geförderten LACOMERA-Programms. Das Experiment wurde von INRNE Sofia (Bulgarische Akademie der Wissenschaften) vorgeschlagen und zusammen mit dem Forschungszentrum Karlsruhe definiert. Das Ziel war die Untersuchung des Bündelverhaltens während des Ausdampfens und des nachfolgenden Abschreckens mit reduzierter Wassereinspeiserate. Die analytische Unterstützung durch Einsatz der Rechenprogramme SCDAP/RELAP5 mod 3.2.irs und ASTEC waren für die Durchführung des Versuchs von entscheidender Bedeutung.

Beständiges Ausdampfen mit entsprechendem Absenken des Wasserniveaus im Versuchsbündel wurde durch die elektrische Bündelheizung und eine elektrische Zusatzheizung im Bündelfuß erreicht. Äußere Heizbänder sorgten außerdem für die Kompensation der Wärmeverluste, die sonst eine geringere Ausdampfung im oberen Bündelbereich zur Folge gehabt hätten. Sobald der Wasserspiegel auf die Bündelhöhe -70 mm abgefallen war, wurde Wasser mit ca. 1 g/s in das Bündel eingespeist. Dadurch wurde der Wasserstand stabilisiert, während die Ausdampfphase fortgesetzt wurde. Das Abschrecken des Testbündels mittels Wasser erfolgte bei einer Maximaltemperatur von 2040 K mit einer im Vergleich zur üblichen Einspeisung von 50 g/s geringen Flutrate von 18 (17+1) g/s.

Die Ausdampfphase sorgte für eine verstärkte Oxidation der Hüllrohre und des Dampfführungsrohrs, ähnlich derjenigen bei einer “erzwungenen” Dampfströmung. Der obere Teil des Testbündels wurde durch Oxidation und Schmelzebildung stark zerstört.

Die gesamte erzeugte Wasserstoffmenge wurde mit dem Massenspektrometer zu 141 g gemessen. 132 von den 141 g, d. h. mehr als 90 % der Gesamtmenge, wurde während der Flutphase gebildet. Zusätzlich wurde die integrale Wasserstofffreisetzung auf der Grundlage der Nachuntersuchungen aller oxidierten Bündelkomponenten abgeschätzt: 92 g (64 %) des freigesetzten Wasserstoffs wurde durch die Oxidation prototypischer Bündelmaterialien erzeugt, d. h. Bündelkomponenten, die üblicherweise in SFD-Rechenprogrammen betrachtet werden (wie Hüllrohre, Eckstäbe, Abstandshalter und die Innenseite des Dampfführungsrohrs). 51 g Wasserstoff resultieren von der Oxidation der Dampfführungsrohr-Außenseite, von Heizern, Elektroden und der Schmelze.

Nach dem Experiment wurde entschieden, die QUENCH-11-Daten für einen Rechenprogramm-Benchmark anzubieten, bei dem die Rechenergebnisse mit den experimentellen Daten verglichen werden. Federführend bei dessen Durchführung ist das INRNE-Institut in Sofia, Bulgarien, im Rahmen des Europäischen SARNET-Programms. Die beteiligten Rechenprogramme: ASTEC, ICARE-CATHARE, MELCOR, SCDAP/RELAP5, RELAP/SCDAPSIM, RATEG/SVECHA und ATHLET-CD.

Abstract

The QUENCH experiments are to investigate the hydrogen source term resulting from the water injection into an uncovered core of a Light-Water Reactor (LWR). The typical QUENCH test bundle consists of 21 fuel rod simulators with a total length of approximately 2.5 m.

Boil-off experiment QUENCH-11 was performed at Forschungszentrum Karlsruhe (Karlsruhe Research Center) on 8 December, 2005 as the second of two experiments in the frame of the EC-supported LACOMERA program. The experiment focused on studying bundle behavior during boil-off and subsequent quenching at a small water injection rate. It was proposed by INRNE Sofia (Bulgarian Academy of Sciences) and defined together with the Karlsruhe Research Center. The analytical support by using the SCDAP/RELAP5 mod 3.2.irs and ASTEC codes for the preparation of the entire test was essential in conducting the test.

A steady boil-off and a corresponding top-down uncovery of the test bundle was achieved by applying power from an electric auxiliary heater at the bundle bottom in addition to the electric bundle power. An additional outer heating system compensated heat losses that would lead to a reduction in boiling off the covered part of the bundle. When the water level had fallen to -70 mm elevation water was injected into the lower plenum at a rate of ca. 1 g/s enabling a nearly stable water level and an extension of the boil-off phase. Quenching of the bundle was performed at a maximum measured bundle temperature of 2040 K with a rather low mass flow rate of water, i.e. 18 (17+1) g/s, compared to the standard water injection rate of approx. 50 g/s.

The conditions led to an enhanced cladding and shroud oxidation, quite similar to standard conditions of forced-convection steam flow. In the upper part the test bundle was significantly degraded by oxidation and melt formation.

The total generation of hydrogen measured by the mass spectrometer was 141 g, of which 132 g, i.e. more than 90 % of the total, was produced during the reflood phase. Based on posttest bundle examinations the integral hydrogen release was additionally estimated by consideration of all oxidized components. 92 g (64 %) of the hydrogen released was produced by the oxidation of prototypical bundle components, usually considered in SFD code systems, i.e. cladding tubes, corner rods, spacer grids, and inner shroud surface. 51 g hydrogen resulted from the oxidation of shroud outer surface and melt, heaters, electrodes.

After the experiment it was decided to choose QUENCH-11 as a benchmark exercise comparing code results with experimental data. The exercise is managed by INRNE Sofia, Bulgaria, in the frame of the European SARNET program. Computational results were received from the different computer codes: ASTEC, ICARE-CATHARE, MELCOR, SCDAP/RELAP5, RELAP/SCDAPSIM, RATEG/SVECHA, and ATHLET-CD.

Contents

List of Tables

List of Figures

Introduction

The most important accident management measure to terminate a severe accident transient in a Light Water Reactor (LWR) is the injection of water to cool the uncovered degraded core. Analysis of the TMI-2 [1] accident and the results of integral out-of-pile (CORA [2, 3]) and in-pile experiments (LOFT [4], PHEBUS [5]) have shown that before the water succeeds in cooling the fuel pins there may be an enhanced oxidation of the zircaloy cladding that in turn causes a sharp increase in temperature, hydrogen production, and fission product release.

Besides, quenching is considered as a worst-case accident scenario regarding hydrogen release to the containment. For licensing and safety analyses one has to prove that the hydrogen release rate and total amount do not exceed limits for the considered power plant. The hydrogen generation rate must be known to design appropriately accident mitigation measures like passive autocatalytic recombiners and ignitors.

The physical and chemical phenomena of the hydrogen release are, however, not sufficiently well understood. The increased hydrogen production during quenching cannot be completely explained on the basis of the available zircaloy/steam oxidation correlations [6]. In most of the code systems describing severe fuel damage, phenomena, e.g. melt oxidation and steam starvation prior to flooding, which lead to an enhanced oxidation and hydrogen generation are either not considered or only modeled in a simplified empirical manner.

In addition, no sophisticated models are available to predict correctly the thermal-hydraulic or the clad behavior of the quenching processes in the CORA and LOFT LP-FP-2 tests. An extensive experimental database is therefore needed as a basis for model development and code improvement.

The Forschungszentrum Karlsruhe is performing the QUENCH program on the investigation of coolability and determination of the hydrogen source term. The main objectives of this program are:

- The provision of an extensive experimental database for the development of detailed mechanistic models,
- The examination of the physico-chemical behavior of overheated fuel elements under different flooding conditions and at different stages of core degradation,
- The determination of cladding failure criteria, cracking of oxide layers, exposure of new metallic surfaces to steam,
- The investigation of the oxide layer degradation under steam starvation conditions and influence of this phenomenon on subsequent flooding,
- The investigation of the melt oxidation process,
- The determination of the hydrogen source term.

The QUENCH program began with small-scale experiments using short zircaloy fuel rod segments [7-9]. On the basis of these results well-instrumented large-scale bundle experiments with fuel rod simulators under nearly adiabatic conditions are performed in the

QUENCH facility of the Forschungszentrum Karlsruhe. The large-scale bundle experiments are more representative of prototypic reactor accident conditions than are the single-rod experiments. Important parameters of the bundle test program (see Table 1) are: quench medium, i.e. water or steam, fluid injection rate, cladding oxide layer thickness, and the temperature at onset of flooding.

Within the scope of severe fuel damage (SFD) research, reflood-related experiments dealt mainly with conditions above the lowered water level inside the reactor pressure vessel (RPV). So far, no integral experiment has been performed with a controlled evaporation of a free water surface in the test section, neither for reactor-operating nor for non-power conditions. Another issue is a slow re-flooding from the bottom [11].

So, the QUENCH-11 experiment was set up to study bundle behavior during boil-off and subsequent quenching at a moderate water injection rate. It was performed at Forschungszentrum Karlsruhe (Karlsruhe Research Center) on 8 December, 2005 was the second of two experiments in the frame of the EC-supported LACOMERA program [10]. It was proposed by INRNE Sofia (Bulgarian Academy of Sciences) and defined together with Forschungszentrum Karlsruhe.

Prior to the main test, three pre-tests were performed to quantify heat losses and so improve pretest calculations [12]. Further, they were to test the new auxiliary heater system, and the instrumentation (water level, fluid mass balance), which was originally not designed for boil-off conditions. The pre-tests comprised three non-destructive tests, designated QUENCH-11v1 through v3. QUENCH-11v1 was set up to calibrate the heat balance, in particular lateral losses in the lower plenum and entry pipes, to test the control of the cooling water temperature of the off-gas pipe, upper plenum, and upper electrode zone, and to become familiar with the accuracy under low evaporation.

In QUENCH-11v2 with a temperature range of up to 600 K it was an aim to detect the power level of the auxiliary heater at which flashing could occur [13].

The last pre-test QUENCH-11v3 was to simulate boil-off and core heat-up to app. 1350 K to learn about system behavior, bundle response, and controllability. In QUENCH-11v3 the bundle was flooded with the same rate as foreseen in QUENCH-11 [14]. QUENCH-11v3 was also considered to simulate an accumulator-driven core refill, whereas the main test, QUENCH-11, simulates delayed reflood with a rather low mass flow rate.

Moreover, QUENCH-11 was chosen a benchmark exercise defined as a comparison between the QUENCH-11 experimental data and analytical results and managed by INRNE in the frame of the European SARNET program. The experimental data supplied to the participants to perform their calculations were data sets for initial and boundary conditions. In total, 13 participants from eight countries participated in this exercise. Computational results received from the different computer codes such as ASTEC, ICARE-CATHARE, MELCOR, RELAP/SCDAPSIM, SCDAP/RELAP5, RATEG/SVECHA and ATHLET-CD will be documented later.

This report describes the test facility and the test bundle, and the main results of the QUENCH-11 experiment including the posttest examination and computational results using the CALUMO computer code. The analytical support by using the SCDAP/RELAP5 mod 3.2.irs, SCDAPSIM, MELCOR, and ASTEC codes for the preparation of the entire test was essential in conducting the test. The results are published in [15-18].

1 Description of the Test Facility

The QUENCH test facility consists of the following component systems:

- the test section with 21 fuel rod simulators,
- the electric power supply for the test bundle heating,
- the water and steam supply system,
- the argon gas supply system,
- the hydrogen measurement devices,
- temperature, pressure, mass flow measurement devices,
- the process control system,
- the data acquisition system.

A simplified flow diagram of the QUENCH test facility is given in Fig. 1, a three-dimensional schematic of the components in Fig. 2. The thickness of the safety containment is 5.6 mm. Its inner and outer diameters amount to 801.8 and 813 mm, respectively.

The main component of the facility is the test section with the test bundle (Figs. 3 and 4). Different to the forced-convection mode, the steam inlet is closed off in the boil-off mode (QUENCH-11) so that the test bundle can be filled with water which can be boiled off by applying electric bundle power and additional electric power by an auxiliary heater located in the lower plenum of the bundle. The system pressure in the test section is around 0.2 MPa. The carrier gas argon injected at the bundle head, the steam not consumed, and the hydrogen produced in the test section by oxidation of the various materials flow from the bundle outlet at the top through a water-cooled off-gas pipe to the condenser where the steam is condensed and separated from the non-condensable gases (Figs. 1 and 2). The test section has a separate inlet at the bottom to inject water for reflood (bottom quenching, see Figs. 1-4).

The design characteristics of the test bundle are given in Table 2. The test bundle is made up of 21 fuel rod simulators, each with a length of approximately 2.5 m, and of four corner rods (see cross section in Fig. 5). The fuel rod simulators (Fig. 6) are held in their positions by five grid spacers, four of zircaloy, and one of inconel in the lower bundle zone. The cladding of the fuel rod simulators is identical to that used in PWRs with respect to material and dimensions, i.e. Zircaloy-4, 10.75 mm outside diameter, 0.725 mm wall thickness. Two fuel rod simulators, i.e. rods 14 and 20, were made with duplex claddings of the “DX-D4” type provided by Framatome ANP. The rod designation can be taken from Fig. 8.

The rod internal pressure is usually held at 0.22 MPa (rod filling with helium), i.e. 0.02 MPa above the system pressure.

Twenty fuel rod simulators are heated electrically over a length of 1024 mm, the unheated fuel rod simulator is located in the center of the test bundle. The unheated fuel rod simulator (Fig. 7) is filled with ZrO_2 pellets (bore size 2.5 mm). For the heated rods (Fig. 6) tungsten heating elements of 6 mm diameter are installed in the center of the rods and are surrounded by annular ZrO_2 pellets. The tungsten heaters are connected to electrodes made of molybdenum and copper at each end of the heater. The molybdenum and copper electrodes are joined by high-frequency/high-temperature brazing under vacuum ($2x10^{-3}$ mbar) using an AuNi 18 powder (particle size <105 µm). For electrical insulation the surfaces of both types of electrodes are plasma-coated with 0.2 mm ZrO_2. To protect the copper electrodes and the O-ring-sealed wall penetrations against excessive heat they are water-cooled (lower and upper cooling chambers filled with demineralized water). The copper electrodes are connected to the DC electric power supply by means of special sliding contacts at the top and bottom. The total heating power available is 70 kW, distributed among two groups of heated rods with 35 kW each. The first group consists of the inner eight rods (rod numbers 2-9), the second group consists of the outer twelve rods (rod numbers 10-21). Electrical resistances of inner and outer ring (without cables on both ends) as well as of a single heater and a single slide contact at the copper electrode can be taken from Table 4.

The lower boundary for the lower cooling chamber is a sealing plate made of stainless steel with plastic inlays for electrical insulation, sealed to the system by O-shaped rings. The upper boundary of the lower cooling chamber is a sealing plate of stainless steel. An insulation plate made of plastic (PEEK) forms the top of the upper cooling chamber, and a sealing plate of Al_2O_3, functioning as a heat-protection shield, is the lower boundary of the upper cooling chamber (see Fig. 6).

In the region below the upper Al_2O_3 plate the copper electrode is connected firmly to the cladding. This is done by hammering the cladding onto the electrode with a sleeve of boron nitride put between electrode and cladding for electrical insulation. The axial position of the fuel rod simulator in the test bundle is fixed by a groove and a locking ring in the top Cu electrodes. Referred to the test bundle the fixing point of the fuel rod simulators is located directly above the upper edge of the upper insulation plate. So, during operation the fuel rod simulators are allowed to expand downwards. Clearance for expansion of the test rods is provided in the region of the lower sealing plate. Also in this region, relative movement between cladding and internal heater/electrode can take place.

The test bundle is surrounded by a 2.38 mm thick shroud (80 mm ID) made of zircaloy with a 37 mm thick ZrO_2 fiber insulation and an annular cooling jacket made of inconel (inner tube) and stainless steel (outer tube; see Fig. 5). The annulus between shroud and cooling jacket was filled (after several cycles of degasing) with stagnant argon of 0.22 MPa and was connected to a flow-controlled argon feeding system in order to prevent steam access to the annulus after shroud failure. The 6.7 mm annulus of the cooling jacket is cooled by an argon flow. Above the heated zone, i.e. above the 1024 mm elevation there is no ZrO_2 fiber insulation to allow for higher radial heat losses. This region of the cooling jacket is cooled by

a water flow (Figs. 3 and 4). Both the lack of ZrO_2 insulation above the heated region and the water cooling force the axial temperature maximum downward.

The four corner positions of the bundle are occupied either by solid zircaloy (Zry) rods with a diameter of 6 mm or by solid rods (upper part) / Zry tubes (lower part) of ∅ 6 x 0.9 mm for thermocouple instrumentation at the inside (Figs. 5 and 8). The positioning of the four corner rods avoids an atypically large flow cross section at the outer positions and hence helps to obtain a rather uniform radial temperature profile. In the QUENCH-11 test bundle two of them, i.e. rods “A” and “C” were used for thermocouple instrumentation whereas the other two rods, i.e. rods “B” and “D” (solid Zry rods) were reserved for withdrawal from the bundle at the end of pre-oxidation and prior to quenching, respectively, to check the amount of ZrO_2 oxidation at those times.

Changes concerning the test facility which were realized prior to the QUENCH-11 test were: (1) An auxiliary heater system with a resistance of 16.6 Ω which can be controlled between 0.1 and 3.5 kW was installed at the flow distributor located in the lower bundle plenum. A thermocouple was mounted in contact with the internal heater and could be used to control the electric power of the auxiliary heater. The heater material was stainless steel 1.4571. The total surface area of the heater amounts to 116627.6 mm², its volume to 127600 mm³, and its mass to 1.025 kg. (2) Externally, a heating band with a resistance of 6.8 Ω was wrapped around the structure of the lower bundle plenum. This external heating system was to provide adiabatic conditions at the bundle foot. (3) A water dosing system (~0.1-4 g/s) was connected to the lower plenum to make up for the boil-off of the water-filled test section. (Calibration at a water injection rate of 1 g/s resulted in an error of +4%). (4) New heated and insulated pipes were installed for the flow of the argon carrier gas from the gas pre-heater to the bundle head inlet. (5) Temperature control units were added to the water cooling circuits for bundle head and off-gas pipe to guarantee that the steam/gas temperature is high enough so that condensation at test section outlet and off-gas pipe, respectively, can be avoided. The temperature at the bundle head is kept at 348 K, and the flow rate of the cooling water is 250 g/s. The off-gas pipe consists of a water-cooled inner pipe with a countercurrent flow and a flow rate of 370 g/s. The water inlet temperature is controlled at 393 K. Between the off-gas pipe and inner cooling jacket there is stagnant off-gas. The main dimensions of the tubes are:

Inner pipe:	outer diameter 139.7 mm, wall thickness 4.5 mm total length 3256 mm, material: stainless steel
Inner cooling jacket:	outer diameter 154 mm, wall thickness 2 mm, material: stainless steel
Outer cooling jacket:	outer diameter 168.3 mm, wall thickness 5 mm, material: stainless steel

2 Test Bundle Instrumentation

The test bundle was instrumented with sheathed thermocouples (TC) attached to the rod claddings at 17 different elevations between -250 mm and 1350 mm and at different orientations according to Figs. 8 and 9. The elevations of the surface-mounted shroud thermocouples are from -250 mm to 1250 mm. In the lower bundle region, i.e. up to the 550 mm elevation, NiCr/Ni thermocouples (1 mm diameter, stainless steel sheath 1.4541, MgO insulation) are used for temperature measurement of rod cladding and shroud as is illustrated in Fig. 9. The thermocouples of the hot zone are high-temperature thermocouples with W-5Re/W-26Re wires, HfO_2 insulation, and a duplex sheath of tantalum (internal)/zirconium with an outside diameter of 2.1 mm (see Table 3 and for final dimensions after the sheath treatment Fig. 10).

The thermocouple attachment technique for the surface-mounted high-temperature TCs is illustrated in Fig. 11. The TC tip is held in place by two clamps of zirconium (0.2 mm thick). As these clamps are prone to oxidation and embrittlement in a steam environment an Ir-Rh wire of 0.25 mm diameter is additionally used in the experiments with pre-oxidation as was the case in test QUENCH-11. The leads of the thermocouples from the -250 mm to the 850 mm level leave the test section at the bottom whereas the TCs above 850 mm are routed to the top avoiding to route TC cables through the hot zone. Additionally, the cables of shroud thermocouples (designated TSH xx/x “I”) were routed toward outside the shroud insulation to avoid heat transfer from the shroud into the TC cable, apart from the TC junction.

The designations of the surface-mounted cladding and shroud thermocouples are “TFS” and “TSH”, respectively. The unheated fuel rod simulator of the QUENCH-11 bundle (Fig. 7) is instrumented with two centerline thermocouples, i.e. TCRC 9 (at 550 mm, NiCr/Ni, ∅ 1 mm, routed to bottom) and TCRC 13 (at 950 mm, W/Re, ∅ 2.1 mm, routed to top).

The wall of the inner tube of the cooling jacket is instrumented between -250 mm and 1150 mm with NiCr/Ni thermocouples (designation “TCI”). The thermocouples that are fixed at the outer surface of the outer tube of the cooling jacket (designation “TCO”) are also of the NiCr/Ni type. The designation of the centerline thermocouples inside the zircaloy corner rods is “TIT”. According to Fig. 12 two of the four corner rods of the QUENCH-11 test bundle are instrumented as follows:

- Rod A: W/Re, 2.1 mm diameter, Zr/Ta duplex sheath, 950 mm elevation (TIT A/13)
- Rod C: W/Re, 2.1 mm diameter, Zr/Ta duplex sheath, 850 mm elevation (TIT C/12).

A list of all instruments for experiment QUENCH-11 installed in the test section and at the test loop is given in Table 5. The thermocouples that failed prior or during the test are listed in Table 6.

3 Hydrogen Measurement Devices

The hydrogen is analyzed by two different measurement systems: (1) a Balzers mass spectrometer (MS) “GAM 300” (Fig. 13) and (2) a hydrogen detection system ”Caldos 7 G” (Fig. 15) located in a bypass to the off-gas line downstream the condenser. Due to their different locations in the facility the mass spectrometer “GAM 300” responds almost immediately (less than 5 s) to a change in the gas composition whereas the Caldos device has a delay time of about 20-30 s. The time delay of the off-gas analyzing systems has been determined with several bundle flows and gas injections at the 700 mm level of a dummy test section particularly installed for calibration purposes. Besides the time delay, the signal shapes are different for the Caldos H_2 analyzer resulting in a broader peak due to the diffusion of the hydrogen in the offgas.

The mass spectrometer “BALZERS GAM 300“ used is a completely computer-controlled quadrupole MS with an 8 mm rod system which allows quantitative measurement of gas concentrations down to about 10 ppm. For the MS measurement a sampling tube is inserted in the off-gas pipe located approx. 2.7 m downstream from the test section outlet (see also Fig. 21). It has several holes at different elevations to guarantee that the sampling of the gas to be analyzed is representative (see Fig. 14). To avoid steam condensation in the gas pipes between the sampling position and the MS the temperature of the gas at the MS inlet is controlled by heating tapes to be between 110 °C and 150 °C (the upper operating temperature of the MS inlet valves). This allows the MS to analyze the steam production rate. Besides, the concentrations of the following species were continuously measured by the mass spectrometer during all test phases: argon, hydrogen, steam, nitrogen, oxygen, and helium. The fuel rod simulators are filled with helium as a tracer gas which can be used as an indicator for a cladding failure. Additionally, the MS is used to control the atmosphere in the facility, e.g., to monitor the gas composition at the beginning of the test.

The temperature and pressure of the analyzed gas are measured near the inlet valve of the MS. The MS is calibrated for hydrogen, oxygen and nitrogen with well-defined argon/gas mixtures and for steam with mixtures of argon and steam supplied by a Bronkhorst controlled evaporator mixing (CEM) device. The MS off-gas is released into the atmosphere because the amount of hydrogen taken out of the system is negligible. A heated measuring gas pump was used to ensure a continuous flow of the steam-gas mixture from the off-gas pipe to the mass spectrometer.

The principle of measurement of the Caldos system is based on the different heat conductivities of different gases. The Caldos device is calibrated for the hydrogen-argon gas mixture. To avoid any moisture in the analyzed gas a gas cooler, which is controlled at 276 K, is connected to the gas analyzer (see also Fig. 15). The response time of the gas analyzer is documented by the manufacturer to be 2 s, i.e. a time in which 90 % of the final value should be reached. In contrast to the mass spectrometer the Caldos device only measures the hydrogen content. Gases other than H_2 cannot be analyzed by this system.

For the Caldos device as well as for the MS the hydrogen mass flow rate is calculated by referring the measured H_2 concentration to the known argon mass flow rate according to equation (1):

$$\dot{m}_{H_2} = \frac{M_{H_2}}{M_{Ar}} \cdot \frac{C_{H_2}}{C_{Ar}} \cdot \dot{m}_{Ar} \tag{1}$$

with M representing the molecular masses, C the concentrations in vol-% and $\dot{m}$ the mass flow rates of the corresponding gases.

With an argon-hydrogen (two-component) mixture that in fact exists at the location of the Caldos analyzer equation (1) can be written as follows

$$\dot{m}_{H_2} = \frac{M_{H_2}}{M_{Ar}} \cdot \frac{C_{H_2}}{100 - C_{H_2}} \cdot \dot{m}_{Ar} \tag{2}$$

As in QUENCH-10, an **aerosol** collection system was deployed by AEKI Budapest (see Figs. 16-18), comprising two independent devices: a nickel plate with a pocket (Fig. 19) was mounted to collect the larger aerosols and a ten-stage impactor assembly which was actuated for one minute at various times during each of the main test phases (Table 11). As previously, the connection of the sampling line is located 1033 mm from the flange at test section outlet (Figs. 20 and 21).

4 Data Acquisition and Process Control

A computer-based control and data acquisition system is used in the QUENCH facility. Data acquisition, data storage, online visualization as well as process control, control engineering and system protection are accomplished by three computer systems that are linked in a network.

The data acquisition system allows recording of about 200 measurement channels at a maximum frequency of 25 Hz per channel. The experimental data and the date and time of the data acquisition are stored as raw data in binary format. After the experiment the raw data are converted into SI units and stored as ASCII data.

For process control, a system flow chart with the most important actual measurement values is displayed on the computer screen. Furthermore, the operating mode of the active components (pumps, steam generator, superheater, DC power system, valves) is indicated. Blocking systems and limit switches ensure safe plant operation. Operating test phases, e.g. heating or quenching phases, are pre-programmed and can be started on demand during the experiment. The parameter settings of the control circuits and devices can be modified online.

Online visualization allows to observe and to document the current values of selected measurement positions in the form of tables or plots. Eight diagrams with six curves each

can be displayed as graphs. This means that altogether 48 measurement channels can be selected and displayed online during the course of the experiment.

The data of the main data acquisition system and of the mass spectrometers were stored on different computers. Both computers were synchronized by radio-controlled clocks.

The data of the main acquisition system were stored at a frequency of 1 Hz for all test phases. The data of the mass spectrometer were collected with a frequency of 0.4 Hz and afterwards interpolated to 1 Hz to be compatible with all other data.

5 Test Conduct and Pertinent Results

The test conduct is illustrated in Figure 22 together with schematics of temperature, power and mass flow histories. The sequence of events of the QUENCH-11 main test is listed in Table 10. The QUENCH-11 test phases can be summarized as follows.

	Water filling of the bundle to 982 mm elevation. Bundle heatup to ~383 K.
Phase I	**Boil-off** of the water-filled bundle to -190 mm elevation accompanied by bundle heatup (~0.3 K/s to ~1480 K).
Phase II	Continued **boil-off** with enhanced bundle heatup (~0.7 K/s at 1480 to 1830 K and >3 K/s from ~1830 K) with water level kept at the minimum between -190 and -175 mm by injecting ~1 g/s of water.
Phase III	**Quenching** of the bundle by a water flow of 18 (17+1) g/s.

During the QUENCH-11 test a more or less steady evaporation and hence flow of steam through the uncovered part of the bundle should be maintained. The test conduct was based on pretest calculations [12] as well as the pretest QUENCH-11v3. (The sequence of events of the QUENCH-11v3 pretest is given in Table 7 and results of the progression of superheated steam front during boil-off of the pretest QUENCH-11v2 in Table 8). Corner rod B was removed after the QUENCH-11v3 pretest resulting in a maximum oxide scale thickness of ~20 µm (see Fig. 30) and was re-inserted into the bundle prior to the main test.

A steady boil-off and a consequent top-down uncovery of the test bundle was initiated by applying 7 kW of electric bundle power. To assure that water evaporated in the lower plenum, the auxiliary heater was turned on and its power was increased step-wise as the uncovery progressed to a maximum of 3 kW and continued until after initiation of reflood phase. The auxiliary heater thus compensated the reducing rate of boiling from the covered part of the bundle. In order to maintain sufficient level to keep the auxiliary heater covered and thus continue the evaporation rate, water was injected into the lower plenum at a rate of ca. 1 g/s at 2575 s when the water level had fallen to -70 mm. This enabled a nearly stable level to be maintained as well as a constant steam flow.

The bundle and auxiliary power input history is shown in Fig. 23 top and the heating rates of QUENCH-11 in Fig. 23 bottom. The water level in the bundle vs. time is given in Fig. 24 together with power, temperature and hydrogen release histories. Cladding (TFS) and shroud temperature (TSH) readings for the entire test duration are compiled in Figs. 25 and 26, respectively.

A significant delay of the thermocouple (TC) response by comparing the TC levels and the water level indicator (L 501) during the decrease of the water front was observed during the QUENCH-11v2 pretest and confirmed in the main test as can be seen in Fig. 27 and Table 9. The TC signal is a clear indication that superheated steam has locally reached the TC level. With dropping water front the superheated steam follows saturation conditions (boiling water and two-phase region above the water surface).

As the temperatures increased, the onset of significant cladding oxidation was first detected with help of the hydrogen measurement at 4900 s with the maximum bundle temperatures at ca. 1433 K. Minor adjustments were made to the bundle power in order to control the rate of temperature rise to facilitate monitoring of the bundle conditions and control of the approach to reflood initiation.

Corner rod B which had experienced the final pretest as described above was removed for good at ~5490 s, i.e. just before reflood was to be initiated. The maximum oxide layer thickness of corner rod B removed from the bundle prior to flooding was determined to be 170 µm at 950 mm elevation (Fig. 30). During pulling of corner rod B, corner rod D was accidentally moved downward for ~95 mm where it got stuck so that corner rod D could not be removed from the bundle after completion of the test as was planned.

The injection ~1 g/s of water was continued, even during the quench phase. The quench flow of 17 g/s water at 293 K was initiated at 5500 s, according to the criterion of hydrogen generation reaching 50 mg/s, and the water level started rising in the bundle at 5520 s (Fig. 28). The maximum observed temperature in the bundle at this time was 2043 K. At 5560 s the water level has reached the bottom of the heated zone.

Three events occurred within a few seconds after the initiation of bundle quench. Failure of the heater rods was first indicated at 5563 s by detection of helium by the mass spectrometer device (see Fig. 28) and by a small drop in helium rod pressure P 411. There was indication of shroud failure at the same time by a drop in pressure in the annular region between the shroud and inner cooling jacket (P 406 in Fig. 28). Furthermore, it was at almost exactly this time that the melting point of zircaloy (2033 K) was reached and the hydrogen generation rate increased sharply, reaching a maximum of almost 800 mg/s for a short time, before gradually decreasing and eventually terminating during the next few minutes.

At 5573 s the bundle power was reduced to 3.9 kW, approximating effective decay heat levels. Thus the reduced power applied during most of the quench phase. The bundle power was shut off at 5713 s.

The thermal response exhibited two contrasting trends in different elevation ranges. At elevations below 800 mm the progressive filling of the bundle led to a progressive bottom-up

quenching, with no significant temperature increase after the initiation of reflood. Locations above 800 mm exhibited an initial and significant temperature excursion, despite the power reduction, which began soon after the temperature dropped at the lowest elevations and caused temperatures to exceed 2300 K. The excursion corresponded to an increase in hydrogen generation and is attributed to the heat produced by the oxidation which more than compensated the reduction in electrical heating. The delay in bundle cooling due to the relatively low flooding rate is demonstrated quite well in Fig. 28. One can see that the temperature at level 950 mm (TFS 5/13) does not decrease before the bundle and auxiliary power are shut off completely.

In Fig. 29 the evolution of H_2 is to be seen, particularly that the majority of the H_2 is generated when the temperatures exceed the melting point of β-Zr and later of the α-Zr(O). Both diagrams of cladding and shroud temperatures demonstrate a consecutive achievement of the melting point at elevations 950-1250 mm and a decrease in hydrogen generation due to effective cooling. Thermocouples at elevation 850 mm also showed rapid cool-down, but delayed until ca. 5800 s and only after the initial escalation.

The temperature response is consistent with the observed water level in the bundle, which increased more or less progressively up to 800 mm, where it remained despite the continued injection. Refilling was limited by the breach in the shroud, apparently at this level, through which the quench water leaked. Locations above 850 mm were slowly cooled down after terminating the electrical heating, by the combined transfer of heat to the flowing steam and ambient losses, reaching temperatures close to saturation only after a further 3000 s. The quench front progression listed in Table 13 is evaluated from thermocouple readings and pertinent elevations. The times given in this table are those at which the saturation level (boiling point ~395 K) is reached for the first time at the different elevations. The evaluation of the water-steam balance (accumulated masses of water and steam) is provided in Table 12.

6 Evaluation of Hydrogen Measurements

The total generation of hydrogen measured by the mass spectrometer was 141 g, of which 132 g, i.e. more than 90% of the total, was produced during the reflood phase. The corresponding value of the total generation of hydrogen measured by the Caldos analyzer is 114 g.

To determine the portion of hydrogen that results from zirconium-based materials, i.e. prototypical bundle components, the integral hydrogen release is additionally estimated by posttest determination of all oxidized components. This analysis is based on metallographic examination of the bundle and on the procedure described in report FZKA 6968 [21]. It complements and checks the online hydrogen measurements conducted during the experiment.

Because of the limited data available, extra- and interpolations and various estimations had to be made. The assumptions made and the results for the individual components are summarized in Table 17.

The sum of hydrogen produced by the oxidation of the various components (143 g) is in excellent agreement with the value measured online by mass spectrometer (141 g). Obviously, the MS measurements are plausible; of course, the posttest determination method is not able to analyze hydrogen production rates during the test.

92 g (64 %) of the hydrogen released was produced by the oxidation of prototypical bundle components, usually considered in SFD code systems, i.e. cladding tubes, corner rods, spacer grids, and inner shroud surface. 51 g hydrogen resulted from the oxidation of shroud outer surface and melt, heaters, electrodes and high-temperature thermocouples. This has to be taken into account for comparison of experimental and calculated results.

7 Estimated Accuracies of the Measurements in the QUENCH-11 Experiment

The general accuracy of thermocouples is better than ± 50 K. The individual mounting as well as the fluid environment have to be taken into account. In gaseous atmosphere the temperatures measured by surface-mounted high-temperature thermocouples show an up to 50 K lower value than the corresponding cladding temperature. In two-phase flow environment the fin effect may become dominant for these thermocouples (droplets deposition and evaporation). Inner thermocouples do not suffer from such effect, but they show a delay due to thermal inertia of surroundings.

Uncertainty data of various measurement devices given by the manufacturer are:

Device	Operating range	Accuracy
Thermocouples NiCr/Ni (type K)	0-1350 °C	T < 333 °C: ± 2.5 °C T > 333 °C: ± 0.0075•T /according to standard IEC 584-2 (1989)/
Thermocouples W5%Re/W26%Re (type C)	430-2320 °C	± 0.01•T /according to standard ASTM E988 (1990)/
DC generator	P = 0-70 kW	± 0.01•P
Auxiliary heater	P = 0-6 kW	± 0.005•P
Water level transmitter L 501	L = 0-1725 mm	L > 170 mm: ± 0.00038•L L < 170 mm: ± 0.00075•L

The mass spectrometer is calibrated with certified argon-gas mixtures for the non-condensable gases and with a well defined argon-steam mixture for steam. The minimum detectable value for H_2O and H_2 is given to 20 ppm, that for other non-condensable gases app. 1 ppm. The mass spectrometer accuracy is generally better than 5 %. It may be worse (30 %) during the highly transient quench phase with high steam and low argon (reference

gas) concentrations. The time delay of the MS measurement is short; test measurements with hydrogen injection into the bundle resulted in values less than 5 seconds.

8 Results of Aerosol Measurements (AEKI)

After the test the aerosol samples were delivered to AEKI, and the posttest examination was carried out in Budapest, Hungary [19]. The examination included

- Mass gain measurements,
- SEM and EDX analysis,
- Application of mass spectrometric methods.

The largest amount of aerosols was found on the last impactor that was activated at ~2000 ^{o}C temperature indicating a correlation of aerosol release and oxidation process.

In accordance with the results of the SEM+EDX and those of the SSMS (Spark Source Mass Spectroscopy), the escaped aerosol contained different elements depending on the phase of the experiment.

In the collector samples working in the whole period, Zr, Sn, Fe, Cr and Zn were detected besides some impurities. At the high temperature stage, Ta and Hf appeared. Most of the “interesting elements” were detected in the quenching phase. In collector samples Nos. 7 through 10, Zr, Sn, W, Mo, Ta, Fe, Cr, Ni were found. It is a typical feature of the sample series of this experiment, that W, i.e. the material of the heating rod, was an element which could be detected frequently. It was found on some of the collector plates and on some quartz fiber filters, further on the Ni plate. Its appearance in the aerosol shows that the temperature was high enough. Zr, Mo and Y were found in the powder collected in the pocket. Interesting that rather high amounts of Mn were found by SSMS on the Ni plate.

The analysis pointed out that most of the released aerosol originated from the structural elements of the facility and not from the fuel bundle. Contrary to the QUENCH-10 test no Zr was found by SSMS on the impactor samples, only in the pocket of the Ni plate.

So, the most important conclusions based on the comparison between the QUENCH-10 test carried out in air atmosphere and QUENCH-11 performed in steam with respect to aerosol release are the followings:

- reduced amount of Zr containing aerosols was observed in steam conditions, i.e much less in QUENCH-11 than in QUENCH-10,
- in QUENCH-10 the steel components were found most frequently in the aerosols,
- in QUENCH-11 W, Mo and other impurities were the dominating elements in the released aerosols.

9 Posttest Examination

9.1 QUENCH-11 Posttest Appearance Prior to Bundle Sectioning

Fig. 31 (left) demonstrates the posttest appearance of test bundle and shroud before removing the thermal insulation of the shroud. During dismantling the shroud fell off above an elevation of ~1000 mm (see photograph on the right hand side of Fig. 31). After dismantling the QUENCH-11 bundle and its shroud appear severely damaged, i.e. in the region above ~750 mm the shroud and bundle were partially molten, and the shroud was shaped to a large "bubble" (Figs. 32 and 33), similar to the QUENCH-07 and QUENCH-09 test bundles. A look into the test bundle at ~800 mm elevation showed melt rivulets solidified in the flow channels. Furthermore, the shroud in the bubble-shaped region is severely oxidized and has reacted with the ZrO_2 fiber insulation.

The photographs which were taken by a videoscope system inserted into the bundle from the bottom (-50 mm elevation) at the (voided) position of corner rod B demonstrate loose debris at the top of grid spacers 2 and 3, i.e. at 150 and 550 mm elevation, respectively (Fig. 34), and circumferential cracks of rod claddings as well as relocated molten debris at 650 and 770 mm elevation in Fig. 35.

9.2 Encapsulation and Sectioning of the Test Bundle

For encapsulation the test bundle and shroud are set up vertically. Prior to filling, a cap is placed over the bottom of the copper electrodes and a low-melting metal alloy (similar to Wood's metal containing 48 % Bi, 18 % Pb, 23 % In, 11 % Sn; density of ~10 kg/dm^3; melting point of 331 K) is used to seal the bottom of the bundle. The low-melting metal is also used for sealing the bundle foot so that it can be re-used for the next experiment. For this purpose an inner cage is inserted into the bundle foot from the bottom. Filling of this auxiliary structure is from above the bundle foot, i.e. through holes in the shroud at elevations above –300 mm. Then a plexiglas® tube as mould with an inner diameter of 190 mm is put over test bundle with shroud and fixed at the flange of the bundle foot by a glue (see also schematic in Fig. 36). Encapsulation of the bundle is performed by filling the mould with the epoxy resin (Bakelite EPR 0273 with the pertinent hardener Bakelite EPH 350) from the bundle foot over the entire bundle length. The epoxying process generally shows a little heating due to the exothermal heat that develops during the curing stage and some shrinkage effect. Scale readings on the mass gain of epoxy resin per cm of filling are recorded and given in Fig. 84 and Table 15, respectively. The photographs in Fig. 37 show two consecutive steps of bundle filling. After epoxying the bundle the resin is allowed to harden for one week. Sectioning of the bundle is done by a saw with a diamond blade approximately 3 mm thick and with an OD of 500 mm. The elevations of the cross sections are listed in Table 14. Figs. 38-41 present an overview of the QUENCH-11 cross sections available. They are described and interpreted in the subsequent sections.

9.3 Metallographic Examination

9.3.1 Investigation Procedures

The post-test examination of the bundle is based on the metallographic preparation of cross section slabs (generally of the top side) by careful grinding and polishing, the visual inspection, and a comprehensive photo documentation. The evaluation uses a selection of the available macrographs and micrographs for illustration within composed, thematic figures. The final bundle state is described, and an interpretation is given, as far as possible, of its behavior with respect to different aspects: The mechanisms of the physical-chemical interaction of the components and of their oxidation are deduced, paying special attention to the cladding oxidation and to consequences of the rising water level and the increasing evaporation during the final phase. Supporting information on the bundle status has been gained by scanning electron microscopy (SEM), using the secondary electron (SE) image contrast and the energy dispersive X-ray (EDX) analysis for element identification. The bundle is described from bottom to top, following the increase in extent of interactions with increasing temperature.

The oxidation extent of the corner rod B as function of the elevation in the bundle was determined by a non-destructive technique based on the eddy current principle (pre-test and main test), as well as by scale measurement for polished cross sections (main test only). (As already mentioned, corner rod B was withdrawn from the bundle after the QUENCH-11v3 pre-test for non-destructive oxide scale thickness measurement, re-inserted for the main test into the bundle, from which it was removed at the end of the transient phase, just before refill.) For the bundle itself, the scale thickness on simulator rod and corner rod surfaces as well as inner shroud surfaces was measured. This was done, if possible, in four directions around rods and shroud, and for all prepared cross sections. The scale thickness of the outer shroud surface was determined metallographically only at 1250 mm bundle elevation. It was not possible to determine the oxide scale of the outer shroud surface at other levels due to spalling effects.

9.3.2 Axial Distribution of ZrO_2 Scale Thickness

For the corner rod B, Fig. 30 summarizes the results of the eddy current and the metallographic method of scale thickness measurement, plotted against the axial elevation of the rod in the bundle. The scale thickness profile gained after the pre-test, and that determined for the rod condition after removal near the end of the transient in the main test, give a common peak position at 950 mm elevation. For the main test, a satisfying correspondence in peak shape and maximum determined by the independent methods has been registered. (Note: The eddy-current measurement is not presented in this figure.)

The scale thickness measurements performed for the bundle at the series of cross-section elevations are compiled in Figs. 42-46. The lateral variations turned out to be small, corresponding to rather flat lateral temperature profiles. With increasing elevation and related to melt relocation, some local scatter was realized. Moreover, loss of cladding wall by melt relocation or apparent gain of thickness by accumulated metallic melt, respectively, is the simple reason for smaller or larger resulting values of locally measured scale thickness, and thus deviation from the idealized standard value.

The determined axial scale thickness profile, as given in Fig. 47, combines the separate results for simulator rods, corner rods, shroud inner side, with the standard deviation range of the simulator rods. Accordingly, the extent of oxidation is rising steeply from unimportant values for the lower levels to complete cladding oxidation, which is reached for all rods at 900 mm and is maintained in the upper electrode zone.

9.3.3 Documentation and Interpretation of the Bundle Status

Cross sections QUE-11-1 and QUE-11-2 (bundle elevations 650 and 750 mm)

The top sides of the cross section slabs QUE-11-1 and QUE-11-2 are depicted in Fig. 48, both in top view towards south direction. The overview at 650 mm bundle elevation, which includes the conventional rod numbering, shows the intact arrangement of the fuel rod simulators, the three remaining corner rods (corner rod B removed in the transient test phase), and the shroud. A fallen shroud fragment and some other rubble are present in addition. In the 750 mm overview small amounts of melt are seen, apparently relocated by falling or candling, respectively. The aspect of melt relocation will be covered later and in detail for elevations for which it is essential. The oxidation state of two rods (marked in red in the overviews) is illustrated in Figs. 49 and 50. At 650 mm (Fig. 49) the cladding of both rods shows thin scale. In polarized light contrast the grains of the α-Zr(O) layer and the beginning grain growth of the β-Zr matrix are better visible. The latter indicates a peak temperature close to 1000 °C. For the 750 mm level (Fig. 50) much thicker and still protective scale, block-shaped α-Zr(O) layer, and coarse β-Zr matrix microstructure are typical. In conclusion, the lower three quarters of the heated bundle length are found essentially intact, despite all the changes of exposure conditions in the course of the experiment.

Cross section QUE-11-6, bundle elevation 810 mm

This elevation has been chosen for cross sectioning as the lower limit of meaningful melt relocation within the bundle and related to the shroud. Fig. 51 gives the overview together with a magnified view of the NE bundle quarter, at which the agglomeration of such melt is most obvious. The distribution of melt in the bundle indicates distinct relocation events, stopped at the temperature of re-solidification. Advanced shroud degradation on SE at the external side has given rise to a concentration of melt at this orientation and its extension into the fiber insulation package.

Abstracting from the heat transferred by the melt lumps and its release during solidification, the solid structures are comparatively intact, as documented in closer view in Figs. 52 and 53 for two groups of rods: For one group (Fig. 52), no melting of the rod cladding is identified, and practically no internal oxidation could take place in spite of local contact with the simulator pellets after gap closure. For the other group (Fig. 53), some internal cladding melt relocation took place, according to the voids, seen e.g. for rod 10 at bottom/left. The lower limit of melting, ~1760 °C, was not exceeded enough and sufficiently long to initiate any important chemical interaction between cladding and pellet.

The interaction of rods with relocated melt is documented in Figs. 54 to 58. A melt “pillow” between shroud and rod 12 (Fig. 54, left) is found disrupted from the fractured shroud and in

contact with the rod. In the final state the scales of melt and rod form a common enclosure, though the rod had been oxidized at the whole circumference at the time of melt relocation. This apparent contradiction is resolved in the “necking” mechanism: The contact is stabilized by the dissolution of embedded scale, which is not only isolated from steam, but loses oxygen due to diffusive transfer into the metallic melt and the cladding matrix. The neck has to be seen as axially elongated contact area. The same oxidation / scale dissolution sequence explains the also depicted neck formation between rod 13 and a melt rivulet, which contains a void, into which steam access was provided. The elements of the given description are sufficient to explain the melt agglomerate between neighboring rods in Fig. 55: Separate necks have formed, steam access was provided to channels within the incoherently relocated melt rivulets, and embedded scale got dissolved. Figs. 56 and 57 provide more detailed information in higher magnification. Illumination in polarized light (Fig. 56) shows that the cladding scale of rod 9 consists of a columnar external sub-layer, grown at lower temperature and cracked, a tetragonal part, and the inner, previously cubic part, both intact and coarse-grained. Below the scale, the α-Zr(O) layer, the cladding core of previous β-Zr, an inner α-Zr(O) layer, a thin ZrO_{2-x} interaction layer, and the ZrO_2 pellet follow. Fig. 57 shows the contact between cladding and melt with increasing magnification. The larger oxygen content along the contour of the mostly dissolved scale and within the melt compared to the cladding is obvious from the remaining or precipitated ZrO_2 lace or particle distribution, respectively. Fig. 58 deals with the melt oxidation state at the cut through another melt rivulet: A duplex tetragonal/cubic scale is found according to growth within the stability range of the cubic modification. The metallic matrix of the melt contains considerable fractions of ceramic precipitates, namely ZrO_2 phase. By SEM/EDX analysis only the elements Zr, O, and Sn, but no contamination were found, confirming the cladding origin. Notice further the diminished scale growth for both structures within the narrow gap between melt and shroud due to limited supply, and the avoided neck formation.

The description of the level is concluded by summarizing the shroud damage. Fig. 59 compares melt microstructures in high magnification: Close to the internal shroud scale, the microstructure looks as expected for melt from shroud origin. However, the SEM/EDX analysis at different spots within a small area has identified the presence of different phases, precipitated from the (Zr,O) matrix, and containing Ta as main, and Cr, Fe, and Mo as minor constituents. Thus, contaminations are identified, attributed to thermocouple sheath, stainless steel wire used for insulation package fixing, and the degradation of the upper rod electrodes in the late phase of the test. (More information on SEM/EDX results will be given for higher elevations.) Below the outer rim of the melt agglomerate, where a scale was formed under steam after shroud melt-through, the melt microstructure looks as if it would indicate embedded individual ZrO_2 fibers of the insulation package, or an extra oxygen fraction from fiber consumption. The void formation within the shroud melt was not expected because it cannot be interpreted by partial relocation, since this is the lowest level of re-solidification. The time of fracturing events cannot be deduced from minor or missing scale formation along the cracks, because the local temperatures during the last phase of the experiment are not known.

Cross section slab QUE-11-3, bundle elevations 837 (bottom) and 850 mm (top)

In Fig. 60 the bottom of the slab macrograph is shown mirror inverted to facilitate the comparison with the overview at the top side. Along the axis of the thin slab the rod arrangement is almost identical, whereas the melt agglomerates show more axial variation: At the higher level the melt lump between the outer shroud shell towards SE and the bundle is more massive and voluminous, and more inward extended. Notice that the shroud segment towards W is an inner partial shell, and that all other parts of the shroud are missing due to breaking off during test section dismantling. The essential melt agglomerates within the bundle are more dense at the lower level compared to larger voids at the higher one. The partial enclosure of corner rods A, C, and D by melt follows from their contribution to meltdown. Notice further that the shroud has limited the lateral melt distribution at the NE bundle corner. In the following, more information is given on the oxidation state of the rods and the melt microstructure.

Fig. 61 compares the two cross sections at top and bottom elevation, respectively, for three rods, shown as examples. The more advanced cladding oxidation at the higher level is obvious in spite of the close axial distance. Moreover, for rod 7 the dissolution of melt embedded cladding scale is more advanced at top level, due to the higher temperature. Melt movements did not follow straight downward paths. Notice melt relocation within the annular pellet of the central rod, stopped above the bottom level. For more details Fig. 62 illustrates the oxidation state of rod 6 as typical example of the partial cladding consumption at the bottom level. More available micrographs than documented confirm that the cladding scale consists of a cracked outer sub-layer, a dense tetragonal one, and an inner previously cubic sub-layer. The cladding matrix consists of α-Zr(O) phase containing ZrO_{2-x} precipitates. In contact to the pellet and due to oxygen diffusion an interaction layer of ZrO_{2-x} was formed. It is mentioned that the double-sided oxidation of the cladding often leads to the formation of tin enriched phase, which marks the oxygen poor cladding core, previously consisting of β-Zr phase. Fig. 63 illustrates the range of cladding oxidation extent for the top level. Rod 16 shows a quite similar state as described for the bottom level in the previous figure: The external scale can be seen as composed of sub-layers; remaining metallic cladding with voids from cladding relocation, and an interaction layer follow towards the pellet. As result of higher temperature, the cladding of rod 12 is completely converted to a coarse-grained ceramic oxidation/ interaction product. The radial position of voids, formed by local relocation of melt from the metallic cladding core, indicates the competition between the oxygen diffusion from both sides, steam and pellet. After having summarized the status of the rods, the melt agglomerates will be characterized and documented by several illustrations:

Figs. 64 to 66 are dedicated to the melt agglomerate towards NE. Fig. 64 illustrates for bottom elevation 837 mm the non-coherent development of melt relocation: After considerable oxide formation due to steam exposure of a first melt rivulet, more peripheral rivulets have covered such scale. In the final state those rivulets show own oxide formation as well, whereas embedded scale is mostly dissolved. The presence or absence of an oxide rim allows to distinguish open channels from closed voids. Fig. 65 depicts for the same level the microstructure of re-solidified (first rivulet) melt in high magnification. ZrO_{2-x} phase primary crystal growth from the melt results in a dendritic distribution within the α-Zr(O) matrix. Such a perfectly undisturbed melt decomposition should have proceeded under slight

sub-cooling conditions, plausibly related to the continuing melt relocation around. The cladding of rod 9 at the melt-embedded position has exceeded the melting temperature and re-solidified as well, according to the quite similar microstructure. For the top level 850 mm, the macrograph in Fig. 66, depicting the NE bundle corner, shows the partial embedding of several rods by melt which is containing some large voids, isolated from steam access. The microstructure of this melt compared for two positions in large distance does not show much difference, and is also comparable to the melt microstructure at the bottom level, described above: ZrO_{2-x} phase primary crystals, distributed within the α-Zr(O) matrix phase, have similar size and fraction.

The melt at NW and at S is illustrated in Figs. 67 to 69 for bottom and top elevations: At NW and the bottom level according to Fig. 67, the melt between four rods is compact except crack formation during re-solidification, and contains only a small fraction of ZrO_{2-x} phase precipitates. It is clear that the source was poorly oxidized cladding from higher elevation, and the oxide scale around the rim of the melt indicates rather early relocation. Fig. 68 shows for the top level at comparable NW position a higher fraction of ZrO_{2-x} phase precipitates in the melt matrix, related to a higher oxygen content. The other depicted melt (right side) leads over to the large melt agglomerate at south of the bundle. In the given typical example the much higher oxygen content of this melt is most obvious: ZrO_{2-x} phase dominates, and α-Zr(O) phase decorates the narrow rims of those primary crystals. The character of the originally metallic melt pool has changed to ceramic. Fig. 69 comes back to the bottom level of the melt at S. Here the change to a ceramic character is less advanced: Dendritic ZrO_{2-x} phase growth with more residual α-Zr(O) phase has taken place. The melt microstructure is similar to that of the once molten cladding of a neighboring rod.

Fig. 70 shows typical microstructures of the shroud at SE in different magnifications. The phase distribution within this previously molten structure is comparable with that shown and described for the 810 mm level (see Fig. 59).

Cross section slab QUE-11-3, 837 (bottom) and 850 mm (top)

In the following, results of SEM/EDX analyses are presented, which were necessary for the explanation of melts with other character and origin, and for conclusions about the suspected contaminations of cladding and shroud melt at various positions. This treatment allows summarizing statements for the cross section slab and refers to confirmation, which will follow for the 900 and 950 mm elevations. As coarse explanation in advance, the superheating of the test section including structural components at high elevation has given rise to interactions, oxidation of products, and relocation of multi-component melt.

Fig. 71 deals with the metallic melt, found distributed close to the central rod. The figure shows the analysis position as given in the SEM secondary electron image and the obtained EDX spectrum for the area (top and bottom, left). The Mo peak in the spectrum is dominant enough to conclude, that Mo is the main component, that Zr and Sn are present, and that W seems to contribute as well. For comparison, the SEM/EDX element spectrum of the ZrO_2 scale of cladding melt is included in the figure, in order to stress that this scale has grown and remained non-contaminated. The metallic state of the Mo-rich melt and its distribution on

top of cladding melt indicate relocation during the final phase of the experiment, related to the temperature escalation above the electrically heated zone of the bundle.

The destruction mechanism of the Mo electrodes and the conditions leading to W heater rod degradation are interpreted for another position: Fig. 72 illustrates the contamination of the agglomerate of shroud melt at SE orientation (Pos. s-1-1). The light-optical micrograph gives an indication of the composition variations around a certain embedded melt lump close to rod 13, which was analyzed in detail. Accordingly, this melt lump shows a dendritic microstructure, resulting from decomposition during re-solidification. The EDX element spectra allow the conclusion that dendritic primary crystals, rich in Mo and W with some oxygen content (spot 2), have grown in the residual molten matrix, which is rich in Zr and contains Sn, Ni, Fe, O, and some Mo. In the residual melt, the Mo signal might be only due to the close Mo rich phase, but the identified Ni and Fe peaks indicate a contribution of stainless steel. The same melt lump was analyzed at top position (Pos. top_melt-rod 13-2-1); the confirmation of the described dendritic microstructure and composition is mentioned. One could speculate that Zr rich superheated melt was able to dissolve the metals Mo and W as soon as direct contact was given: Of course, heater rod dissolution could not occur, before pellet fragmentation or infiltration, electrode dissolution would only proceed after failure of the ZrO_2 protection layer. The relocation of such molten dissolution products should thus have occurred later than the relocation of pure cladding and shroud melt, consistent with the observed melt distribution. But the high Mo content in the melt is the reason of some doubt in a simple dissolution process.

It is misleading, to expect for Mo and W the physical behavior of refractory metals (T_m ~2620 and ~3410 °C, respectively), and to neglect their chemical properties. Since both metals do not form protective scales and oxide sublimation can play a role as well, their stability under oxidizing conditions is rather limited. According to literature on the Mo-O system [20], the oxide MoO_2 has a melting point of 2300+/-150 °C, and forms together with the metal an eutectic system with eutectic point data 2150+/-100 °C and ~4.5 mass-% O. Accordingly, a field of eutectic melt is extending from the given composition to both sides at temperatures above. Most often, third interaction partners expand melt regimes to lower temperatures compared to the binary systems. In the given case, the degradation of Mo electrodes could be due to, or more probable, could be enhanced by steam attack, eventually in combination with the attack of Zr-rich melt. The wide spread distribution of interaction products supports the assumption of various melt sources and variable degradation speeds, and secondary interactions complicate the final state further.

EDX analysis results for other positions at the 837 mm level and within the melt agglomerate at SE are summarized without illustrations. At one of two positions (Pos. s-2-1), close to the above analyzed lump and to rod 13, three phases can be distinguished by image contrast and element signals, two Zr phases and a (Zr,W,Mo) phase. At the other one (Pos. s-2-2), the area analysis has identified the main components Zr, Mo, and W, whereas spot analysis at various positions has distinguished Zr-rich phases (Zr,O; Zr,Sn; Zr,Mo) from (Mo,W,Zr)-phase. Spot analyses within two further fields (Pos. s-1-2-1 and s-1-2-2) confirm the presence of various phases between ZrO_2, $(Zr,Sn)O_2$, Zr(O) on the one hand and mostly metallic (Mo,W) on the other hand. At top elevation (Pos. top_melt-rod 13-1) mostly oxidized (Zr,O,Sn) melt was identified close to the once molten rod cladding.

The indications given by the analysis should be sufficient in the context of this report; much more effort needed for quantitative phase analysis and statistical evaluation would not be justified, inasmuch as the melt formation and interaction conditions are not sufficiently accessible.

Cross sections QUE-11-7 and QUE-11-4, bundle elevations 900 and 950 mm

Both cross section elevations, which represent the hottest region during almost the whole duration of the experiment, are described in close connection to facilitate the comparison. The overviews in Fig. 73 represent the completely oxidized rods, demonstrate the corner rod destruction, and give an impression of the complexity of melt formation and movement. Besides serious cladding degradation, some rods show pellet damage at the 900 mm level, and in addition even heater rod damage at 950 mm. The most obvious items concerning the shroud are the expansion of the outer part, the porosity within those structures, melt retention within the gap (only at 900 mm), and the deformed scale segments of the inner shroud surface contour.

The same selection of four rods is depicted in Figs. 74 and 75 for the both elevations. For 900 mm, previous cladding melt relocation is indicated for all the rods by the generated voids, melt release can be assumed to have occurred for two of them (Fig. 74, bottom). Remnants of oxidized pellet interaction zones are identified for all depicted rods. The previously discussed Mo-rich melt is still mostly metallic, and found dispersed within oxidized cladding melt. In comparison, Fig. 75 shows more advanced cladding damage, and more melt release is plausible to have occurred: At the time of cladding melting, the oxidation was less advanced (compare cladding scale remnants for both figures), so that easier melt penetration should be the reason.

Fig. 76 illustrates the melt conglomerate of Zr- and Mo-rich zones, the difference in their oxidation state, the limited effect of Mo-rich melt in contact to the pellet of rod 2, and the EDX analysis of its composition. The melt of cladding origin is fully converted to ceramic, The Mo-rich melt contains Zr, Sn, W, and some Cr, Fe, and O, confirming previously given analysis results. The melt is metallic, but the obvious penetration into the ceramic pellet along the grain boundaries indicates good wetting. It is not clear if an interaction with the pellet combined with oxygen transfer takes place under the given conditions. In relation to the Mo-rich melt, SEM/EDX results gained at the next higher level 950 mm between rod 3 and 4 are given without illustration: The matrix phase within this melt was found to consist only of Mo with small amount of Ta (from thermocouple sheath involvement), but no Zr, whereas small volume fractions of grain boundary precipitates are identified as (Zr,Sn,O) or the respective oxide, or as (Zr,O) plus (Zr,Sn) (at Pos. 3-4_1-1 or Pos. 3-4_2-1, respectively). The results for both analysis positions confirm a smaller fraction of Zr for the melt compared to results for lower elevations.

A separation of the shroud into outer and inner shells, occurring after melting and related to external oxidation, has been found as for several previous QUENCH experiments. As example for retained melt within the gap, a lump at NE is illustrated in Fig. 77. The melt, fixed by loose contact to the fully oxidized inner shroud rim, is showing an own oxide scale and a mostly converted matrix according to the high fraction of precipitated ZrO_{2-x} phase.

Contamination is indicated for the melt by SEM/EDX analysis: According to a small-area spectrum (Pos. -ne-1-1_area), some Mo is detected in addition to Zr, Sn, and O; spot analyses distinguish besides ZrO_2, Zr(O), and (Zr,Sn) a metallic (Zr,Mo,Sn) phase enriched in Mo. At the same NE orientation, the external shroud shell is depicted in Fig. 78. The duplex phase microstructure looks as described for lower elevations. Full conversion to oxide is seen at the outer surface and for an inner band. The presence of large voids cannot be decisively explained. Their rounded shape and their distribution may be due to formation by the evaporation of a certain gas from the melt. Since less voids were found at lower elevations, melt superheating may be necessary for gas bubble formation. One can speculate about an effect of stabilizer elements in the ZrO_2 fiber insulation package, which got partly dissolved already prior to shroud failure and steam outward leakage. The presence of melt porosity is confirmed besides the melt microstructure itself for the outer shroud zone in SE direction, according to Fig. 79.

The described and commented results of the investigation of the shroud remnants at 900 mm are comparable with the state at the elevation 950 mm: The inspection and photo documentation for this level at NE and SW has confirmed the partial conversion from the molten and metallic to ceramic products and also the presence of porosity, so that no illustration is presented here. Some damaged heater rods reflect the high peak temperatures, finally reached at this level: After serious degradation of cladding and pellets, as shown in Fig. 80, the depicted rods have lost visible to considerable fractions of their cross section. Since the interaction products have vanished or are not obvious, the mechanism is not known in more detail than discussed earlier. Steam oxidation and oxide sublimation may have contributed to a dissolution mechanism, in which oxygen pick-up from molten cladding or (Zr,Mo,O) melt should have initiated the formation of composed eutectic product melt. Finally bare positions around the heater rods may have been affected by previous exposure to such melt, as well. It appears convincing to assume the role of oxygen exchange as dominant factor for the degradation.

Cross section QUE-11-8, bundle elevation 1000 mm

The state of the whole test section close to the upper end of the electrically heated zone is depicted in Fig. 81. Accordingly, all rods show serious and similar damage, whereas remaining melt is mainly distributed in the central part of the bundle and not retained around. One can conclude that melt relocation was complete in the periphery, and that further relocation from central, higher elevations has compensated loss of melt in the center. Fully oxidized cladding melt can be distinguished from metallic melt of Mo electrode origin. None of the heater rods shows the large mass loss, mentioned for a few heaters at 950 mm, but here all of them show surface roughness in higher magnification, indicating some attack. The residues of a porous shroud melt are found as ceramic shell structures. The bundle degradation history is described referring to the depicted rod 19 (Fig. 81, right): After growth of a relatively thin cladding scale, melting of the rod took place, as consequence of fast heat-up. Favorable melt release and relocation conditions have terminated the interaction of the oxygen-poor melt with pellets at all positions, for which no melt remained at place. Generally, retained melt was not able to dissolve embedded scales or to degrade pellets to important extents before getting completely converted to the ceramic state. The distribution of the melts, relocated from above, is too complex to be commented in more detail than the

following: The clear boundaries between ceramic and metallic fractions, Zr-rich and Mo-rich, indicate that the Zr-rich material is able to oxidize due to high affinity to oxygen, instead of losing oxygen by transfer to the Mo-rich melt.

Cross section QUE-11-5, bundle elevation 1050 mm

The elevation to be described is close above the lower limit of the upper Mo electrodes (1024 mm). According to manufacturing and rod assembly, the Mo rods were provided with a plasma sprayed ZrO_2 protection layer, onto which the cladding was forged for good thermal contact. At this level a zircaloy spacer grid was installed. Compared to those initial conditions, the cross section overview in Fig. 82 represents the arrangement of electrodes, damaged along most of their contours. The cladding is found opened after splitting and outward bending ("flowering"), and partial fracture into relocated rubble. Only some more straight structures are to be identified as spacer remnants. Re-solidified melt of cladding origin is dispersed between the rods and oxidized. Melt in close contact to individual rods is addressed for the typical rod, depicted to the right in Fig. 82: One can distinguish circumferential positions with intact ZrO_2 layer from others, at which melting has occurred. The previously given interpretation of Mo dissolution seems to be confirmed, namely the steam oxidation of Mo and the eutectic melt formation, known for the Mo-O binary system. Some of the molten product material is present, another fraction has relocated, according to many visible voids between the massive rods and their protection layer.

A crude estimation of the peak temperature within the electrode zone is based on the Mo-O phase diagram information, the extent of melt formation and large distance relocation, as well as the limited time period of electrode zone escalation during the quench phase of the experiment. Accordingly, the peak temperature should have been about 2500 to 2600 K to explain the massive degradation of the Mo electrodes. This result seems to be consistent with several thermocouple failures in a range up to 2400 K.

Cross section QUE-11-shroud at 1250 mm elevation

A cross section of the removed upper part of the shroud at the given elevation has been prepared and investigated separately, in order to get information about oxidation state and peak temperature. The shroud oxidation from both surfaces follows from steam leakage after shroud perforation. Inspection at N showed a not much smaller external oxide scale thickness compared to the inner one, as expected for shorter duration of steam exposure but otherwise comparable conditions at both surfaces. The presence of prior β-Zr phase in solid state according to the martensitic microstructure indicates a peak temperature not exceeding β-Zr melting (for the non-oxidized alloy ~2030 K, here some tens of K higher). At S direction, one of the investigated positions has confirmed those conclusions totally, according to the ZrO_2 + α-Zr(O) double layers sequence and the β-Zr matrix contrast in polarized light. At the other, directly adjacent position, the β-Zr matrix underwent incomplete meltdown, leading to the exposure of α-Zr(O) and β-Zr residues to steam, and indicating an estimated peak temperature in the range 2050 to 2100 K.

Fig. 83 illustrates the final state for an inner shell position. The inner scale (overview) is seen to consist of the primary part as formed by solid state oxidation (no micrograph) and a

secondary part (left, bottom), next follow the partly oxidized melt (β- to α-Zr(O) conversion, ZrO_2 phase precipitation), and the ZrO_2 "crust", scale formed on the melt (right, bottom and top).

Summary and Conclusions

Complementary information on the QUENCH-11 experiment has been gained by a comprehensive metallographic post-test examination of the rod bundle on cross sections at several elevations, including cladding scale thickness measurements and SEM/EDX analyses. The results are given and discussed on basis of the degradation phenomena, deduced from the final bundle state.

Up to about 800 mm the bundle is intact, and the rod claddings show protective external scales of axially increasing thickness. Internal cladding oxidation in contact to pellets is obvious for the 810 mm level, at which gap filling versus void formation due to internal melt relocation took place. Considerable amounts of melt of rod and shroud origin are kept here and above; only small fractions of relocated melt are found down to 750 mm. In its lower range, the partial flow channel blockage has been formed by non-coherent melt candling and re-solidification in consecutive events: Melt rivulet flow proceeded with poor cladding wetting, and pillow formation was favored. Embedded cladding scale got mostly dissolved during the continued growth of scale at the steam exposed surfaces of the metallic melt itself, so that "necks" between rod and melt are formed, surrounded by common scale. Rivulets relocated later are seen to have dissolved covered scale of earlier melt. At other positions voids, which became isolated from steam access, can be distinguished from open flow channels. In the center of the partial blockage and around the elevation 850 mm, an additional melt type was analyzed to contain, besides Zr and Sn from cladding origin, Mo and W from the degradation of electrodes and heater rods, which is obvious at higher elevations. (Both refractory metals are known to form multi-component melts in case of oxidative attack and far below their own melting points.) Here, ceramic residues of converted cladding and the pellets remain without excessive fragmentation.

In the transient and the reflood phase of the experiment, the accelerating temperature increase together with the moderate evaporation rate have given rise to a continuing upward movement of the escalation front into the upper electrode zone. This indicates that sufficient steam was available for oxidation during the entire test. The involvement of facility specific molten products, the presence of a thick-walled shroud, and the restriction related to the simulation of fuel by zirconium oxide pellets have to be taken into account, but the gained results are qualitatively prototypical: In anticipated LWR accidents of this type, elongated partial blockages of the observed character would be formed, containing considerable fractions of dissolved and thus relocated fuel. In respective refill scenarios, temporal damage progression to higher core elevations would take place.

The behavior of the two fuel rod simulators made with duplex claddings of the "DX-D4" type did not show differences to those with zircaloy-4 claddings.

9.3.4 Global Assessment of Melt Distribution in the Selected Cross Sections

To determine the area occupied by structural parts (rods, shroud, pellets, melt) in cross-sections along the bundle elevation, the data of the mass of epoxy that has been filled into the bundle can be used. As mentioned above, these data was gained by measuring the epoxy consumption for every 10 mm filling level during embedding (Table 15). With the known density of the epoxy (1.1 g/cm^3) the volume of it, and therefore the cross-sectional area occupied by it, can be calculated in steps of 10 mm. As a negative of this area the structural area is obtained. Fig. 84 illustrates the results of bundle filling listed in Table 15. Inserted epoxy mass per 10 mm (top) and cross-sectional area of the material (bottom) are plotted versus elevation. Smoothing of the data by averaging over 5 points was necessary due to considerable fluctuations. To judge the accuracy of this epoxy method it has to be kept in mind, that with every 10 mm the empty Plexiglas mould, without any structural parts inside, could be filled with 302 g epoxy. Filling the mould with an inserted undamaged bundle would take a theoretical amount of 273 g of epoxy per 10 mm. So the structural parts, analyzed here, make a difference of only 29 g (~10 %). In addition, errors due to voids and blind holes and the fact that an unknown amount of fiber insulation got involved into the melt pools between ~800 and 1000 mm lead to the impression of an overall gain of structural area without losses in the same dimension elsewhere.

Finally, a very rough axial profile of masses is obtained by looking at the masses of all cut segments (those intended for polishing and the slabs between them).

Bundle segment	Bottom, mm	Top, mm	Thickness, mm	Sample mass, g	Rel. mass, g/mm
QUE-11-d	544	634	90	4761	52,90
QUE-11-1	~636	650	13,9	718	51,65
QUE-11-6	~793	810	16,9	882	52,19
QUE-11-f2	813	835	22	1224	55,64
QUE-11-3	~838	850	11,5	771	67,04
QUE-11-g1	853	880	27	1758	65,11
QUE-11-7	~883	900	17,3	1041	60,17
QUE-11-g2	903	935	32	1934	60,44
QUE-11-4	~939	950	11,4	678	59,47
QUE-11-h1	953	981	28	1606	57,36
QUE-11-8	~982	1000	18,1	991	54,75
QUE-11-h2	1002	1034	32	1591	49,72
QUE-11-5	~1038	1050	12,0	526	43,88

The mass of epoxy of each segment has not yet been subtracted in the last column of the table given above to obtain the mass of structure. Between 650 and 790 mm the epoxy mass cannot be subtracted because the data are not complete for any of the three segments. Fig. 85 shows the resulting masses. Assuming that there have been no major changes in heaters and pellets, the sum of masses of cladding, shroud and relocated melt (dark pink color) can be determined. Additionally a comparison to the original bundle structure is drawn (light colors). Again, the unknown mass of fiber insulation together with the fact that the axial profile is only patchy, gives the idea of mass gain only, without mass losses. All the data have to be judged carefully.

A second method for determination of melt distribution are direct measurements of areas by means of image analysis (Figs. 86-88). These works have been performed on the polished surfaces at 750, 810, 850, 900, 950, 1000 and 1050 mm. It was also tried to determine the areas of cladding, pellets and heaters because for elevations at 900 mm and above there actually have been changes in pellets and heaters. So wherever possible, up to seven different fractions have been discriminated: Metallic melt of zircaloy origin between rods, oxidic melt of zircaloy origin between rods, metallic melt of electrode origin between rods, oxidized cladding, metallic cladding, pellets, heaters/electrodes. In respect to shroud, only data of 810 and 850 mm were collected, for higher elevations the influence of the fiber insulation is indeterminate. All the data collected thereby are summarized in Table 16. For the evaluation of these data one has to keep in mind, that the data are obtained by looking at the surface of each polished disc only, thus giving single two-dimensional snap-shots at different elevations, not the complete data of all the three-dimensional space between them.

Some remarks on how the data were obtained: The values for zircaloy cladding and oxide scale at 650, 750, and all but six rods at 810 mm are calculated from the oxide scale thickness presuming that there has been no relocation of molten metallic zircaloy cladding material, just plain oxidation consuming the metallic phase. Data of six rods at 810 mm and of all the rods at 850 mm and higher are determined by image analysis. The areas of intact shroud are calculated as well, while molten shroud is determined by image analysis. Areas of heaters/electrodes and pellets are only determined where significant changes could be detected, otherwise they are calculated. Melt between the rods is always subject to image analysis. As pellets and oxidized cladding or oxidized relocated melt can sometimes come in the same color it was up to the eye and experience of the operator to distinguish between them. Of course the pattern of cracks and grain growth was very helpful for this task.

From 900 mm upwards the metallic cladding material is completely vanished, either consumed by oxidation or relocated. There must have been relocation of molten cladding material as the area of oxidized cladding material does not reach the theoretical value of 100 %. For the 1050 mm position it was impossible to distinguish between oxidized cladding and relocated melt between the rods and therefore only the sum of both material classes is given in Table 16.

There are no or only minor changes in pellets and W-heaters up to an elevation of 900 mm. The greatest loss in pellets is at 950 mm where 11 % of the original area is missing. At the same elevation the maximum of 3 % of the area of the W-heaters is gone. The losses for the Mo-electrodes at 1050 mm are much bigger. Only 952 mm^2 of the original 1162 mm^2 are left,

that is a loss of 18 %. This corresponds to the high content of Mo and low content of W in the relocated melt at lower elevations.

The once fully intact circumference of the shroud reduces to smaller and smaller segments of a circle and is given as degree information in Table 16. Melt on the outside of the shroud was included in the table for the 810 and 850 mm elevation. In Figs. 86-88 melt pools are shown as either oxide or metallic melt depending on their overall appearance. But almost all of the melt pools with an overall metallic appearance show, when looking at the micrographs (Figs. 59 and 70), that they consist of a metallic melt matrix with oxide precipitates. The oxide contents of these melts were determined by optical phase analysis and thus the total area of oxide and metal were calculated and are given in Table 16.

The first lumps of melt between the rods are visible at 750 mm; almost complete metallic melt, the small oxide scale is neglected. The melt pools of 810 and 850 mm are, as stated before relating to the shroud melts, a mixture of oxide particles in metallic matrix (see Figs. 58, 65-68) and a phase analysis was performed to determine the amount of oxide within these pools. From 900 mm and upward, no more metallic Zr phase of melt was found, it is all completely oxidised. But there are those metallic Mo/W containing melt pools at every elevation from 810 mm upward.

Additionally, an attempt was made to find out something about the remaining fluid channels. As it is impossible to check the molded bundle with regard to flow resistance, the following method was used to get at least some information on the geometry of fluid channels. The thinner bundle cross-sections with only 10 to 16 mm thickness were placed on top of a uniform light source thus allowing to take photos of the light shining through the epoxy. These pictures were edited by setting brightness and contrast to create a more or less black and white picture (black is the structure) and were checked by visual control for wrong information, e.g. voids and cracks in the epoxy pretending bundle structure by blocking the light or by reflection. All the pictures created this way can be seen in Figs. 89 and 90.

In order to evaluate these pictures it has to be kept in mind that by using this simple method rectangular projections of all the bundle structure within the corresponding cross-section were created. This method does not account for actual fluid channels which not necessarily run at right angles to the cross-sections. Fluid channels actually can be even bigger than the white areas in the pictures. On the other hand it is not clear whether, by cutting the bundle, blind holes or undercuts were opened and therefore the area of fluid channels seem to be increased.

However, to the eye of the beholder, pictures like these do give an impression of blockages. It was therefore tried to quantify the remaining fluid channels.

For elevations of 850 mm and above, where the shroud was (partially) destroyed, a photo mount was used with a hole the size of the inner diameter of the original shroud. I.e. this procedure does not consider all changes in shroud shape during the test before it actually broke but it reduces all the pictures of different elevations to a common size and boundary. Pictures altered in that way are marked “with photo mount” and can be found in the left column. The pictures in the right column are only altered in a way, that (in case the outline of

the molten shroud is open to the environment) the outline of the shroud was closed by photo editing tools. A photo analysis tool then allowed to determine the white area, that is the area open for the flow, and these values are also given in the pictures of Figs. 89 and 90.

9.4 Hydrogen Absorption by Zircaloy

The hydrogen absorbed in the remaining zircaloy-4 metal was analyzed at the zircaloy corner rod B by neutron radiography. No remaining hydrogen was found in the whole rod so that no further analysis of hydrogen absorption was performed.

10 Results of Real Case Calculations with the Bundle Code CALUMO

The calculations for QUENCH-11 were done with the most advanced code version CALUMOqx. In this version of the code there are balance equations for the outer ring of 12 heated fuel rods (+ 4 corner rods), balance equations for the inner cluster of 8 heated fuel rods, and balance equations for the central rod or absorber rod with its guide tube, and, of course, balance equations for the shroud and the coolant.

But this version of the code CALUMO does not contain a mechanistic model for boiling of the coolant. In order to be able to do calculations for QUENCH-11, a simplified model based on a heat balance equation has been implemented, which should allow to approximately calculate the rate of steam production and the variation of the water level during boil-out of the bundle. The basic idea was to use the fraction of electrical power released in the bundle up to the water level (plus some two-phase transition region) plus the auxiliary electrical power as long as the water level is situated within the heated length and a fraction of auxiliary electrical power if the water level is below 0 cm. Unfortunately, this simple scheme did not give satisfying results. The calculated water level lagged very much behind the measured one. Satisfying results could only be obtained by using the total electrical power for the first stage (water level above 0 cm). On the other hand, the simple model worked rather well in the second stage (water level below 0 cm).

The model for convective heat transfer included in CALUMO is only for superheated steam and not for two-phase flow conditions as would be needed for the calculations of QUENCH-11. We have amended this deficiency by introducing an empirical factor of enhancement into the heat transfer model.

In the following figures the average temperature in the outer ring of fuel rod simulators is denoted ‘tsurz’, that of the inner cluster of 8 fuel rod simulators ‘tcenz’ , that of the central rod ‘tcrz’, and the average shroud temperature ‘tshrz’. The calculated tempereatures are compared to the available thermocouple readings. In the same way ‘dox’ denotes the oxide scales of the inner cluster of 9 heated fuel rods, ‘doxc’ that of the oxide scale on the unheated central rod, ‘doxa’ that of the outer ring of 12 heated fuel rods, and ‘doxshi’, ‘doxsha’ the inner and outer oxide scale of the shroud, respectively.

The temperature evolution in the test bundle and the shroud is satisfactorily well simulated by the code up to about 900 mm axial position (see Fig. 91 and 92). The temperature escalation monitored by the thermocouples above this axial position is not reproduced by the calculation. Posttest examinations revealed that in this axial zone a mechanical effect occurred in QUENCH-11 also observed in other tests as QUENCH-07 and QUENCH-09, namely an enhancement of the oxidation rate due to clad distension, cracking and split opening. This effect seems to have started at about 4900 s into the test. The bundle temperatures at 950 mm increase by about 400 K up to the onset of quenching. This temperature increase was most probably decisive for the further course of the test in the upper part of the test section. The effect of clad distension was assumed to start at higher temperatures (1800 K). If this interpretation is correct, then the change of the slope of the temperature curves after 4900 s (at 950 mm) must be caused by a different unidentified mechanism.

The absence of temperature escalation in the upper part of the test section in the code calculation has, of course, consequences on the oxidation and hydrogen production. The calculated total hydrogen production (see Fig. 93) is 60 g, much lower than the measured value of 141 g. This is also reflected in the hydrogen production rate with a calculated maximum value of about 0.16 g/s.

The calculation concerning oxidation (see Fig. 94) yields an axial zone of about 150 mm with fully oxidized cladding around the 800 mm position. Posttest examinations yielded a more extended zone with fully oxidized claddings, a consequence of the temperature escalation in the upper part. The oxidation results of the withdrawn corner rod indicate that up to the onset of quenching the amount of oxidized material is satisfactorily well calculated by the code. But the calculated oxide scale profiles are displaced downwards by about 100 mm. This is the consequence of some bias in the thermal simulation of the test section by the CALUMO code.

The evolution of the water level and the steam flow rate as calculated by the code are shown in Fig. 95. There is a problem with the quench model implemented in CALUMO, as the water level in the quench phase does not sufficiently rise upwards. Also, there is a step change in the steam flow rate as the water level falls below the heated zone. This means that the simple procedure for the simulation of boil-out of the test bundle is not fully adequate.

Acknowledgments

Test QUENCH-11 (QUENCH-L2) was co-financed in the frame of the LACOMERA Project FIR1-CT-2002-40158 of the EU 5th Framework Program. Special thanks are due to Dr. A. Miassoedov, FZK/IKET, who initiated this project within the Karlsruhe Research Center. In general, the broad support needed for preparation, execution, and evaluation of the experiment is gratefully acknowledged. In particular, the authors would like to thank Mr. J. Moch for the assembly of the entire test section, Mr. S. Horn, FZK/IK, for the preparation of the hydrogen measurement with the “Caldos” analyzer and the various support, Mrs. J. Laier for processing the test data, Mr. M. Große for the investigation of the remaining hydrogen content in the corner rod, and Dr. L. Steinbock for the posttest videoscope inspection of the bundle.

The determination of the test protocol was based on numerous calculations with SCDAP/RELAP5, SCDAPSIM, ASTEC, and MELCOR, prepared by FZK/IRS and performed in collaboration between the Institute for Nuclear Research and Nuclear Energy of the Bulgarian Academy of Sciences INRNE, Sofia and Paul-Scherrer-Institut (Drs. J. Birchley, B. Jäckel, and T. Haste). Agreement between the prediction by SCDAP/RELAP5 and experiment evolution as it was monitored on-line facilitated an efficient execution of the planned test protocol and enabled the desired bundle behavior during the important quenching phase to be achieved.

Aerosol measurements were performed by Messrs. I. Nagy and P. Windberg of the AEKI Atomic Energy Research Institute, Budapest, Hungary.

The supply of duplex claddings of the “DX-D4” type by Areva (Framatome ANP) used for fabrication of two fuel rod simulators is also acknowledged.

References

[1] J.M. Broughton, P. Kuan, and D.A. Petti, “A Scenario of the Three Mile Island Unit 2 Accident,” Nuclear Technology, 87, 34, 1989.

[2] P. Hofmann, S. Hagen, V. Noack, G. Schanz, L. Sepold, “Chemical-Physical Behavior of Light Water Reactor Core Components Tested under Severe Reactor Accident Conditions in the CORA Facility,” Nuclear Technology, vol. 118, 1997, p. 200.

[3] S. Hagen, P. Hofmann, V. Noack, L. Sepold, G. Schanz, G. Schumacher, “Comparison of the Quench Experiments CORA-12, CORA-13, CORA-17,” FZKA 5679, Forschungszentrum Karlsruhe, 1996.

[4] S.M. Modro and M.L. Carboneau, “The LP-FP-2 Severe Fuel Damage Scenario; Discussion of the Relative Influence of the Transient and Reflood Phase in Affecting the Final Condition of the Bundle,” OECD/LOFT Final Event, ISBN 92-64-03339-4, 1991, p. 388.

[5] B. Clement, N. Hanniet-Girault, G. Repetto, D. Jacquemain, A.V. Jones, M.P. Kissane, P. von der Hardt, “LWR Severe Accident Simulation: Synthesis of the Results and Interpretation of the First Phebus FP Experiment FPT0,” Nuclear Engineering and Design, 2003, Vol. 226, p. 5-82

[6] L. Sepold, A. Miassoedov, G. Schanz, U. Stegmaier, M. Steinbrück, J. Stuckert, C. Homann, “Hydrogen Generation in Reflooding Experiments with LWR-type Rod Bundles (QUENCH Program),” Journal Nuclear Technology, Vol. 147, Aug. 2004, pp. 202-214.

[7] P. Hofmann, V. Noack, M.S. Veshchunov, A.V. Berdyshev, A.V. Boldyrev, L.V. Matweev, A.V. Palagin, V.E. Shestak, “Physico-Chemical Behavior of Zircaloy Fuel Rod Cladding Tubes During LWR Severe Accident Reflood,” FZKA 5846, Forschungszentrum Karlsruhe, 1997.

[8] P. Hofmann, A. Miassoedov, L. Steinbock, M. Steinbrück, A.V. Berdyshev, A.V. Boldyrev, A.V. Palagin, V.E. Shestak, M. Veshchunov, “Quench Behavior of Zircaloy Fuel Rod Cladding Tubes. Small-Scale Experiments and Modeling of the Quench Phenomena,” FZKA 6208, Forschungszentrum Karlsruhe, 1999

[9] J. Stuckert, M. Steinbrück, U. Stegmaier, "Single Rod Quench Tests with Zr-1Nb. Comparison with Zircaloy-4 Cladding Tests and Modelling," FZKA 6604, Forschungszentrum Karlsruhe, 2001

[10] A. Miassoedov, H. Alsmeyer, B. Eppinger, L. Meyer, M. Steinbrück, “Large Scale Experiments on Core Degradation, Melt Retention and Coolability (LACOMERA),” FISA-2003: EU Research in Reactor Safety, Luxembourg, Nov. 10-13, 2003, Preproc., p. 239-244

[11] W. Hering, Ch. Homann, “Degraded Core Reflood: Consequence Evaluation Based on Available Data,” 11th International Topical Meeting on Nuclear Reactor Thermal-Hydraulics (NURETH-11), Avignon, France, October 2-6, 2005.

[12] J. Birchley, T. Haste and B. Jaeckel, “Calculational Support for the QUENCH-10 and QUENCH-11 Experiments,” 11th International QUENCH Workshop, Forschungszentrum Karlsruhe, October 2005, CD-ROM (ISBN 3-923704-51-8).

[13] J. Stuckert, W. Hering, C. Homann, J. Moch, G. Schanz, L. Sepold, U. Stegmaier, M. Steinbrück, “Status of the QUENCH-11 test preparation: first results of the integral pre-tests,” 11th International QUENCH Workshop, Forschungszentrum Karlsruhe, October 2005, CD-ROM (ISBN 3-923704-51-8).

[14] J. Stuckert, W. Hering, L. Sepold, M. Steinbrück, “First results of the QUENCH-11 experiment,” SARNET 2nd Annual Review Meeting, PSI Villigen, January 30-31, 2006 (http://sarnet.grs.de/sites/WP9).

[15] J. Birchley, T. Haste, W. Hering, Ch. Homann, “Pre-test Analytical Support for Experiments QUENCH-10, -11, and -12,” International Conference on Nuclear Energy for New Europe, Portoroz, SLO, September 18-21, 2006.

[16] W. Hering, “Pre-test calculations of QUENCH-11 (Q-L2) using S/R5 and ASTEC,” 11th International QUENCH Workshop, Forschungszentrum Karlsruhe, October 2005, CD-ROM (ISBN 3-923704-51-8).

[17] C. Homann, W. Hering, “Analytical support for QUENCH-11,” 12th International QUENCH Workshop, Forschungszentrum Karlsruhe, October 2006, CD-ROM (ISBN 978-3-923704-57-6).

[18] W. Hering, Ch. Homann, J. Birchley, T. Haste, P. Groudev, A. Stefanova, “Preparation of QUENCH-11 with SCDAP/RELAP5, SCDAPSIM, MELCOR, and ASTEC,” FZKA-7305, 2007.

[19] Anna Pintér Csordás, Imre Nagy, Péter Windberg, Mihály Kunstár, Lajos Matus, Nóra Vér, Ildikó Pummer, Zoltán Hózer, AEKI internal report, Aug. 2006.

[20] B. Massalski, “Binary Alloy Phase Diagrams,” Vol. 3, 2nd Ed., ASM, 1990.

[21] M. Steinbrück, “Analysis of Hydrogen Production in QUENCH Bundle Tests,” FZKA 6968, Forschungszentrum Karlsruhe, 2004.

Table 1: QUENCH test matrix

Test	Quench medium	Injection rate	Temp. at onset of flooding[1)]	Max. ZrO_2 before flooding[2)]	Max. ZrO_2 layer thickness[3)]	H_2 production before / during cooldown	Remarks, objectives
QUENCH-00 Oct. 9 - 16, 97	Water	80 g/s	≈ 1800 K		≈ 500 µm		COBE Project; commissioning tests.
QUENCH-01 February 26, 98	Water	52 g/s	≈ 1830 K	312 µm	≈ 580 µm	36 / 3	COBE Project; partial fragmentation of pre-oxidized cladding.
QUENCH-02 July 7, 98	Water	47 g/s	≈ 2400 K		completely oxidized	20 / 140	COBE Project; no additional pre-oxidation; quenching from high temperatures.
QUENCH-03 January 20, 99	Water	40 g/s	≈ 2350 K		completely oxidized	18 / 120	No additional pre-oxidation, quenching from high temperatures.
QUENCH-04 June 30, 99	Steam	50 g/s	≈ 2160 K	82 µm	≈ 360 µm	10 / 2	Cool-down behavior of slightly pre-oxidized cladding by cold steam injection.
QUENCH-05 March 29, 2000	Steam	48 g/s	≈ 2020 K	160 µm	≈ 520 µm	25 / 2	Cool-down behavior of pre-oxidized cladding by cold steam injection.
QUENCH-06 Dec. 13 2000	Water	42 g/s	≈ 2060 K	207 µm	≈ 850 µm	32 / 4	OECD-ISP 45; prediction of H_2 source term by different code systems.
QUENCH-07 July 25, 2001	Steam	15 g/s	≈ 2100 K	230 µm	completely oxidized	66 / 120	COLOSS Project; impact of B_4C absorber rod failure on H_2, CO, CO_2, and CH_4 generation.

Test	Quench medium	Injection rate	Temp. at onset of flooding[1)]	Max. ZrO_2 before flooding[2)]	Max. ZrO_2 layer thickness[3)]	H_2 production before / during cooldown[4)]	Remarks, objectives
QUENCH-09 July 3, 2002	Steam	49 g/s	≈ 2100 K		completely oxidized	60 / 400	As QUENCH-07, steam-starved conditions prior to cooldown.
QUENCH-08 July 24, 2003	Steam	15 g/s	≈ 2090 K	274 µm	completely oxidized	46 / 38	As QUENCH-07, no absorber rod
QUENCH-10 July 21, 2004	Water	50 g/s	≈ 2200 K	514 µm	completely oxidized	48 / 5	LACOMERA Project; Air ingress.
QUENCH-11 Dec 08, 2005	Water	18 g/s	≈ 2040 K	170 µm	completely oxidized	9 / 132	LACOMERA Project; Boil-off.

1) Maximum measured bundle temperature at 950 mm.

2) Measured at the withdrawn corner rod.

3) Measured posttest at the bundle elevation of maximum temperature.

4) Best-estimate values include H_2 from oxidation of non-prototypical materials, e.g. Mo, Cu (electrodes); W (heater) etc.

Revised: April 2007

Table 2: Design characteristics of the QUENCH-11 test bundle

Bundle type		PWR
Bundle size		21 rods
Number of heated rods		20
Number of unheated rods		1
Pitch		14.3 mm
Coolant channel area		30.1 cm^2
Hydraulic diameter		11.6 mm
Rod outside diameter		10.75 mm
Cladding material		Zircaloy-4 *)
Cladding thickness		0.725 mm
Rod length	heated rod (levels)	2480 mm (-690 mm to 1790 mm)
	unheated rod (levels)	2842 mm (-827 mm to 2015 mm, incl. extension piece)
Heater material		Tungsten (W)
Heater length		1024 mm
Heater diameter		6 mm
Annular pellet	material	ZrO_2;Y_2O_3-stabilized
	heated rod	∅ 9.15/6.15 mm; L=11 mm
	unheated rod	∅ 9.15/2.5 mm; L=11 mm
Pellet stack	heated rod	0 mm to ~ 1020 mm
	unheated rod	0 mm to 1553 mm
Corner rod (4)	material	Zircaloy-4
	instrumented	tube ∅ 6x0.9 (bottom: -1140 mm)
		rod ∅ 6 mm (top: +1300 mm)
	not instrumented (solid)	rod ∅ 6 mm (-1350 to +1155 mm)
Grid spacer	material	Zircaloy-4, Inconel 718
	length	Zry 42 mm, Inc 38 mm
	location of lower edge	-100 mm Inconel 150 mm Zircaloy-4 550 mm Zircaloy-4 1050 mm Zircaloy-4 1410 mm Zircaloy-4

Shroud	material	Zircaloy-4
	wall thickness	2.38 mm
	outside diameter	84.76 mm
	length (extension)	1600 mm (-300 mm to 1300 mm)
Shroud insulation	material	ZrO_2 fiber
	insulation thickness	~ 37 mm
	elevation	-300 mm to ~1000 mm
Molybdenum-copper electrodes	length of upper electrodes	766 mm (576 Mo, 190 mm Cu)
	length of lower electrodes	690 mm (300 Mo, 390 mm Cu)
	diameter of electrodes:	
	- prior to coating	8.6 mm
	- after coating with ZrO_2	9.0 mm
Cooling jacket	Material: inner/outer tube	Inconel 600 (2.4816)/SS (1.4571)
	inner tube	∅ 158.3 / 168.3 mm
	outer tube	∅ 181.7 / 193.7 mm

09/2006

***)** Rods # 14 and 20 use a duplex cladding of the type “DX-D4” with a Zry-4 base material (thickness 575 µm) and an external liner (thickness 150 µm). The alloy of the external liner: 0.4-0.6 % Sn, 0.4-0.6 % Fe, 0.15-0.25 % Cr, 0.02-0.04 % Ni, 0.12-0.16 % O, and 0.007-0.012 % Si.

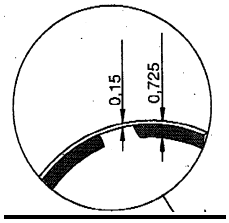

Table 3: As-received dimensions of the materials used for the QUENCH high-temperature thermocouples

Material	Diameter, mm
W/Re wires	Ø 0.254
HfO_2 insulation OD (see drawing below)	Ø 1.1
Ta tube OD / ID	Ø 2.15 / 1.65
Zr tube OD / ID	Ø 2.35 / 1.65 ± 0.013

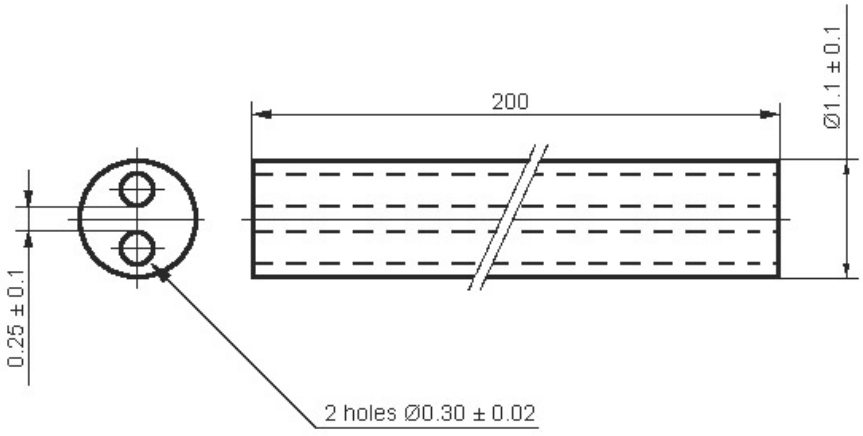

Table 4: Electrical resistances of circuits, contacts, and cables [mΩ]

Circuit of inner ring with 8 rods (measured)	Circuit of outer ring with 12 rods (measured)	One heater (measured, mean value of 20 rods)	Slide contact (calculated)	Cable of each circuit (calculated)
0.77	0.59	3.00	1.46	0.22

Table 5: List of instrumentation for the QUENCH-11 Test

Channel	Designation	Instrument, location	Units
0..1		Reserve	
2	TSH 9/270 I	TC (W/Re) shroud outer surface, 550 mm, 296°, behind shroud insulation	K
3	TFS 2/15	TC (W/Re) fuel rod simulator 4 (type 2), 1150 mm, 315°	K
4		Reserve	K
5	TSH 15/180 I	TC (W/Re) shroud outer surface, 1150 mm, 206°, behind shroud insulation	K
6	TFS 3/10	TC (W/Re) fuel rod simulator 5 (type 3), 650 mm, 45°	K
7		Reserve	
8	TFS 3/13	TC (W/Re) fuel rod simulator 3 (type 3), 950 mm, 315°	K
9	TFS 3/14	TC (W/Re) fuel rod simulator 5 (type 3), 1050 mm, 45°	K
10	TSH 10/90 I	TC (W/Re) shroud outer surface, 650 mm, 116°, behind shroud insulation	K
11		Reserve	K
12	TFS 5/11	TC (W/Re) fuel rod simulator 13 (type 5), 750 mm, 45°	K
13		Reserve	
14	TSH 10/270 I	TC (W/Re) shroud outer surface, 650 mm, 296°, behind shroud insulation	K
15	TFS 5/13	TC (W/Re) fuel rod simulator 15 (type 5), 950 mm, 315 °	K
16	TFS 5/14	TC (W/Re) fuel rod simulator 13 (type 5), 1050 mm, 45°	K
17	TSH 16/180 I	TC (W/Re) shroud outer surface, 1250 mm, 206°, behind shroud insulation	K
18	TSH 13/90 I	TC (W/Re) shroud outer surface, 950 mm, 116°, behind shroud insulation	K
19	TSH 14/90 I	TC (W/Re) shroud outer surface, 1050 mm, 116°, behind shroud insulation	K
20	TSH 11/0 I	TC (W/Re) shroud outer surface, 750 mm, 26°, behind shroud insulation	K
21	TSH 12/0 I	TC (W/Re) shroud outer surface, 850 mm, 26°, behind shroud insulation	K
22	TFS 2/5	TC (NiCr/Ni) fuel rod simulator 2 (type 2), 150 mm, 225°	K
23	TFS 2/7	TC (NiCr/Ni) fuel rod simulator 4 (type 2), 350 mm, 315°	K
24		Reserve	
25	FM 401	Argon gas mass flow rate	g/s
:		Reserve	
32	TIT A/13	TC (W/Re) corner rod A, center, 950 mm	K
33	TCRC 13	TC (W/Re) central rod, center, 950 mm	K

Channel	Designation	Instrument, location	Units
34	TFS 2/12	TC (W/Re) fuel rod simulator 4 (type 2), 850 mm, 315°, *friable* HfO_2	K
35	TSH 9/0	TC (NiCr/Ni) shroud outer surface, 550 mm, 26°	K
36	TSH 9/180	TC (NiCr/Ni) shroud outer surface, 550 mm, 206°	K
37	TFS 3/16	TC (W/Re) fuel rod simulator 7 (type 3), 1250 mm, 135°	K
38	TFS 5/9	TC (NiCr/Ni) fuel rod simulator 10 (type 5), 550 mm, 315°	K
39	TFS 2/9	TC (NiCr/Ni) fuel rod simulator 8 (type 2), 550 mm, 135°	K
40	TIT C/12	TC (W/Re) corner rod C, center, 850 mm	K
41		defect channel	
42	TFS 5/8	TC (NiCr/Ni) fuel rod simulator 21 (type 5), 450 mm, 135°	K
43	TFS 2/8	TC (NiCr/Ni) fuel rod simulator 2 (type 2), 450 mm, 315°	K
44	T 003	Cooling water, outlet of off-gas tube	K
45		Reserve	
46	TSH 6/270	TC (NiCr/Ni) shroud outer surface, 250 mm, 296°	K
47	TFS 5/15	TC (W/Re) fuel rod simulator 19 (type 5), 1150 mm, 225°	K
48	TFS 5/16	TC (W/Re) fuel rod simulator 21 (type 5), 1250 mm, 135°	K
49	TFS 5/17	TC (W/Re) fuel rod simulator 15 (type 5), 1350 mm, 315°	K
50	TFS 5/12	TC (W/Re) fuel rod simulator 18 (type 5), 850 mm, 45°	K
51	TFS 2/11	TC (W/Re) fuel rod simulator 8 (type 2), 750 mm, 135°, bottom penetration	K
52	TSH 13/270 I	TC (W/Re) shroud outer surface, 950 mm, 296°, behind shroud insulation	K
53	TSH 14/270 I	TC (W/Re) shroud outer surface, 1050 mm, 296°, behind shroud insulation	K
54	TSH 11/180 I	TC (W/Re) shroud outer surface, 750 mm, 206°, behind shroud insulation	K
55	TSH 12/180 I	TC (W/Re) shroud outer surface, 850 mm, 206°, behind shroud insulation	K
58	T 308	TC (NiCr/Ni) bundle foot outer surface	K
56..62		Reserve	
63	R 001	Auxiliary water injection, maximum rate 4 g/s	g/s
64..65		Reserve	
66	TSH 15/0 I	TC (W/Re) shroud outer surface, 1150 mm, 26°, behind shroud insulation	K
67	TSH 16/0 I	TC (W/Re) shroud outer surface, 1250 mm, 26°, behind shroud insulation	K
68	T 512	Gas temperature bundle outlet	K
69		defect channel	

Channel	Designation	Instrument, location	Units
72	TFS 2/1 F	TC (NiCr/Ni) fuel rod simulator 4 (type 2), -250 mm, 315°, fluid temperature	K
73	TSH 5/180	TC (NiCr/Ni) shroud outer surface, 150 mm, 206°	K
74	TFS 2/3 F	TC (NiCr/Ni) fuel rod simulator 4 (type 2), -50 mm, 315°, fluid temperature	K
75	TCR 7	TC (NiCr/Ni) fuel rod simulator 1 (type 1), 350 mm, 315°	K
76	TFS 2/6 F	TC (NiCr/Ni) fuel rod simulator 4 (type 2), 250 mm, 315°, fluid temperature	K
77	TCR 9	TC (NiCr/Ni) fuel rod simulator 1 (type 1), 550 mm, 315°	K
78	TFS 2/4 F	TC (NiCr/Ni) fuel rod simulator 4 (type 5), 50 mm, 315°, fluid temperature	K
79	TFS 5/4/180	TC (NiCr/Ni) fuel rod simulator 21 (type 5), 50 mm, 135°	K
80	TFS 5/6	TC (NiCr/Ni) fuel rod simulator 18 (type 5), 250 mm, 45°	K
81		defect channel	
82	TFS 5/7	TC (NiCr/Ni) fuel rod simulator 19 (type 5), 350 mm, 225°	K
83	TSH 4/270	TC (NiCr/Ni) shroud outer surface, 50 mm, 296°	K
84	TSH 3/180	TC (NiCr/Ni) shroud outer surface, -50 mm, 206°	K
85	TSH 2/90	TC (NiCr/Ni) shroud outer surface, -150 mm. 116°	K
86	TSH 7/180	TC (NiCr/Ni) shroud outer surface, 350 mm, 206°	K
87	TSH 4/90	TC (NiCr/Ni) shroud outer surface, 50 mm, 116°	K
88	TSH 1/0	TC (NiCr/Ni) shroud outer surface, -250 mm, 26°	K
89	TSH 5/0	TC (NiCr/Ni) shroud outer surface, 50 mm, 26°	K
90	TSH 7/0	TC (NiCr/Ni) shroud outer surface, 350 mm, 26°	K
91	TCI 9/270	TC (NiCr/Ni) cooling jacket inner tube wall, 550 mm, 270°	K
92	TCI 10/270	TC (NiCr/Ni) cooling jacket inner tube wall, 650 mm, 270°	K
93	TCI 11/270	TC (NiCr/Ni) cooling jacket inner tube wall, 750 mm, 270°	K
94	TCI 13/270	TC (NiCr/Ni) cooling jacket inner tube wall, 950 mm, 270°	K
95	TCRC 9	TC (NiCr/Ni) central rod, center, 550 mm	
96	TCI 1/180	TC (NiCr/Ni) cooling jacket inner tube wall, -250 mm, 180°	K
97	TCI 4/180	TC (NiCr/Ni) cooling jacket inner tube wall, 50 mm, 180°	K
98	TCI 7/180	TC (NiCr/Ni) cooling jacket inner tube wall, 350 mm, 180°	K
99	TCI 11/180	TC (NiCr/Ni) cooling jacket inner tube wall, 750 mm, 180°	K
100	TCI 12/180	TC (NiCr/Ni) cooling jacket inner tube wall, 850 mm, 180°	K
101	TCI 13/180	TC (NiCr/Ni) cooling jacket inner tube wall, 950 mm, 180°	K
102	TCI 15/180	TC (NiCr/Ni) cooling jacket inner tube wall, 1150 mm, 180°	K
103	T 002	Cooling water, inlet of off-gas tube	K
104	TCI 9/90	TC (NiCr/Ni) cooling jacket inner tube wall, 550 mm, 90°	K
105	TCI 10/90	TC (NiCr/Ni) cooling jacket inner tube wall, 650 mm, 90°	K
106	TCI 11/90	TC (NiCr/Ni) cooling jacket inner tube wall, 750 mm, 90°	K

Channel	Designation	Instrument, location	Units
107	TCI 13/90	TC (NiCr/Ni) cooling jacket inner tube wall, 950 mm, 90°	K
108	T 305	TC (NiCr/Ni) water temperature near internal aux. heater	K
109	TCI 1/0	TC (NiCr/Ni) cooling jacket inner tube wall, -250 mm, 0°	K
110	TCI 4/0	TC (NiCr/Ni) cooling jacket inner tube wall, 50 mm, 0°	K
111	TCI 7/0	TC (NiCr/Ni) cooling jacket inner tube wall, 350 mm, 0°	K
112	TCI 11/0	TC (NiCr/Ni) cooling jacket inner tube wall, 750 mm, 0°	K
113	TCI 12/0	TC (NiCr/Ni) cooling jacket inner tube wall, 850 mm, 0°	K
114	TCI 13/0	TC (NiCr/Ni) cooling jacket inner tube wall, 950 mm, 0°	K
115	TCI 15/0	TC (NiCr/Ni) cooling jacket inner tube wall, 1150 mm, 0°	K
116	TFS 2/2 F	TC (NiCr/Ni) fuel rod simulator 4 (type 2), -150 mm, 315°, fluid temperature	K
117	T 309	TC (NiCr/Ni) Ar bundle top	K
118	TSH 8/270	TC (NiCr/Ni) shroud outer surface, 450 mm, 296°	K
119	T 306	TC (NiCr/Ni) outer surface of internal aux. heater	K
120	TCO 1/0	TC (NiCr/Ni) cooling jacket outer tube surface, -250 mm, 0°	K
121	TCO 7/0	TC (NiCr/Ni) cooling jacket outer tube surface, 350 mm, 0°	K
122	TCO 13/0	TC (NiCr/Ni) cooling jacket outer tube surface, 950 mm, 0°	K
123	T 601	Off-gas temp., 2660 mm from test section outlet (flange)	K
:		Reserve	
126	T 307	TC (NiCr/Ni) inner surface of inlet of off-gas pipe	K
127	TSH 6/90	TC (NiCr/Ni) shroud outer surface, 250 mm, 116°	K
128	T 104	Temperature quench water	K
:		Reserve	
135	T 401	Temperature upstream Ar flow instrument (orifice) location	K
136	T 403	Temperature of Ar at inlet cooling jacket	K
137	T 404	Temperature of Ar at outlet cooling jacket	K
138	T 501	Temperature in containment (near from bundle head)	K
139	T 502	Temperature at outer surface of containment, 0°, 2.4 m	K
140	T 503	Temperature at outer surface of containment, 270°, 2.2 m	K
141	T 504	Temperature at outer surface of containment, 270°, 3.2 m	K
142	T 505	Temperature at outer surface of containment, 90°, 3.2 m	K
143	T 506	Temperature at outer surface of containment, 270°, 3.6 m	K
144	T 507	Temperature at outer surface of containment, 90°, 3.6 m	K
145	T 508	Temperature at outer surface of containment, 180°, 4.0 m	K
147	T 510	Temperature at outer surface of containment, 270°, 4.4 m	K
148	T 511	Gas temperature at bundle inlet	K
149	T 901	Temperature upstream off-gas flow instrument F 901	K
150	TSH 8/90	TC (NiCr/Ni) shroud outer surface, 450 mm, 106°	K

Channel	Designation	Instrument, location	Units
:		Reserve	
153	F 406	Ar flow rate into insulation shroud/cooling jacket	g/s
155	P 303	Pressure upstream total flow instrument (orifice) location	bar
156	P 401	Pressure upstream gas flow instrument location	bar
157	P 511	Pressure at bundle inlet	bar
158	P 512	Pressure at bundle outlet	bar
159	P 601	Pressure upstream off-gas flow instrument (orifice) F 601	bar
160	P 901	Pressure upstream off-gas flow instrument F 901	bar
161		Reserve	
162	L 501	Water level	mm
163	L 701	Liquid level condensation vessel	mm
164		Reserve	
165	P 411	Pressure He supply	bar
166	P 403	Pressure Ar cooling of cooling jacket	bar
167	P 406	Pressure insulation shroud/cooling jacket	bar
168	F 104	Flow rate quench water	g/s
:		Reserve	
171	R 002	Auxiliary bottom heater	kW
172	F 401	Argon gas flow rate	g/s
173	F 403	Flow rate cooling gas	g/s
174	F 601	Flow rate off-gas (orifice), 2000 mm from test section outlet (flange)	mbar
:		Reserve	
178	E 501	Electric current inner ring of fuel rod simulators	A
179	E 502	Electric current outer ring of fuel rod simulators	A
180	E 503	Electric voltage inner ring of fuel rod simulators	V
181	E 504	Electric voltage outer ring of fuel rod simulators	V
:		Reserve	
250	E 505	Electric power inner ring of fuel rod simulators	W
251	E 506	Electric power outer ring of fuel rod simulators	W

Table 6: QUENCH-11; Failure of thermocouples

Thermocouple	Elevation [mm]	Time at failure [s]	Failure temperature [K]
TSH 10/90 I	650	5966	274
TFS 2/12	850	5580	2451
TIT C/12	850	5800	463
TFS 3/13	950	5409	2035
TFS 5/13	950	5633*)	2432
TIT A/13	950	5633	2339
TSH 13/90 I	950	5629	2446
TSH 13/270 I	950	5823	1815
TSH 14/90 I	1050	5718	2450
TSH 14/270 I	1050	5817	2180

***)** Only two values incorrect, afterwards correct.

Table 7: Sequence of events for pre-test QUENCH-11v3

Time, s	Action / event
0	Start of data acquisition
219	Start of bundle heating
~300	Start of boil-off
1026	Start of auxiliary power
2540	Start of water supply (R001) to compensate evaporation
4438	Start of quench water injection
4452	Start of power reduction
4455	Decay power level reached
4471	Start of temperature decrease (T 511)
4477	Start of auxiliary power switch-off
4478	Auxiliary power switched off
4505	Start of temperature decrease (TFS 2/1)
4778	Start of quench water switch-off
4788	Auxiliary water switched off (R001)
4795	Quench water switched off
4939	Start of power switch-off
4941	Power switched off
5198	End of data acquisition

Table 8: **QUENCH-11v2 pretest; Evaluation of the height of saturated fluid between water front and superheated steam with help of the difference in thermocouple response and water level (L 501) during the decrease of the water front (boil-off).**

Time [s]	Thermocouple	Thermocouple position [mm]	Water level (L501) [mm]	Height of saturated fluid between water front and superheated steam [mm]
625	TFS 2/15	1150	705	445
790	TFS 3/14	1050	628	422
900	TFS 5/13	950	594	356
1218	TFS 2/12	850	485	365
1541	TFS 2/11	750	373	377
1739	TFS 3/10	650	305	345
1984	TFS 5/9	550	223	327
2200	TFS 2/8	450	136	314
2410	TFS 2/7	350	77	273
2599	TFS 5/6	250	3	247
2876	TFS 2/5	150	-93	243
3008	TFS 5/4	50	-136	186

Table 9: **QUENCH-11; Evaluation of the height of saturated fluid between water front and superheated steam with help of the difference in thermocouple response and water level (L 501) during the decrease of the water front (boil-off).**

Time [s]	Thermocouple	Thermocouple position [mm]	Water level (L501) [mm]	Height of saturated fluid between water front and superheated steam [mm]
629	TFS 2/15	1150	781	369
801	TFS 3/14	1050	705	345
886	TFS 5/13	950	668	282
1312	TFS 2/12	850	484	366
1519	TFS 2/11	750	384	366
1725	TFS 3/10	650	292	358
1882	TFS 5/9	550	220	330
2064	TFS 2/8	450	137	313
2212	TFS 2/7	350	71	279
2365	TFS 5/6	250	7	243
2560	TFS 2/5	150	-72	222
4073	TFS 5/4	50	-129	179

Table 10: QUENCH-11; Sequence of events

Time [s]	Event
0 (11:03:00 h)	Start data recording, bundle at 383 K (TFS 2/4 F), data acquisition frequency at 1 Hz. Ar flow (feed-in at bundle head) 3.04 g/s (385 K). Auxiliary power at 0.48 kW.
224	Switch-on of bundle power (~ 6.7 kW). Auxiliary power at 0.36 kW.
310	Boiling onset (intensive noise at L 501).
1035, 1345, 1640, 1945, 2636, 3275	Auxiliary power increase to 1.16, 1.55, 2.05, 2.44, 2.67, 2.94 kW, respectively.
2578	Start auxiliary water (flow rate 1.1 g/s); L 501= -70 mm.
2730	Auxiliary water flow rate at 1.0 g/s.
2920	Auxiliary water flow rate at 0.8 g/s; L 501= -45 mm.
3013, 4027, 4619, 4827	Changes in bundle power from 7.1 kW to 6.7 kW; from 6.7 kW to 6.45 kW; from 6.45 kW to 6.55 kW; from 6.55 kW to 6.77 kW, respectively.
5030	Auxiliary water flow rate at 1.0 g/s; L 501= -190 mm.
5460	Start of temperature escalation at 950 mm (TFS 5/13=1765 K).
5487	Withdrawal of corner rod B (TFS 3/14, TFS 3/10).
5500	Quench initiation (increase of F 104 to app. 17 g/s during next 40 s). TIT A/13=1959 K, TFS 5/13=1887 K.
5520	Quench water at test section inlet (increase of L 501). TIT A/13=2043 K, TFS 5/13=1972 K.
5563	Shroud failure (drop of P 406); first test rod failure by helium detection.
5573	Reduction bundle power from 6.8 to 3.9 kW. TIT A/13=2211 K, TFS 5/13=2077 K.
5575	Bundle power at decay heat level.
5645	Temperature max.: TFS 5/13=2350 K, TFS 5/12=2236 K, TSH 13/90 I=2384 K.
5656	Maximum of hydrogen production.
5702	Auxiliary power shut off.
5713	Bundle power shut off.

5717	Temperature maximum at 1250 mm: TFS 3/16=2078 K; TSH 16/0 I=1810 K.
5738 - 5763	Temporary interruption of quench water supply (L 501=745 mm).
5770 - 6100	Temporary malfunction of bundle head cooling (water at 90 °C instead of 75 °C).
5795	Water level reached maximum elevation of 868 mm.
6004	Quench pump shut off (F 104). TFS 5/11=340 K, TFS 5/14=1117 K.
6020	Quench water at 0 g/s.
6324	Auxiliary water injection switched off.
6330	Auxiliary water at 0 g/s.
8928	End of data recording. TFS 2/1 F=323 K, L 501=744 mm.

Table 11: QUENCH-11; Sequence of aerosol sampling

Impactor	Start	Stop	Duration [s]
1*)			
2	12:02:19	12:03:18	60
3	12:09:49	12:10:48	60
4	12:14:01	12:15:00	60
5	12:22:23	12:23:22	60
6	12:26:34	12:27:33	60
7	12:34:14	12:35:13	60
8	12:35:37	12:36:36	60
9	12:36:39	12:37:38	60
10	12:37:44	12:38:43	60

***)** Impactor 1 was a service sampler.

Table 12: QUENCH-11; Water/steam balance for the quench phase

Accumulated mass of water [g]	
Water inventory at test begin (L 501)*: 982-(-300) mm	3846
Total water injected: quench (F104)+auxiliary water (R001) 9289+3376	12665
Total used water	**16511**
Condensed water collected (L 701)**: 867-194,55 mm	9616
Water/steam consumed by Zr oxidation (141 g H_2)	1269
Water found posttest in the test bundle (L 501) = 745-(-300) mm	3135
Water found posttest retained in the ZrO_2 fiber insulation***	2300
Water found posttest in the annulus of the upper plenum	170
Total water collected posttest as condensate	**16490**

*) water column of 1 mm corresponds to 3 g
**) water column of 1 mm corresponds to 14.3 g
***) posttest insulation weight (between -300 mm and ~800 mm): 11300 g; weight of the dry insulation (9 annuli): 9x1000 g = 9000 g

Table 13: QUENCH-11; Quench front progression based on the local temperature data at saturation (~395 K)

Elevation [mm]	Thermocouple	Time [s]
50	TFS 5/4/180, TFS 2/4 F	5552
150	TFS 2/5	5573
250	TFS 5/6, TFS 2/6 F	5591
350	TFS 2/7	5608
350	TFS 5/7	5610
350	TCR 7	5609
450	TFS 2/8	5629
450	TFS 5/8	5631
550	TFS 2/9, TFS 5/9	5654
550	TCR 9	5653
650	TFS 3/10	5678
750	TFS 2/11	5703
750	TFS 5/11	5704
850	TFS 5/12	5850

Table 14: QUENCH-11; Cross sections for the metallographic examination

Sample	Sample length (mm)	Axial position (mm) *)		Remarks
		bottom	top	
Cut **)	4	-14	-10	
QUE-11-a	68	-10	58	
Cut	4	58	62	
QUE-11-b	188	62	250	
Cut	4	250	254	
QUE-11-c	286	254	540	
Cut	4	540	544	
QUE-11-d	87	544	631	
Cut	4	631	635	
QUE-11-1	15	635	**650**	TC elevation 10, 650 mm polished
Cut	4	650	654	
QUE-11-e	77	654	731	
Cut	4	731	735	
QUE-11-2	15	735	**750**	TC elevation 11, 750 mm polished
Cut	4	750	754	
QUE-11-f1	36	754	790	
Cut	4	790	794	
QUE-11-6	16	794	**810**	810 mm polished
Cut	4	810	814	
QUE-11-f2	19	814	833	
Cut	4	833	837	
QUE-11-3	13	**837**	**850**	TC el 12, 837 and 850 mm polished
Cut	4	850	854	
QUE-11-g1	26	854	880	

Cut	4	880	884	
QUE-11-7	16	884	**900**	900 mm polished
Cut	4	900	904	
QUE-11-g2	29	904	933	
Cut	4	933	937	
QUE-11-4	13	937	**950**	TC elevation 13, 950 mm polished
Cut	4	950	954	
QUE-11-h1	26	954	980	
Cut	4	980	984	
QUE-11-8	16	984	**1000**	1000 mm polished
Cut	4	1000	1004	
QUE-11-h2	29	1004	1033	
Cut	4	1033	1037	
QUE-11-5	13	1037	**1050**	TC elevation 14, 1050 mm polished
Cut	4	1050	1054	
QUE-11-i	342	1054	1396	
Cut	4	1396	1400	
		1400		Upper remnant

***)** Nominal values.

****)** Width of all cuts is 4 mm (large sawing machine with saw blade diameter of 500 mm).

Table 15: QUENCH-11; Results of bundle filling with epoxy resin

Elevation, mm	Epoxy mass, g/10 mm
300	285
310	269
320	271
330	269
340	265
350	265
360	283
370	274
380	277
390	283
400	271
410	271
420	270
430	274
440	265
450	261
460	277
470	281
480	271
490	269
500	267
510	264
520	264
530	277
540	267
550	263
560	272
570	263
580	261
590	264
600	263
610	257
620	262
630	258
640	259
650	265
660	265
670	261
680	261
790	274
800	241
810	250

Elevation, mm	Epoxy mass, g/10 mm
820	258
830	275
840	247
850	255
860	242
870	233
880	255
890	243
900	255
910	237
920	236
930	238
940	254
950	247
960	253
970	256
980	244
990	258
1000	252
1010	265
1020	260
1030	277
1040	270
1050	277
1060	274
1070	273
1080	277
1090	268
1100	271
1110	263
1120	277
1130	282
1140	271
1150	287
1160	277
1170	278
1180	284
1190	272
1200	275
1210	276
1220	278
1230	276

Table 16: QUENCH-11; Evaluation of various areas from cross sections

	Zry cladding	ZrO_2 cladding (oxide scale)	Pellets	Heater/ electrodes	Zry melt between rods	ZrO_2 melt between rods	Mo/W melt betw. rods	Shroud, still intact	Shroud, melt Zry	Shroud, melt ZrO_2	Shroud, melt Mo/W
650 mm QUE-11-1	475 mm^2	∅ scale 12,4 µm => 8,8 mm^2 or 1,2 % of complete ox.	782 mm^2	565 mm^2	_____	_____	_____	Intact 360°, 616 mm^2 Zry	_____	_____	_____
750 mm QUE-11-2	462 mm^2	∅scale 37,5 µm => 26,6 mm^2 or 3,5 % of complete ox.	782 mm^2	565 mm^2	36 mm^2	_____	_____	Intact 360°, 42 µm scale => 11 mm^2 ZrO_2 and 605 mm^2 Zry	_____	_____	_____
810 mm QUE-11-6	368 mm^2	∅scale 277 µm => 158 mm^2 or 21 % of complete ox.	770 mm^2	565 mm^2	146 mm^2	116 mm^2 (scale) + 56 mm^2 (precipitates in Zry melt)	20 mm^2	Intact 280°; 286 µm scale => 39 mm^2 ZrO_2 and 454 mm^2 Zry	220 mm^2	102 mm^2 (scale) + 165 mm^2 (precipitates)	_____
850 mm QUE-11-3	32 mm^2	∅scale 944 µm) 473 mm^2 or 63 % of complete ox.	782 mm^2	565 mm^2	172 mm^2	417 mm^2 (scale and pool) + 147 mm^2 (precipitates in Zry melt)	89 mm^2	Intact 45°; 712 µm scale => 18 mm^2 ZrO_2 and 77 mm^2 Zry	461 mm^2	1110 mm^2 (scale and pool) + 732 mm^2 (precipitates)	77 mm^2
900 mm QUE-11-7	Completely consumed or relocated	590 mm^2 or 79 % of complete ox.	766 mm^2	564 mm^2	_____	303 mm^2	146 mm^2	_____	NOT DETERMINED		
950 mm QUE-11-4	Completely consumed or relocated	655 mm^2 or 84 % of complete ox.	699 mm^2	547 mm^2	_____	391 mm^2	172 mm^2	_____			
1000 mm QUE-11-8	Completely consumed or relocated	291 mm^2 or 39 % of complete ox.	717 mm^2	556 mm^2	_____	330 mm^2	154 mm^2	_____			
1050 mm QUE-11-5	Completely consumed or relocated	Included in melt between rods	61 mm^2 (Central rod only)	952 mm^2 (max. 1162)	_____	744 mm^2 includes ZrO_2 cladding	90 mm^2	_____			

Table 17: QUENCH-11; Contributions to the total hydrogen release estimated with help of the posttest bundle status.

Component	Location	Assumption	H_2, g
Cladding	0-900 mm	interpolation and integration of oxide scale measurements	14
	900-1300 mm	complete oxidation	55
	>1300 mm	rough estimation, no data	5
Corner rods	B (withdrawn)	interpolation and integration of oxide scale measurements	0.1
	A, C, D 0-900 mm	interpolation and integration of oxide scale measurements	1
	A, C 900-1300 mm	complete oxidation of instrumentation tubes	3
	D 900-1150 mm	complete oxidation of rod	1
Shroud	0-1050 mm inner surface	interpolation and integration of oxide scale measurements	8
	500-1300 mm outer surface	interpolation and integration of oxide scale measurements	8
	1050-1250 mm	80% oxidation of molten and relocated shroud, excluding the remaining oxide (see line above)	24
Grid spacers	550, 1050, 1410 mm	1x completely oxidized plus small contribution of lower and upper one	5
W heaters	900-1024 mm	from metallography: 2% consumption and oxidation over a length of 10 cm	1
Mo electrodes	1024-1200 mm	from metallography: 18% molten of which 50% oxidised over a length of 20 cm	13
HT-TCs	0-900 mm	interpolation and integration of oxide scale measurements at cladding	1
	900-1300, Zry	complete oxidation	2
	900-1300, Ta	complete oxidation	1
Σ			**143**

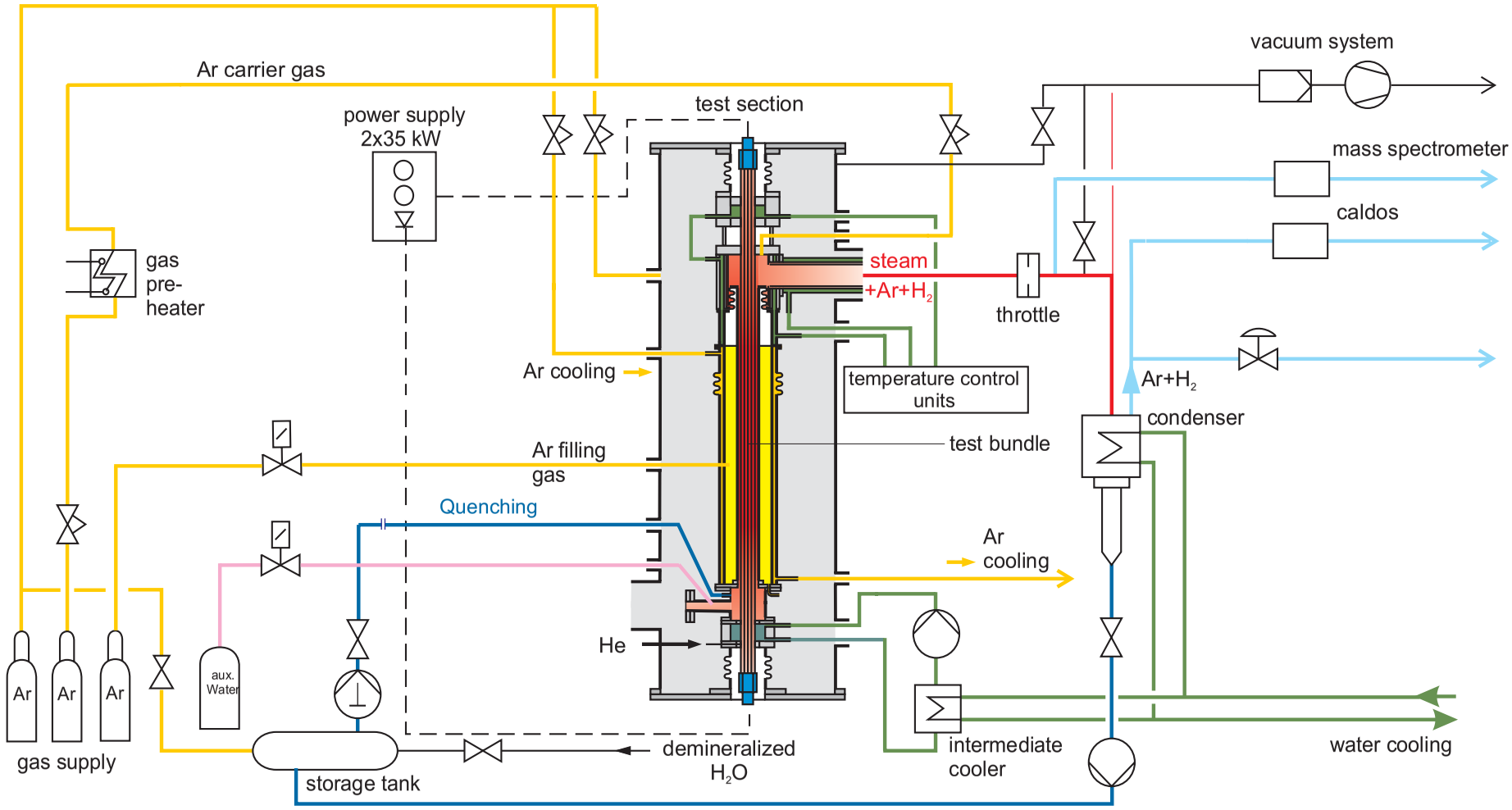

Fig.1-QUE11-Flow diagram.cdr
07.02.06 - IMF

Fig. 1: Flow diagram of the QUENCH test facility.

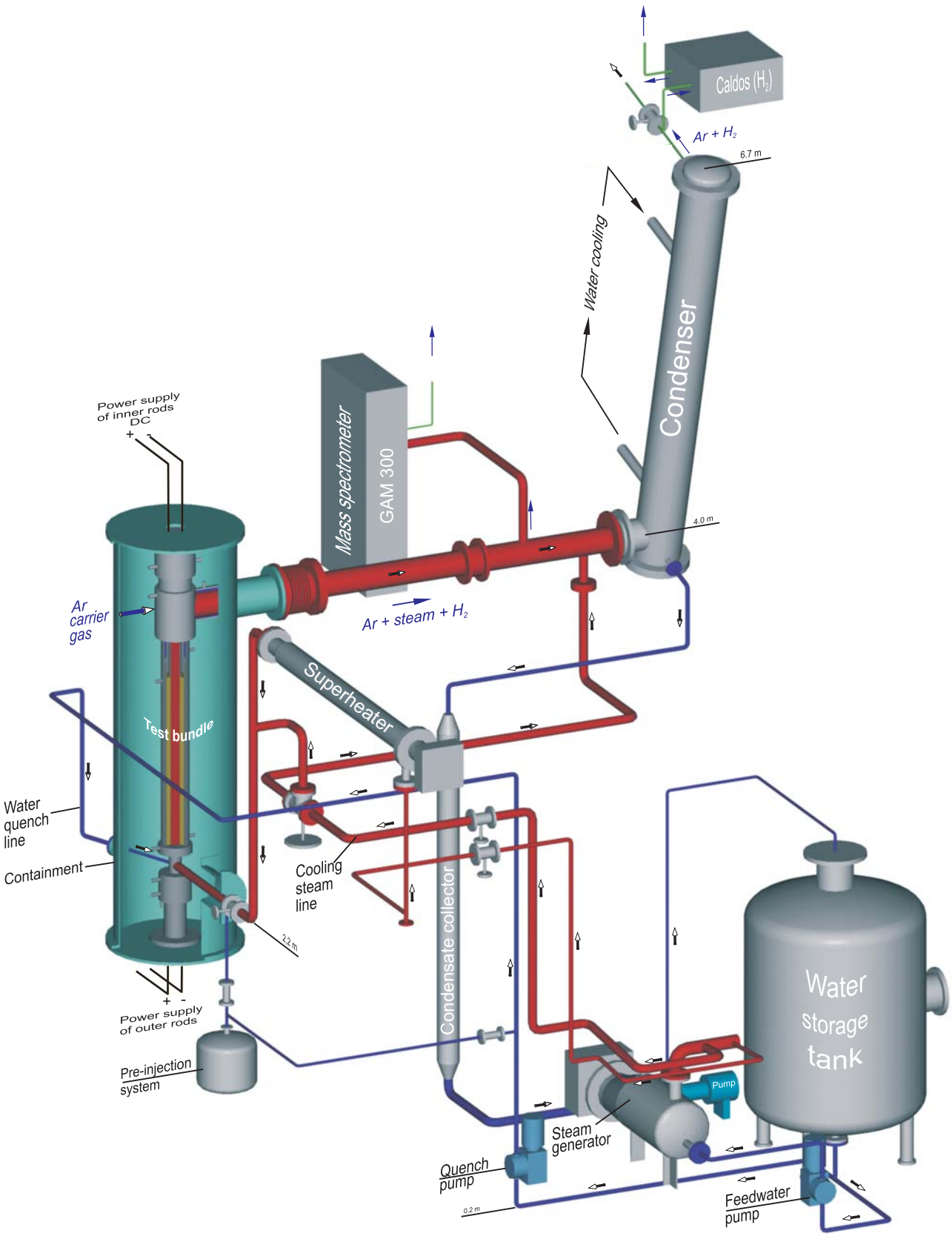

Fig.2-QUE11-Gesamtanlage.cdr
01.09.05 - IMF

Fig. 2: QUENCH Facility - Main components.

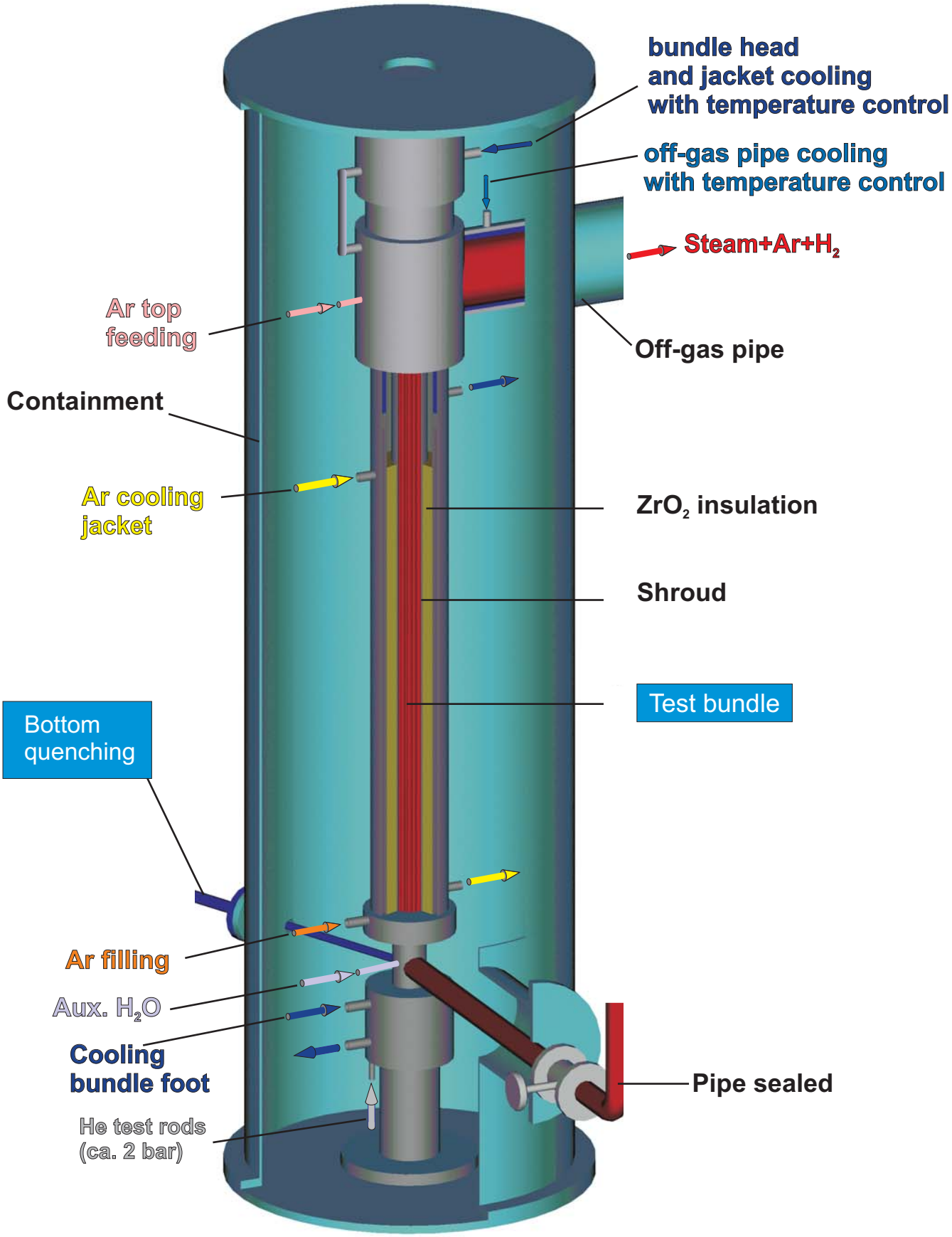

Fig. 3: QUENCH Facility; Containment and test section.

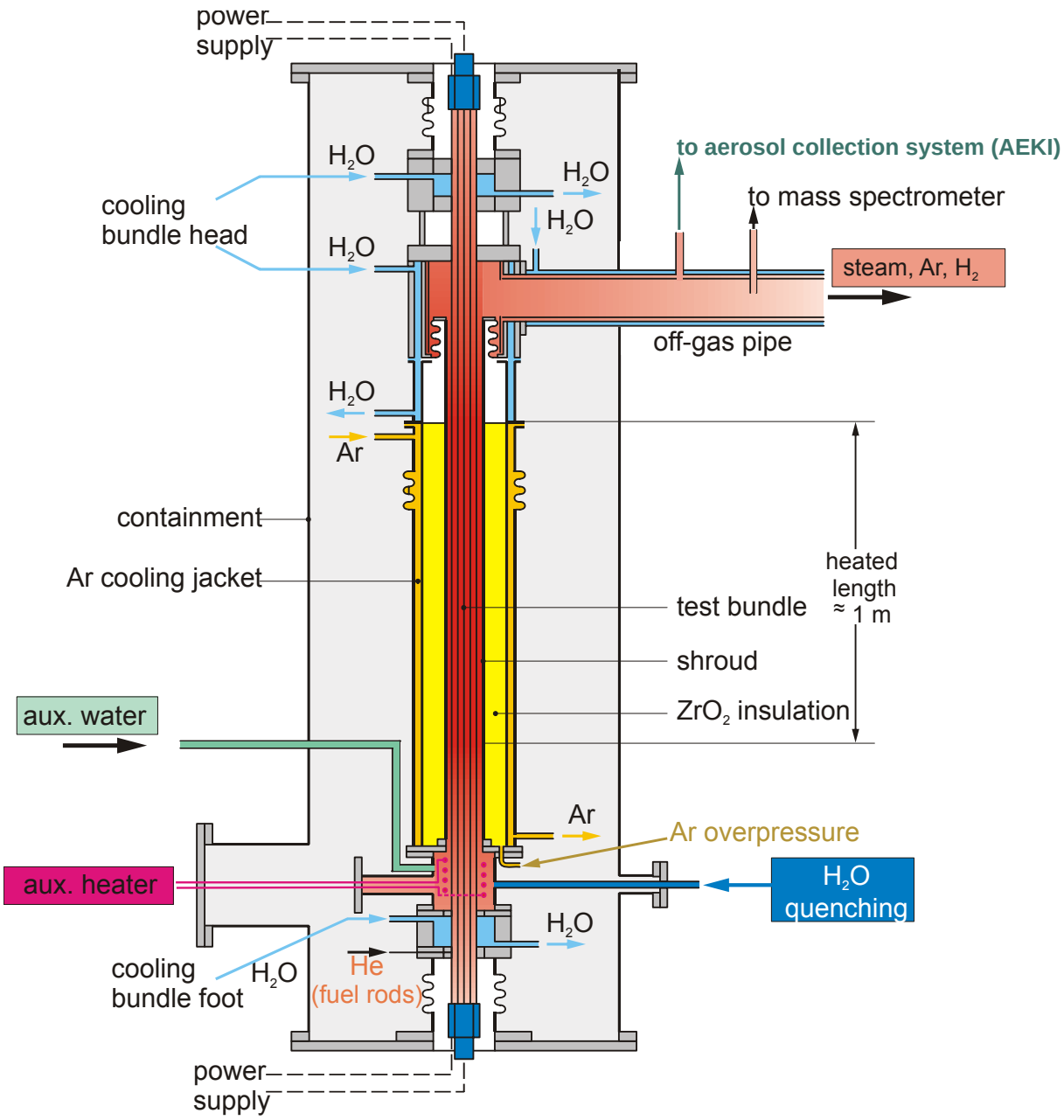

Fig. 4: QUENCH-11; Test section with flow lines.

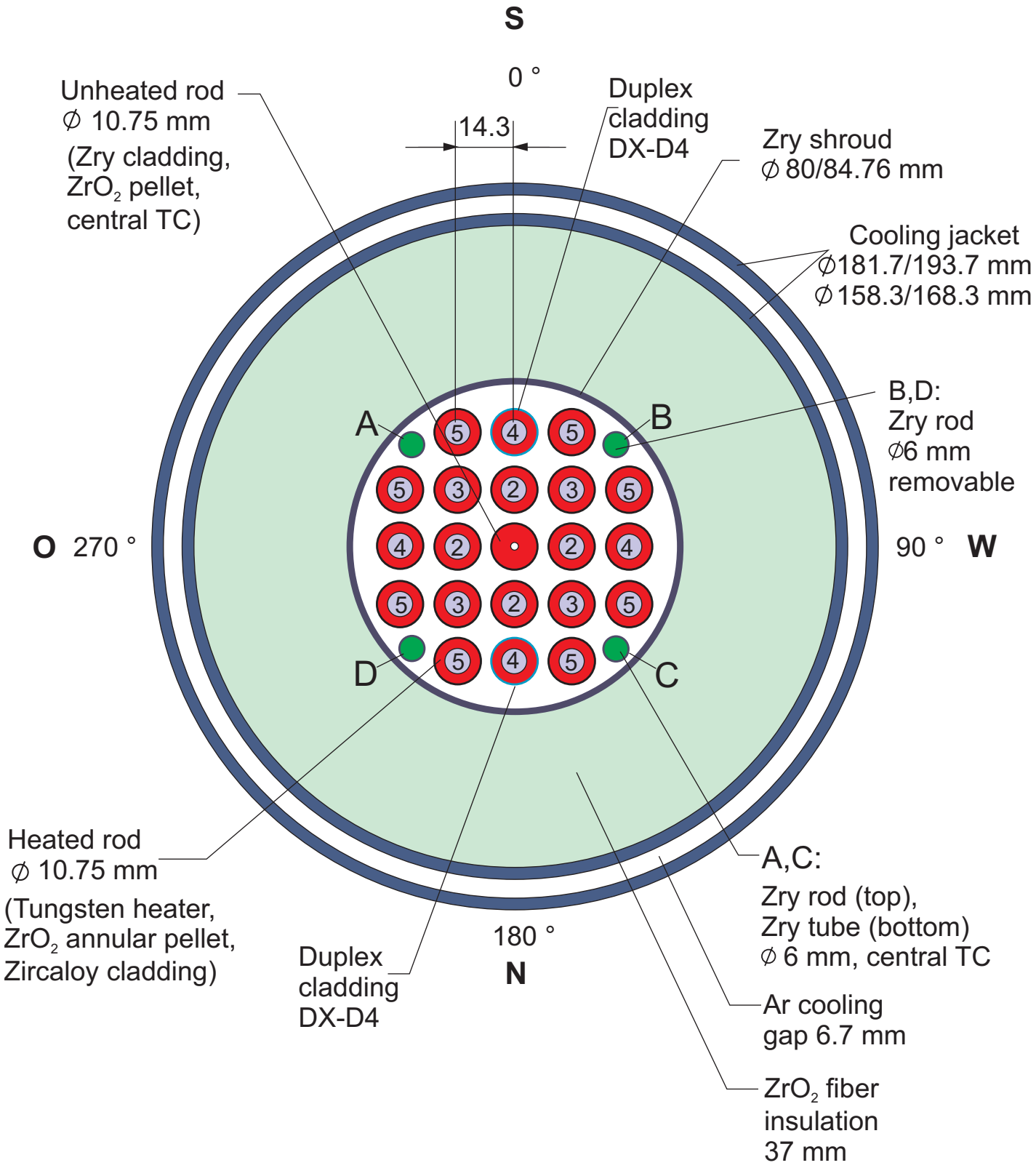

Fig. 5: QUENCH-11; Fuel rod simulator bundle (cross section, top view) including rod type indications.

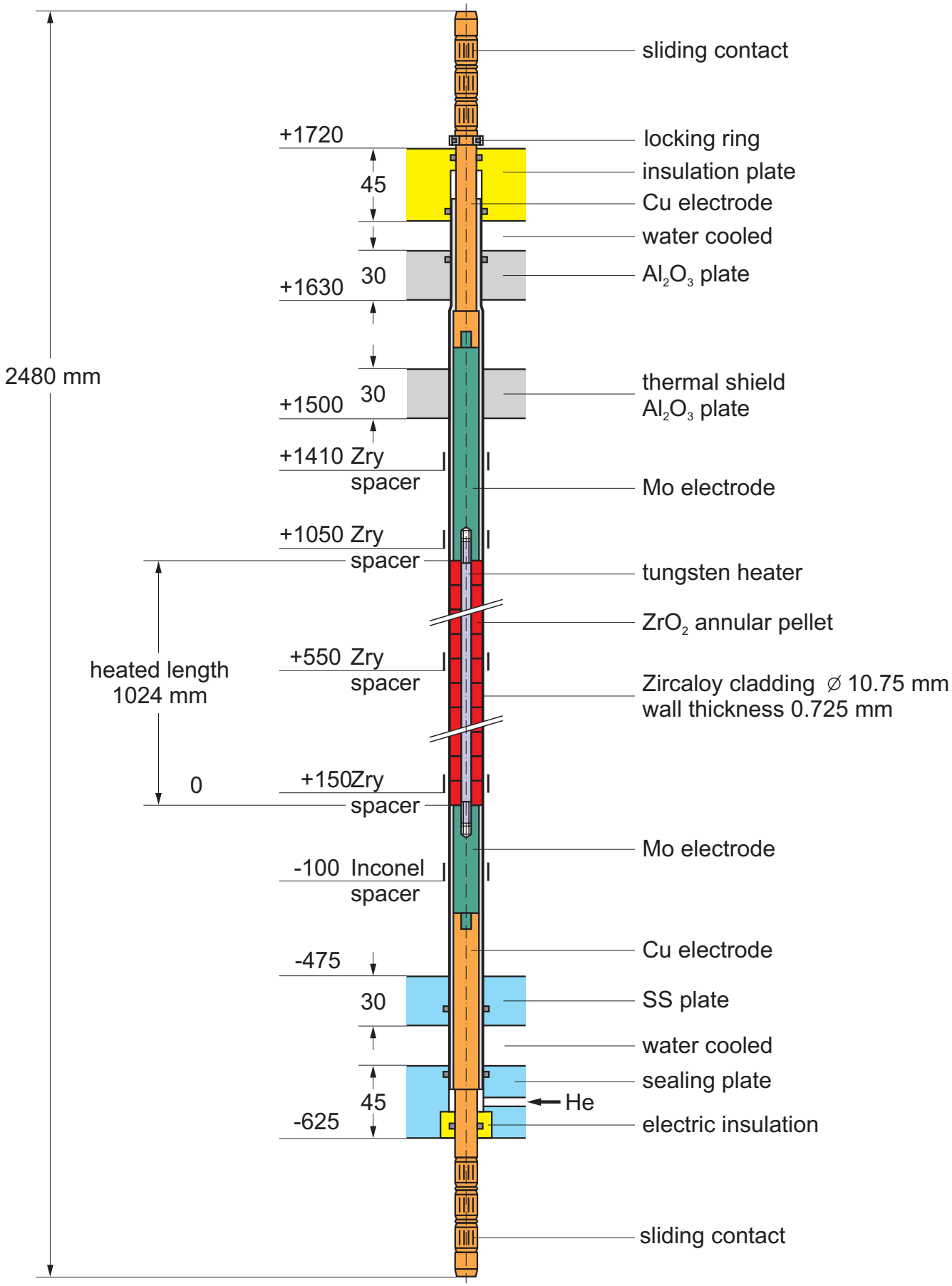

Fig.6-QUE11-Heated fuel rod sim.cdr
27.10.05 - IMF

Fig. 6: Heated fuel rod simulator.

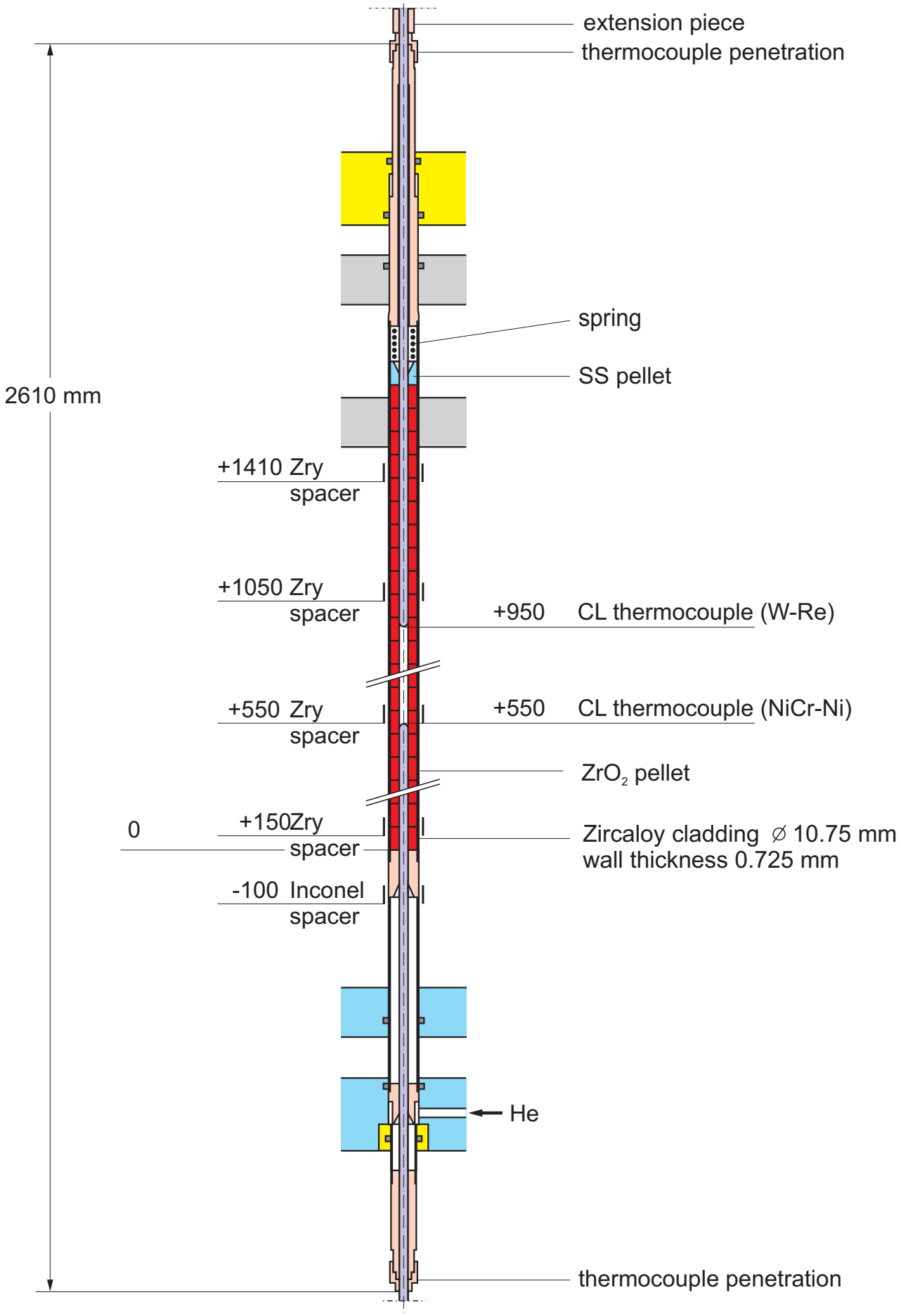

Fig. 7 : Unheated fuel rod simulator.

Fig. 7-QUE11 Unheated fuel rod sim.cdr
27.10.05 - IMF

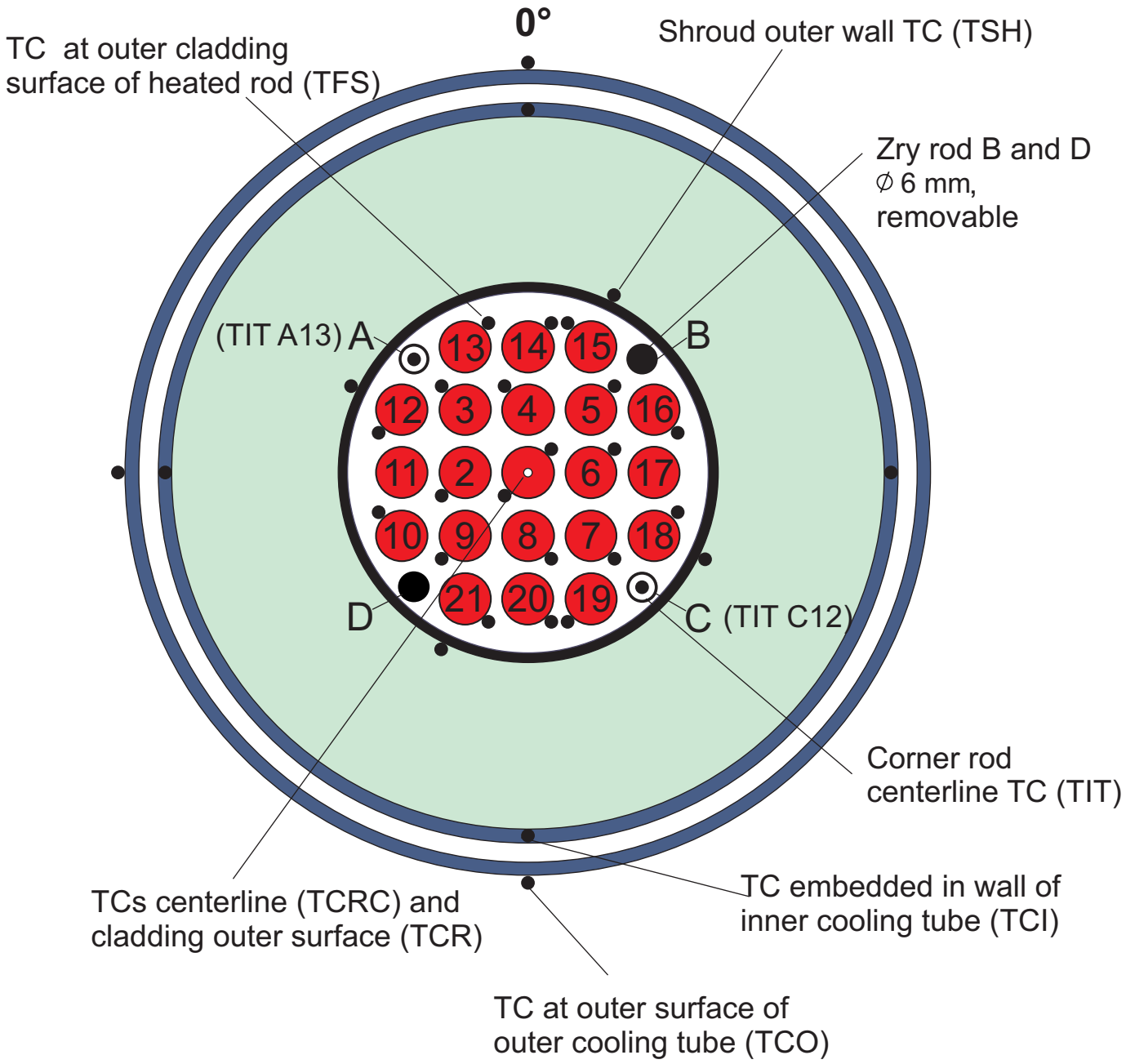

Fig.8-QUE11 TC instr.cdr
06.09.06 - IMF

Fig. 8: QUENCH-11; Test bundle; TC instrumentation and rod designation (top view).

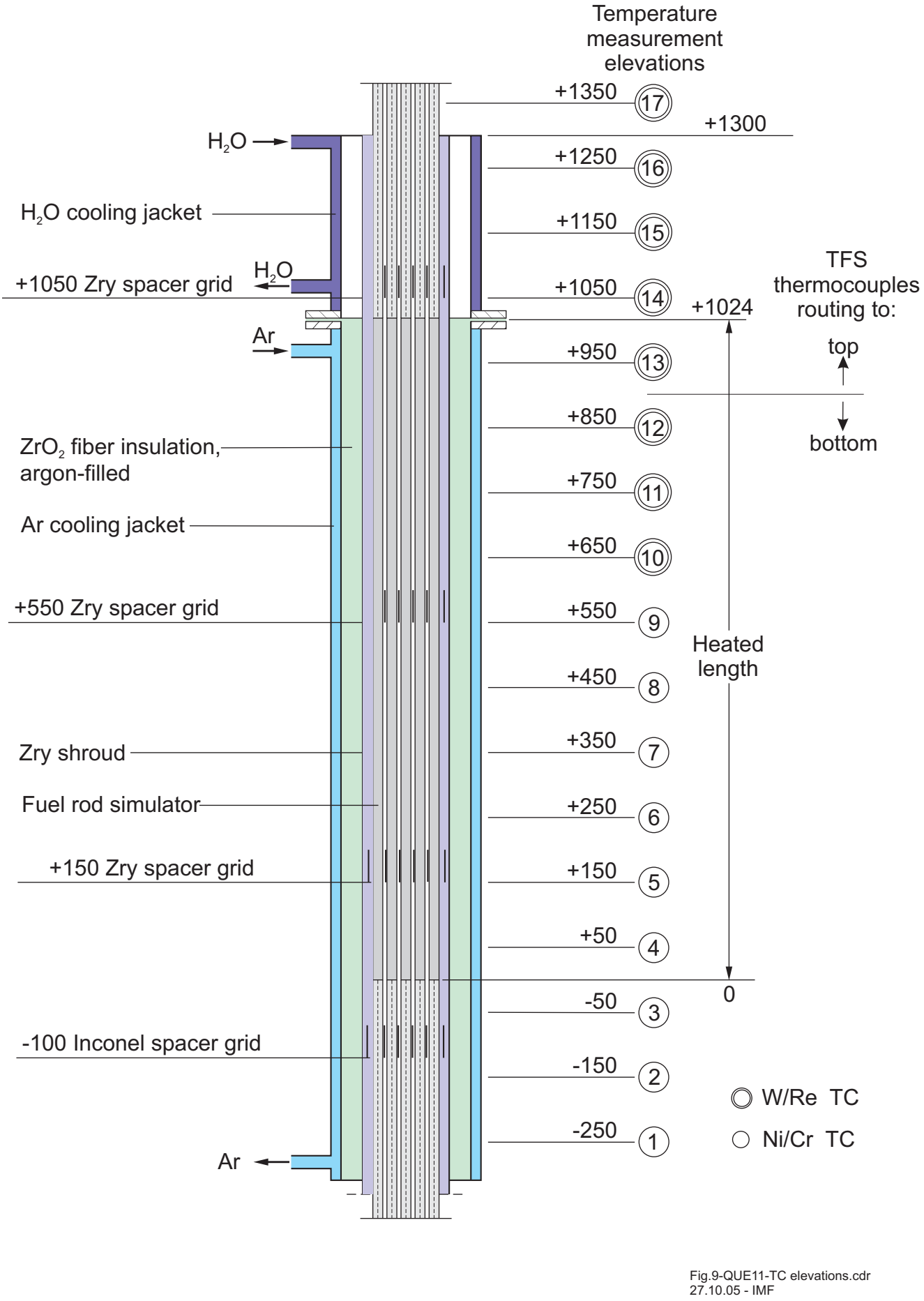

Fig. 9: Axial temperature measurement locations in the QUENCH test section.

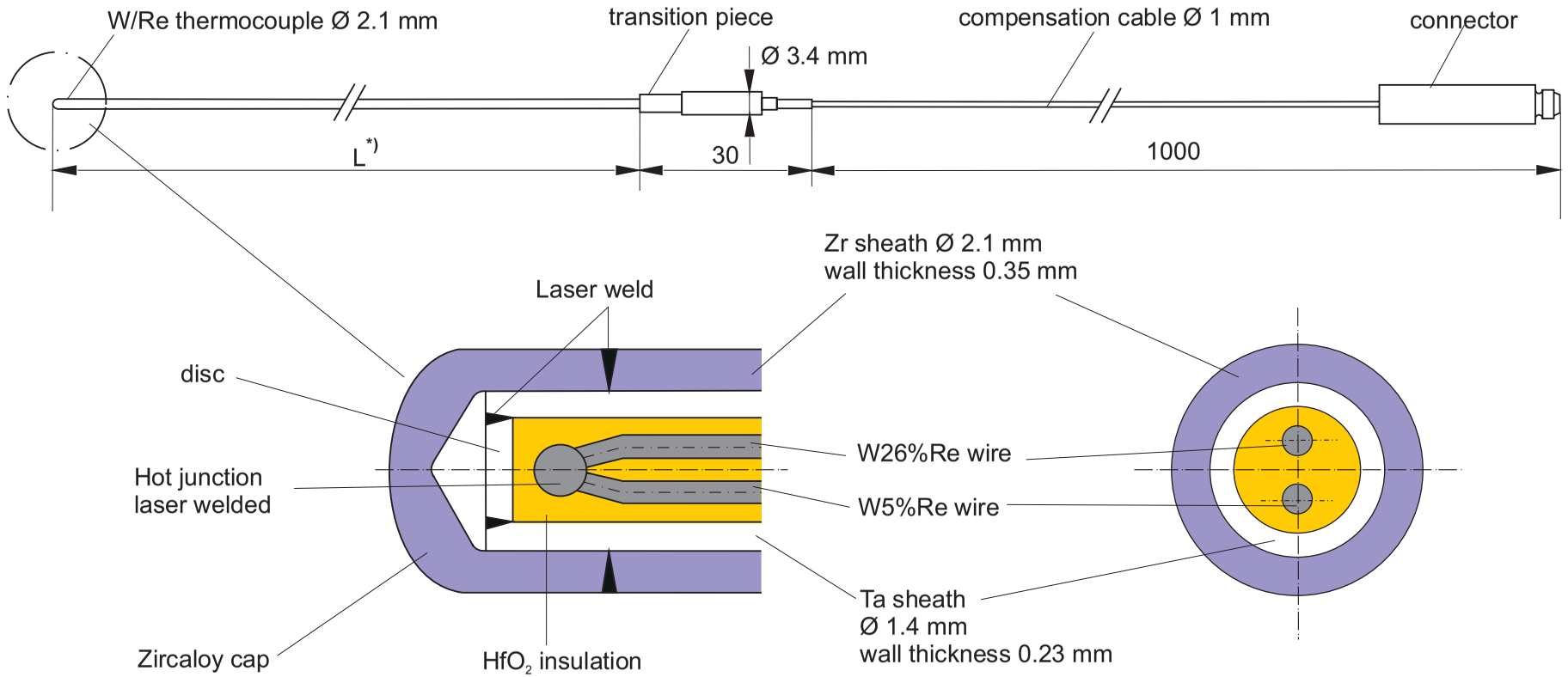

*) L: high-temperature section length dependent on the TC position in the test bundle 500 mm - 1700 mm

Fig.10-QUE11-High-temp thermocouple.cdr
06.09.05 - IMF

Fig. 10: QUENCH; High-temperature thermocouple.

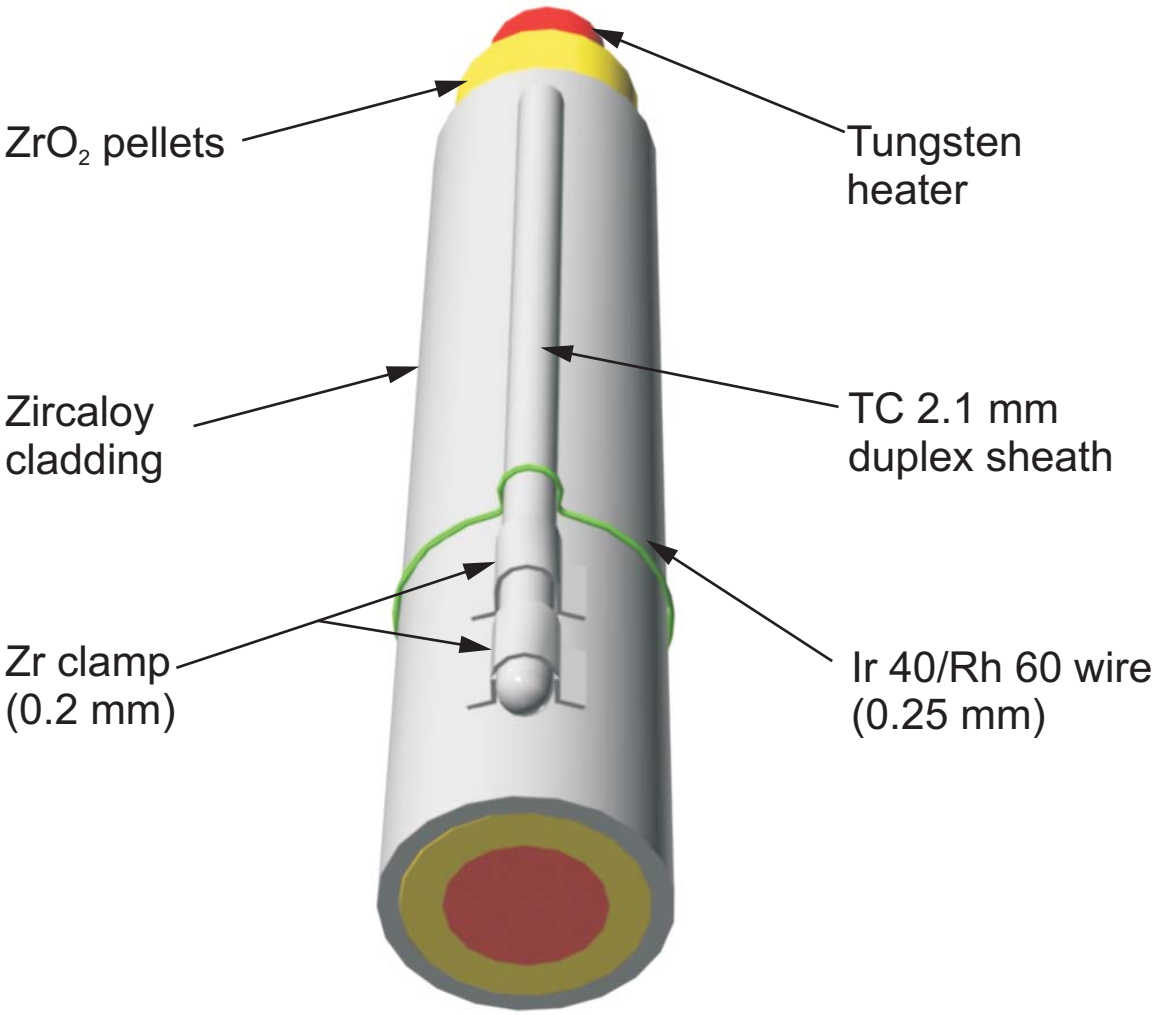

Fig. 11: QUENCH-11; Concept for TC fastening at the test rod.

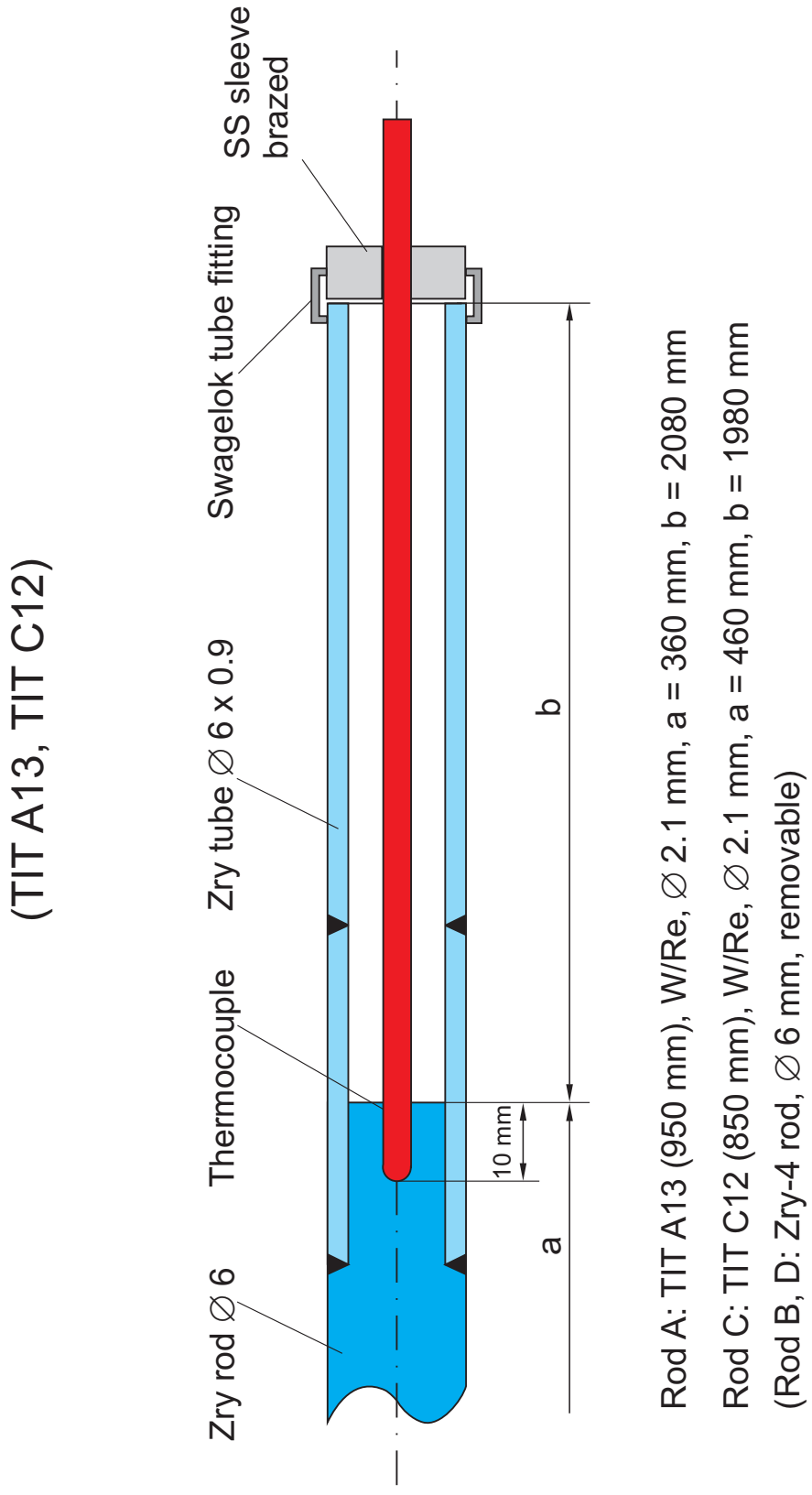

Fig 12-QUE11-TC in corner rod.cdr
07.09.05 - IMF

Fig. 12: QUENCH-11; Arrangement of the thermocouples inside the corner rods.

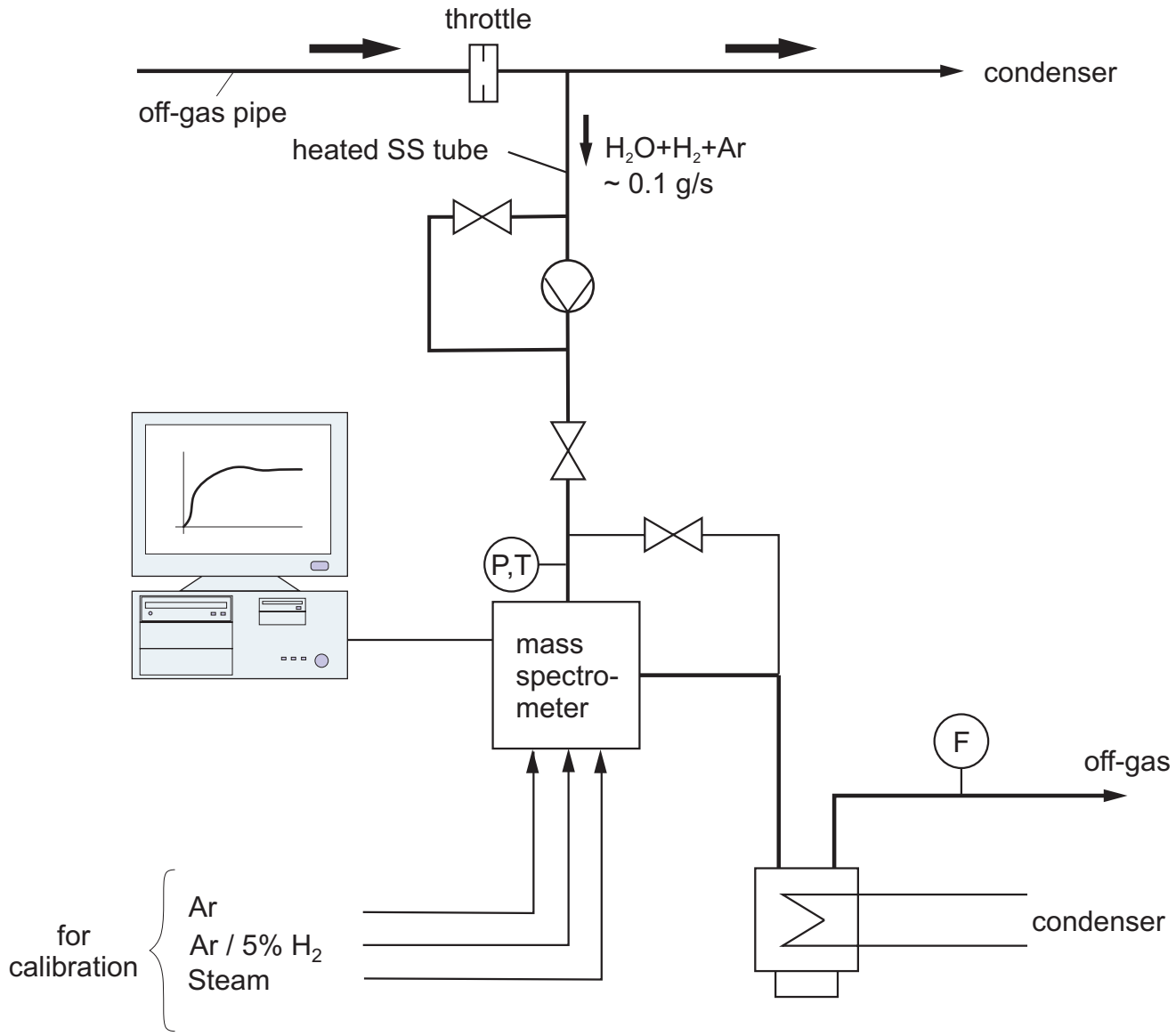

Fig.13-QUE11-MS Quench facility.cdr
18.04.07 - IMF

Fig. 13: QUENCH Facility; H_2 measurement with the GAM 300 mass spectrometer.

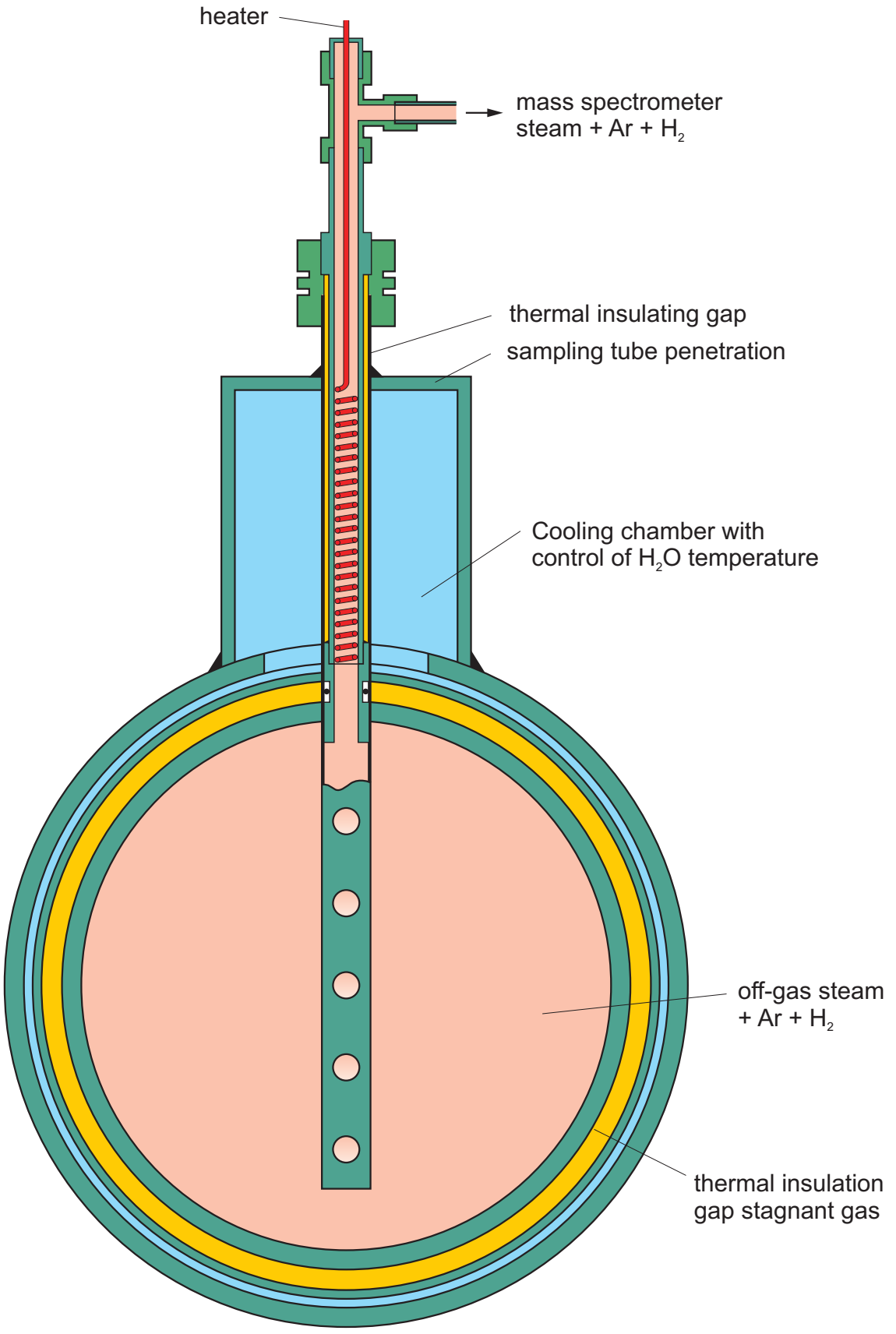

Fig 14-QUE11 MS sampling position new.cdr
07.02.06 - IMF

Fig.14: Mass spectrometer sampling position at the off-gas pipe of the QUENCH test facility.

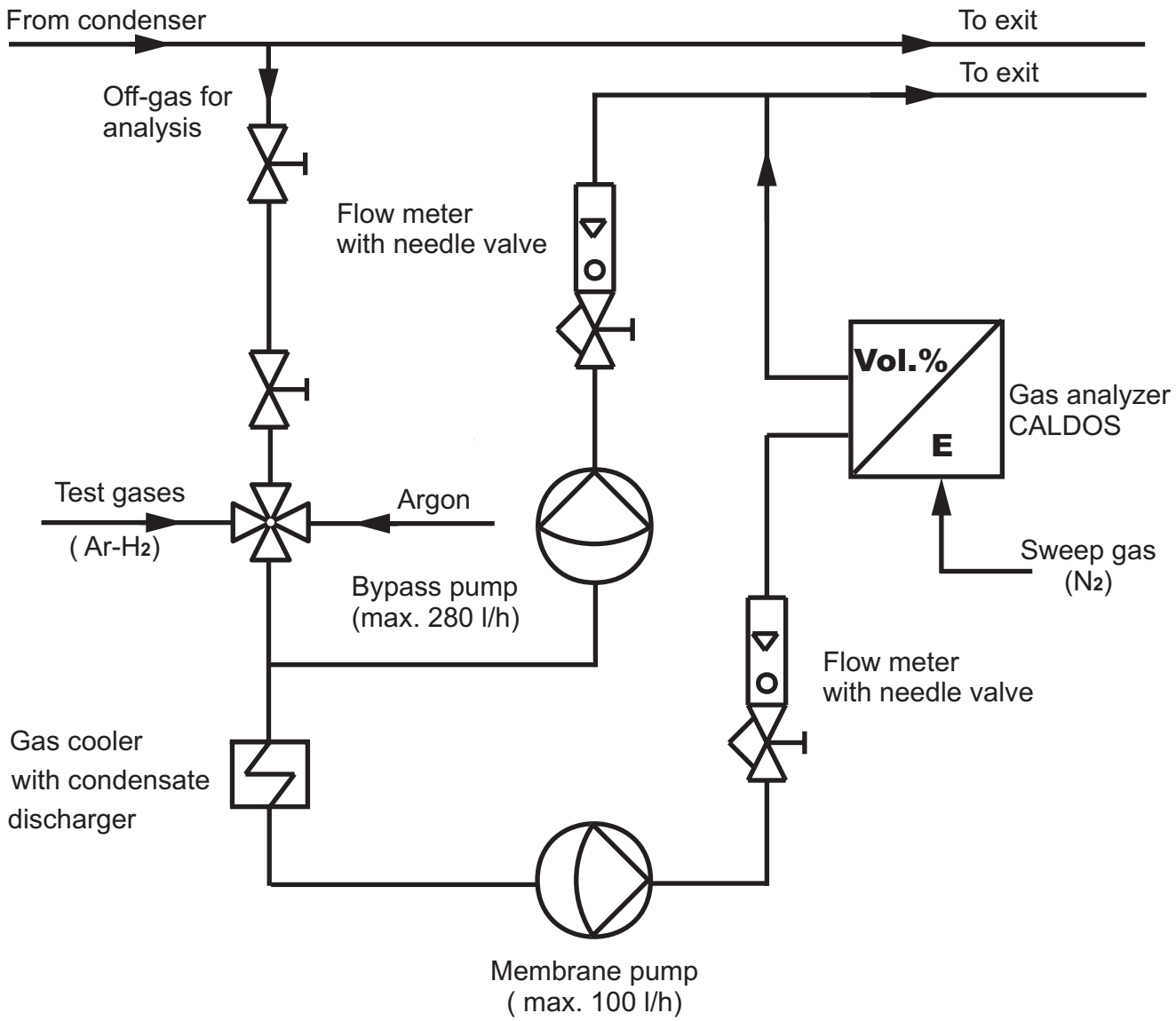

Fig 15 QUE11 Caldos Schema (ab QUE04).cdr
06.09.05 - IMF

Fig.15: Hydrogen measurement with the CALDOS analyzer connected to the exhaust gas pipe of the QUENCH facility.

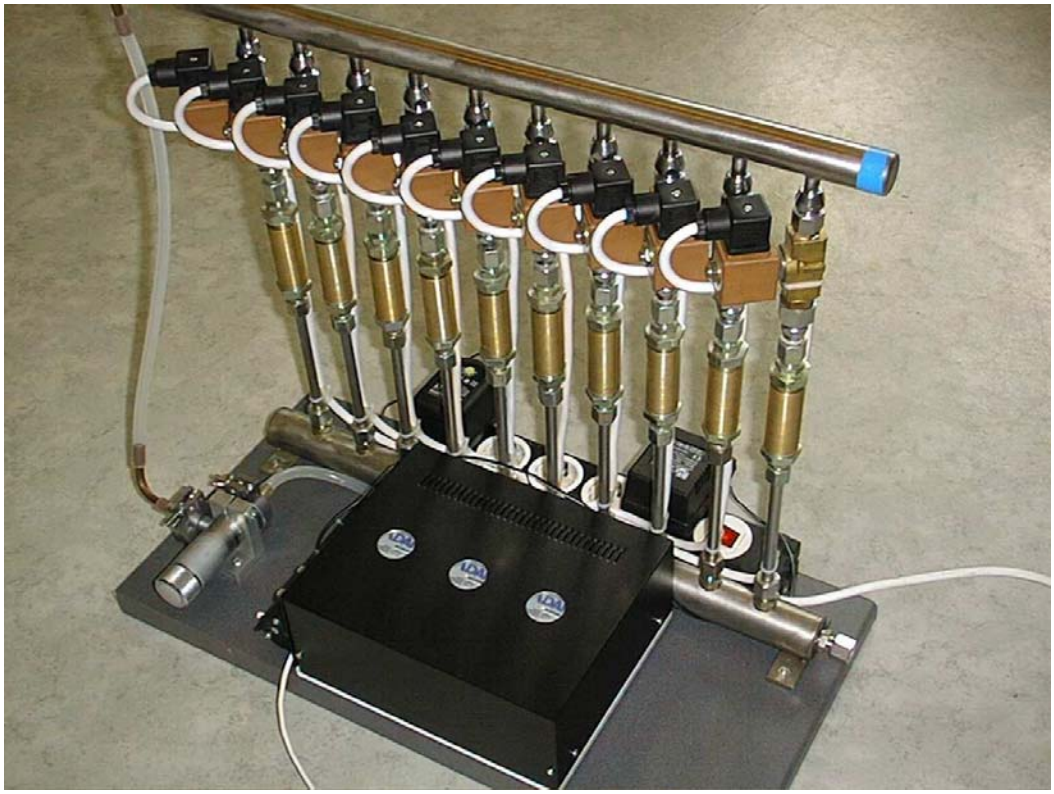

Fig. 16: QUENCH-11; AEKI aerosol sampling system.

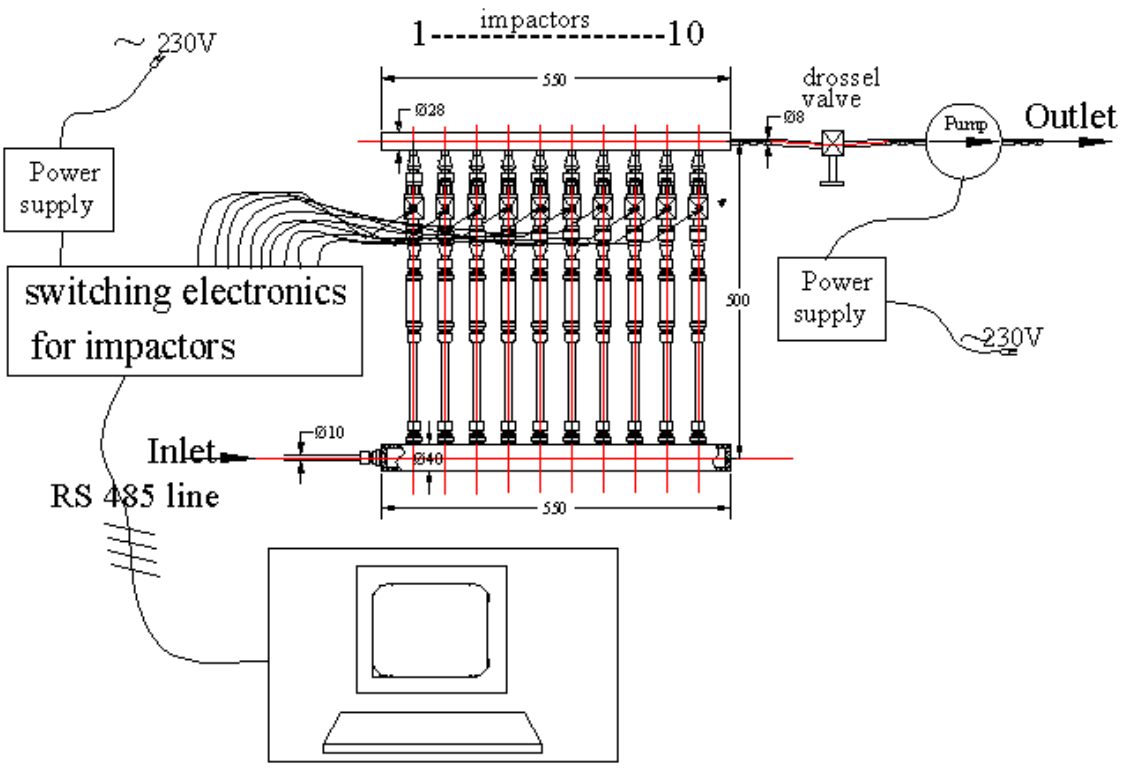

Fig. 17: QUENCH-11; Main components of the AEKI aerosol sampling system.

1 – 1st nozzle,
2 – 1st Si-collector (sample B),
3 – 2nd nozzle,
4 – 2nd Si-collector (sample D),
5 – stream limiter,
6 – quartz fibre filter

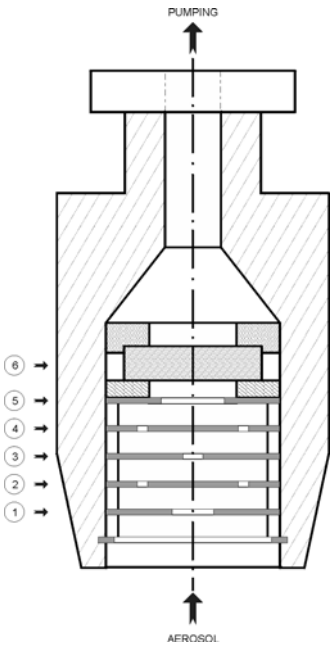

Fig. 18: QUENCH-11; Scheme of the impactor sampler (AEKI).

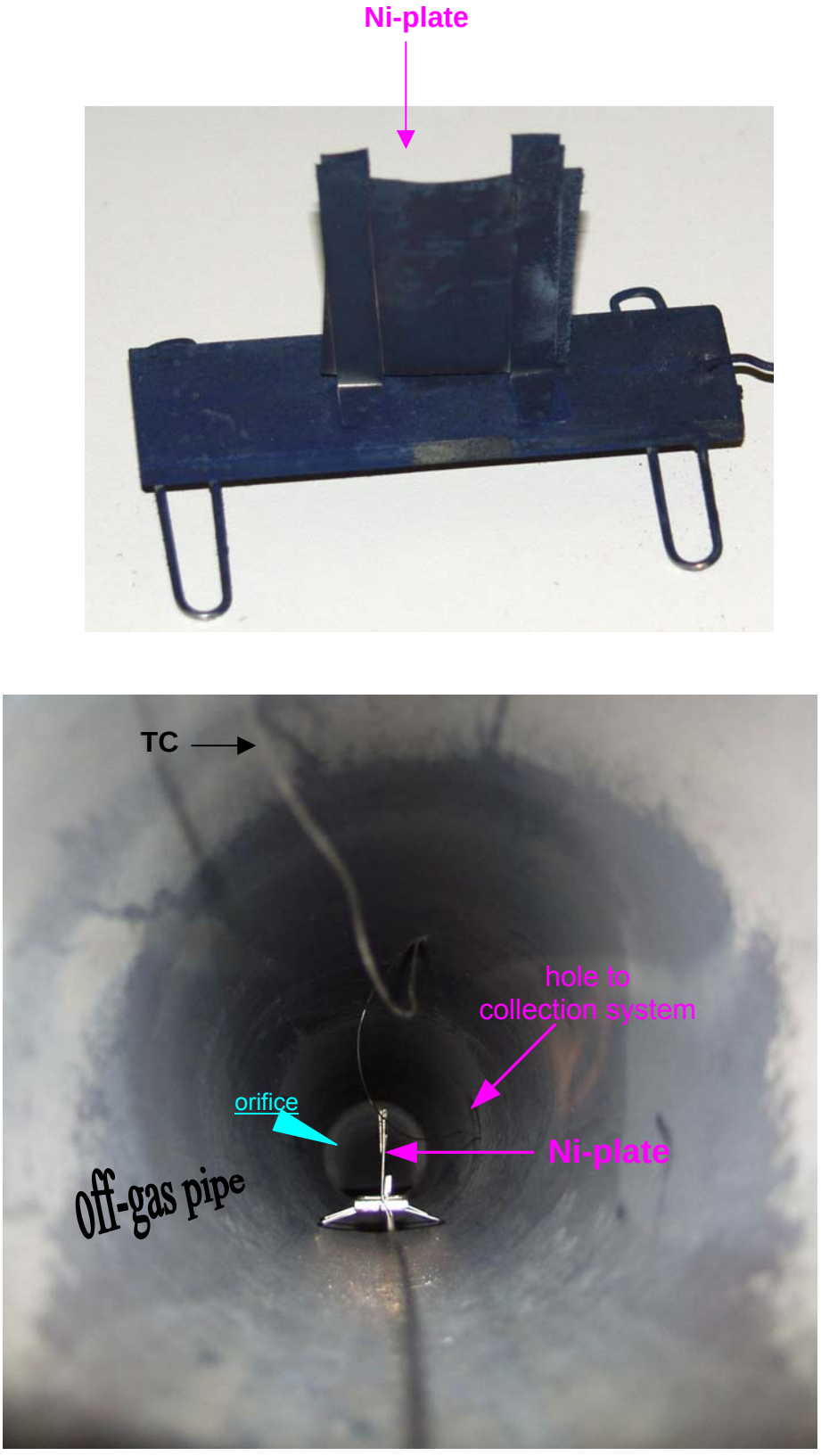

Fig. 19: QUENCH-11; Arrangement to hold the Ni-plate in the off-gas pipe of the QUENCH facility (installed at the bottom of the pipe near the take-up tube for the aerosol collection system).

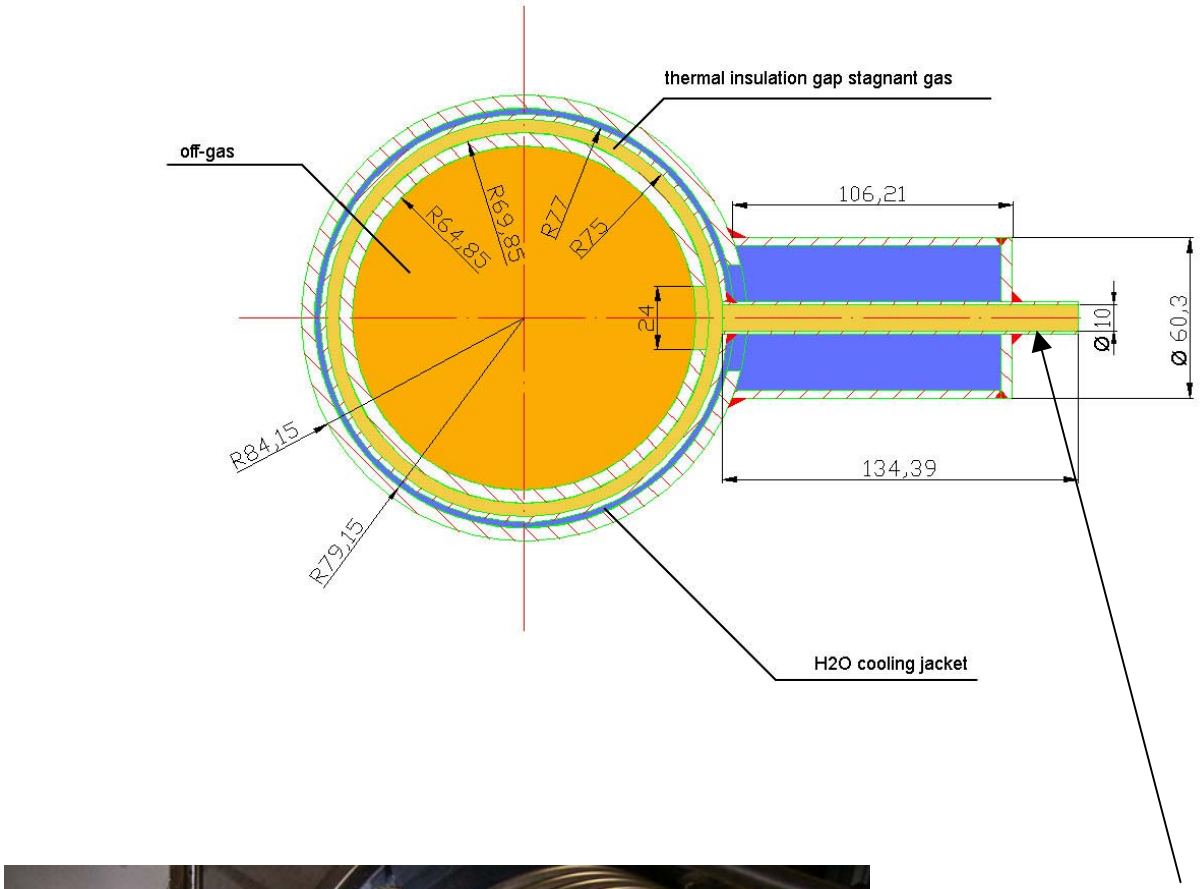

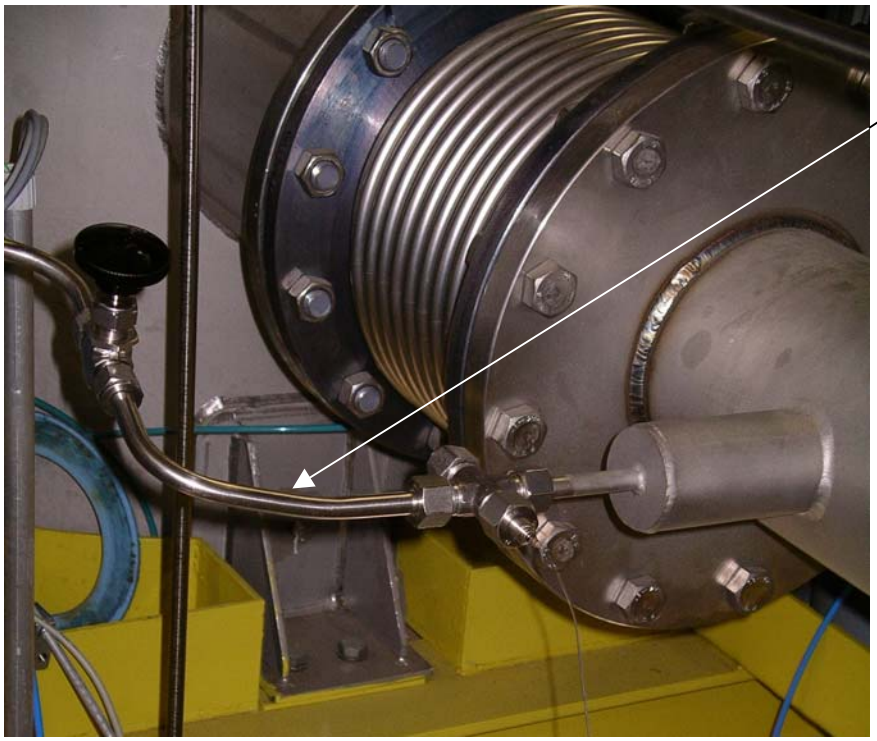

Aerosol feeding line from off-gas pipe to sampler

(distance from flange at test section outlet 1033 mm)

Fig. 20: QUENCH-11; Sampling location at the off-gas pipe for the aerosol sampler,top, and connection of the aerosol sampling device to the off-gas pipe, bottom.

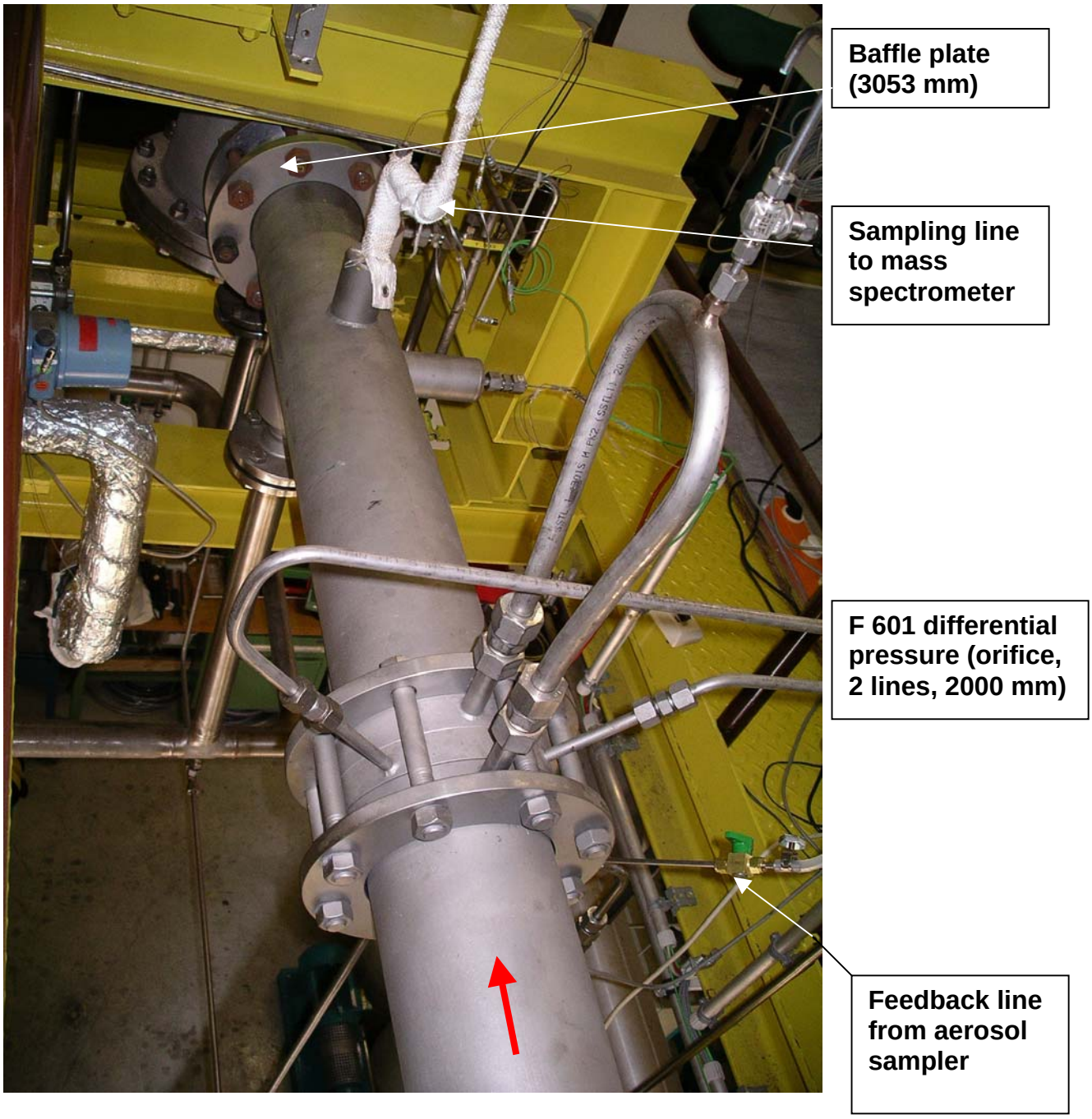

Fig. 21. QUENCH-11; Off-gas pipe (top view) with the standard orifice (F 601) between the two flanges in the center of the photograph. Distances given refer to the flange at the entrance of the off-gas pipe.

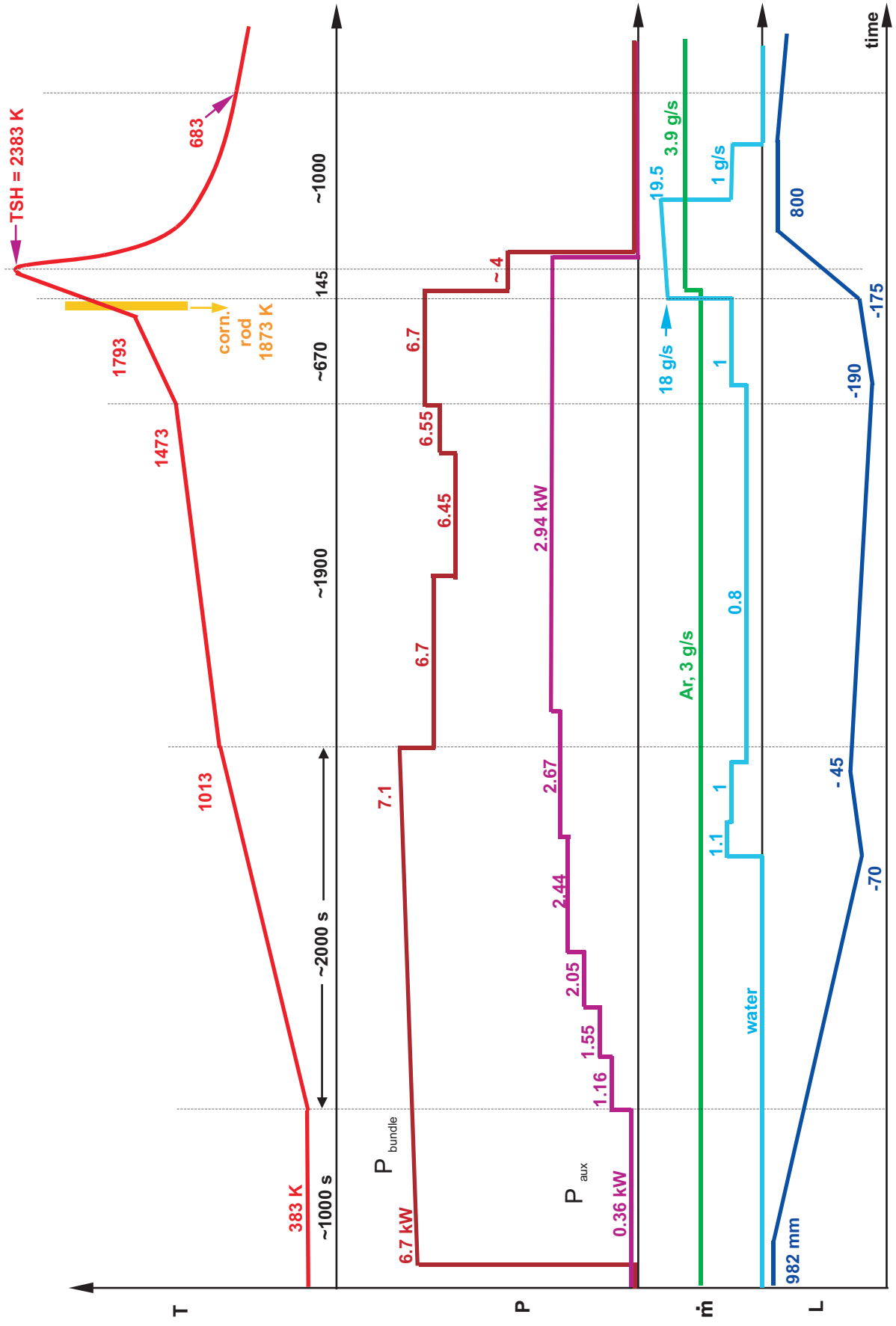

Fig 22 QUE11 test conduct.cdr
13.09.06 - IMF

Fig. 22: QUENCH-11 test conduct (schematics of histories of bundle temperature, bundle and auxiliary power,argon and water flow rate, and water level).

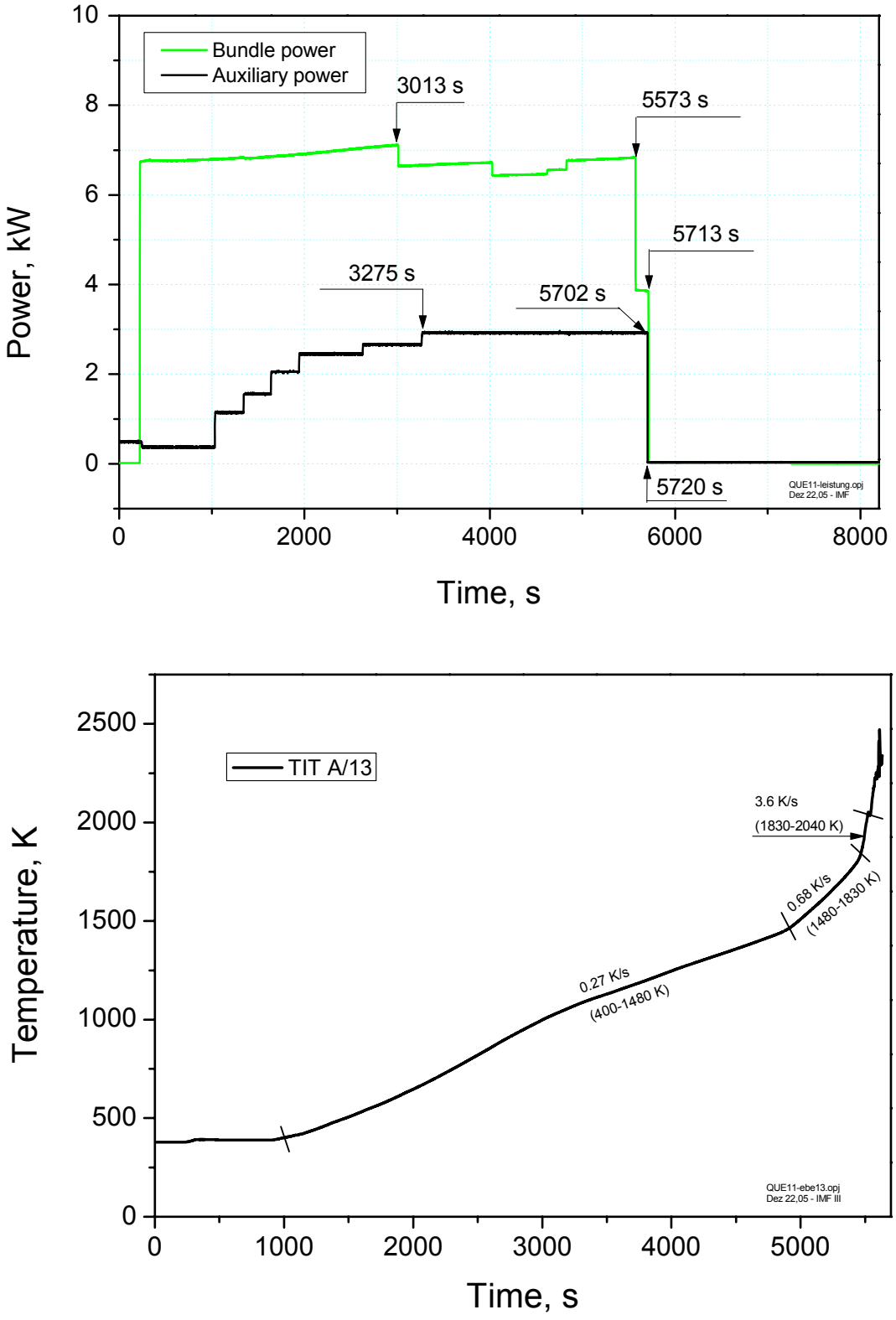

Fig. 23: QUENCH-11; Total electric bundle power and auxiliary power vs. time, top, and heating rates evaluated from TIT A/13, bottom.

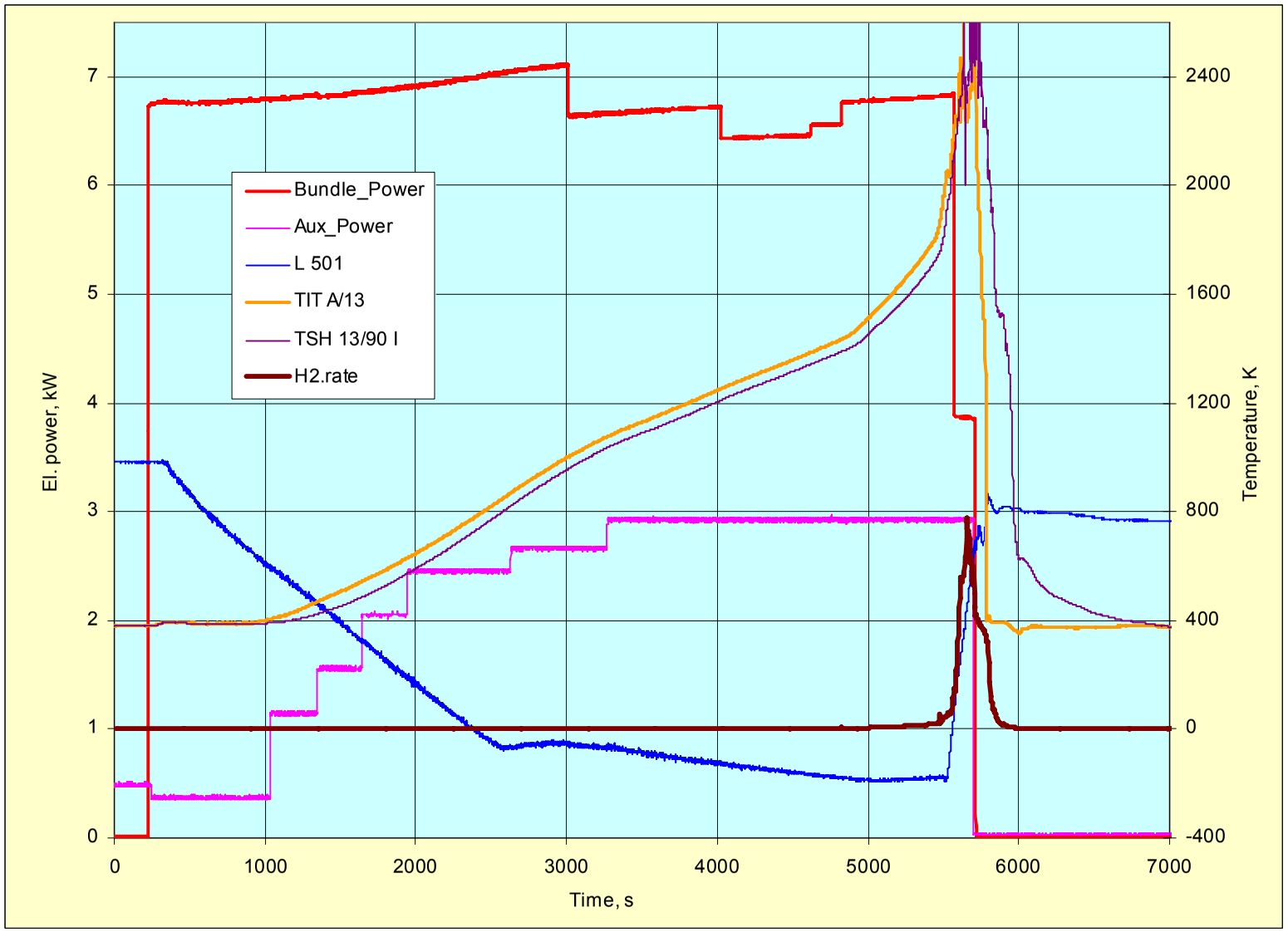

Fig. 24: QUENCH-11; Water level (L 501), bundle and auxiliary power, H_2 generation rate together with temperatures at 950 mm.

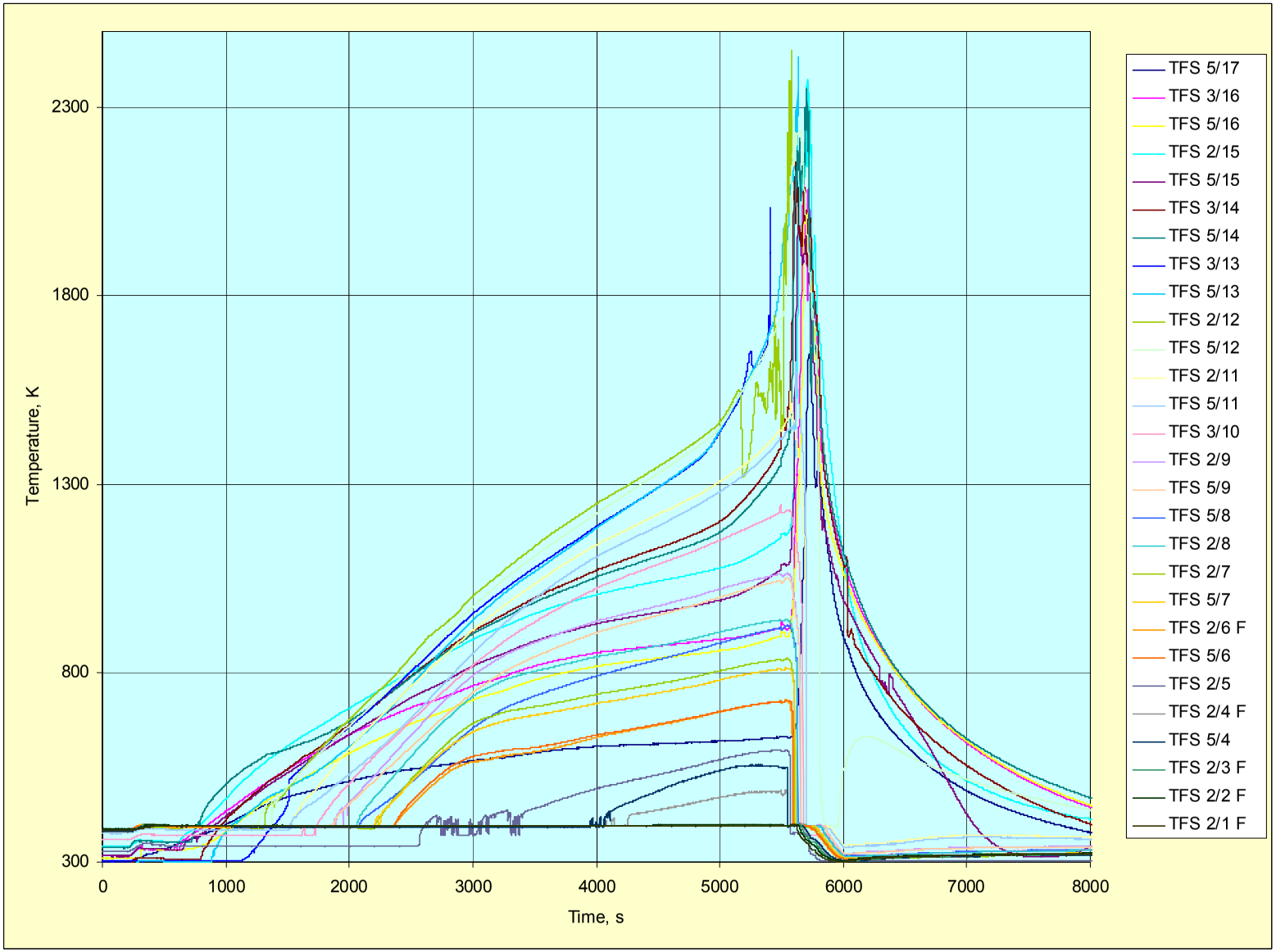

Fig. 25: QUENCH-11; Overview of TFS temperature readings during the quench phase.

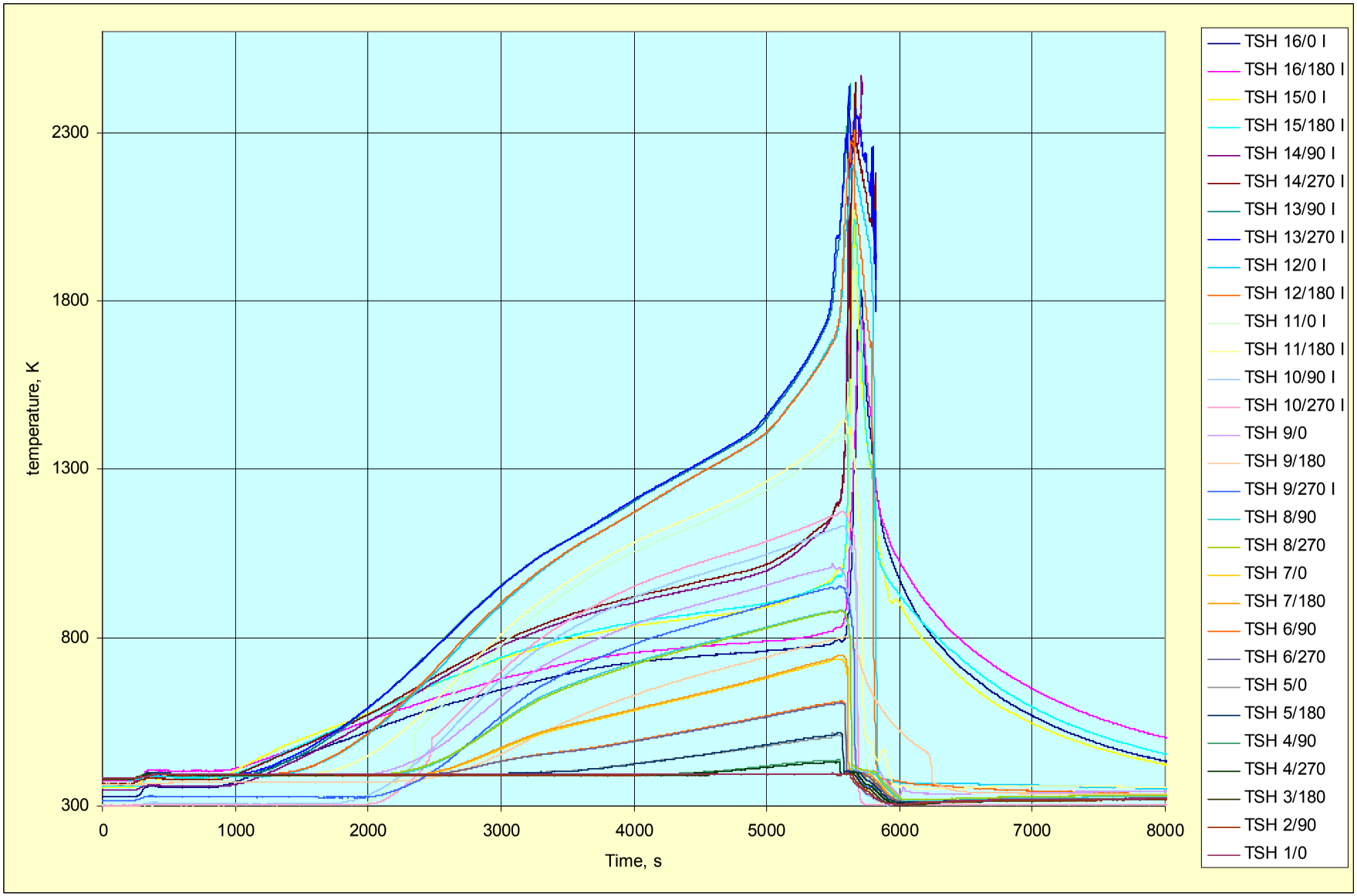

Fig. 26: QUENCH-11; Overview of the shroud temperature readings.

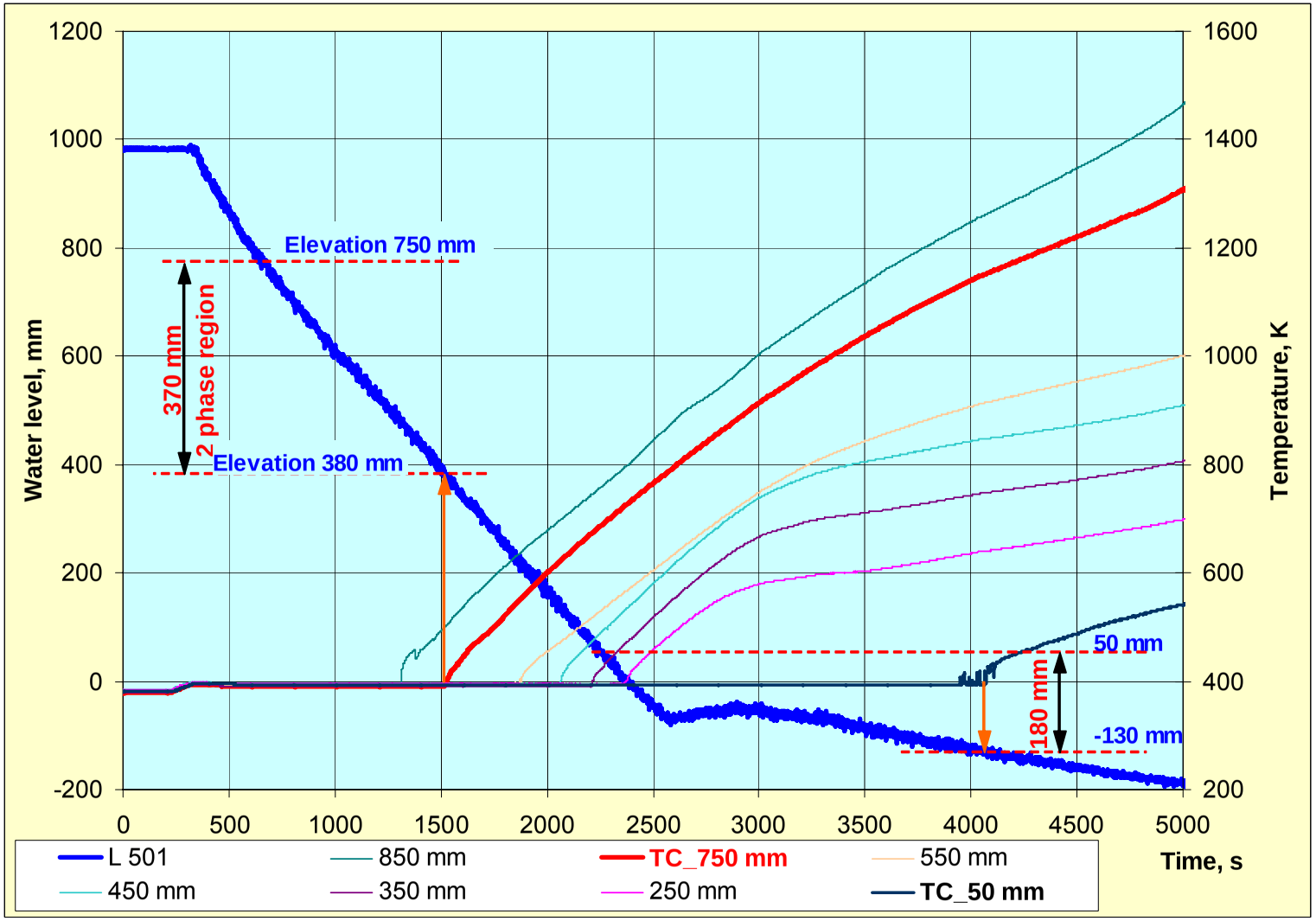

Fig. 27: QUENCH-11; Difference in TC response and water level (L 501) during the decrease of the water front (due to presence of saturated fluid above water surface).

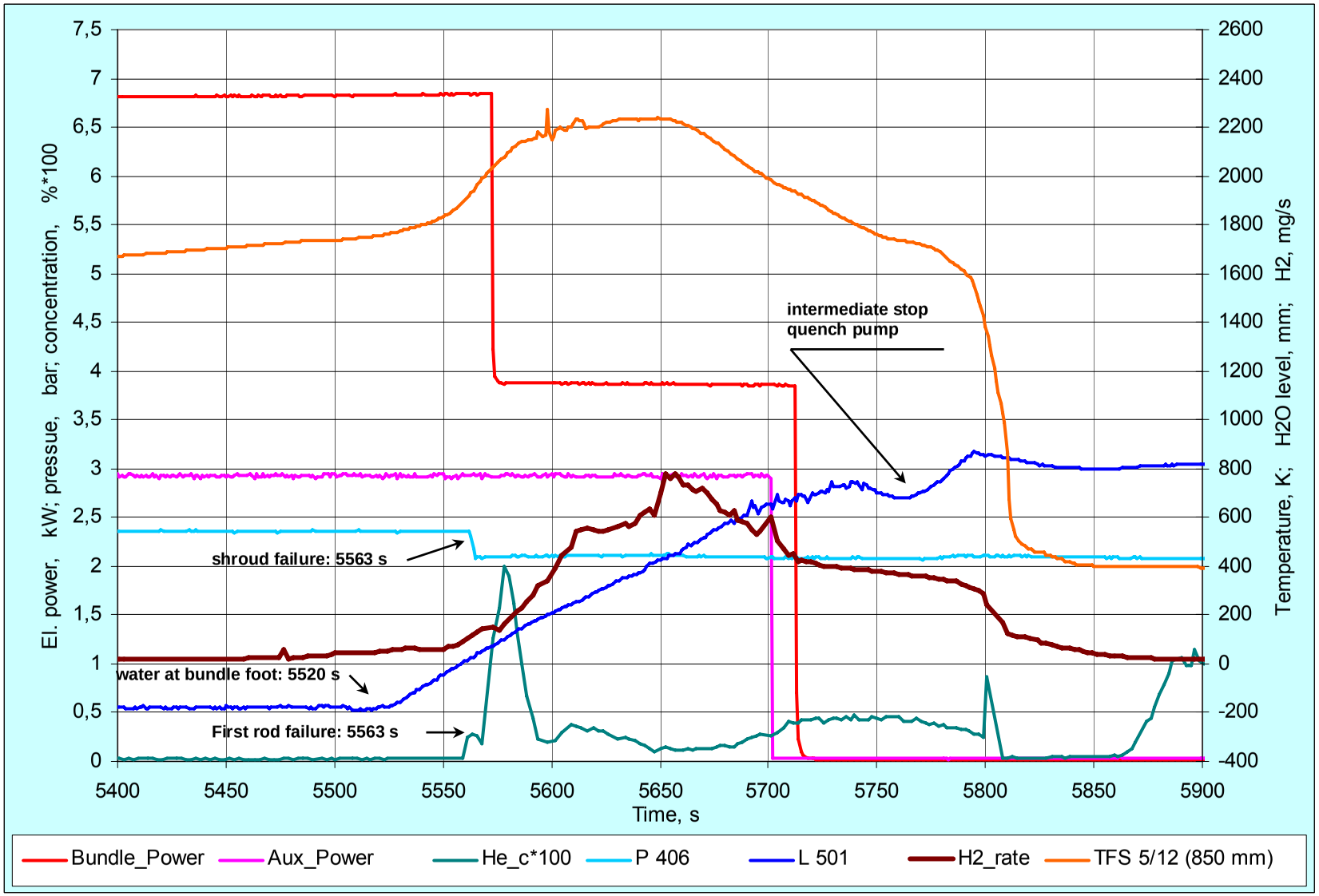

Fig. 28: QUENCH-11; Events during quenching demonstrated with help of water level (L 501), bundle and auxiliary power, H_2 generation rate, He concentration, insulation pressure (P 406) together with temperature at 850 mm.

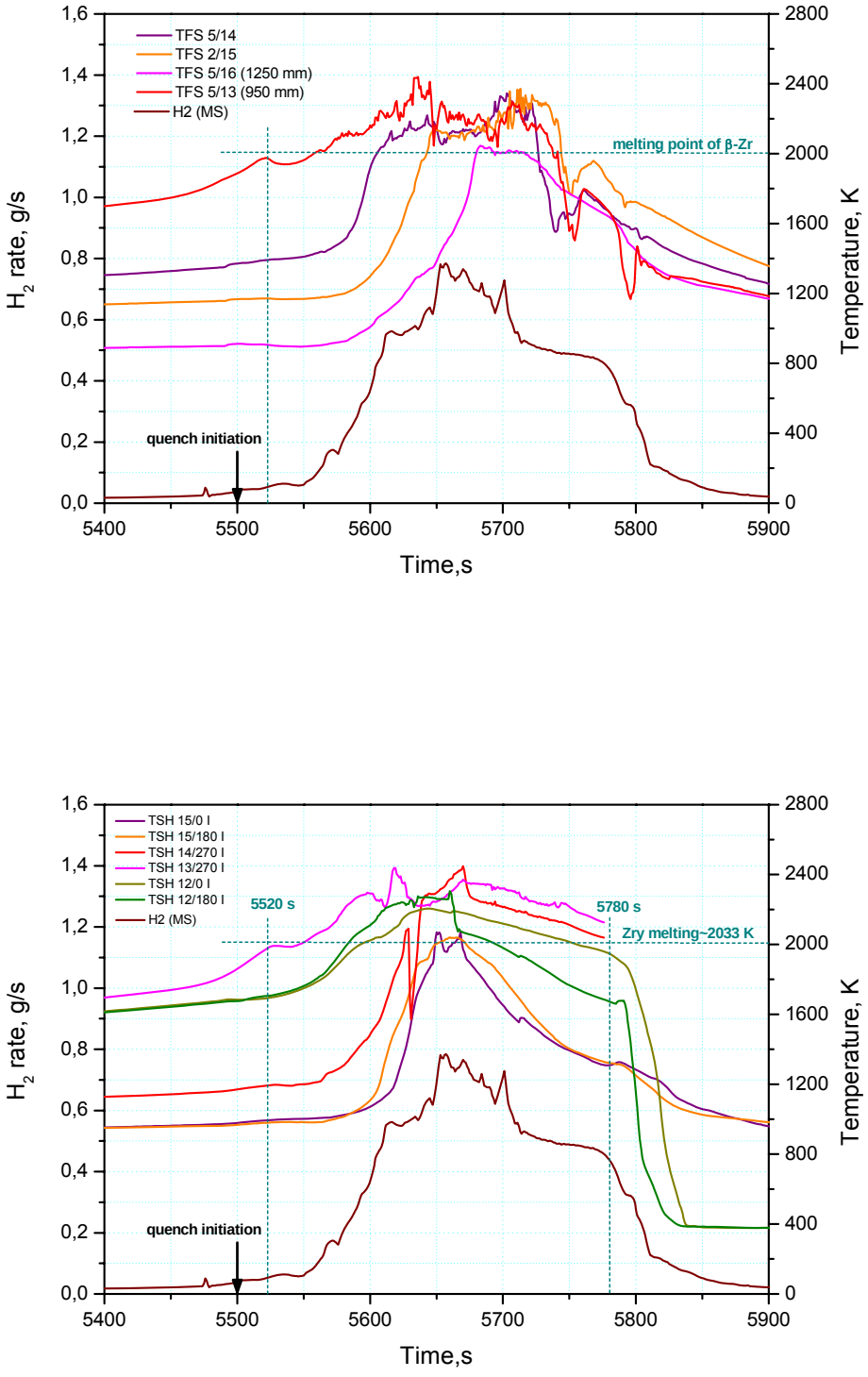

Fig. 29: QUENCH-11; Cladding (top) and shroud temperatures (bottom) together with H_2 rate during the quenching phase.

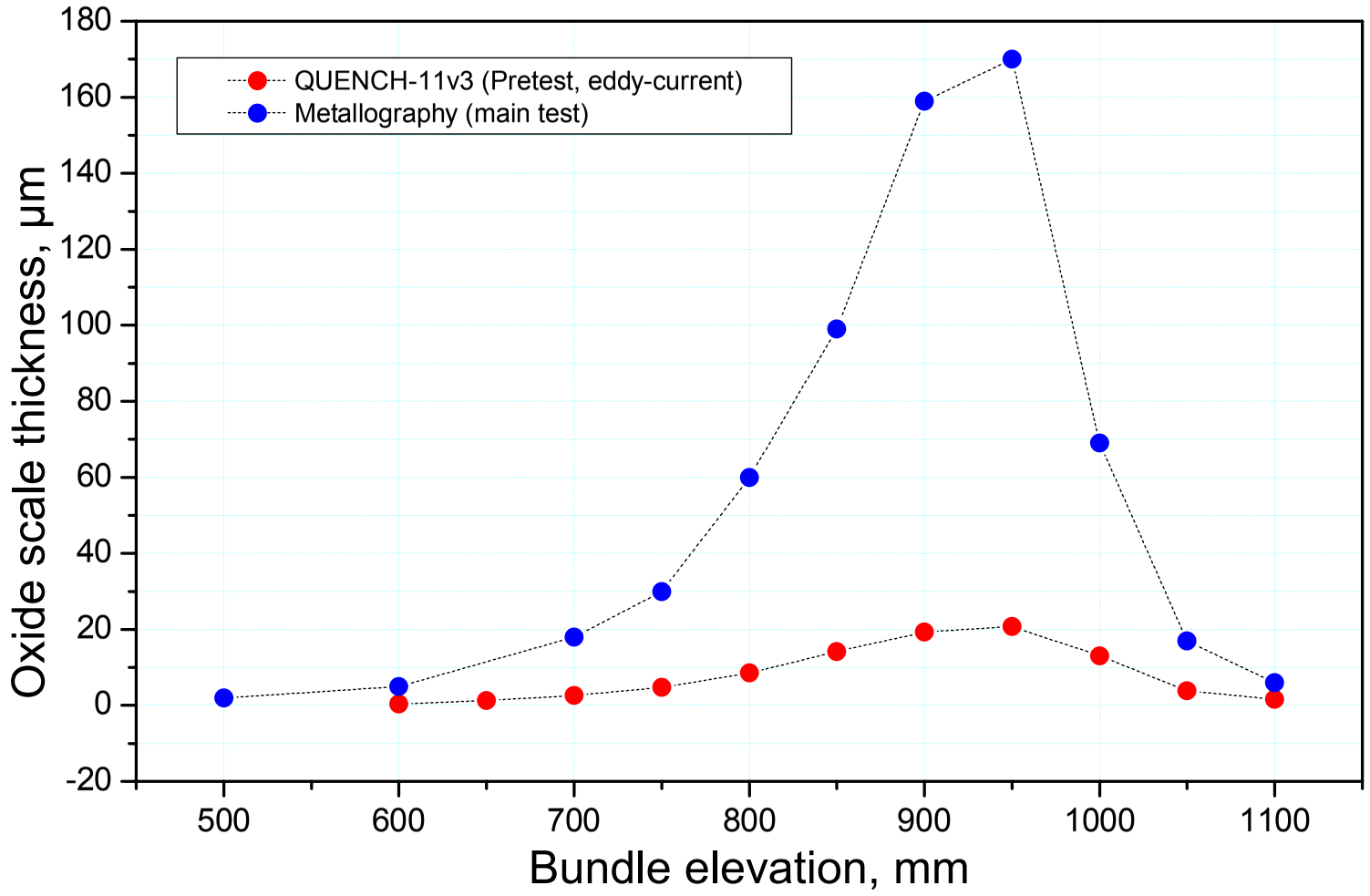

Fig. 30: QUENCH-11; Axial oxide layer profile of corner rod B after pretest QUENCH-11v3 and prior to the quench phase. (After the pretest the corner rod was re-inserted into the test bundle).

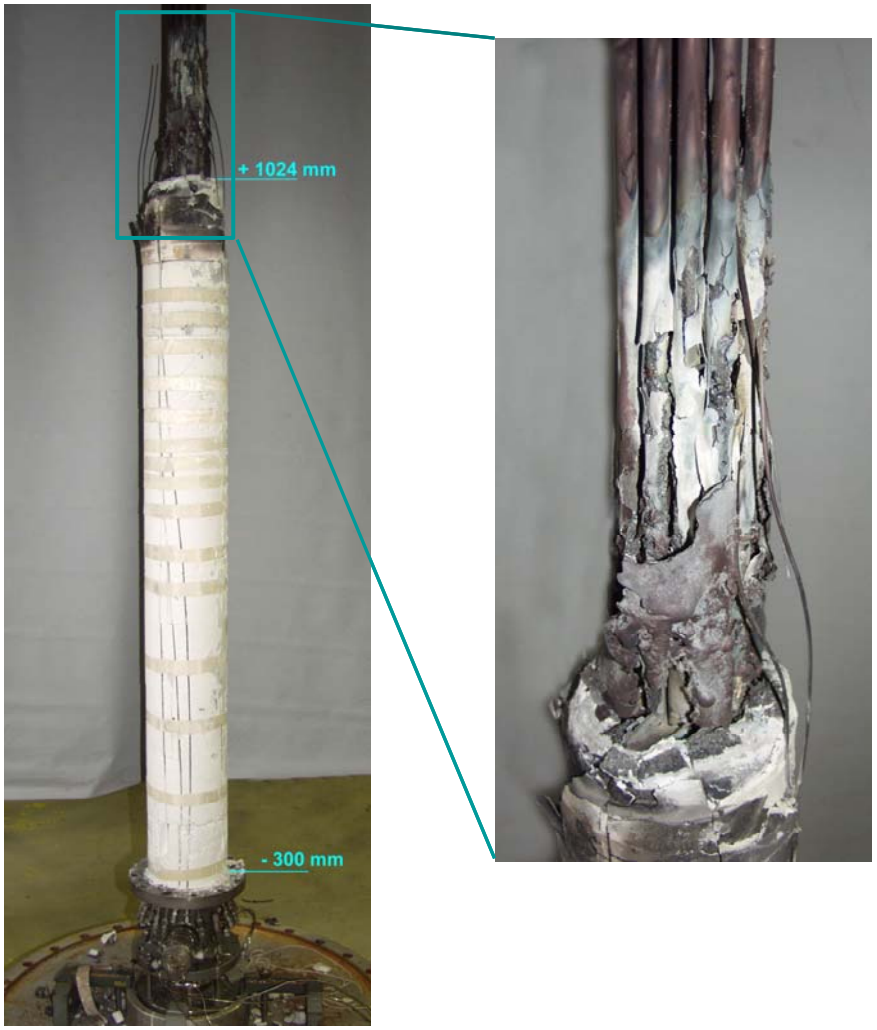

Position: 90°

Upper part of shroud and upper spacer

Fig. 31: QUENCH-11; Posttest view of the bundle before removal of the thermal insulation.

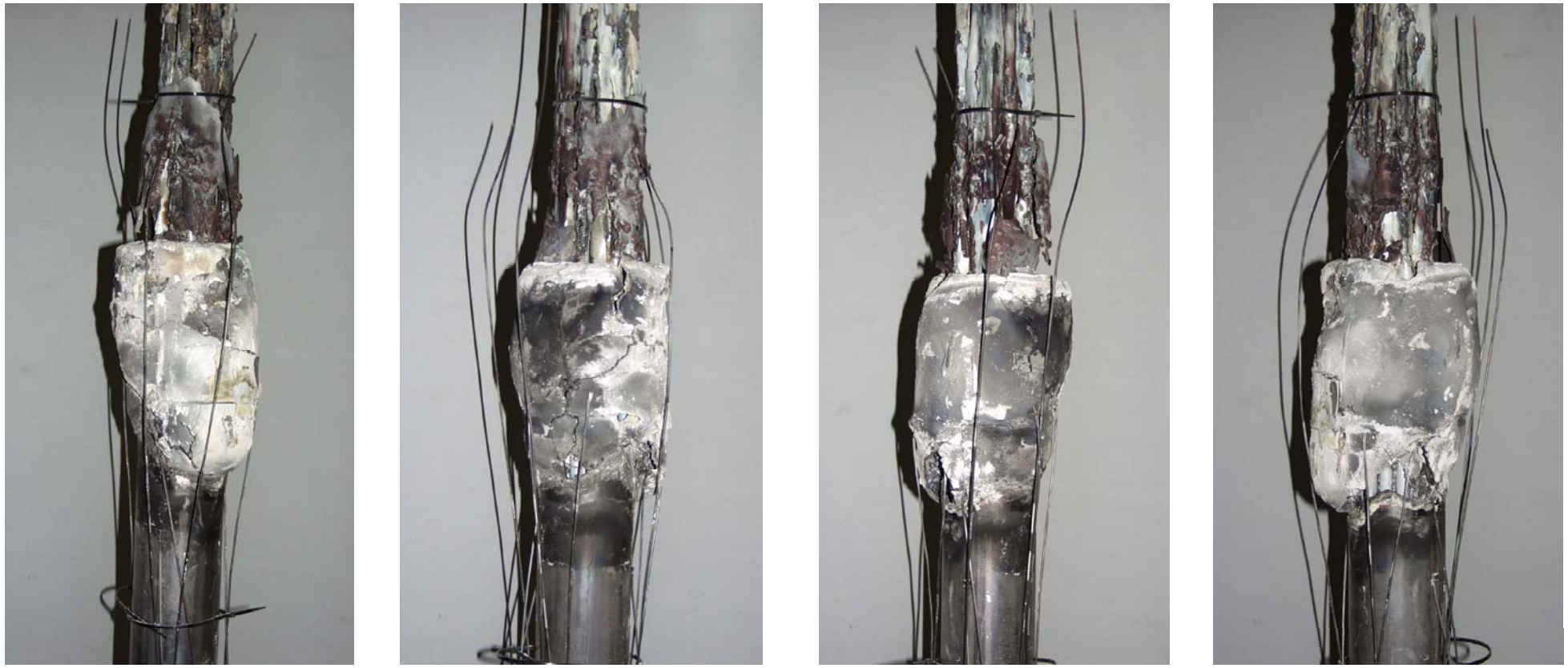

Fig. 32: QUENCH-11; Posttest view of the bundle at the hot region.

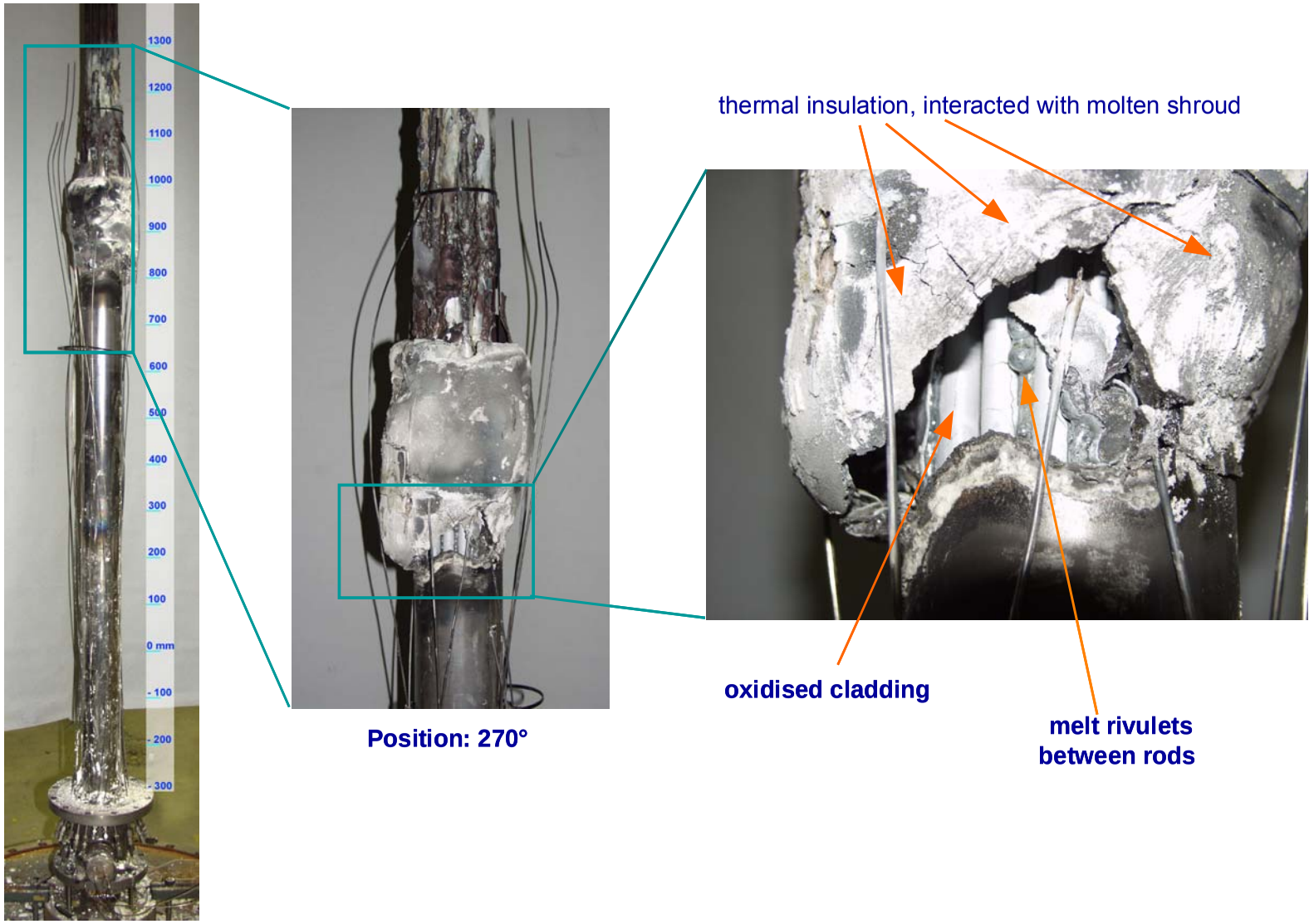

Fig. 33: QUENCH-11; Posttest view of intensive bundle damage above the elevation of 800 mm.

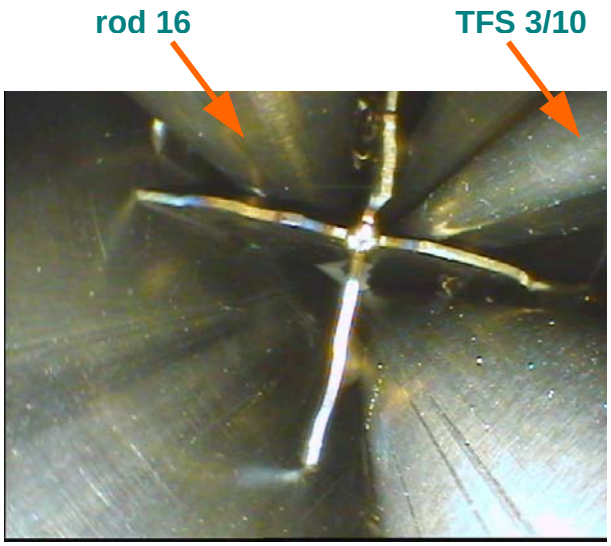

Bottom view of grid spacer 2 at 150 mm

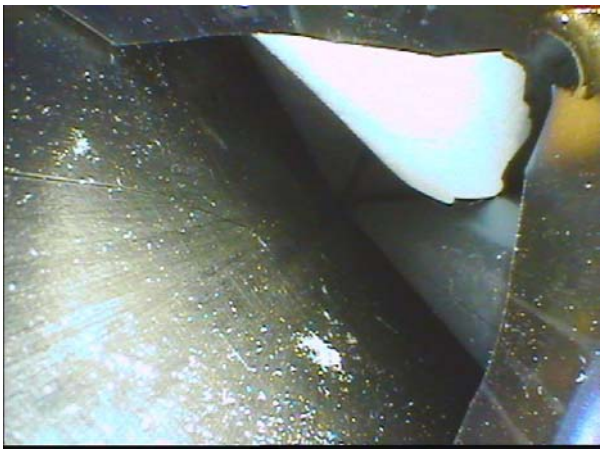

View of the top edge of grid spacer 2 with the piece of spalled oxidized cladding

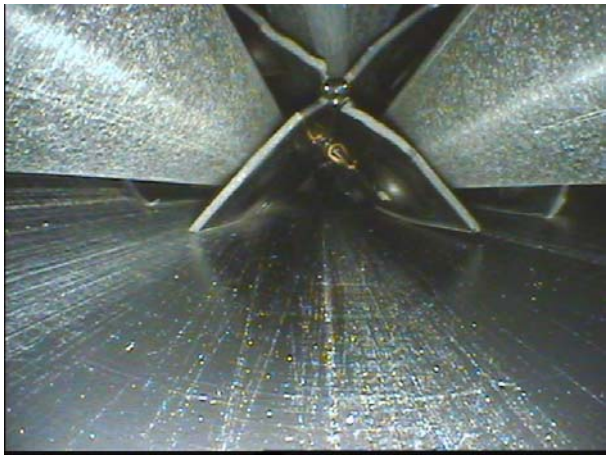

Bottom view of grid spacer 3 at 550 mm

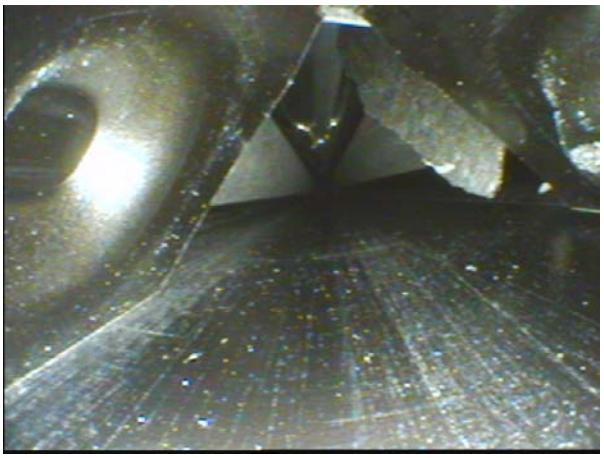

View of the top edge of grid spacer 3 with the piece of spalled oxidized cladding

Fig. 34: QUENCH-11; Posttest photographs taken by a videoscope inserted into the empty position of corner rod B to demonstrate the situation of grid spacers.

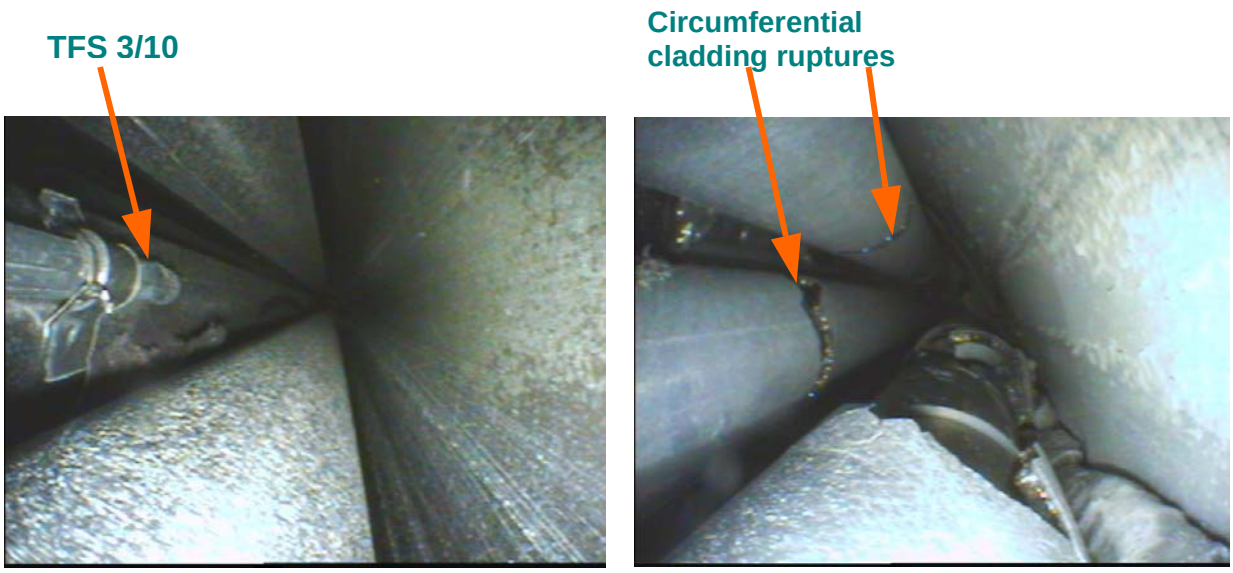

Elevation 650 mm: intact rods

Elevation 750 mm: cladding ruptures

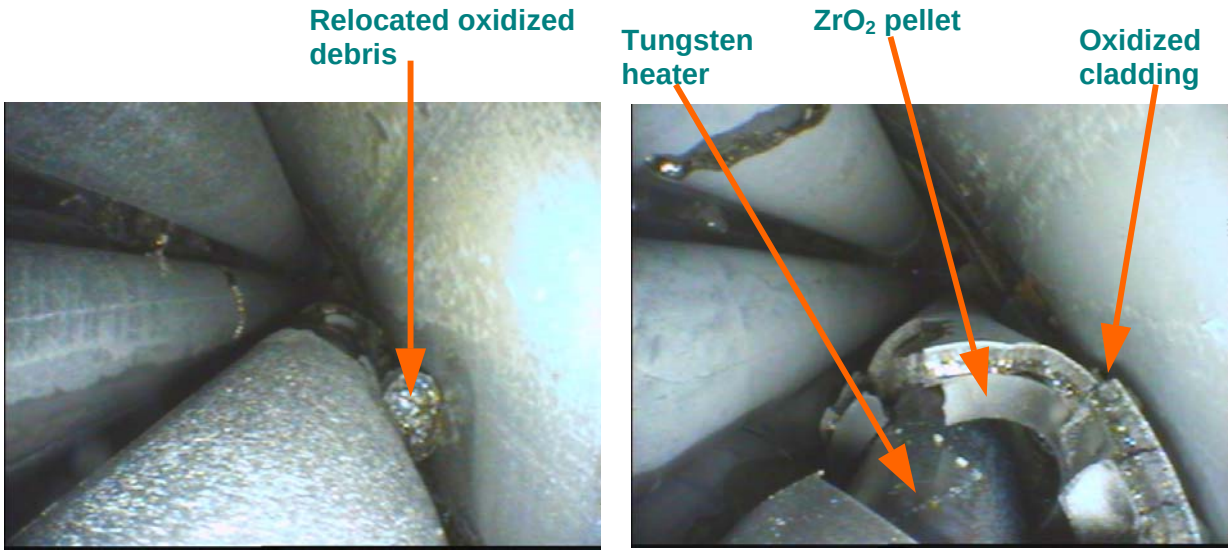

Elevation 720 mm: debris

Elevation 770 mm: broken pellets

Fig. 35: QUENCH-11; Posttest photographs of test rods taken by a videoscope inserted into the empty position of corner rod B.

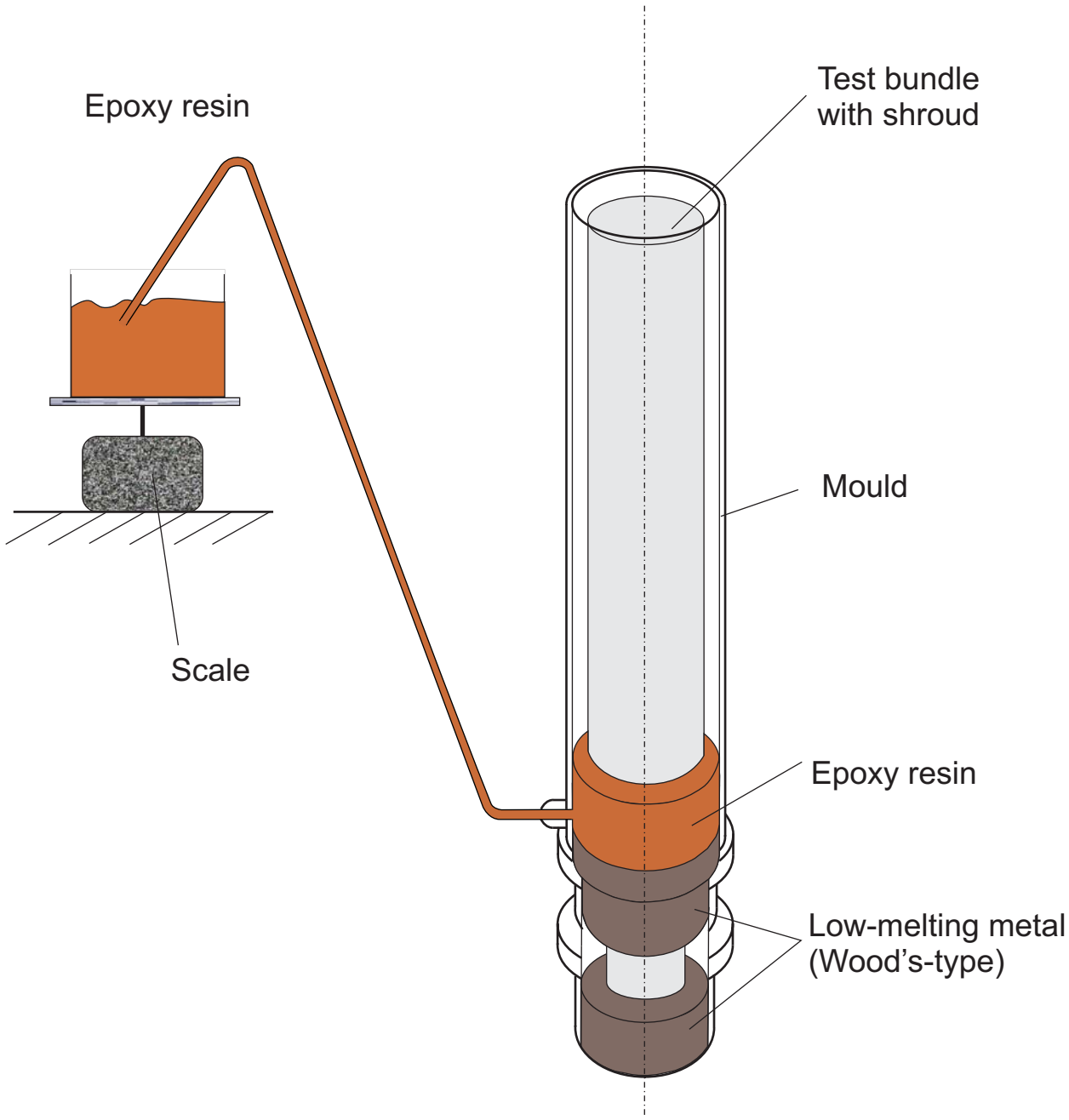

Fig. 36: QUENCH-11; Epoxying process of the tested bundle.

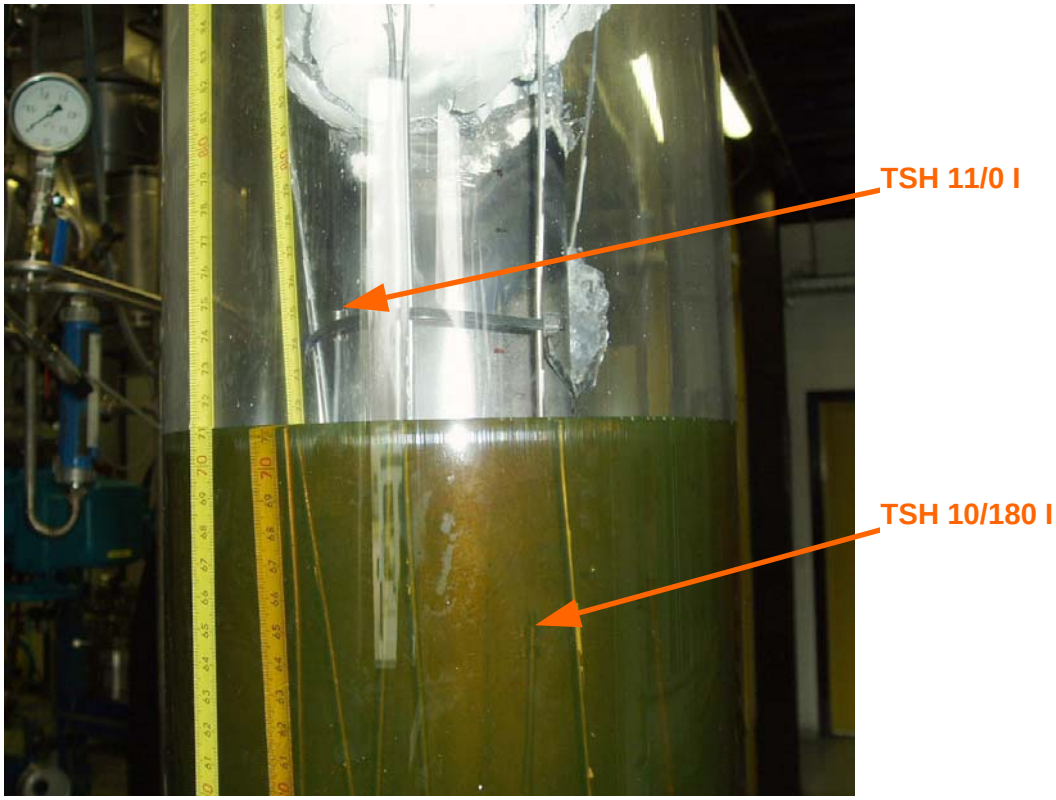

Fig. 37: QUENCH-11; Two sequential stages in bundle filling with steps of 10 mm (epoxy levels at 700 mm, top, and 710 mm, bottom).

QUE-11-1 (**635 mm**, bottom mirrored)

QUE-11-1 (**650 mm**, top)

QUE-11-2 (**735 mm**, bottom mirrored)

QUE-11-2 (**750 mm**, top)

Fig.: 38 QUENCH-11; Cross sections at 635 mm, 650 mm, 735 mm, and 750 mm.

QUE-11-6 (**794 mm**, bottom mirrored)

QUE-11-6 (**810 mm**, top)

QUE-11-3 (**837 mm**, bottom mirrored)

QUE-11-3 (**850 mm**, top)

Fig.: 39 QUENCH-11; Cross sections at 794 mm, 810 mm, 837 mm, and 850 mm.

QUE-11-7 (**884 mm**, bottom mirrored)

QUE-11-7 (**900 mm**, top)

QUE-11-4 (**937 mm**, bottom mirrored)

QUE-11-4 (**950 mm**, top)

Fig.: 40 QUENCH-11; Cross sections at 884 mm, 900 mm, 937 mm, and 950 mm.

QUE-11-8 (**984 mm**, bottom mirrored)

QUE-11-8 (**1000 mm**, top)

QUE-11-5 (**1037 mm**, bottom mirrored)

QUE-11-5 (**1050 mm**, top)

Fig.: 41 QUENCH-11; Cross sections at 984 mm, 1000 mm, 1037 mm, and 1050 mm.

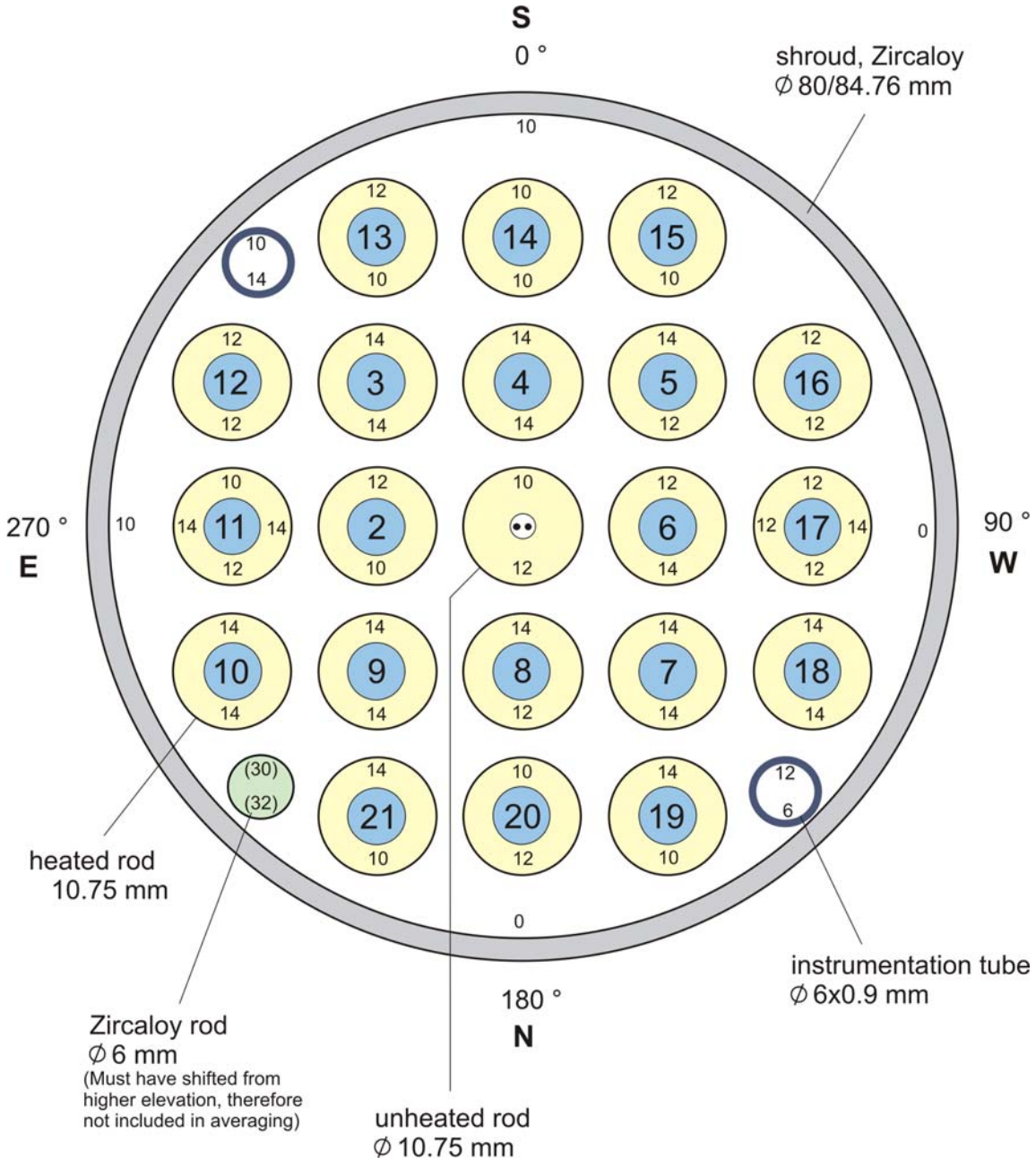

Fig. 42-QUE11 cross section 11-1.doc
16.01.07 - IMF

Fig. 42 : QUENCH-11; Oxide layer thickness at bundle elevation 650 mm (Cross section QUE-11-1).

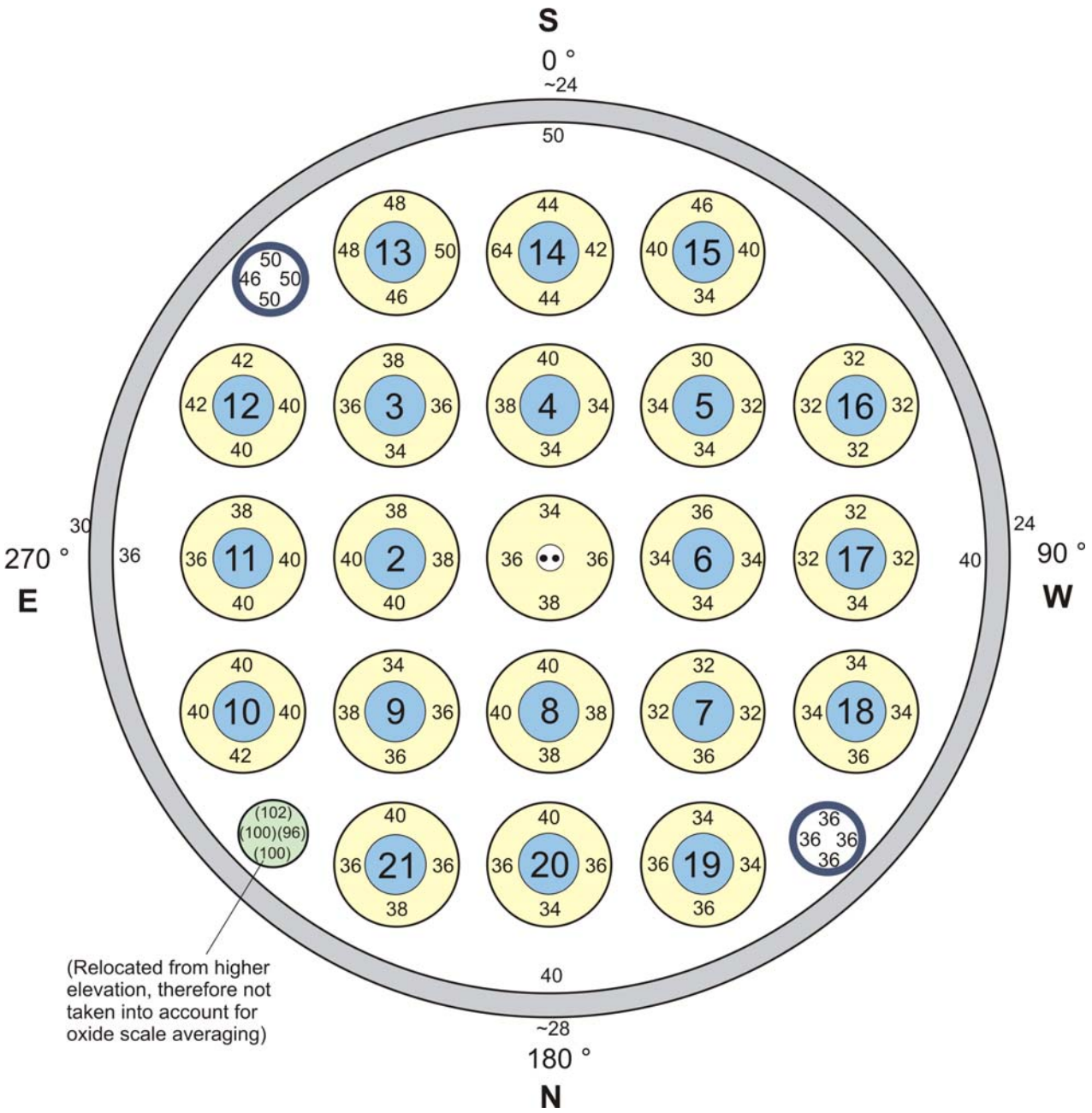

Fig. 43-QUE11 cross section 11-2.doc
16.01.07 - IMF

Fig. 43 : QUENCH-11; Oxide layer thickness at bundle elevation 750 mm (Cross section QUE-11-2).

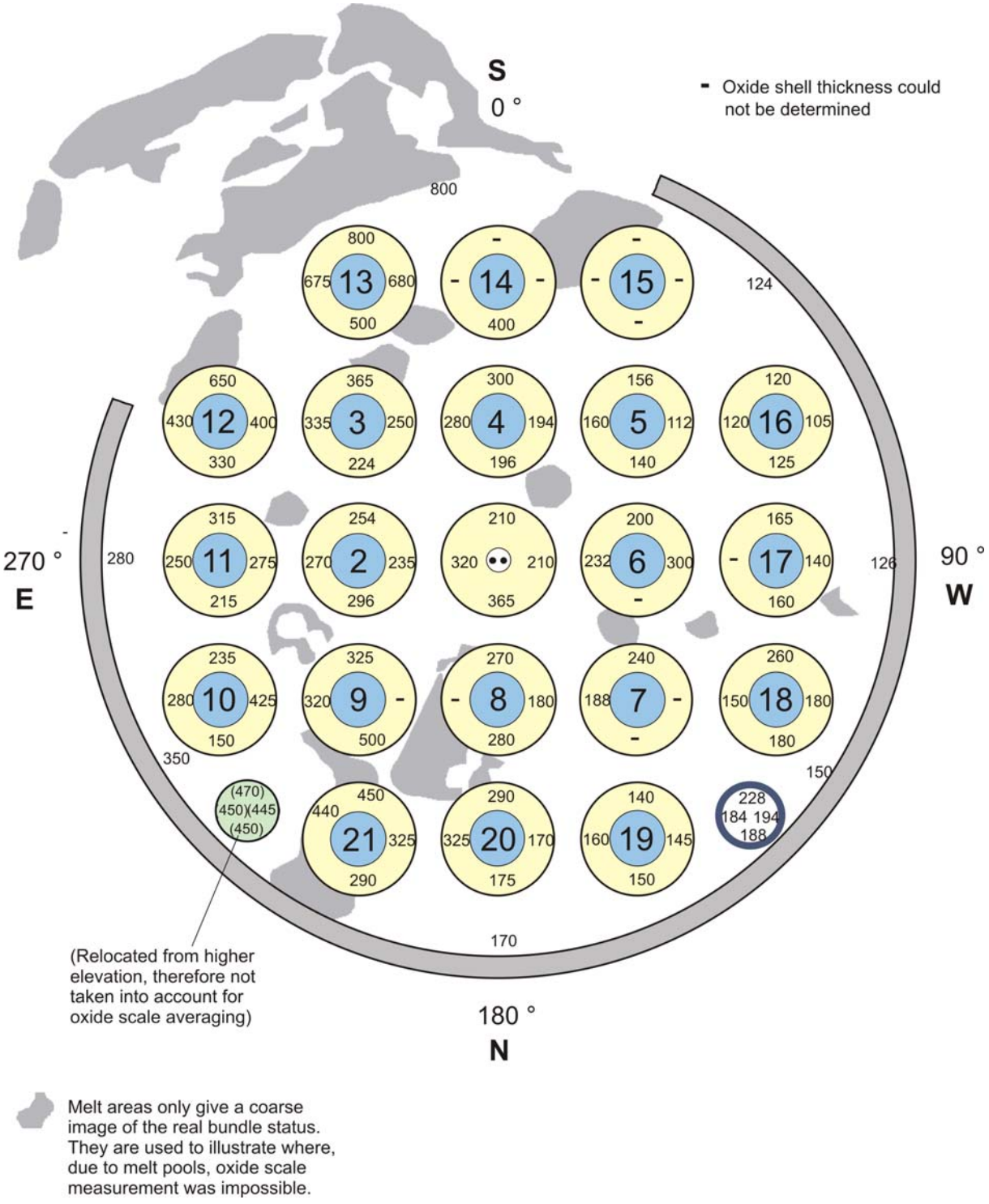

Fig. 44-QUE11 cross section 11-6.doc
19.04.07 - IMF

Fig. 44 : QUENCH-11; Oxide layer thickness at bundle elevation 810 mm (Cross section QUE-11-6).

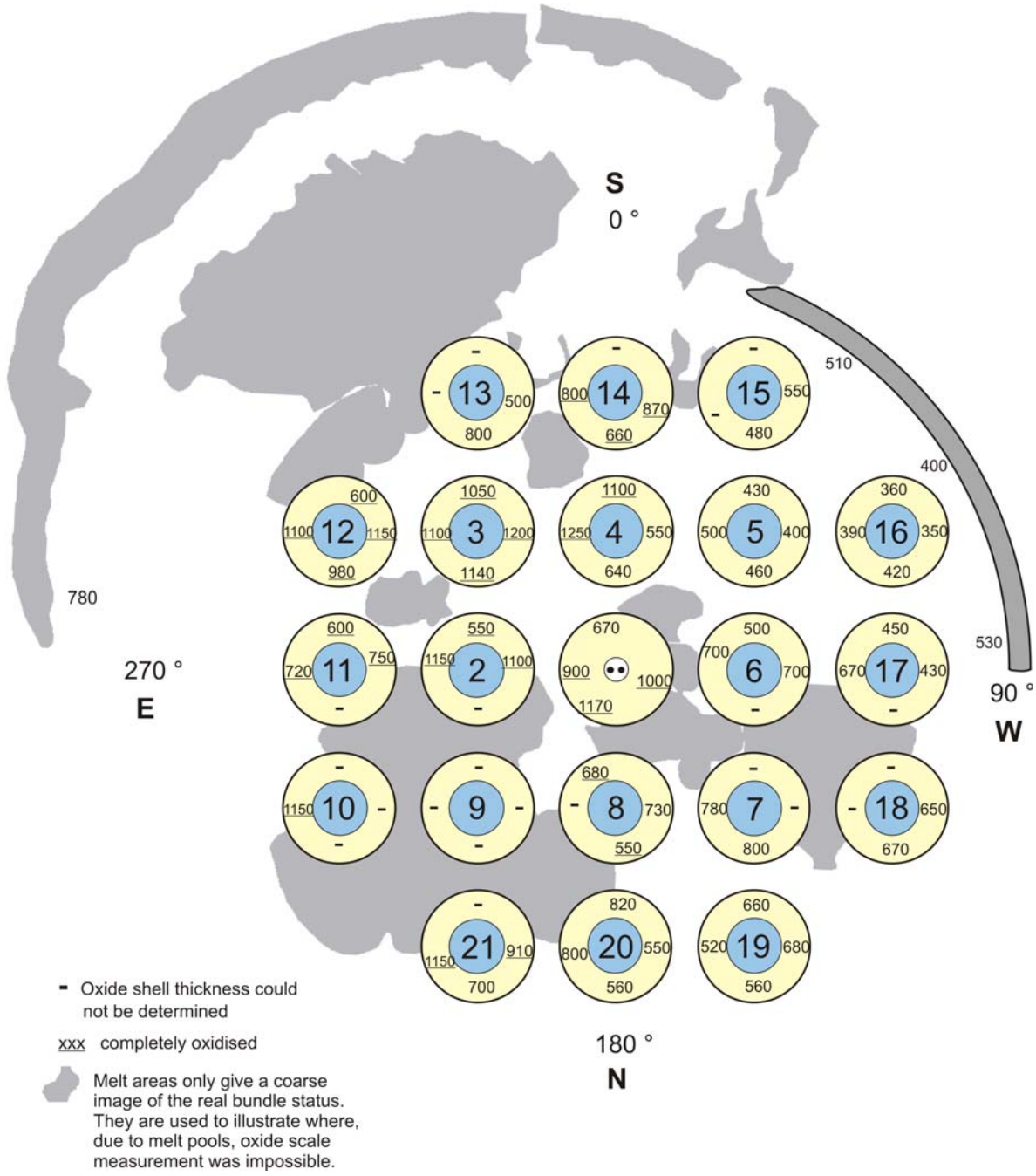

Fig. 45-QUE11 cross section 11-3b.doc
19.04.07 - IMF

Fig. 45 : QUENCH-11; Oxide layer thickness at bundle elevation 837 mm (Cross section QUE-11-3 bottom).

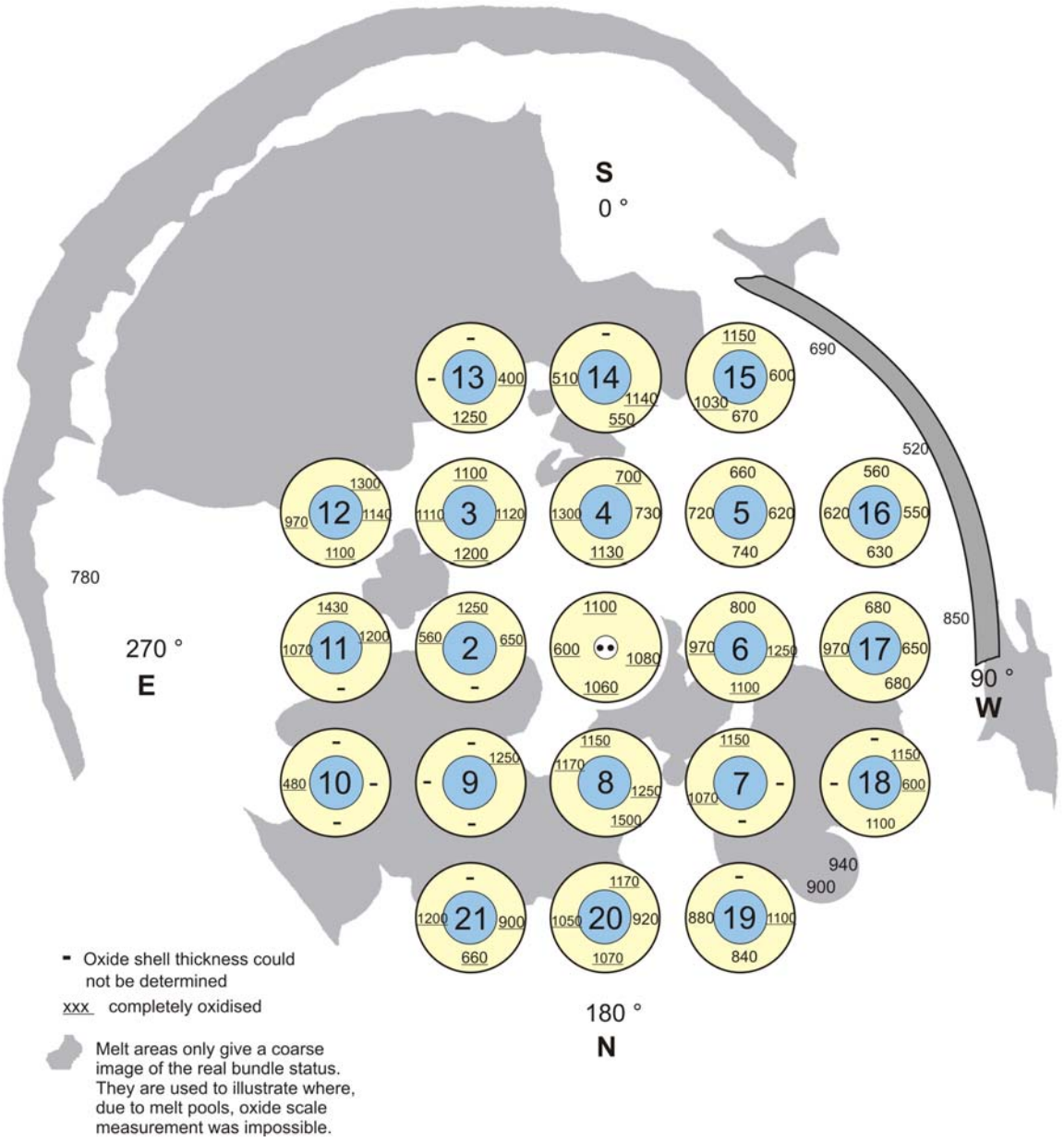

Fig. 46-QUE11 cross section 11-3t.doc
19.04.07 - IMF

Fig. 46 : QUENCH-11; Oxide layer thickness at bundle elevation 850 mm (Cross section QUE-11-3 top).

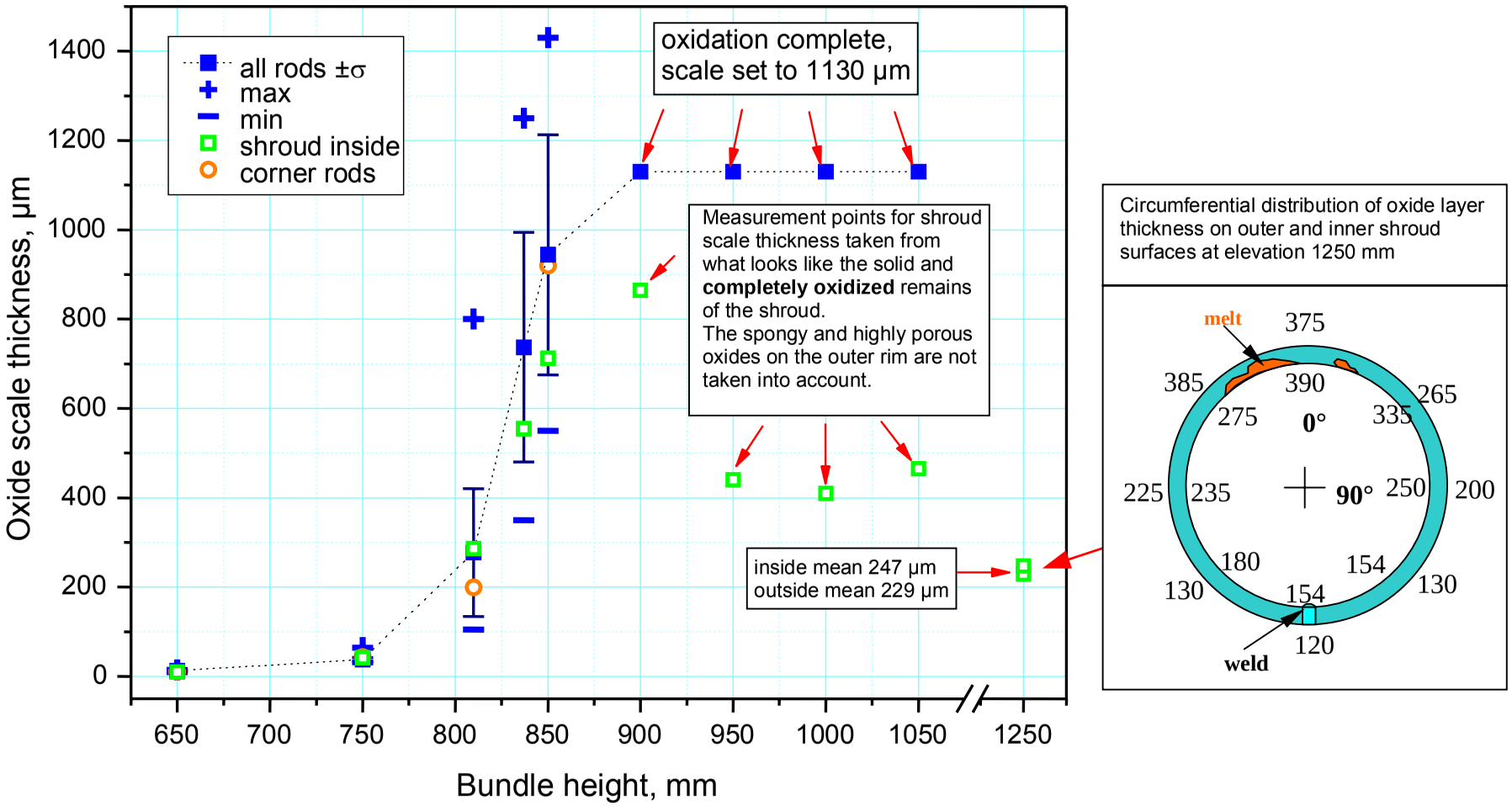

Fig.: 47 QUENCH-11; Axial oxide layer distribution of test rods, corner rods, and shroud.

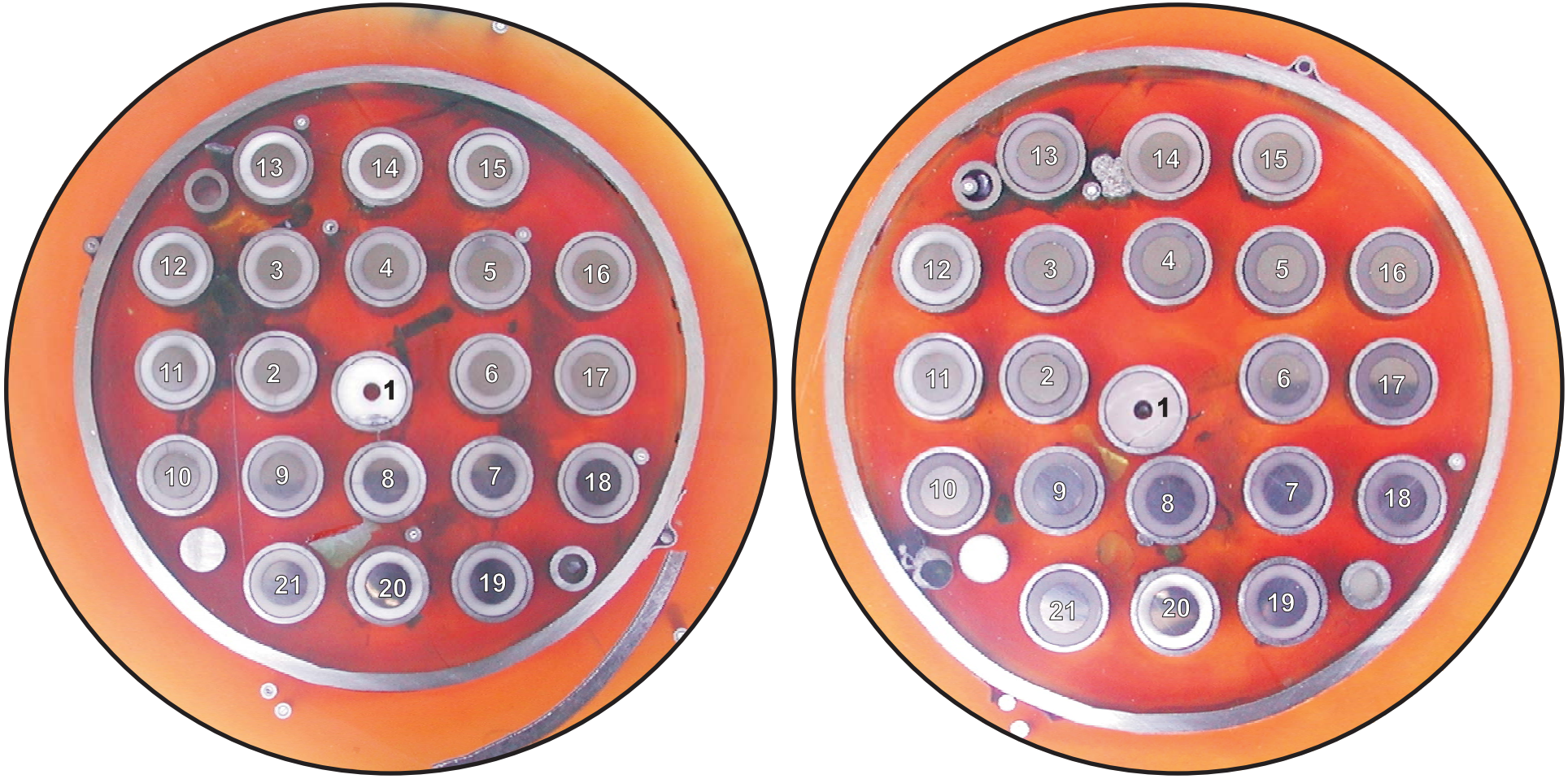

Elevation 650 mm, top view

Elevation 750 mm, top view

Fig. 48: QUE-11-1 and -11-2, levels 650 and 750 mm; overviews

Rod 6

left: bright field
right: polarized light

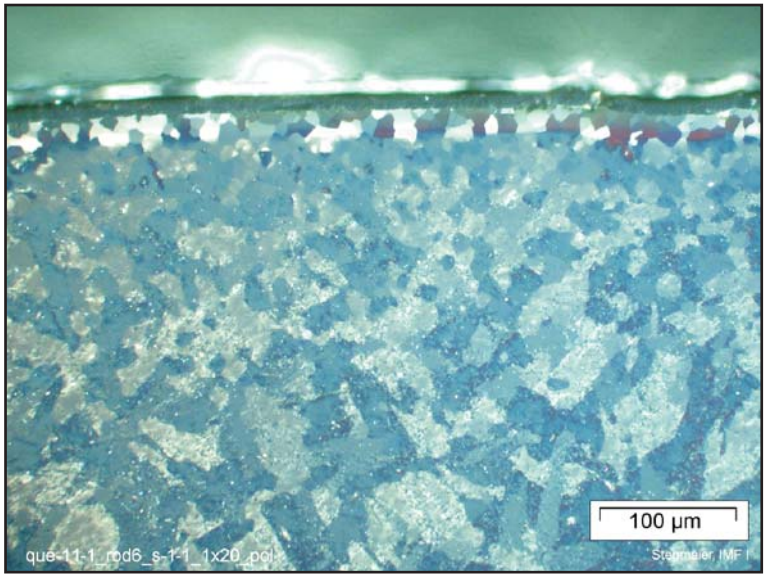

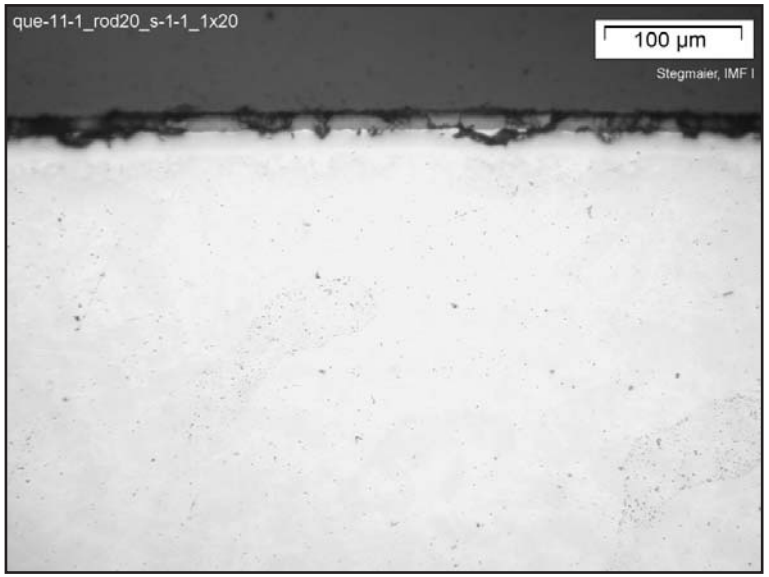

Rod 20
left: bright field
right: polarized light

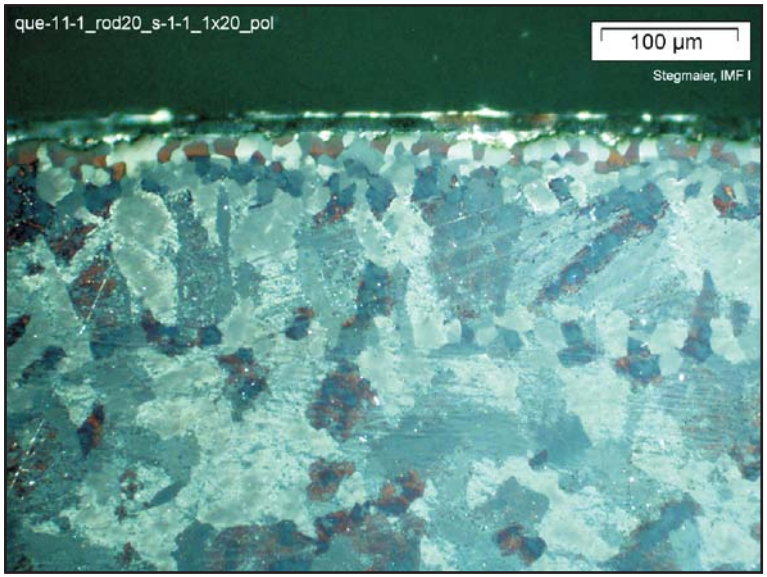

Fig. 49: QUE-11-1, level 650 mm; oxidation status of the cladding

Rod 6
left: bright field
right: polarized light

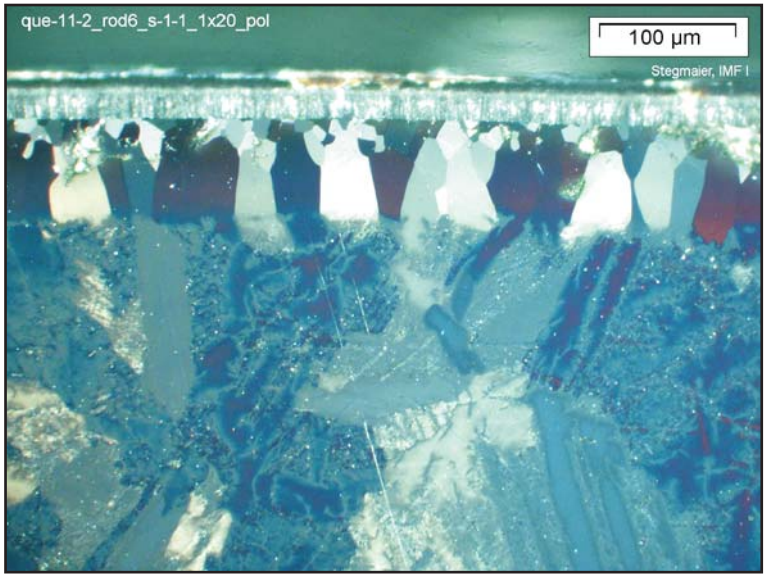

Rod 20
left: bright field
right: polarized light

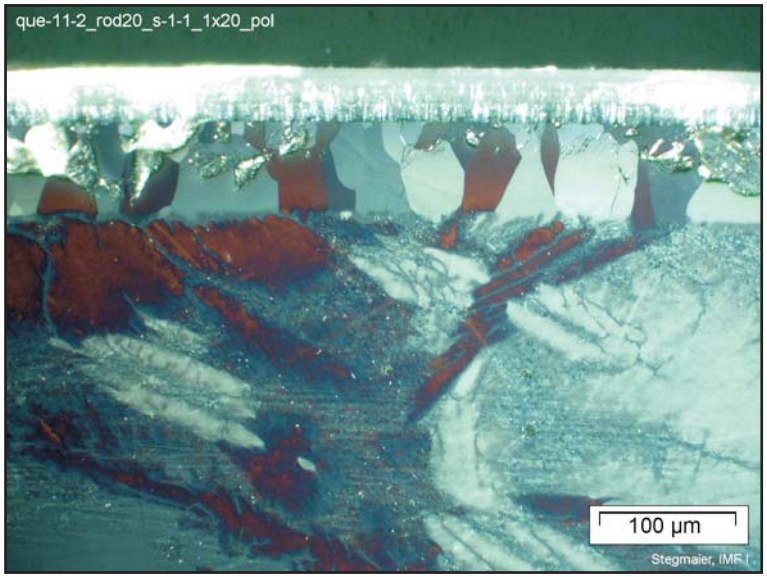

Fig. 50: QUE-11-2, level 750 mm; oxidation status of the cladding

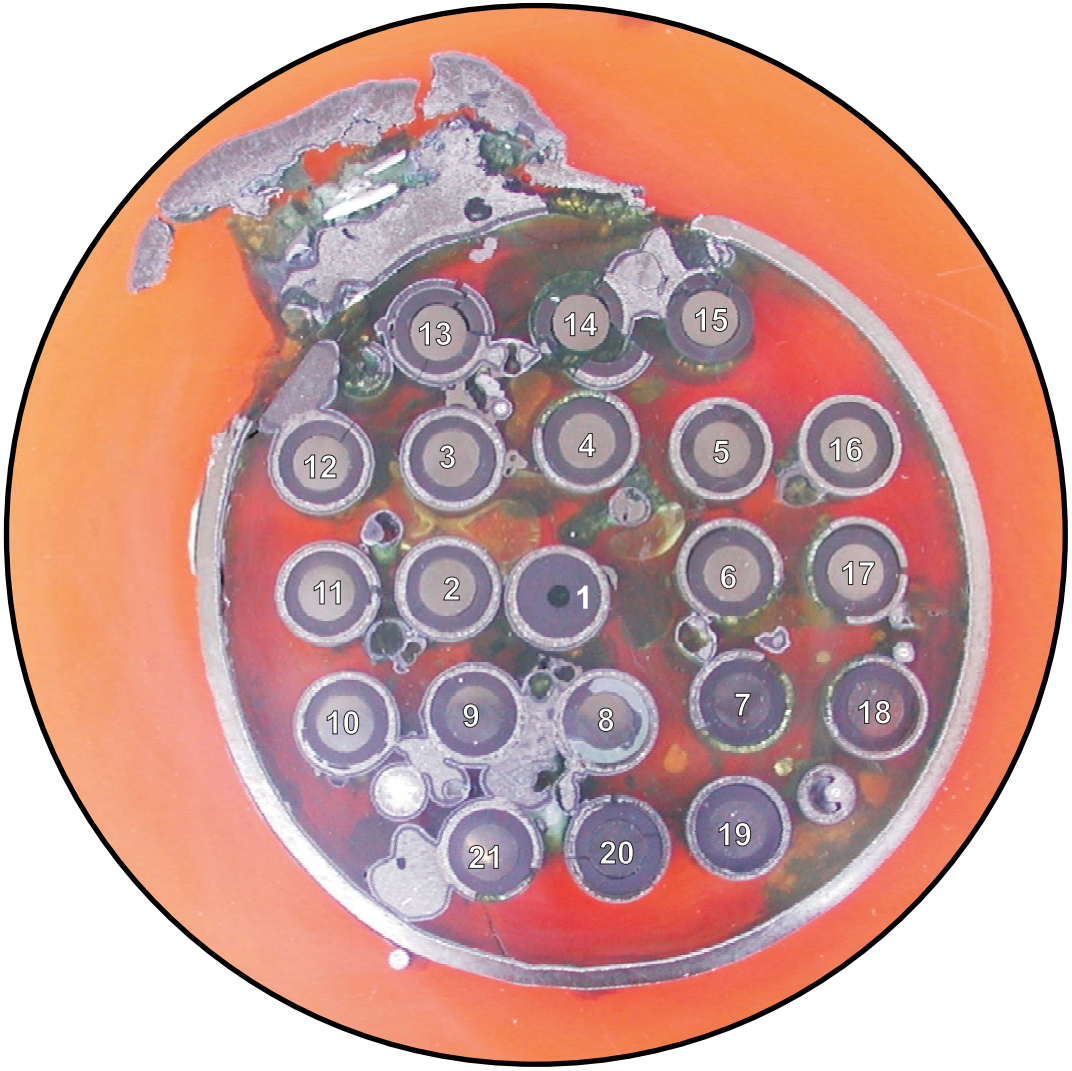

Elevation 810 mm, top view

Structured agglomerate of melt in NE direction

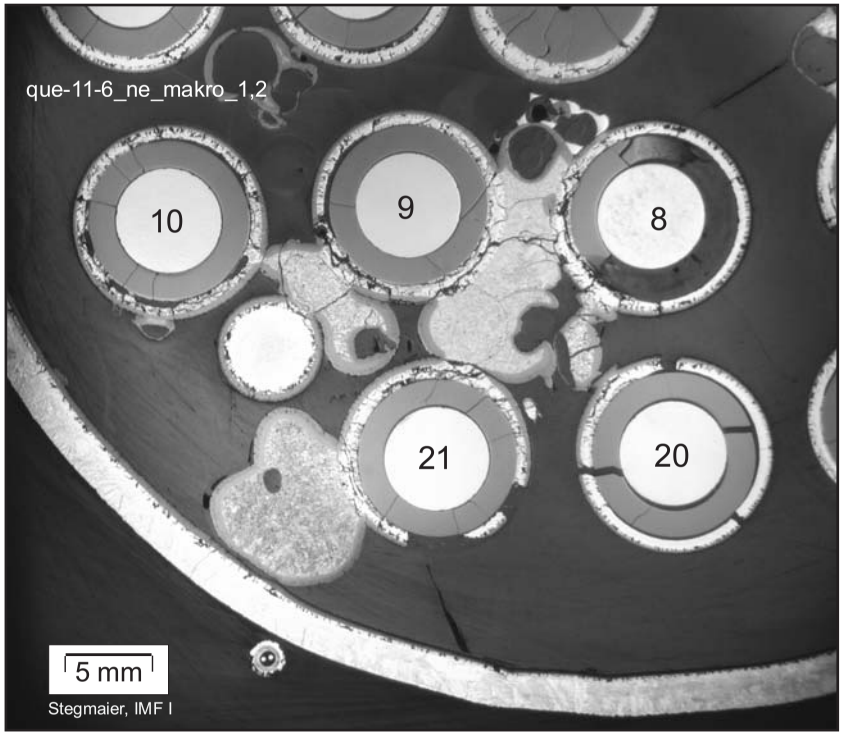

Fig. 51: QUE-11-6, level 810 mm; bundle cross section at the lower limit of melt candling

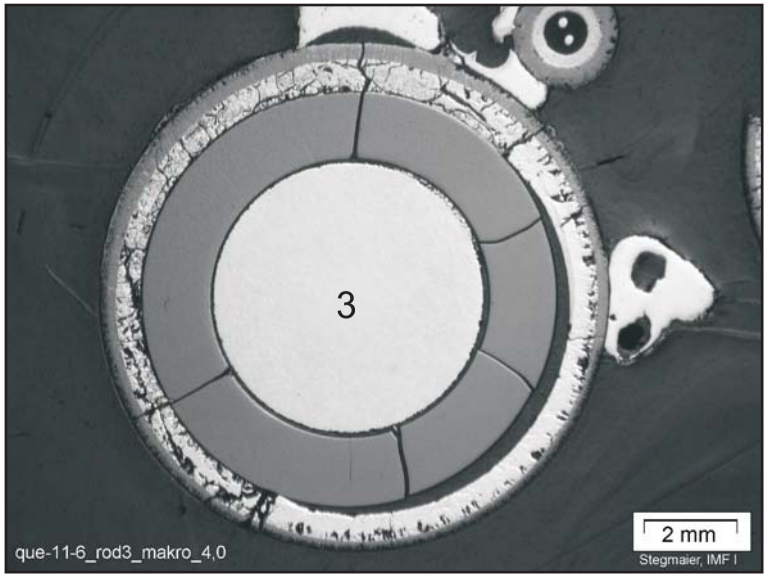

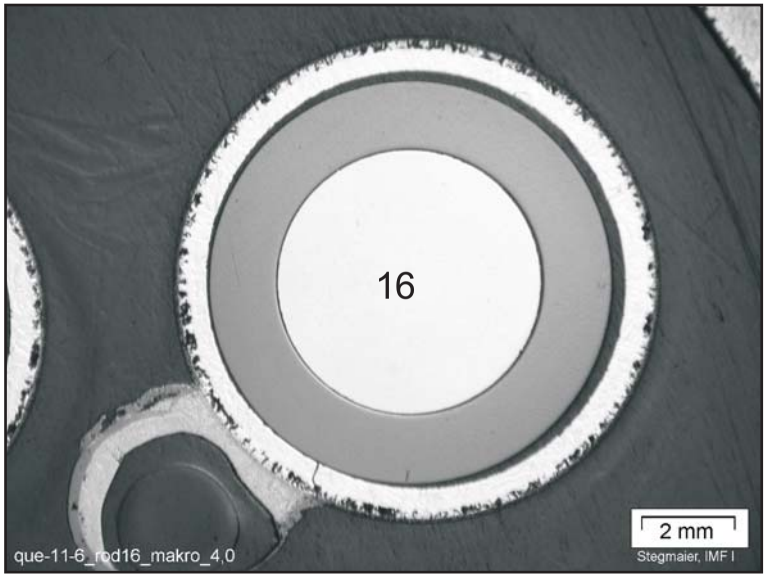

Notice:
gap eccentricity and
local gap closure

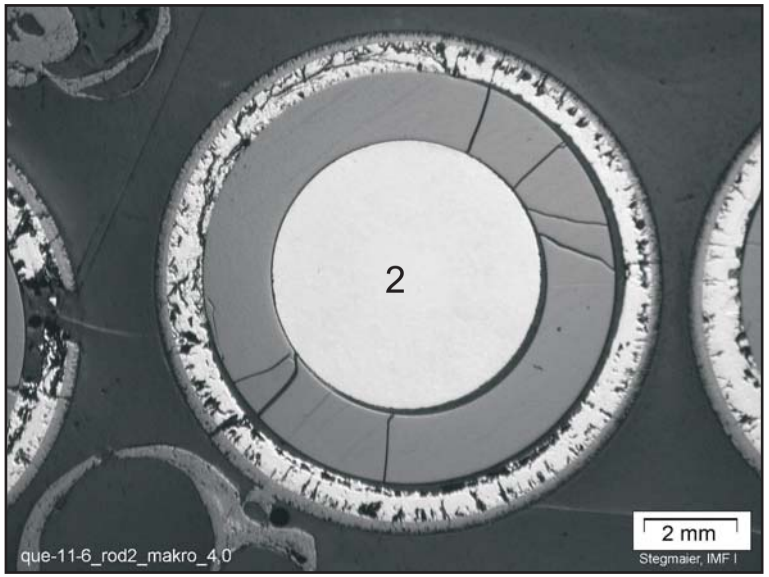

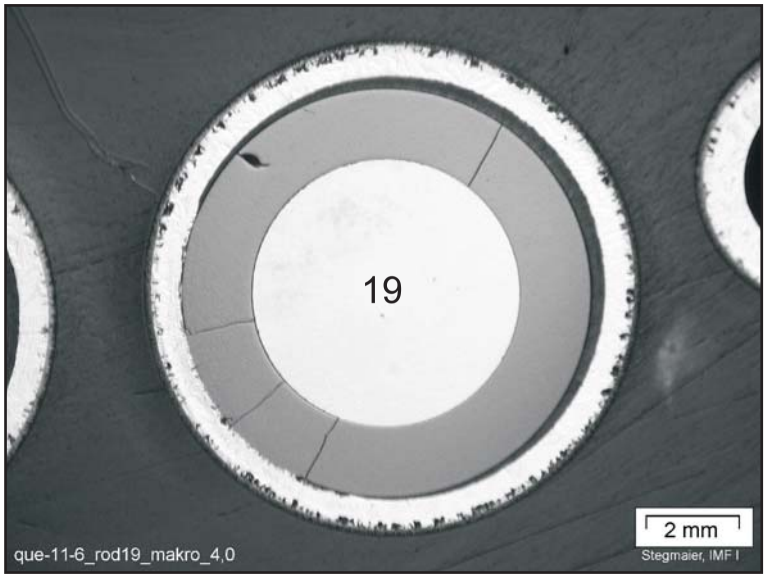

Fig. 52: QUE-11-6, level 810 mm; oxidation status of cladding without melt formation

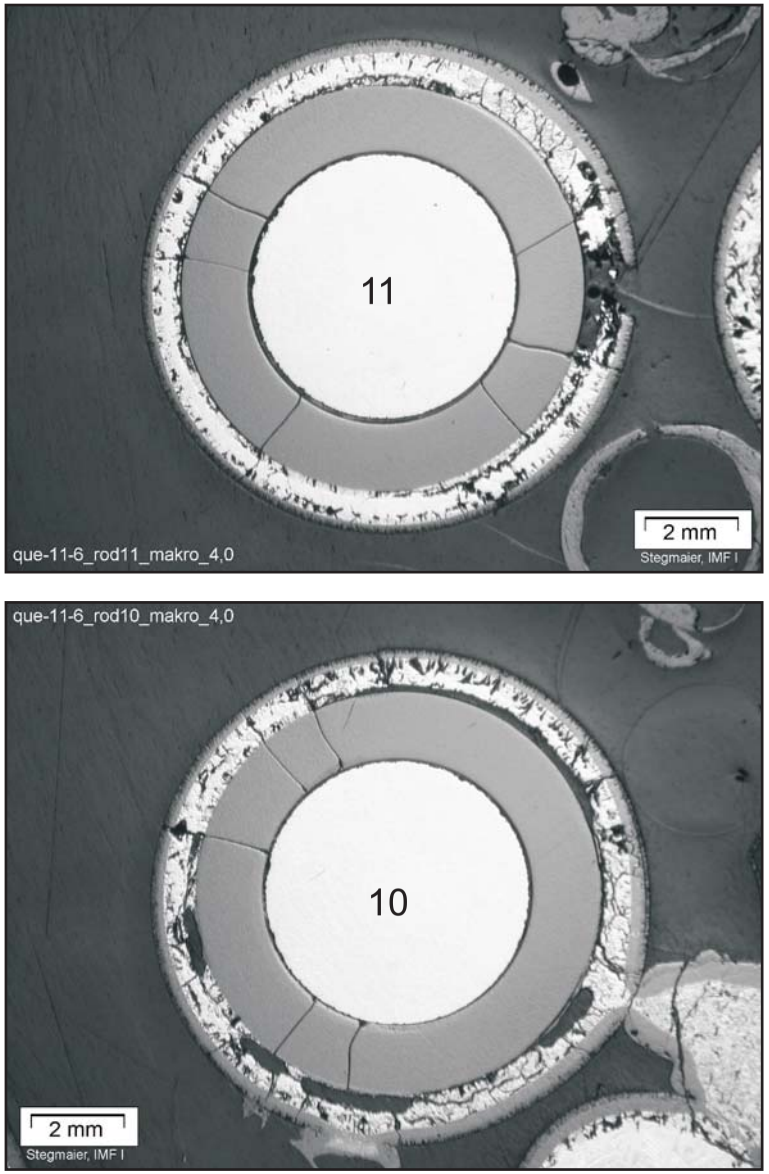

Notice:
gap filling vs. void formation by some internal melt relocation

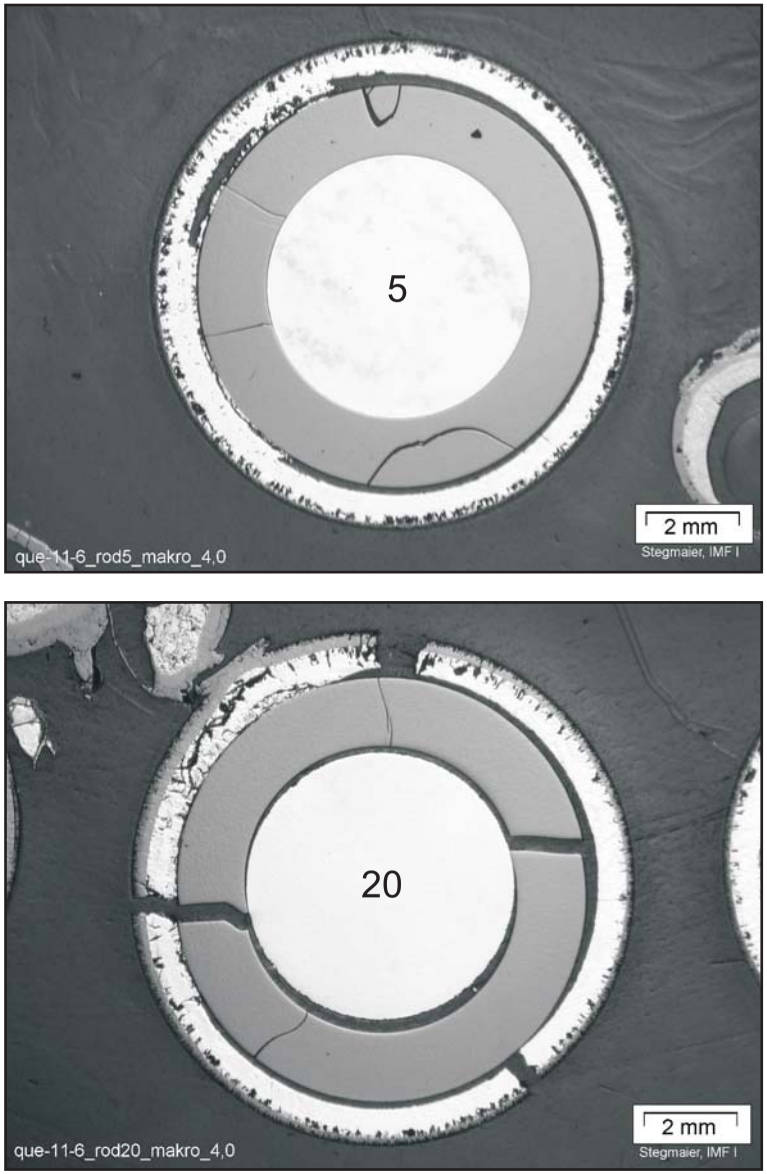

Fig. 53: QUE-11-6, level 810 mm; oxidation status of cladding with internal melt formation

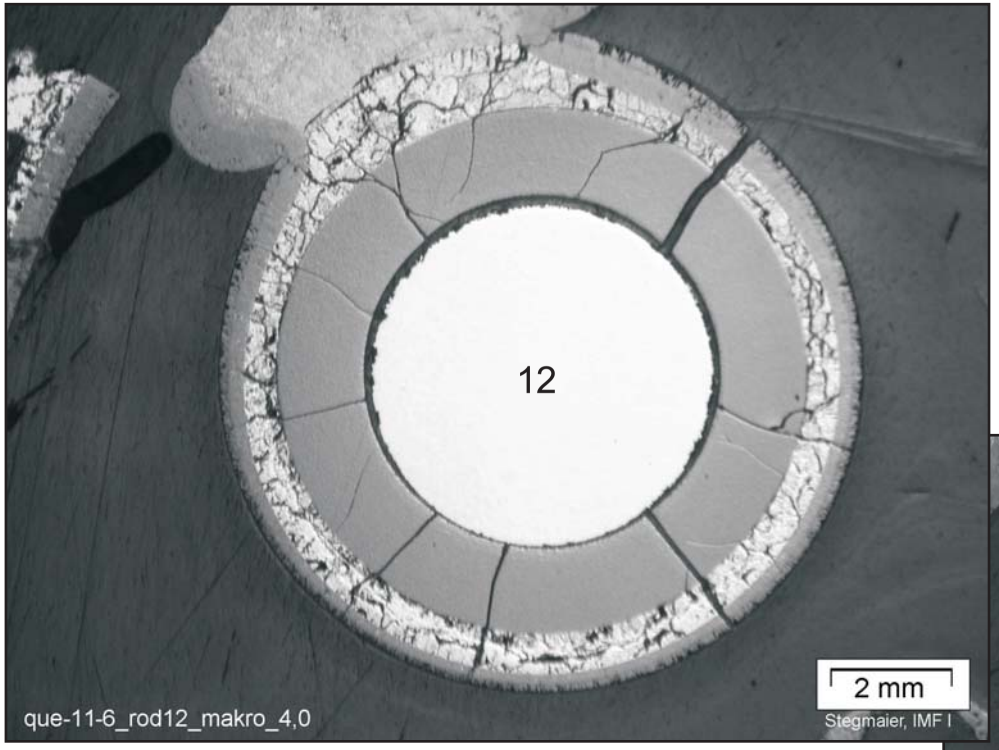

“Neck” between melt pillow and fuel rod, enclosed by common scale

“Neck” between fuel rod and a rivulet of melt, enclosed by common scale

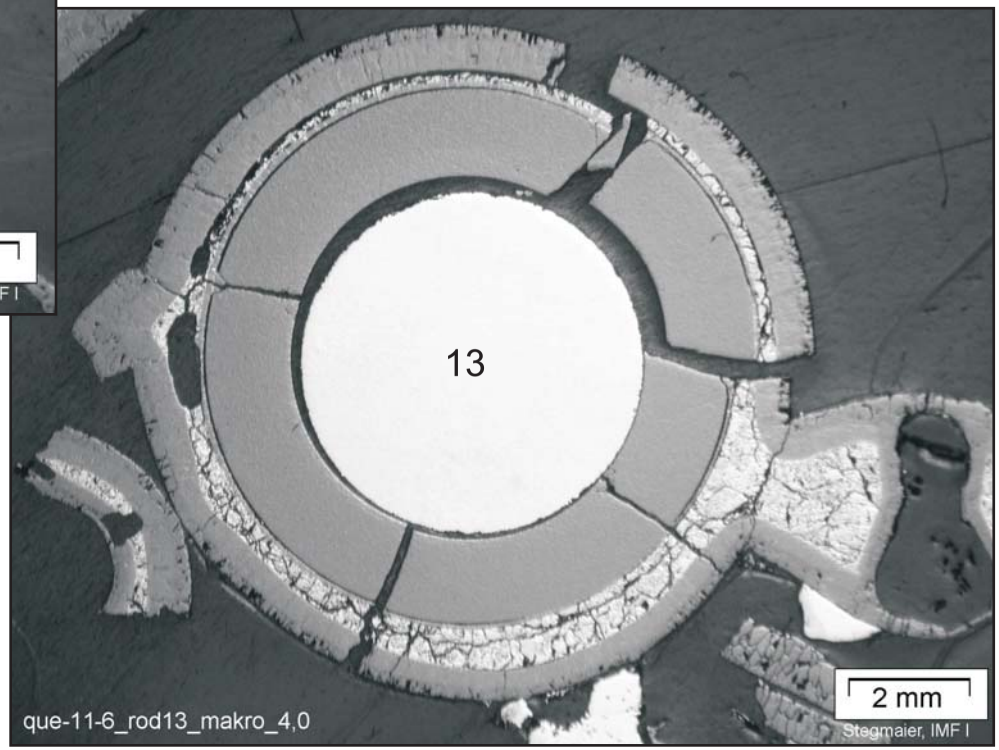

Fig. 54: QUE-11-6, level 810 mm; details of external melt interaction with rods

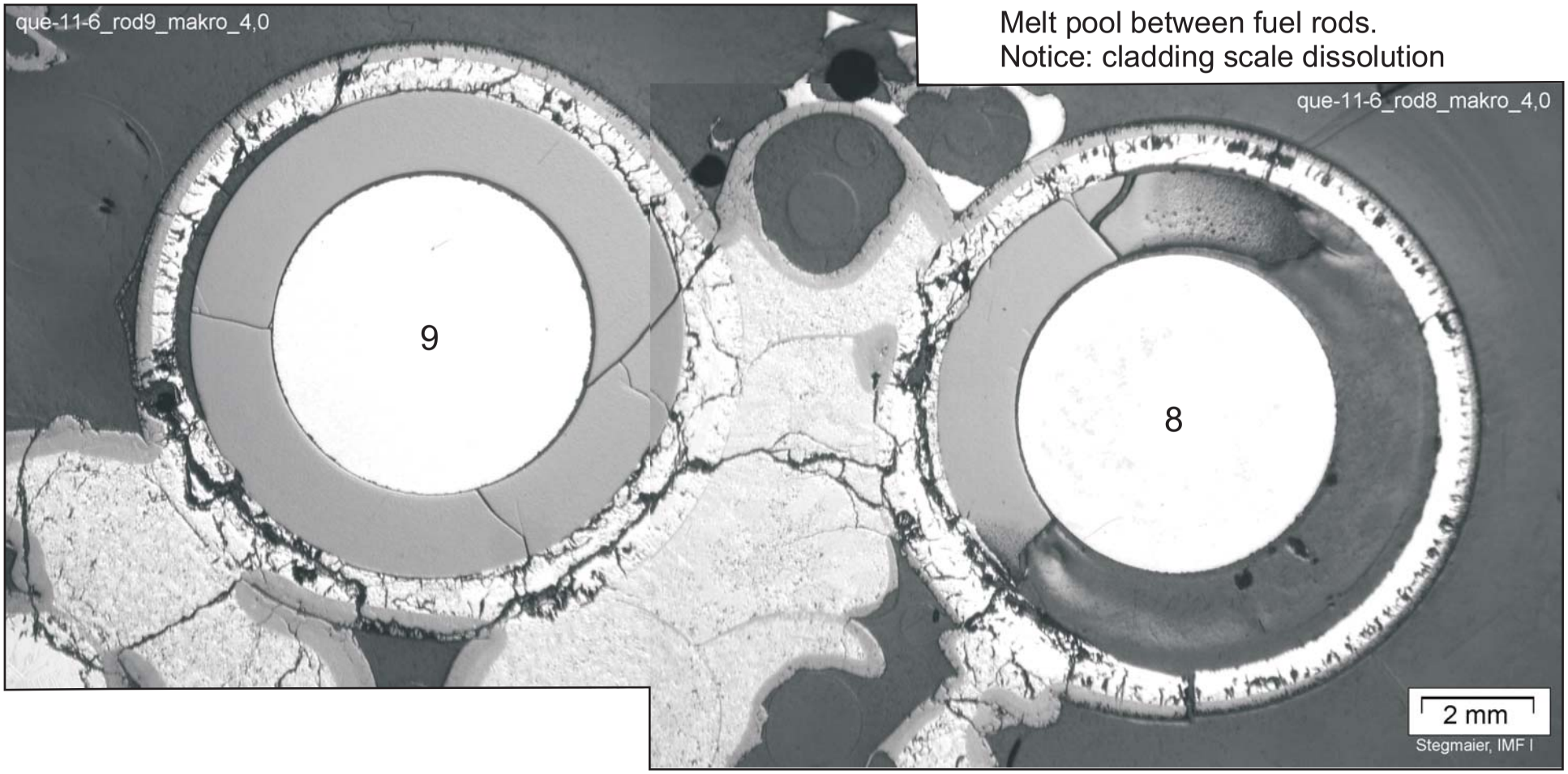

Fig. 55: QUE-11-6, level 810 mm; details of external melt interaction with rods

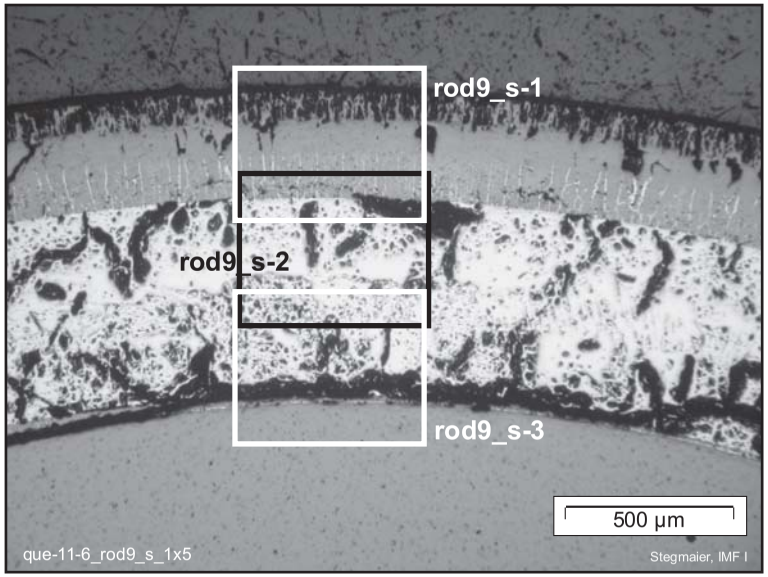

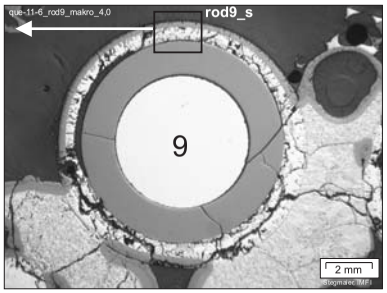

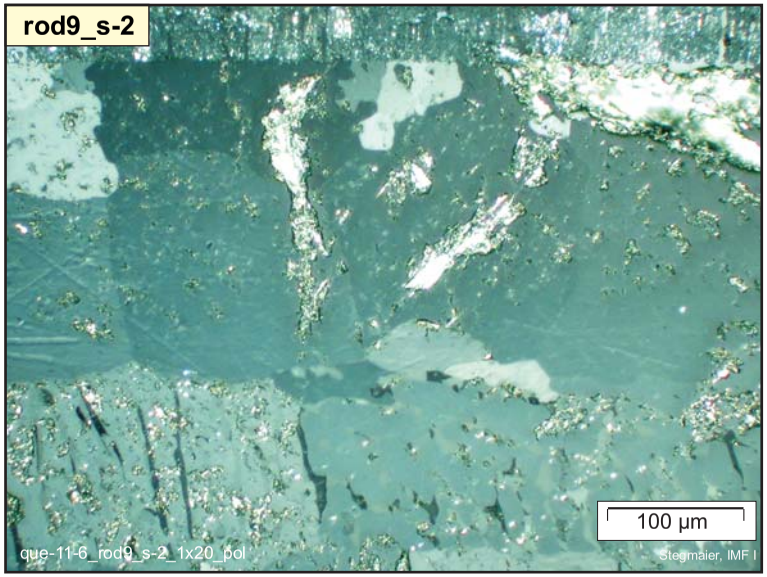

External (top) and internal (bottom) α-Zr(O) layer

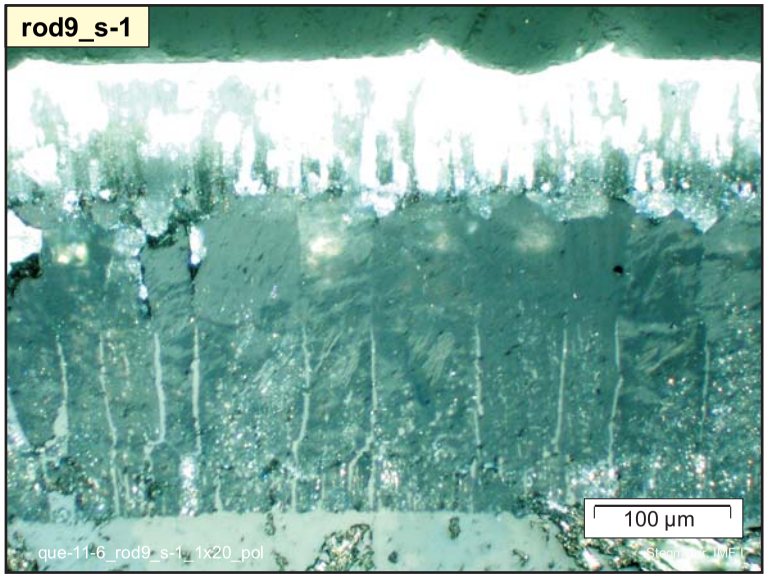

External scale

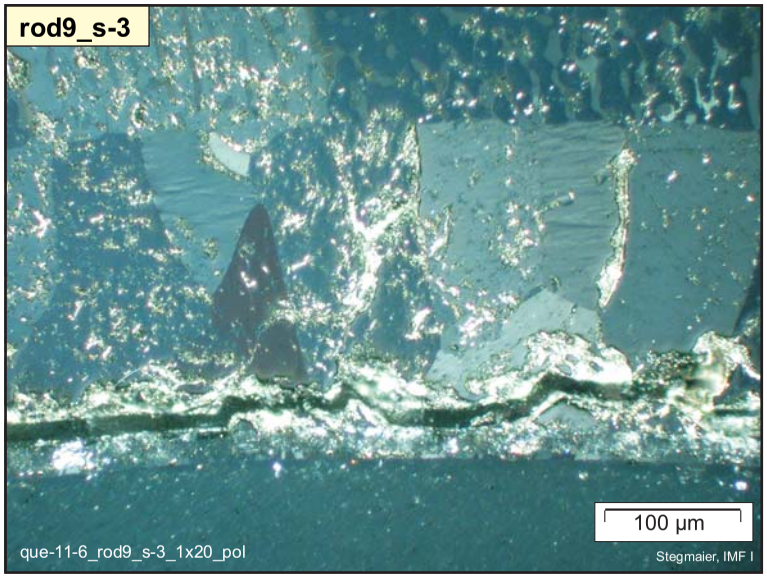

Fig. 56: QUE-11-6, level 810 mm; external and internal cladding oxidation of rod 9 towards S, illustrated in polarized light.

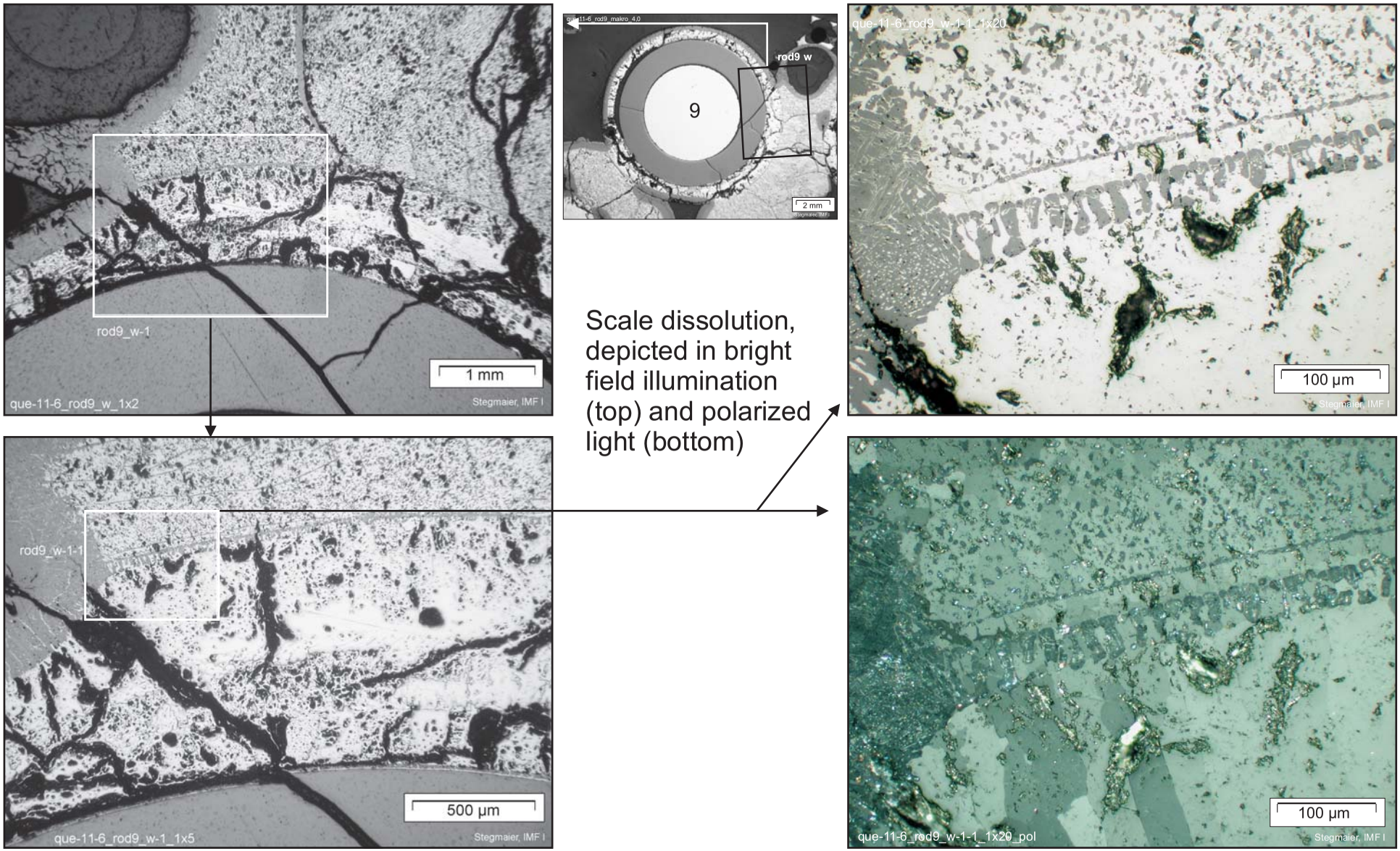

Fig. 57: QUE-11-6, level 810 mm; microstructures of the melt, and of the mostly dissolved scale of rod 9

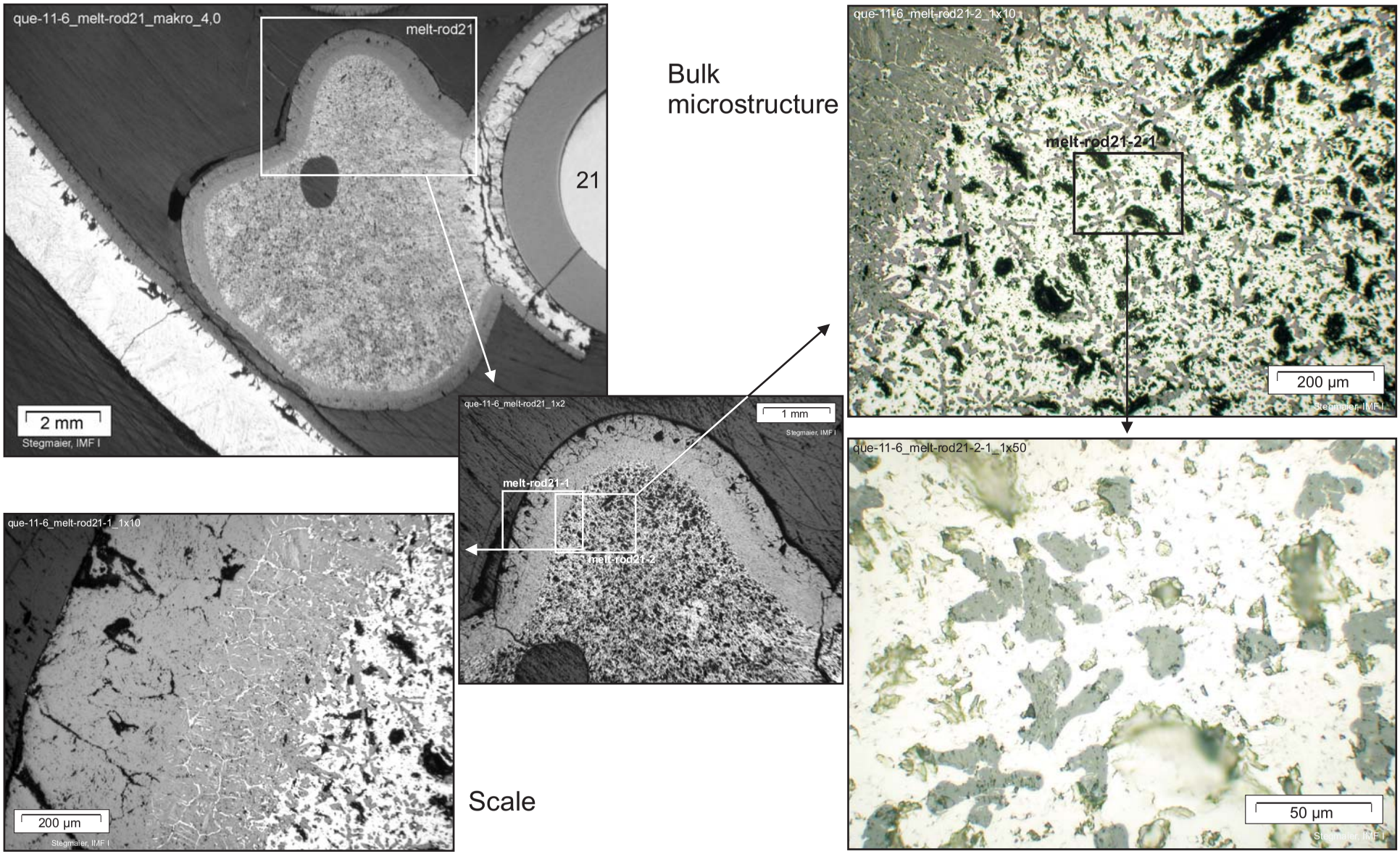

Fig. 58: QUE-11-6, level 810 mm; scale and bulk microstructure of a melt rivulet

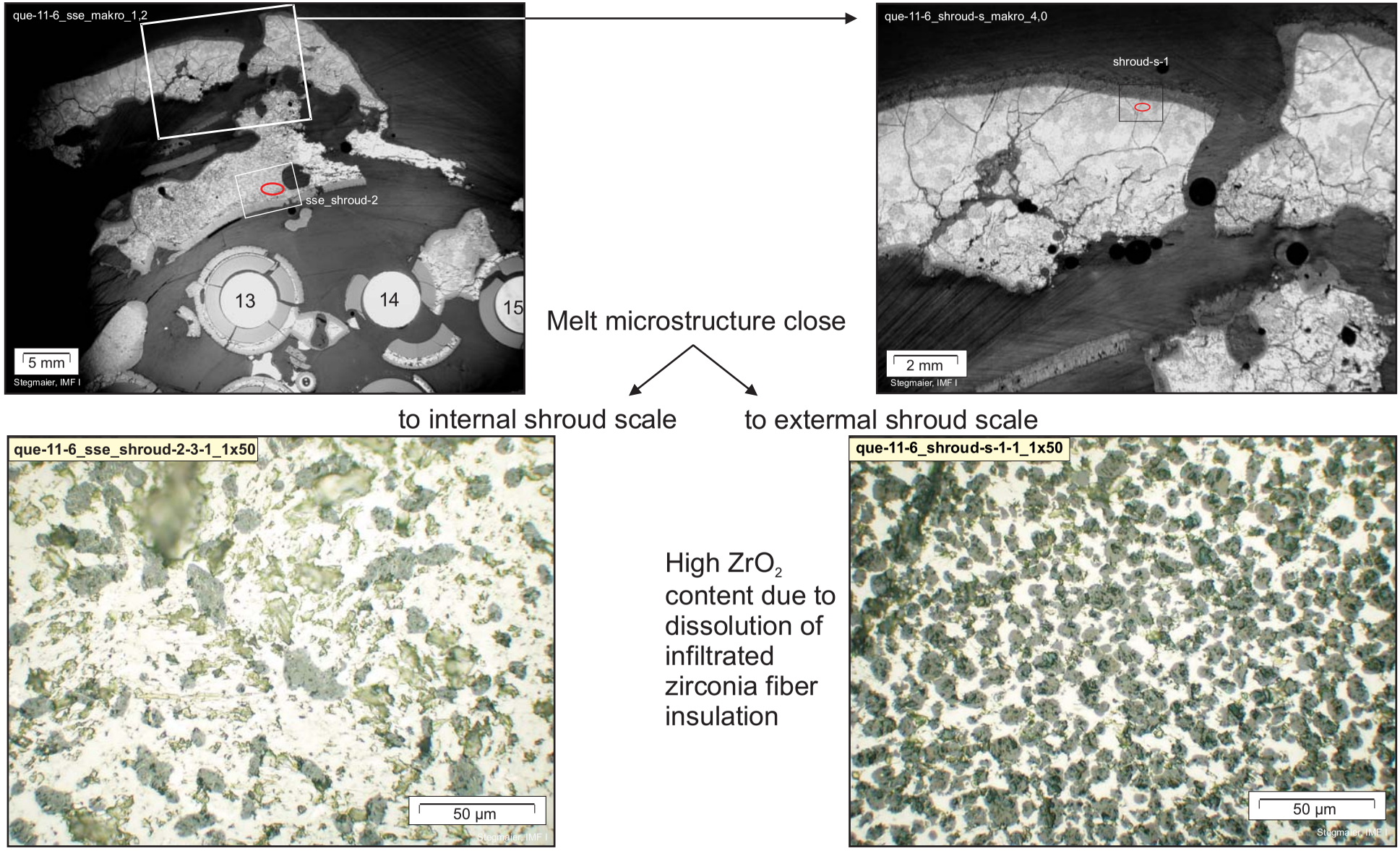

Fig. 59: QUE-11-6, level 810 mm; shroud melt and oxidation status

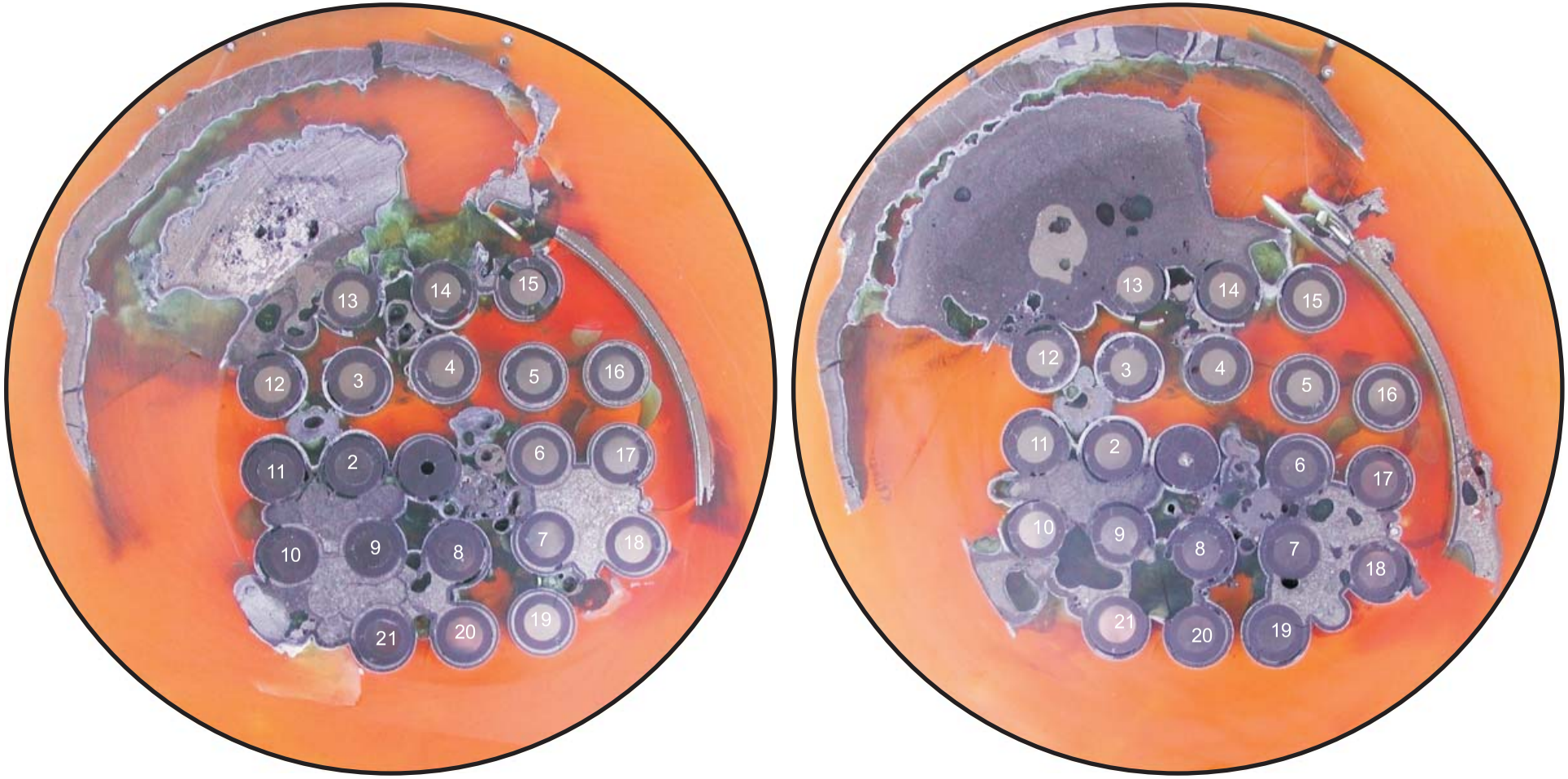

Elevation 837 mm, slab bottom, top view

Elevation 850 mm, top of slab, top view

Fig. 60: QUE-11-3: cross sections, representing the partial bundle blockage

Rods at top level: 850 mm

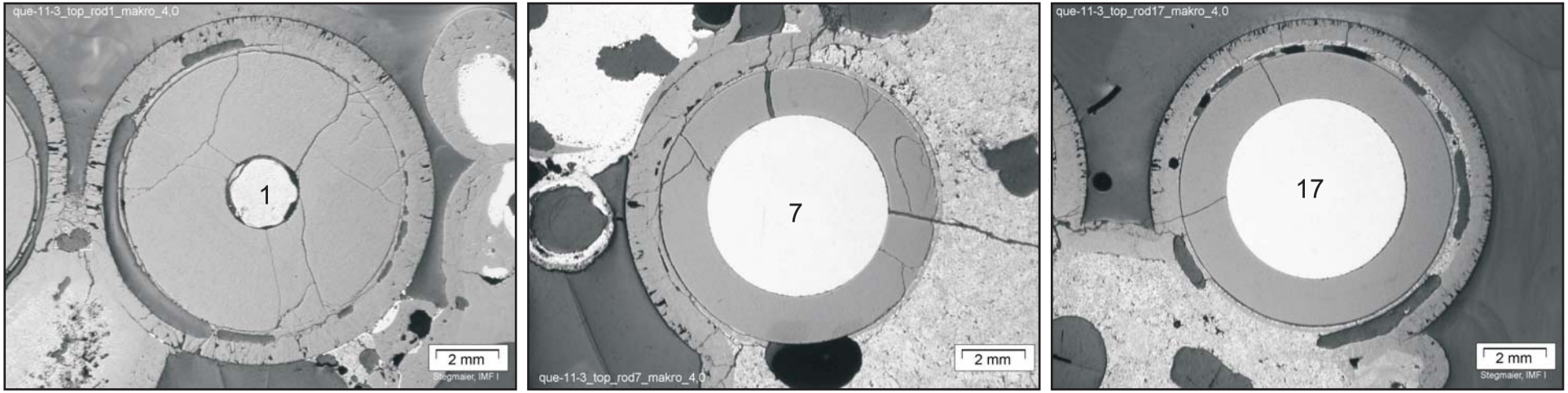

Central rod

Same rods at bottom level: 837 mm

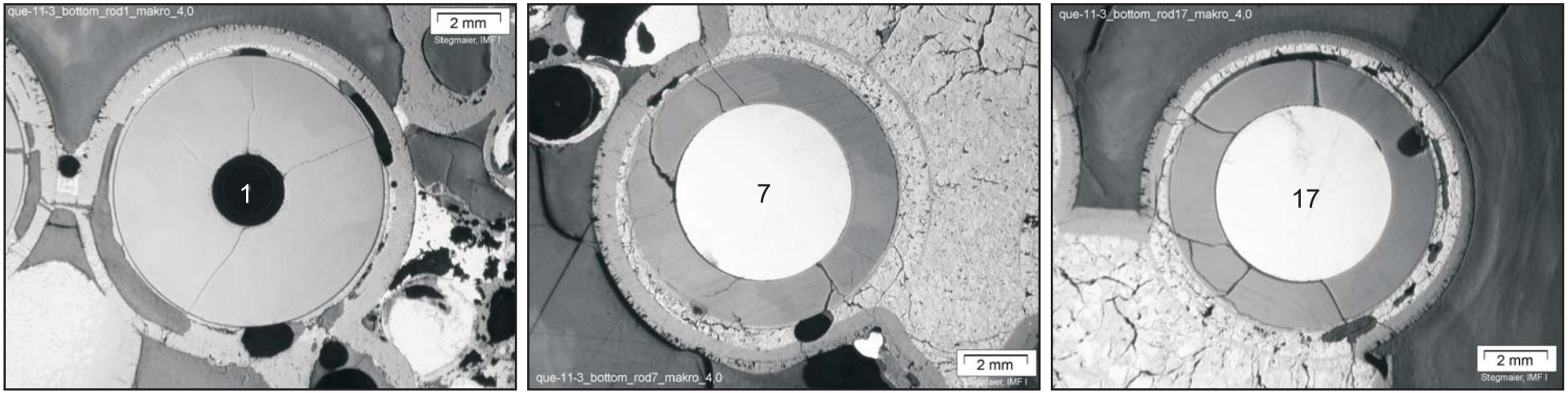

Fig. 61: QUE-11-3; status of three rods in comparison of top and bottom side of the cross section slab

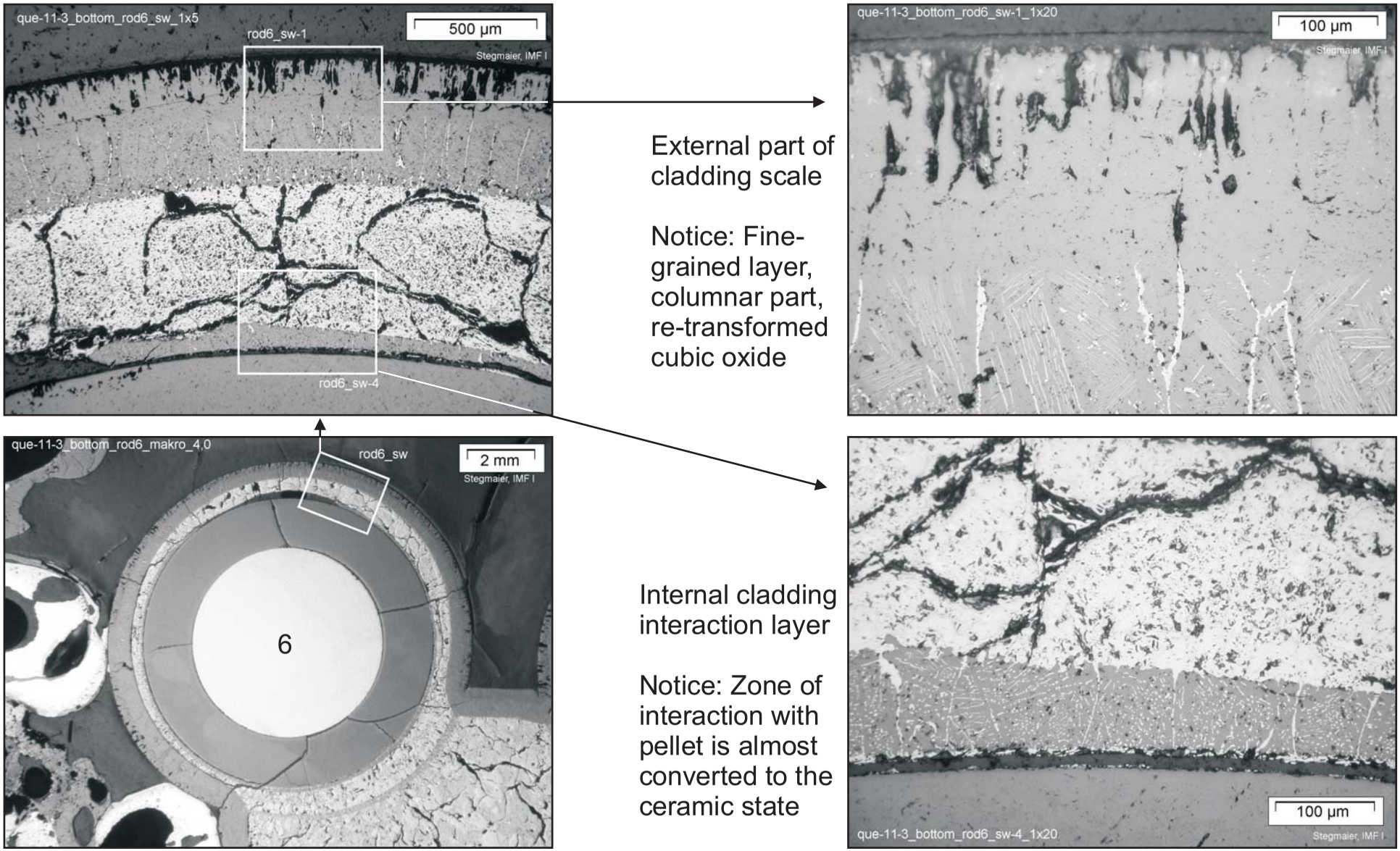

Fig. 62: QUE-11-3, level 837 mm: external and internal cladding oxidation of rod 6

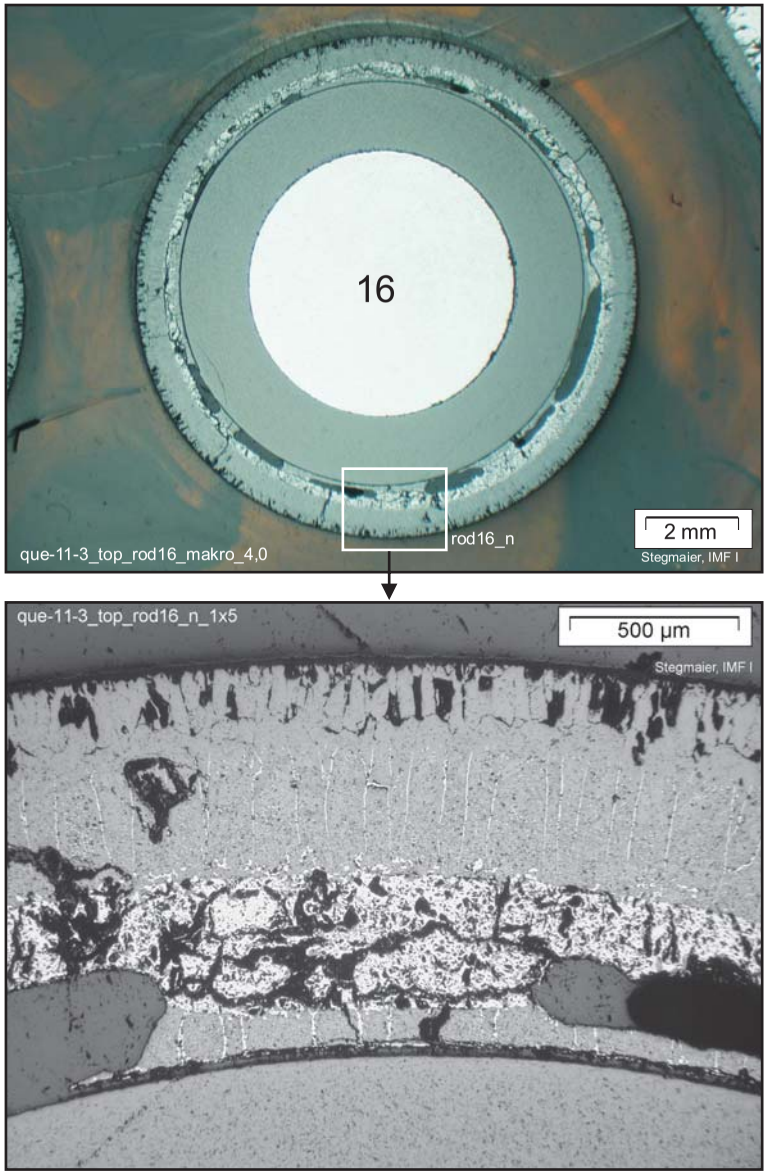

Rod 16: Residual metallic matrix, oxidation from both sides by steam and pellet, respectively

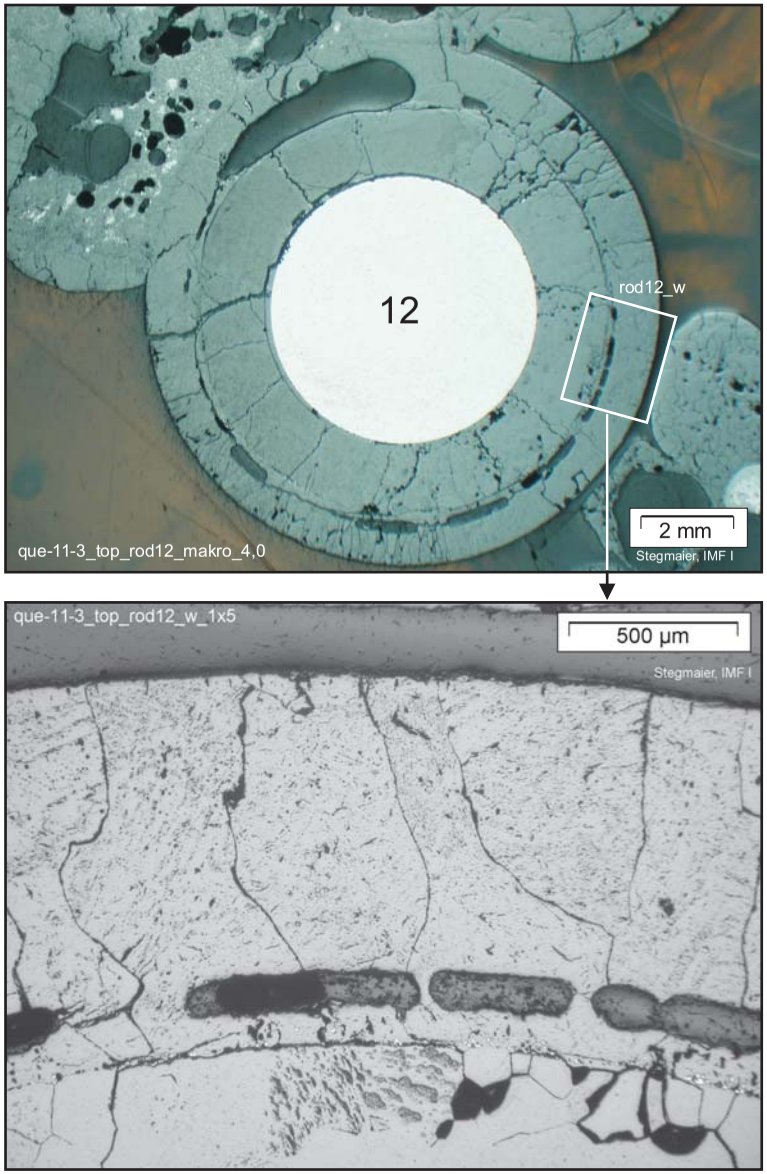

Rod 12: Cladding fully converted to coarse-grained oxide

Fig. 63: QUE-11-3, level 850 mm; oxidation status of two rods, indicating the range of cladding conversion

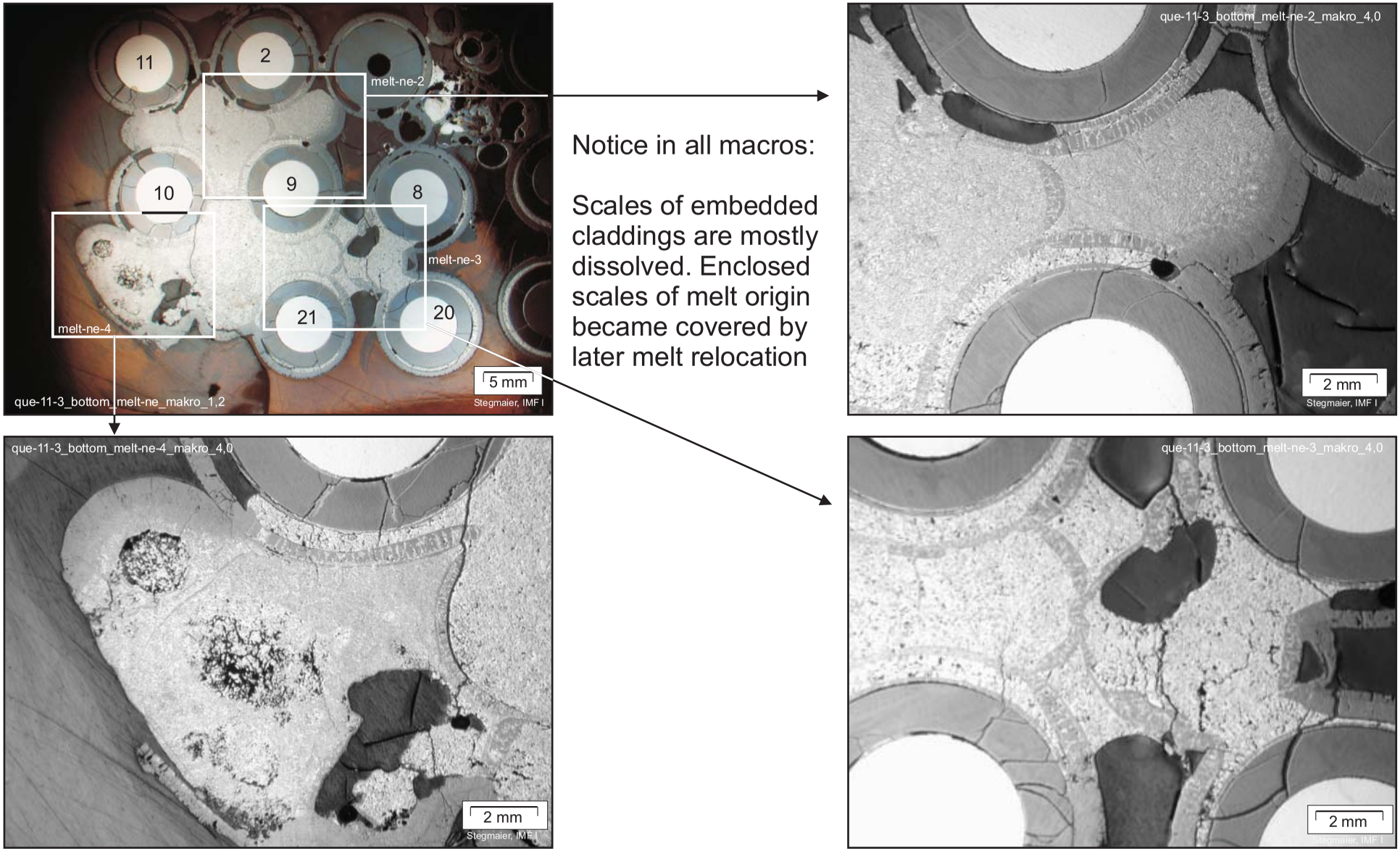

Fig. 64: QUE-11-3, level 837 mm: melt accumulation at NE direction

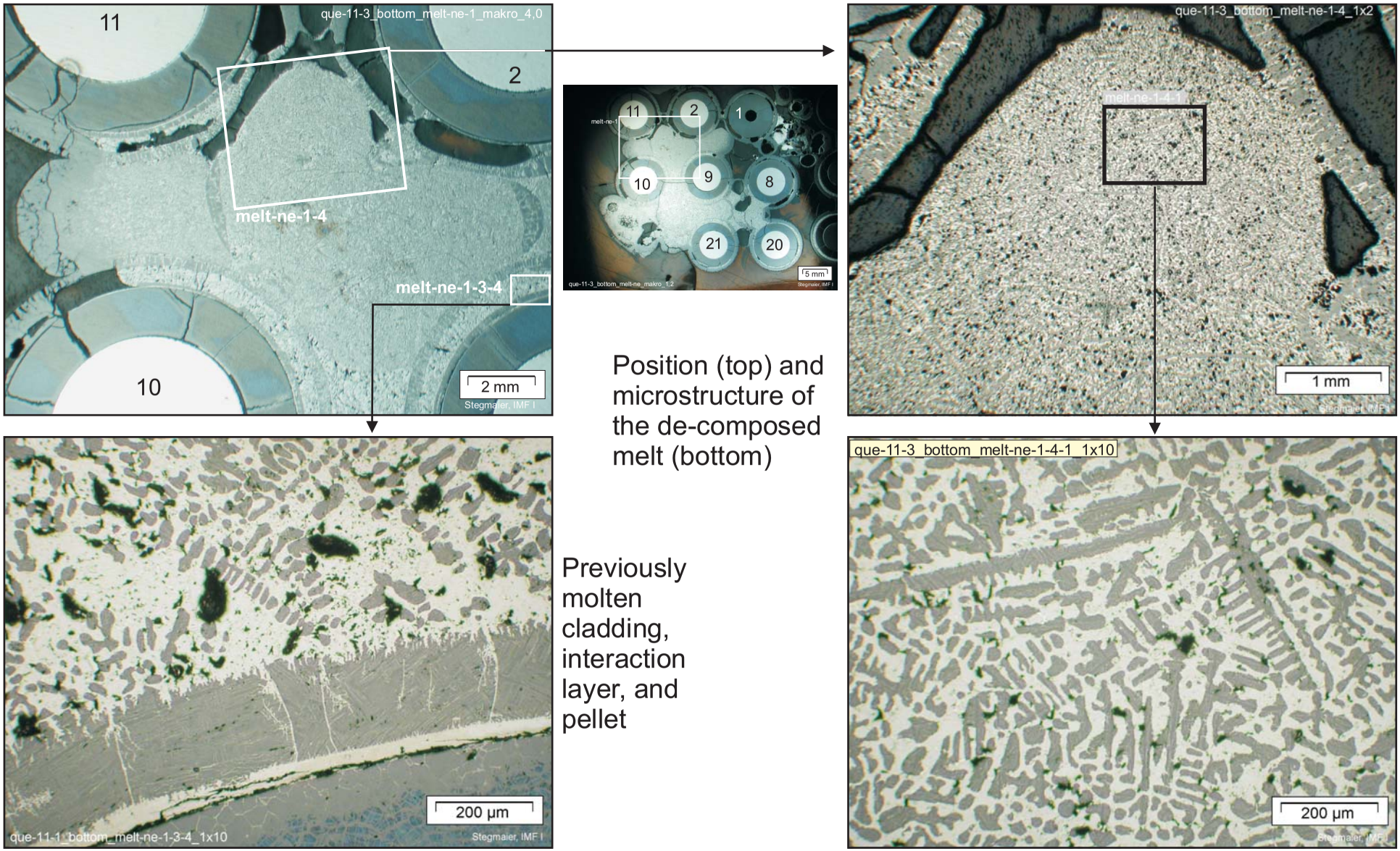

Fig. 65: QUE-11-3, level 837 mm; dendritic distribution of ZrO_2 precipitates in melt agglomerate at NE bundle corner, and similar cladding microstructure of rod 9, proving its re-solidification

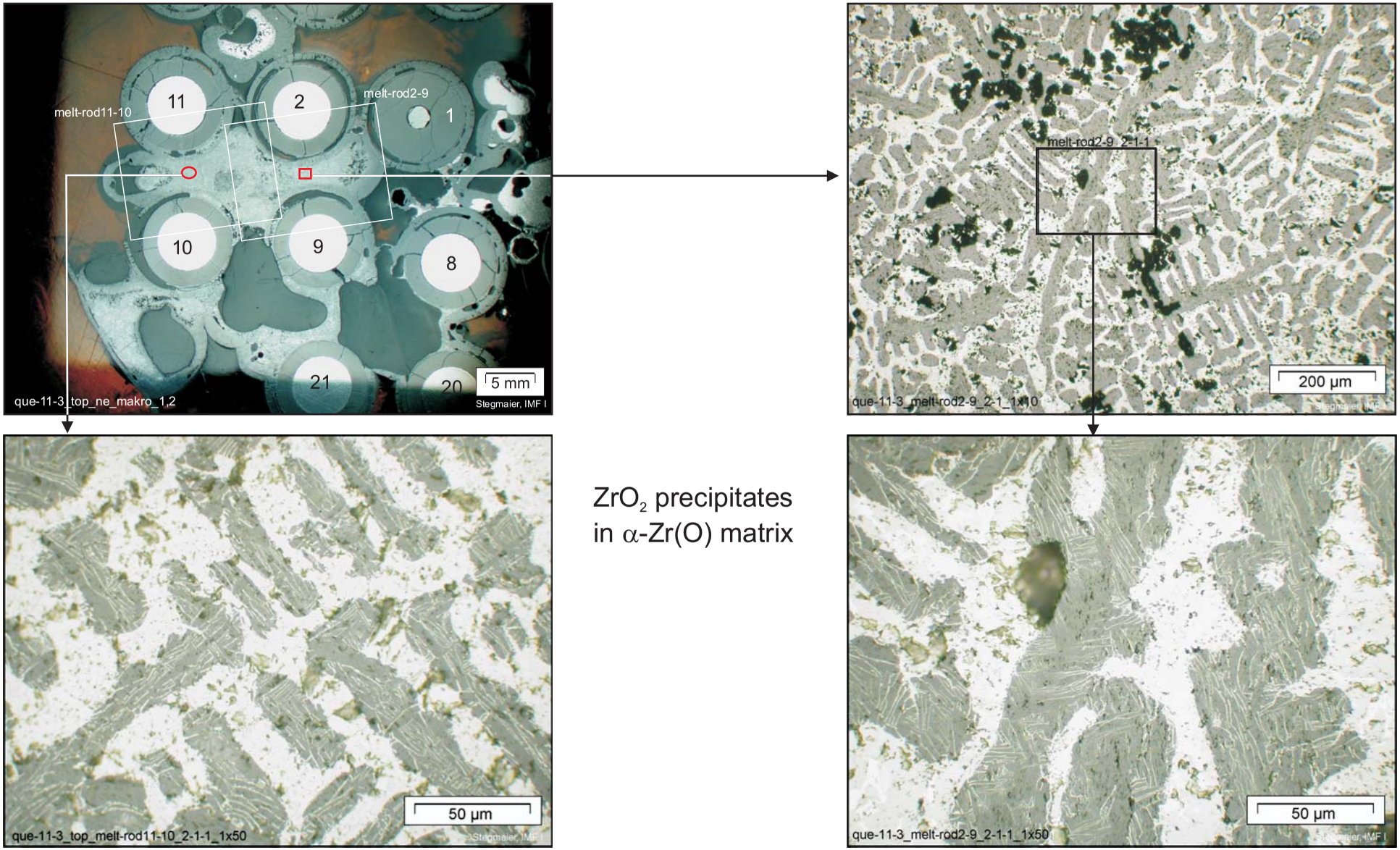

Fig. 66: QUE-11-3, level 850 mm; microstructure of melt at NE bundle corner, indicating minor differences over large distance between two positions

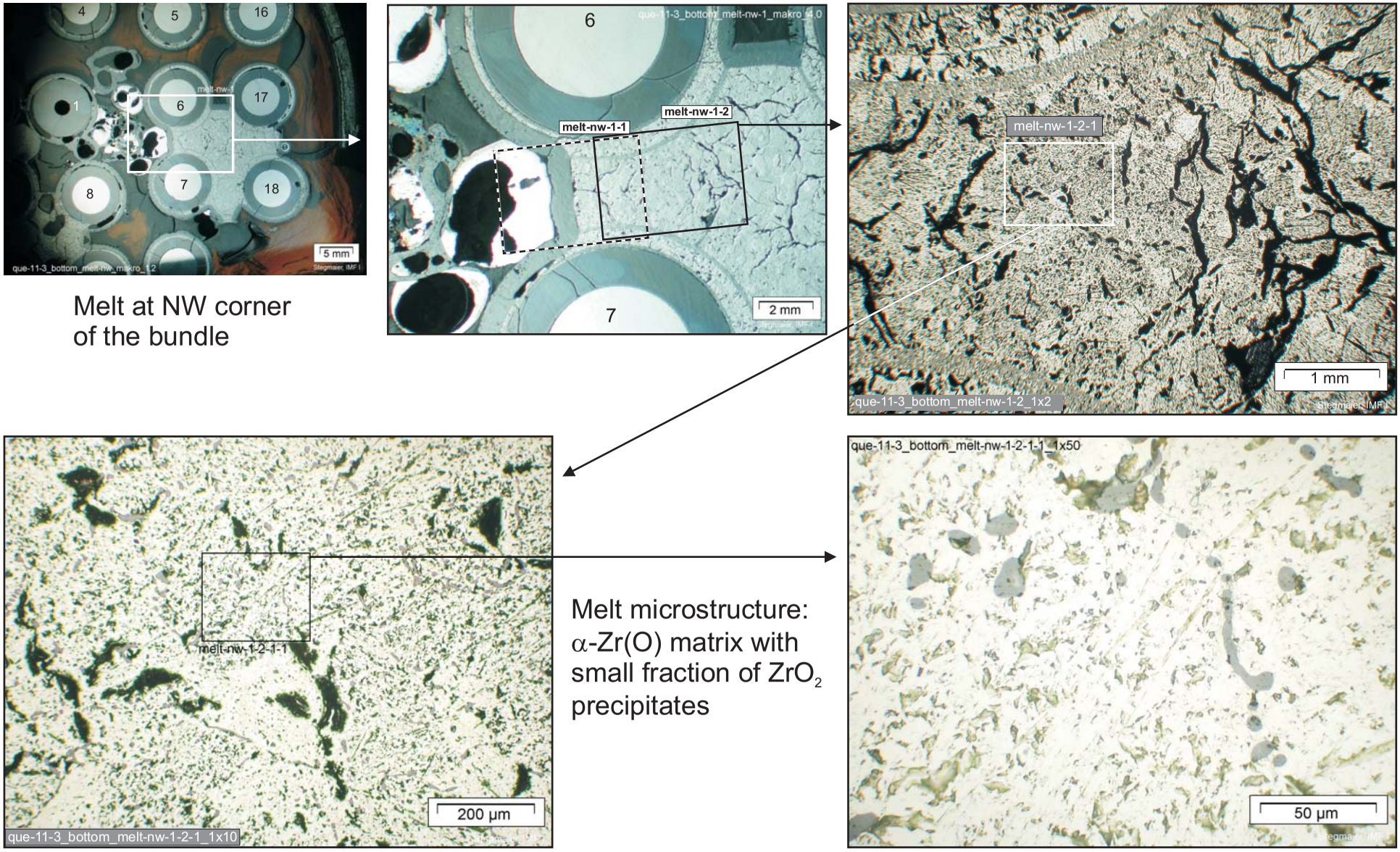

Fig. 67: QUE-11-3, level 837 mm; microstructure of melt at NW bundle corner

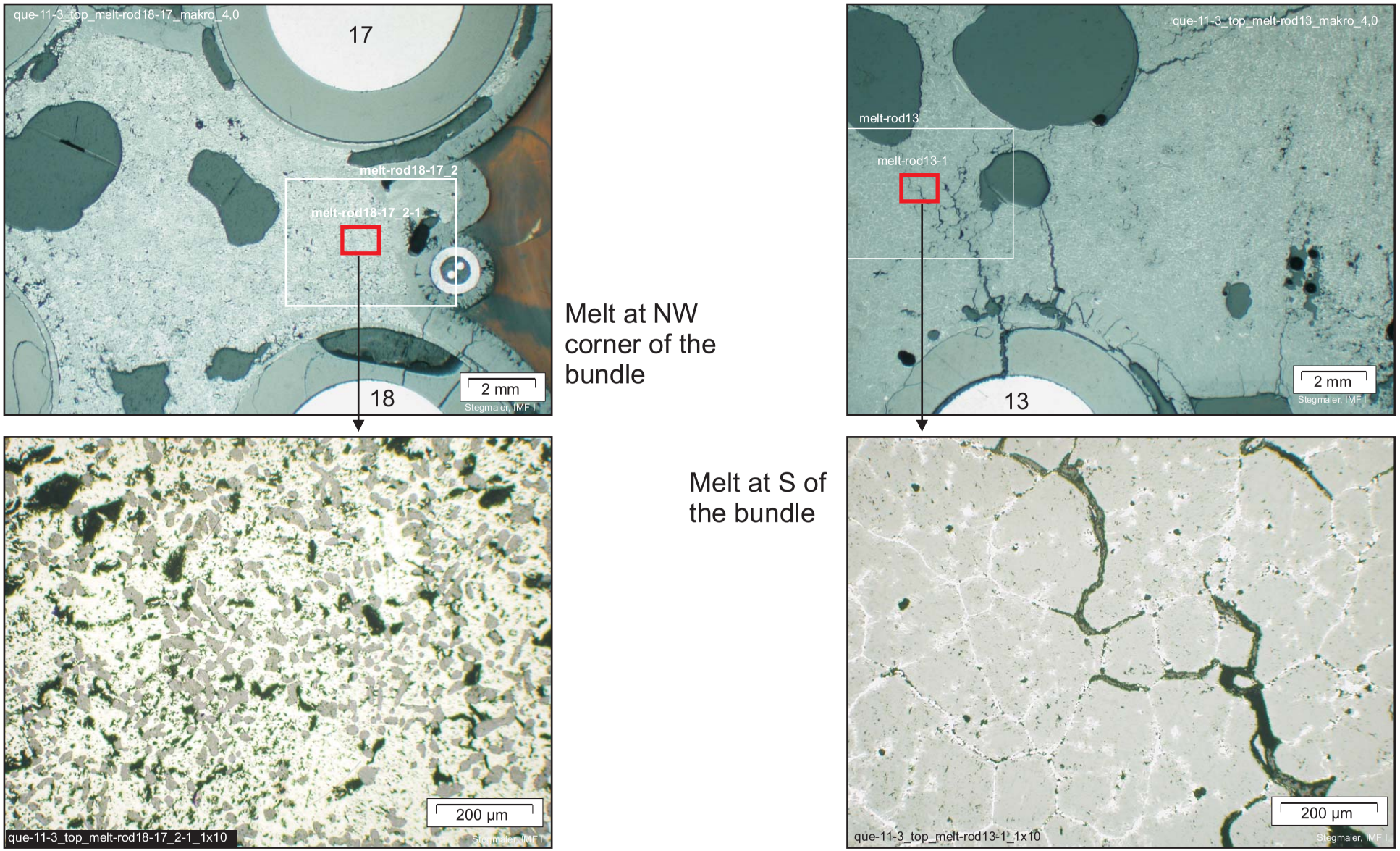

Fig. 68: QUE-11-3, level 850 mm; comparison of microstructures of melt at bundle corner NW and of melt towards S

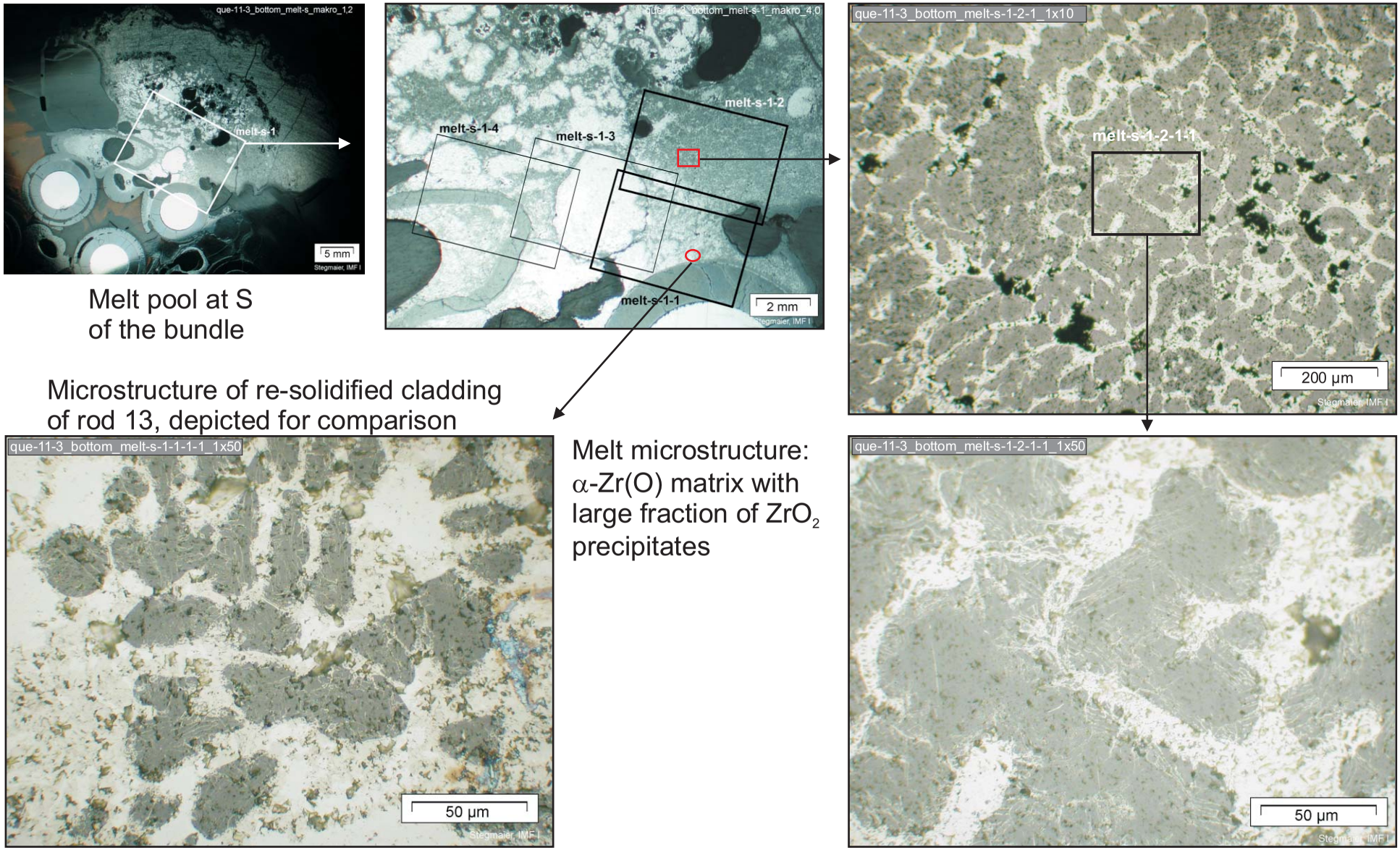

Fig. 69: QUE-11-3, level 837 mm; microstructure of melt pool towards S from the bundle, and comparison with cladding melt of the partly embedded rod 13

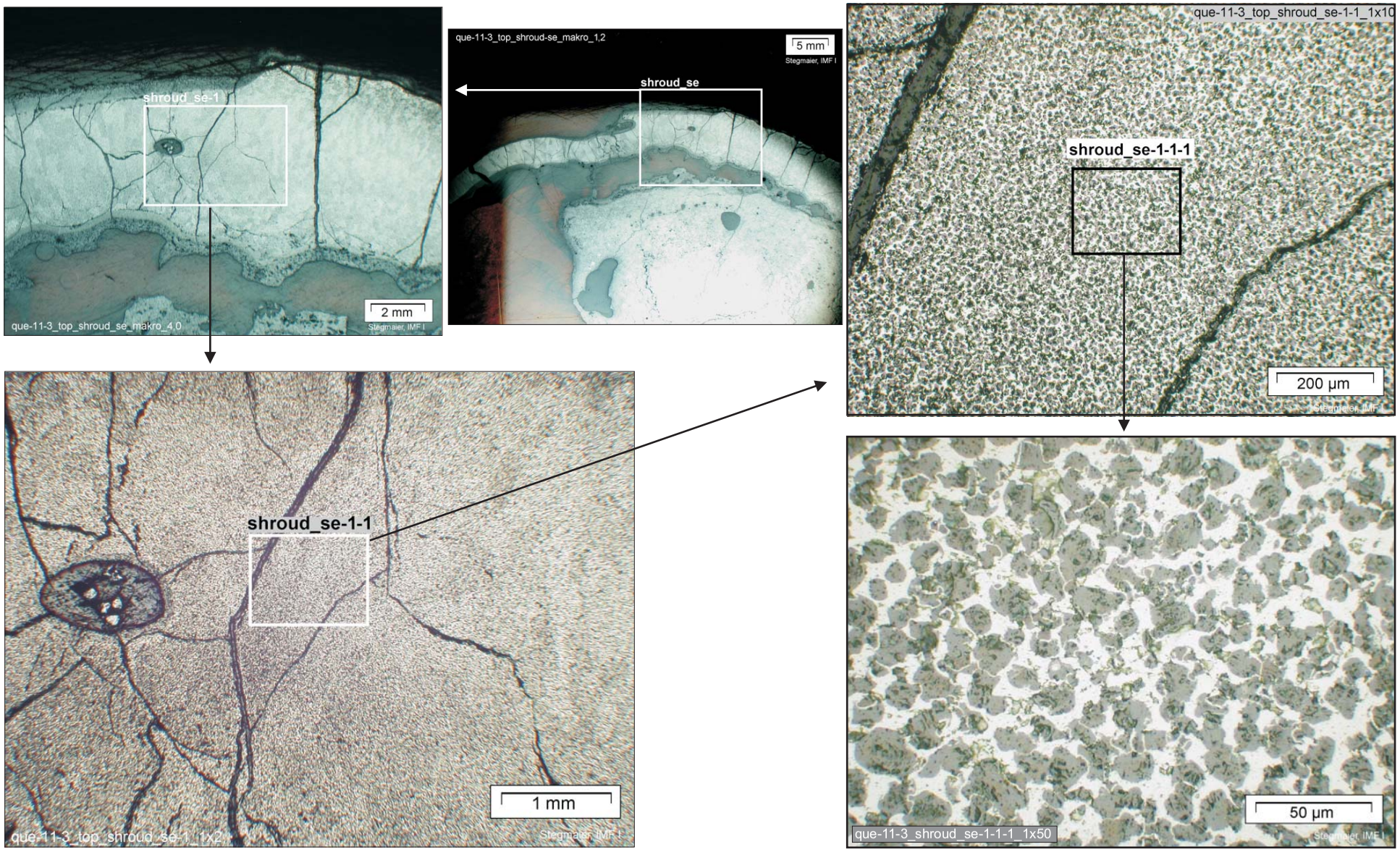

Fig. 70: QUE-11-3, level 850 mm; microstructure of the once molten shroud at SE direction

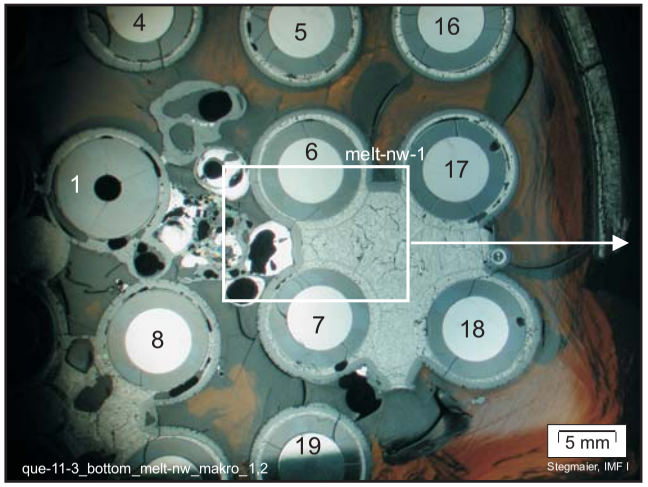

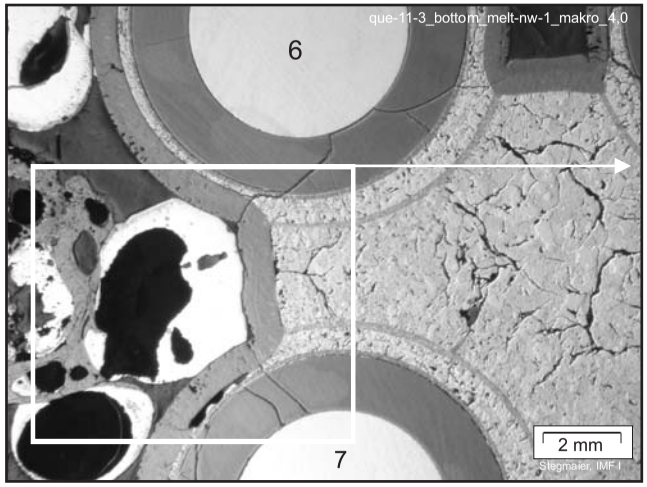

Light-optical images, top view

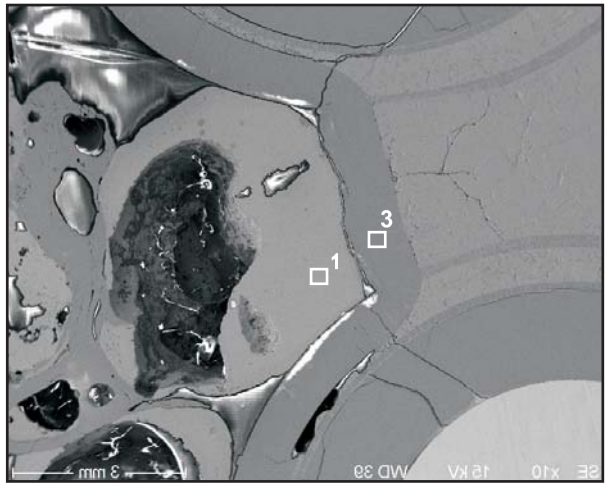

SEM-SE image, top view

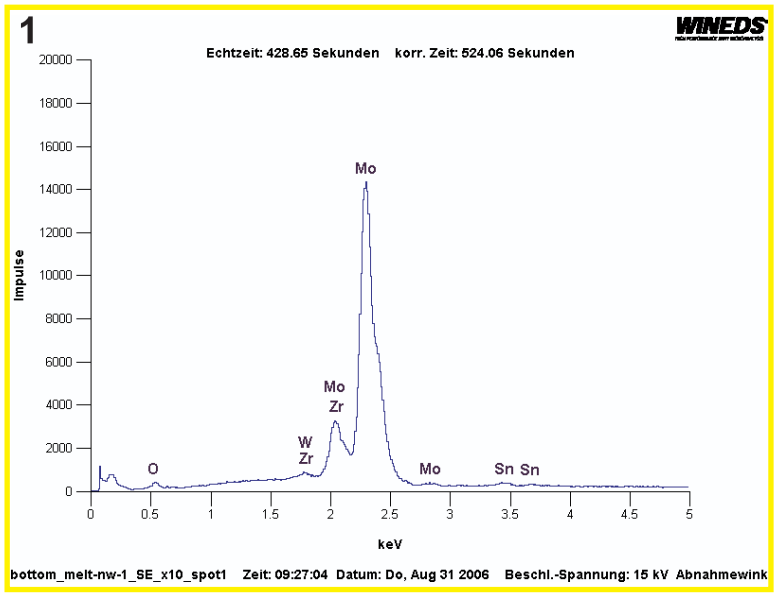

SEM-EDX spectra:

Left: Multi-component melt, containing Mo+W from electrode + heater rod dissolution

Right: Pool of relocated (Zr,O) cladding melt

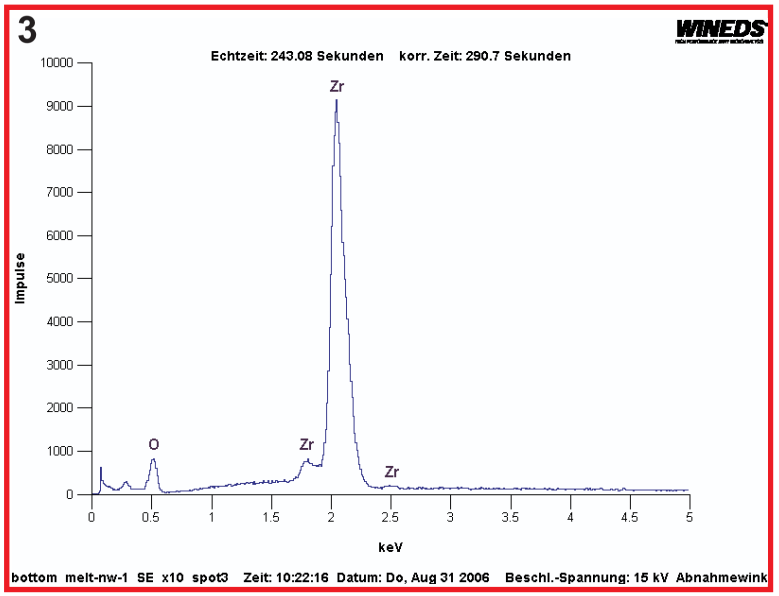

Fig. 71: QUE-11-3, level 837 mm; SEM/EDX analysis of melt in bundle centre

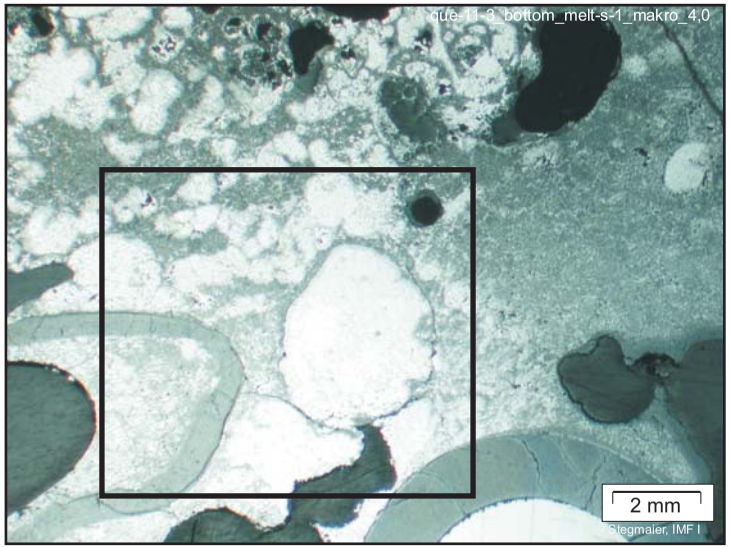

LM micrograph

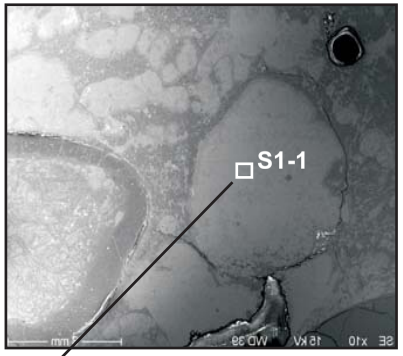

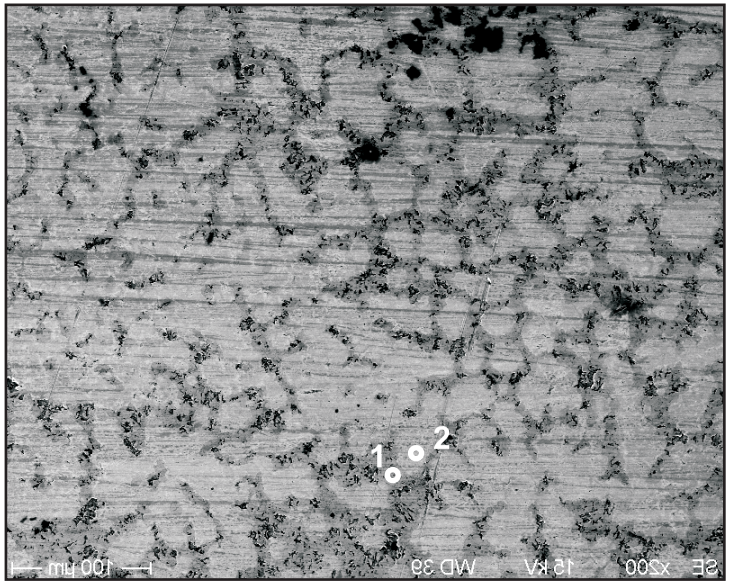

SEM-SE images (secondary electron contrast) and EDX element spectra for residual melt and dendritic primary crystals (spot 1, top and spot 2, bottom)

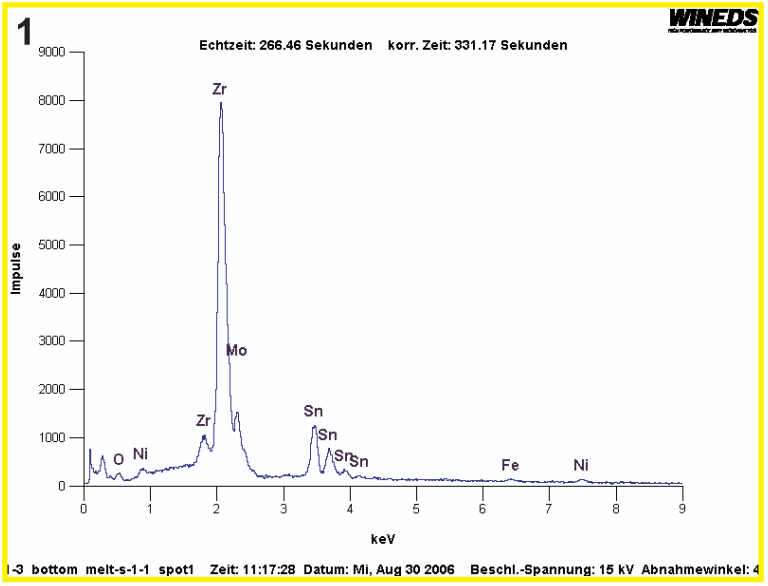

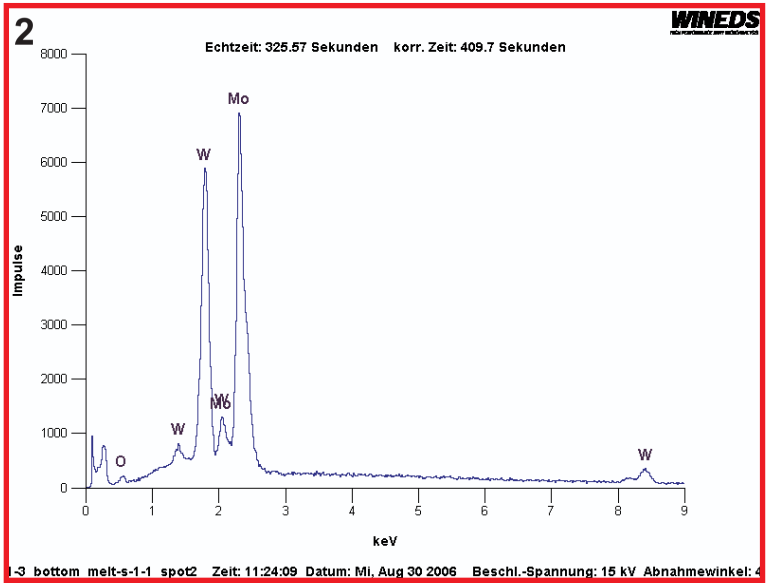

Fig. 72: QUE-11-3, level 837 mm; SEM/EDX analysis of a melt droplet, enclosed by the contaminated agglomerate of shroud melt at SE

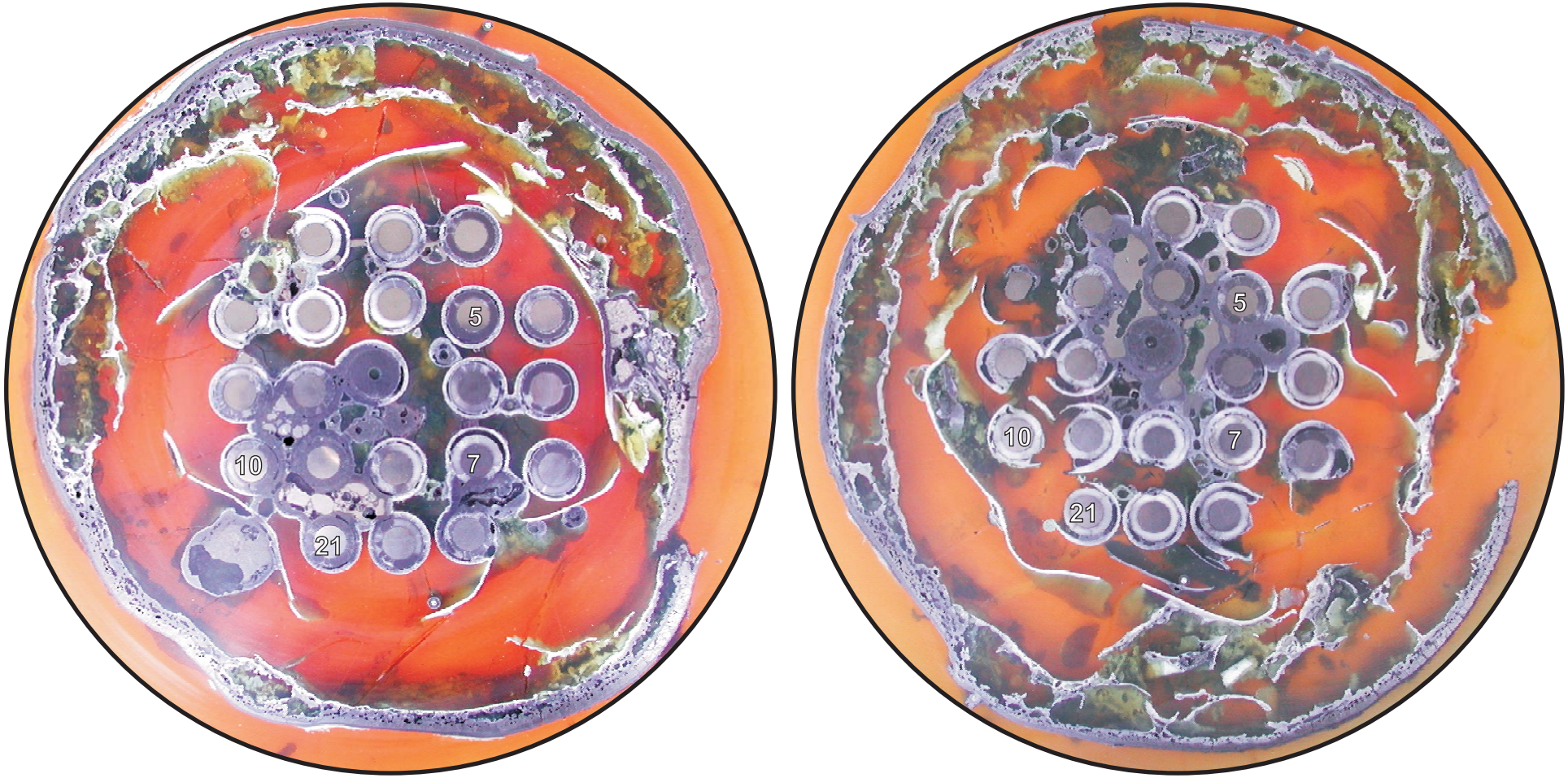

Elevation 900 mm, top view

Elevation 950 mm, top view

Fig. 73: QUE-11-7 and -11-4, levels 900 and 950 mm; cross section overviews within the hottest zone

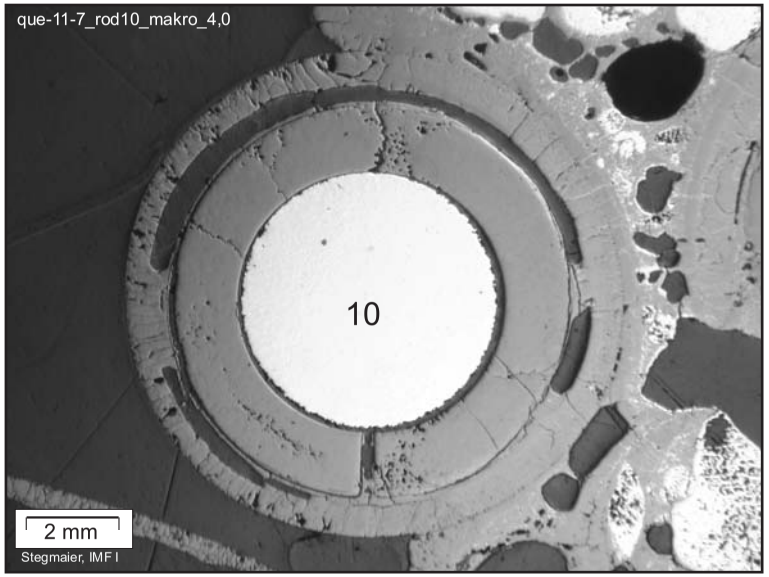

Remnants from cladding / pellet interaction, voids from internal relocation.

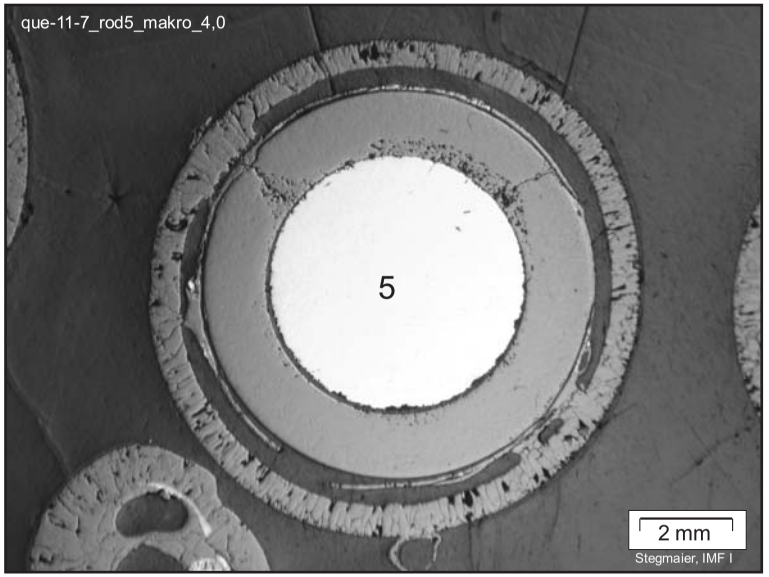

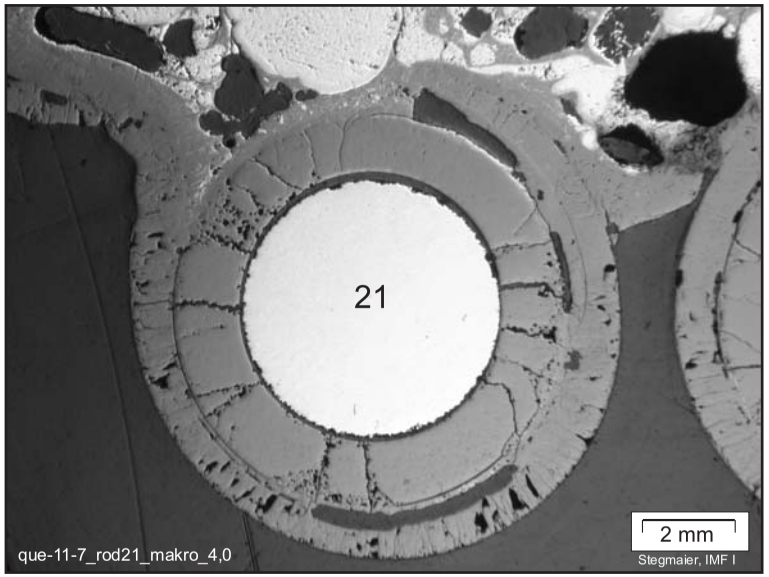

Notice: Multi-component metallic melt, contacting rods <u>at left</u>; same rods shown in next figure.

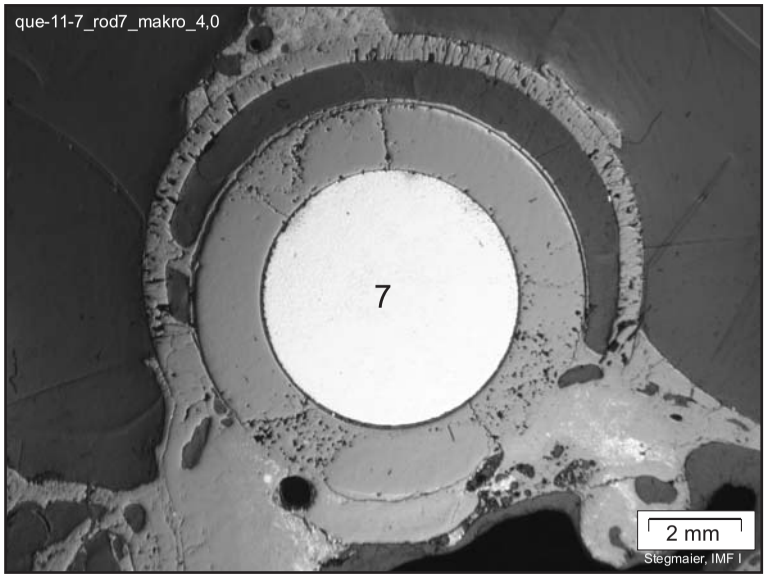

Fig. 74: QUE-11-7, level 900 mm; complete oxidative cladding conversion into scale

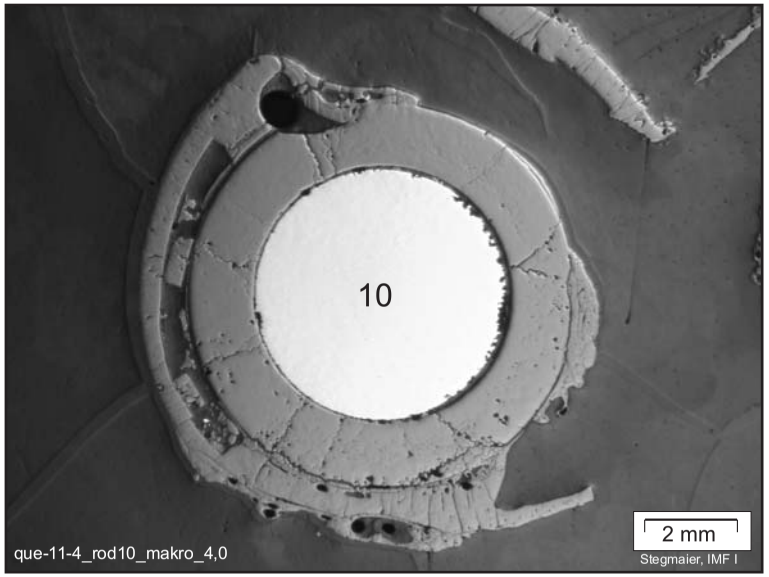

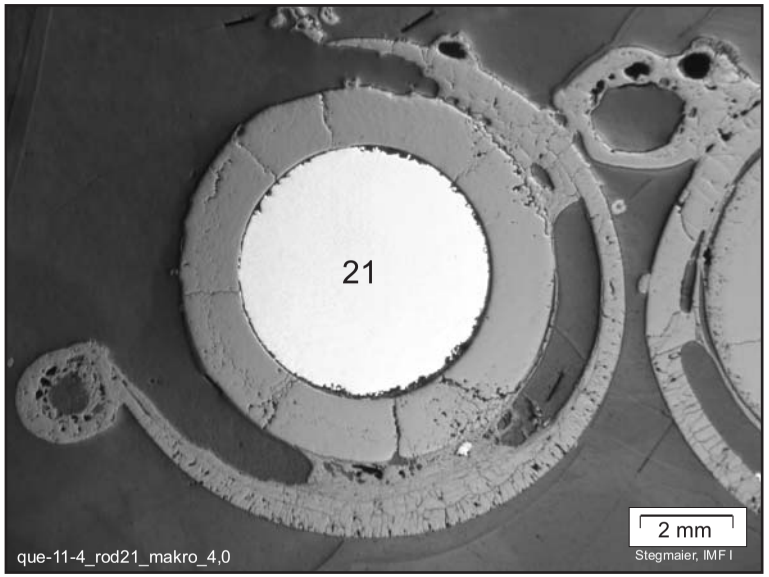

Remnants from cladding / pellet interaction, voids from internal relocation.

Multi-component metallic melt, contacting here the rods at right: Downward relocation not as single event.

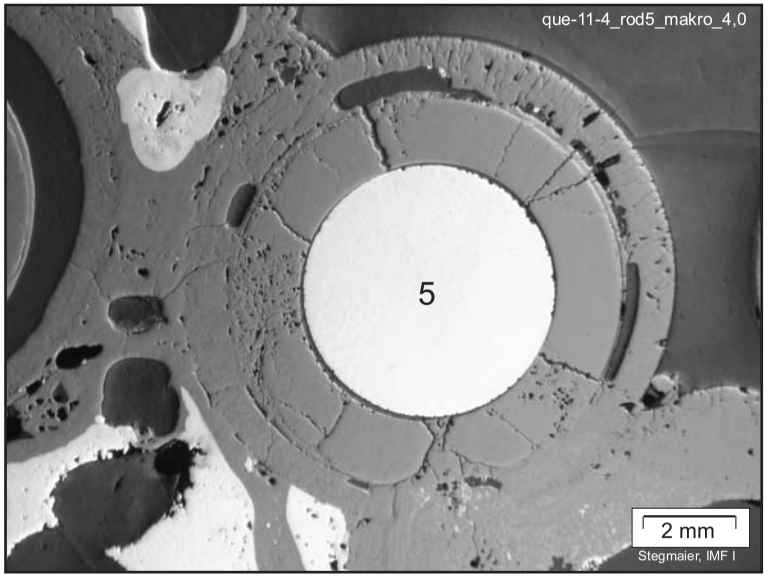

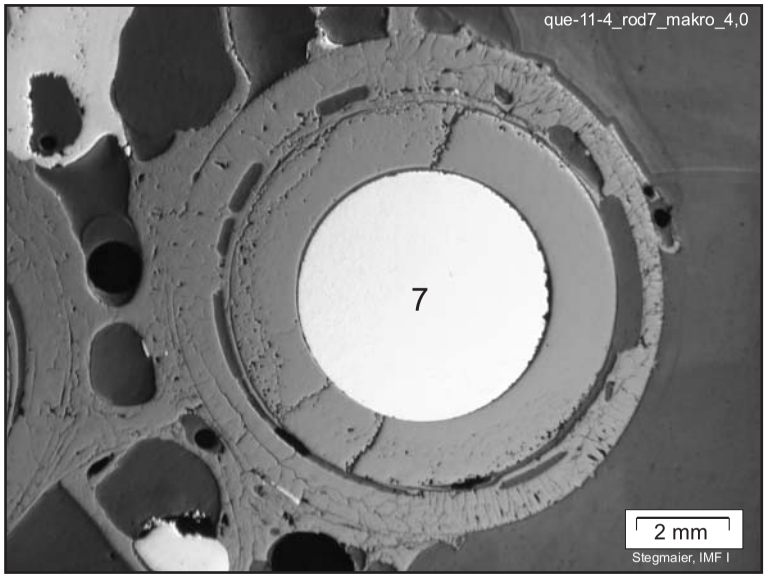

Fig. 75: QUE-11-4, level 950 mm; complete oxidative cladding conversion into scale

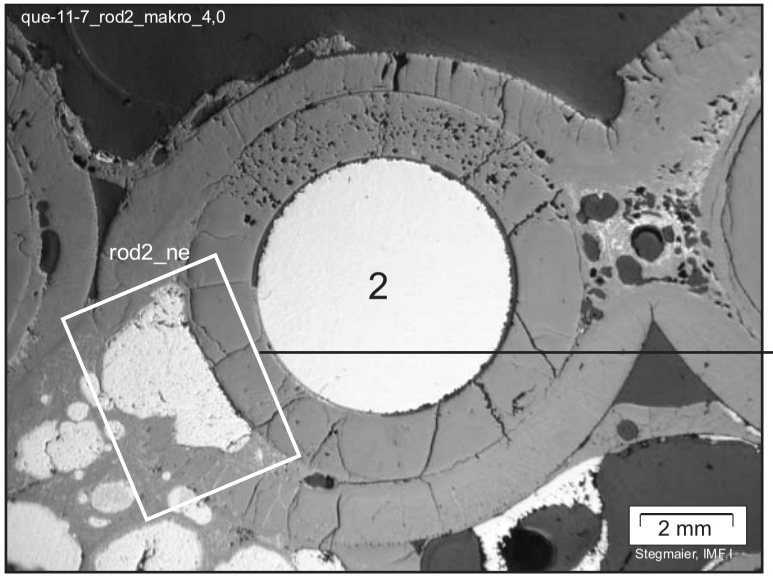

Mo-rich melt (top), SEM/EDX spectrum (bottom)

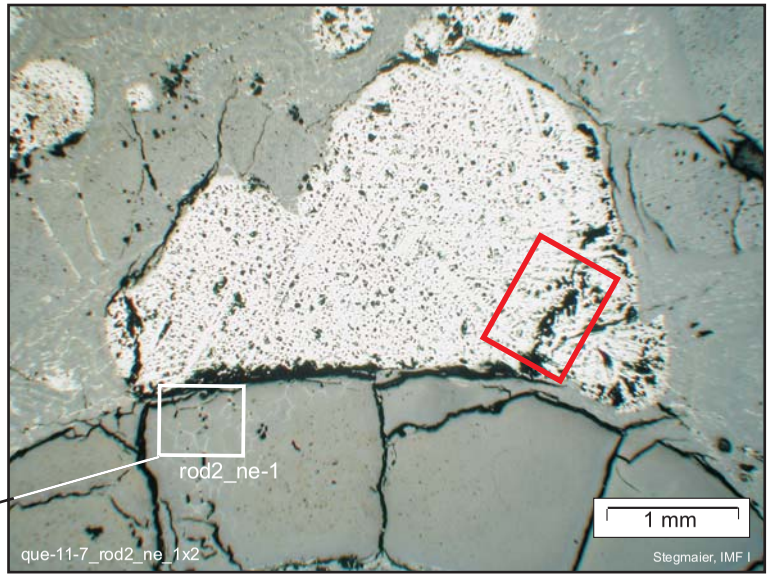

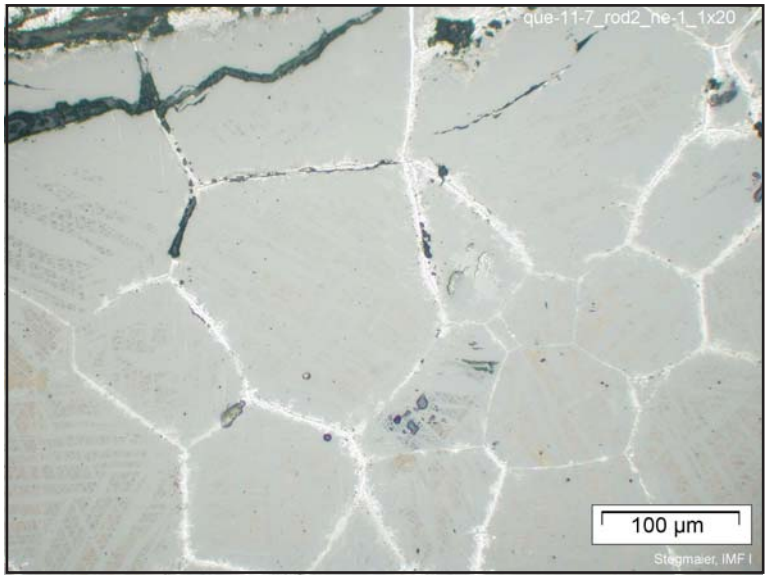

Pellet interaction with Mo-rich melt, indicated by the decoration of grain boundaries

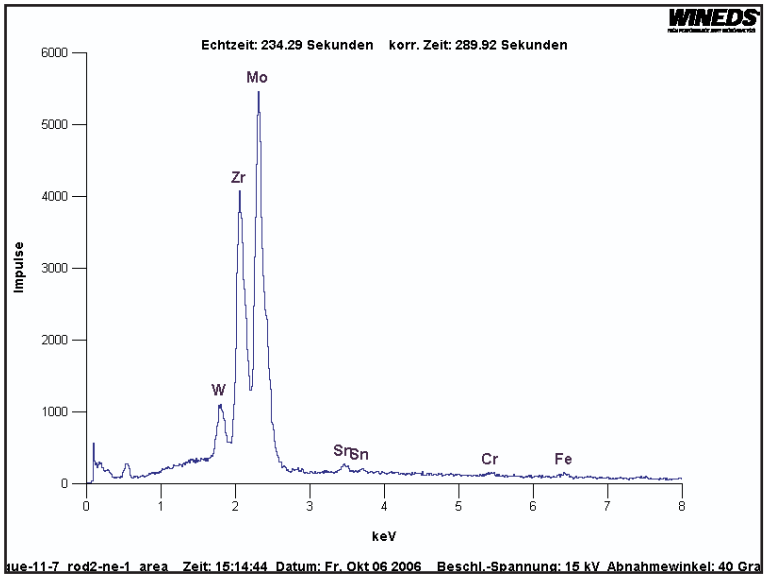

Fig. 76: QUE-11-7, level 900 mm; melt agglomerate, composed of metallic molybdenum-rich and oxidized cladding melt, in contact with the pellet of rod 2

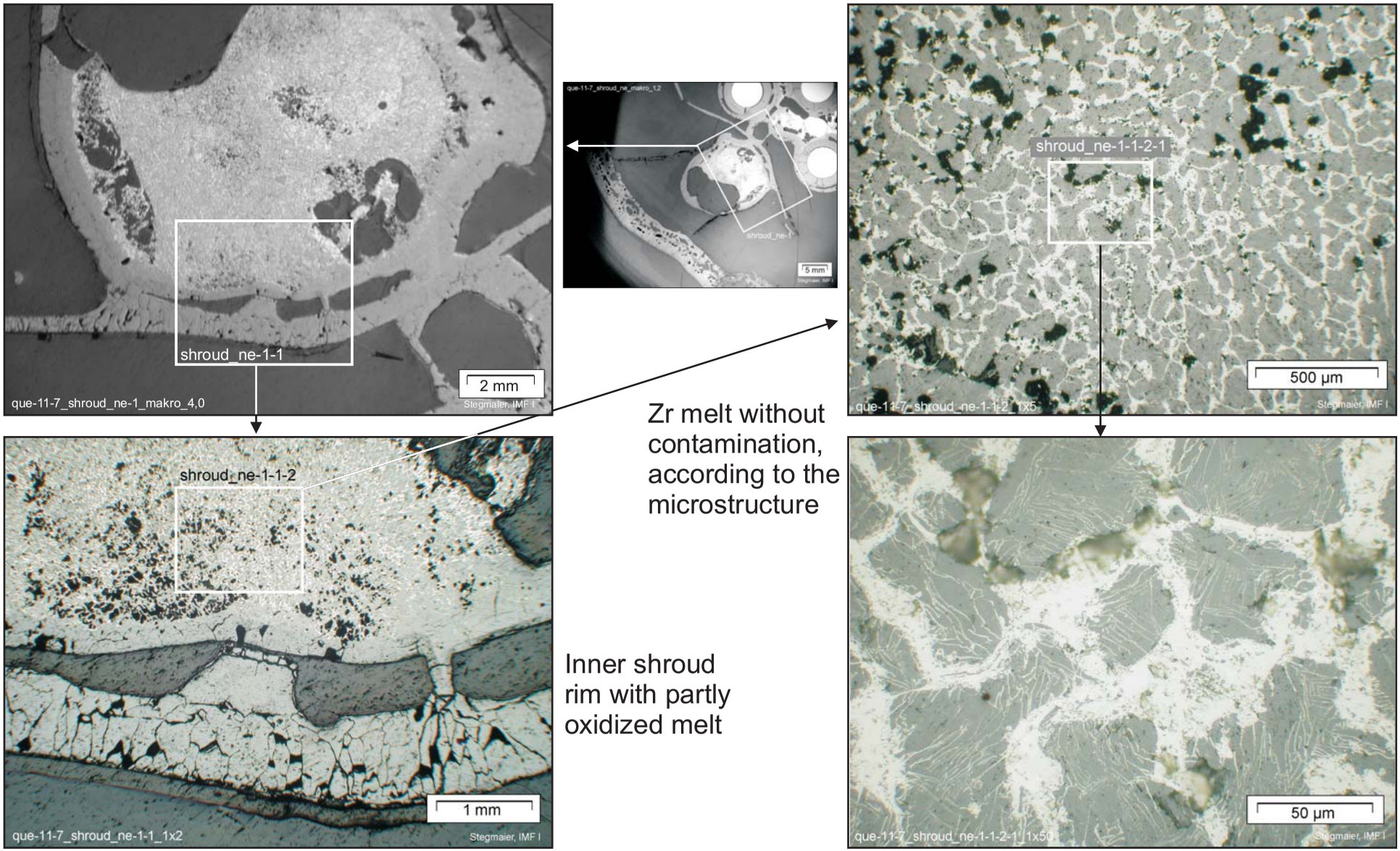

Fig. 77: QUE-11-7, level 900 mm; melt, relocated after splitting of the shroud at NE

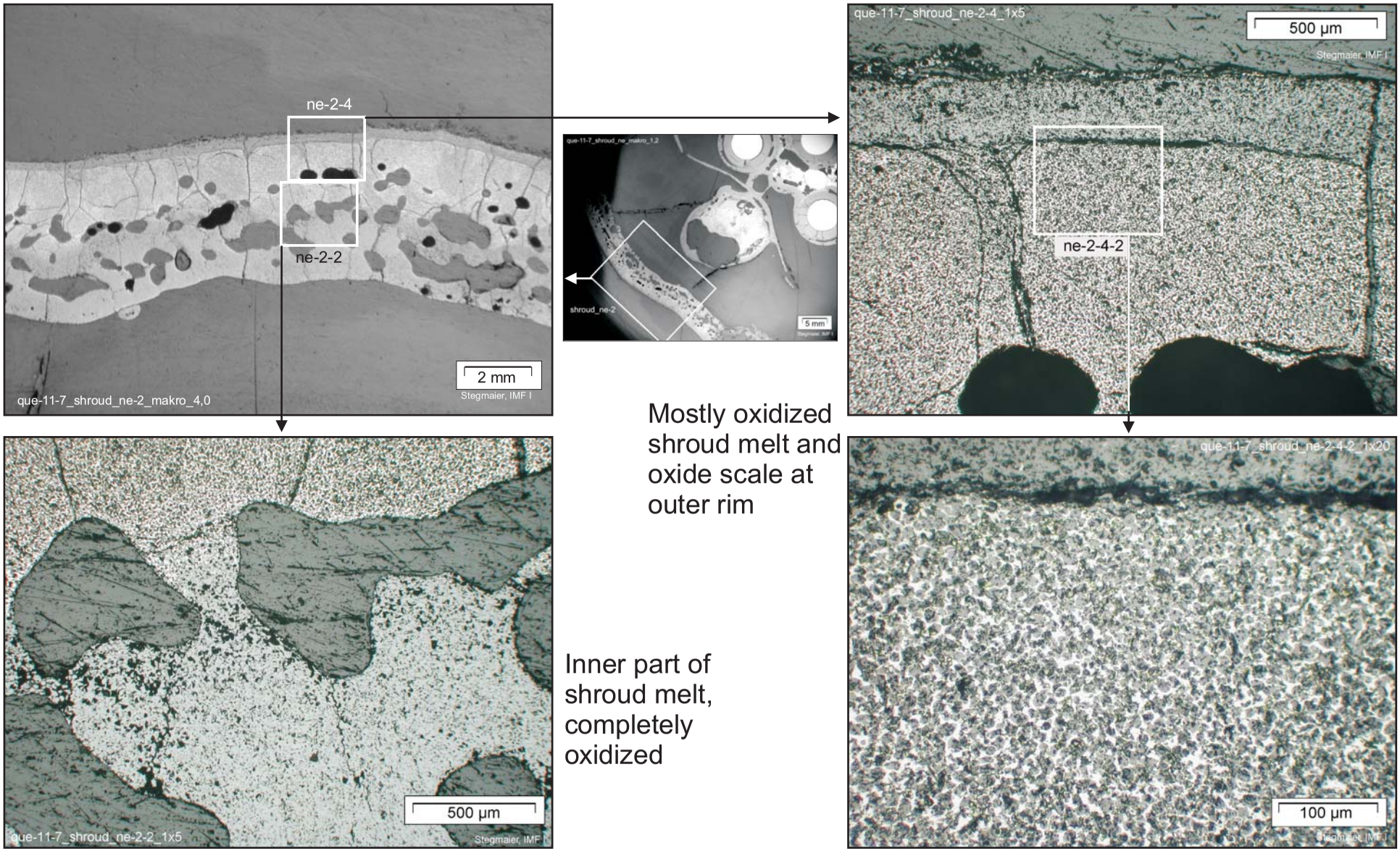

Fig. 78: QUE-11-7, level 900 mm; shroud melt at NE, showing rounded voids, external scale, and partial to total oxidative conversion

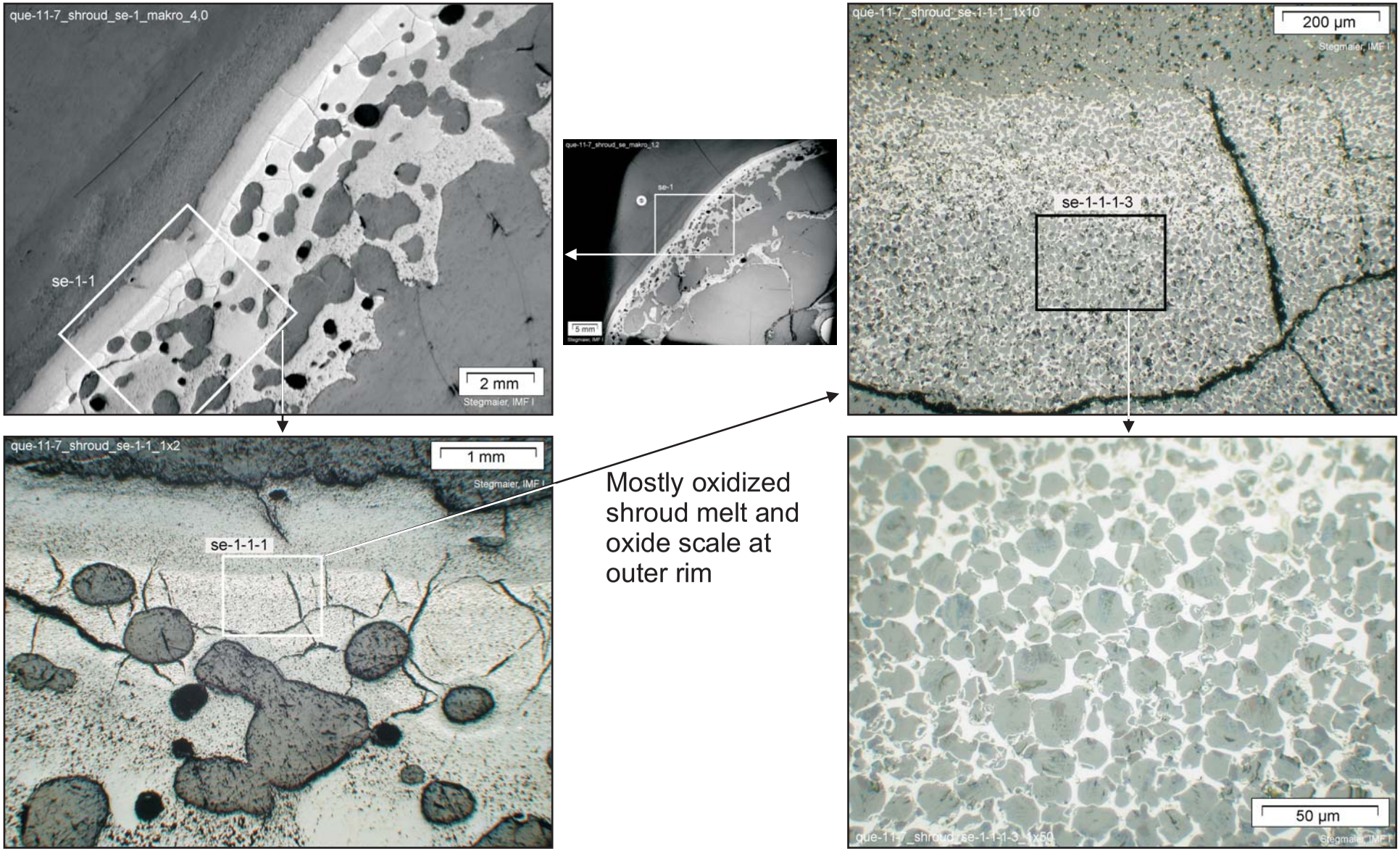

Fig. 79: QUE-11-7, level 900 mm; shroud melt at SE, showing rounded voids, external scale, and partial to total oxidative conversion

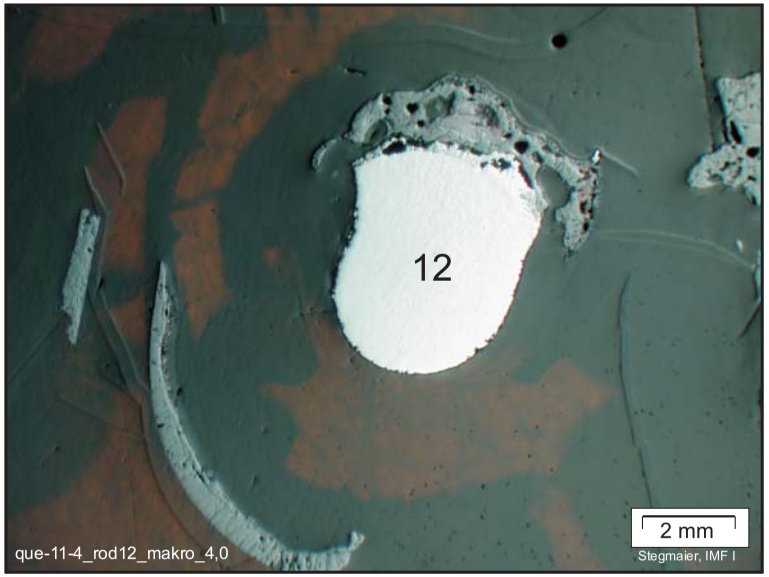

Mass loss of heater rods mainly at bare positions, compared to those, at which solid stuctures or melt remained in close contact; the degradation products are mostly vanished

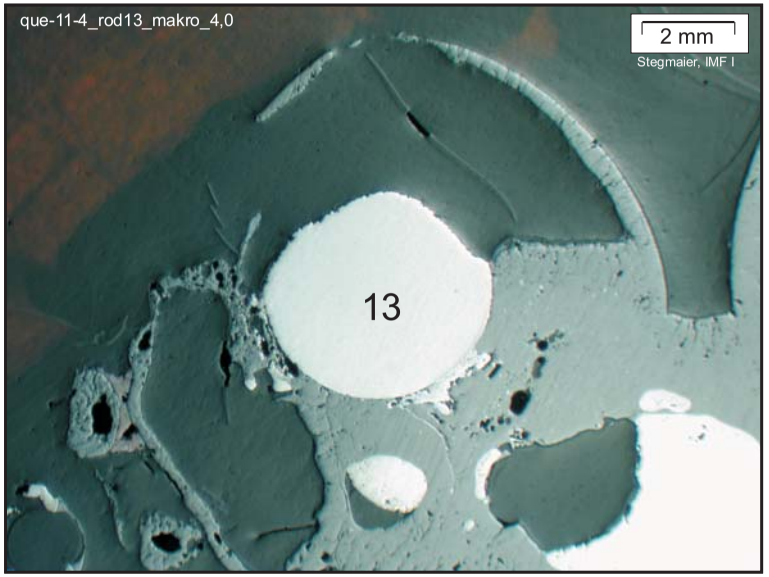

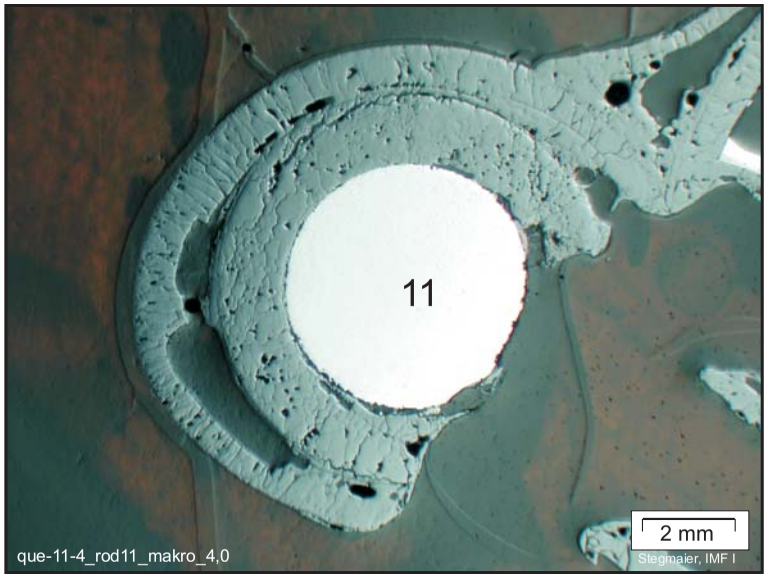

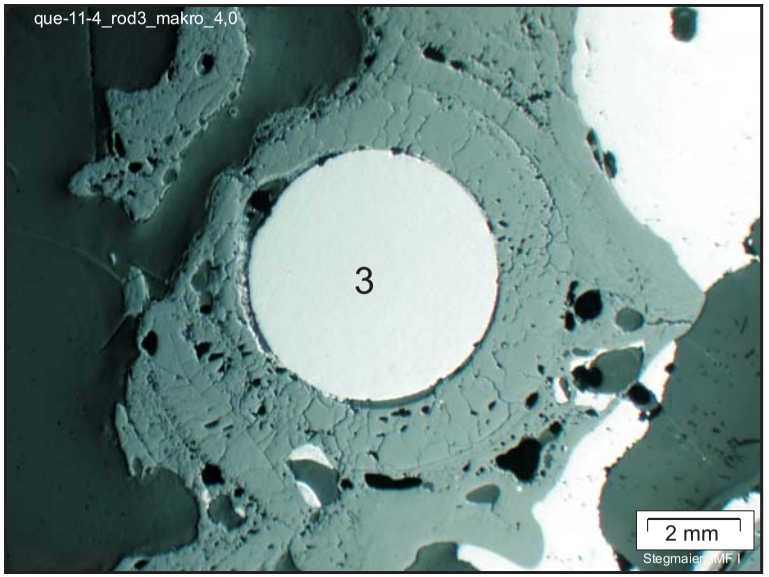

Fig. 80: QUE-11-4, level 950 mm; tungsten heater rod degradation, following loss of protection by cladding and pellets

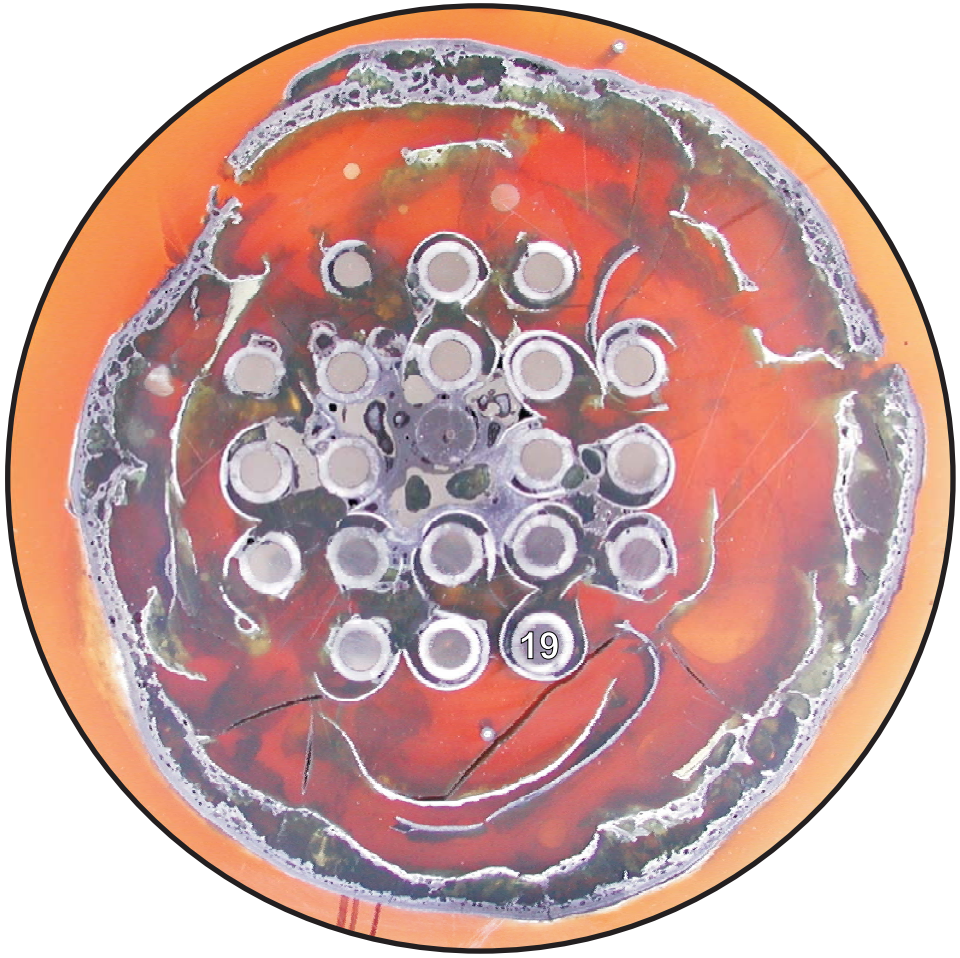

Elevation 1000 mm, top view

Rod 19: Almost complete cladding melt relocation is seen to have occurred after the growth of a thin scale; the tungsten heater rod shows degradation due to oxidative gas exposure

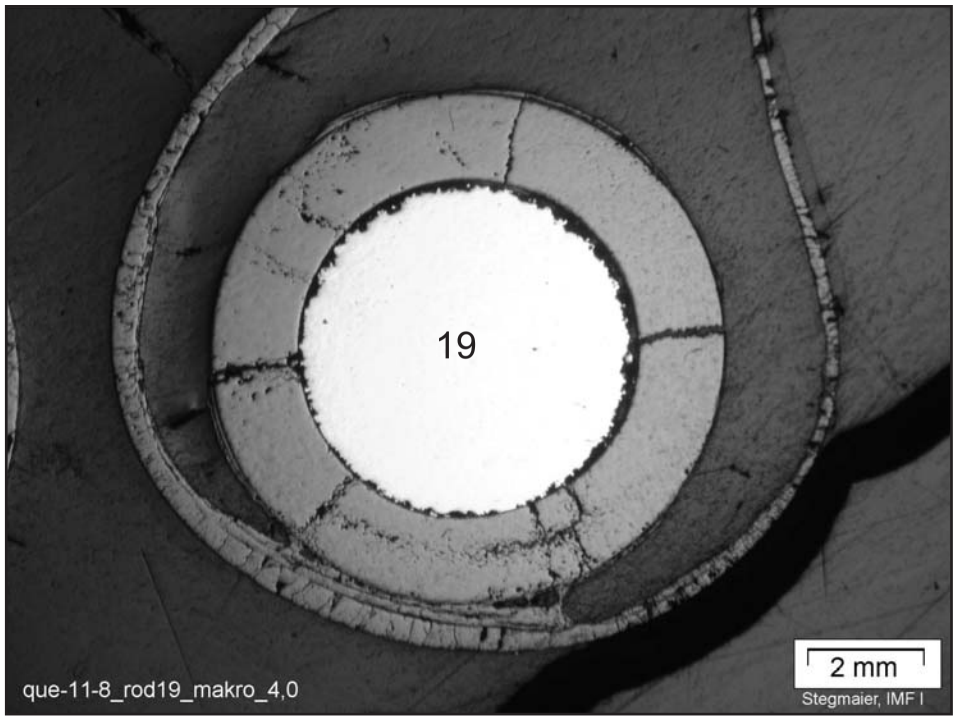

Fig. 81: QUE-11-8, level 1000 mm; cross section at the upper end of the heated zone

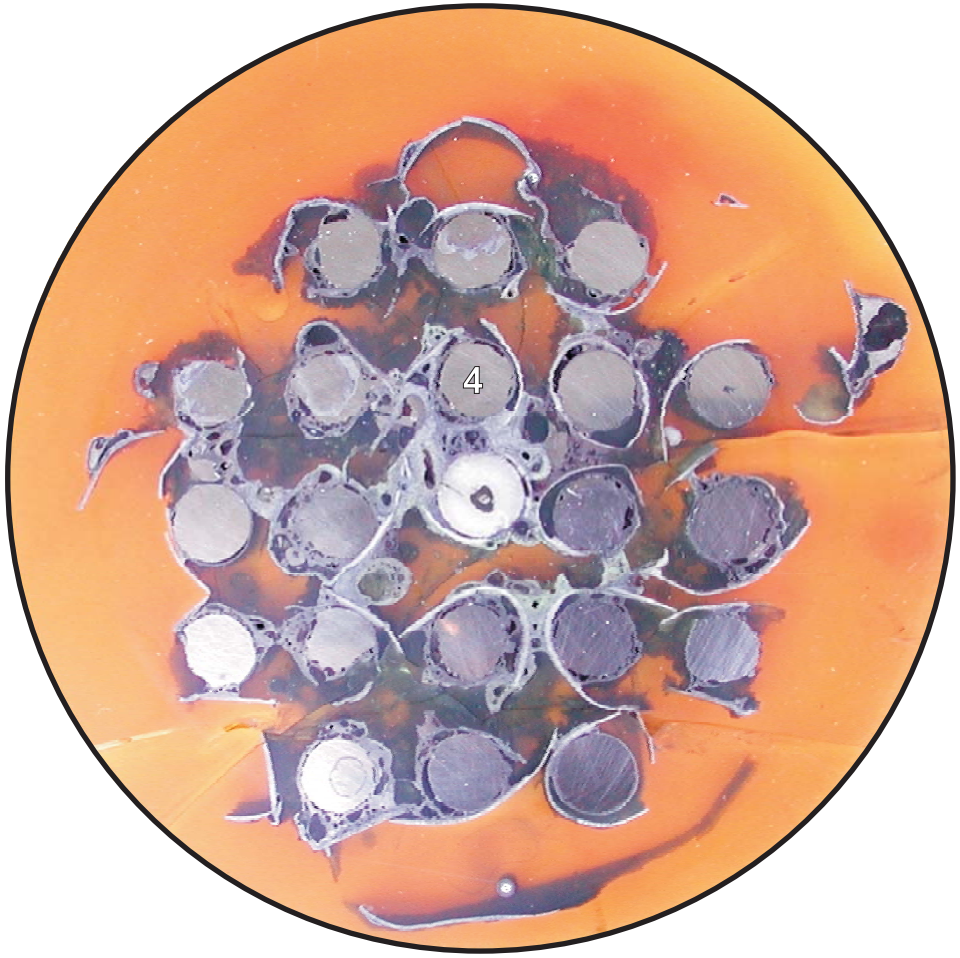

Elevation 1050 mm, top view

Rod 4: Incomplete cladding melt relocation is seen to have occurred after the growth of a thin scale and spacer grid oxidation; the molybdenum electrode rod shows degradation due to oxidative exposure where its protection layer of zirconia has failed

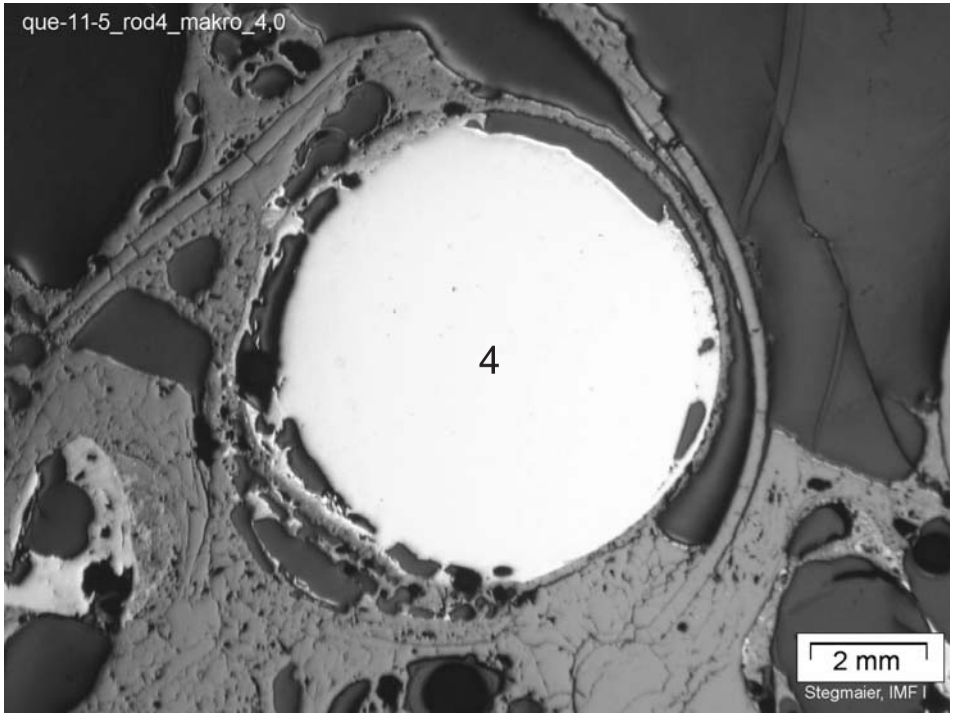

Fig. 82: QUE-11-5, level 1050 mm; cross section within the upper electrode zone

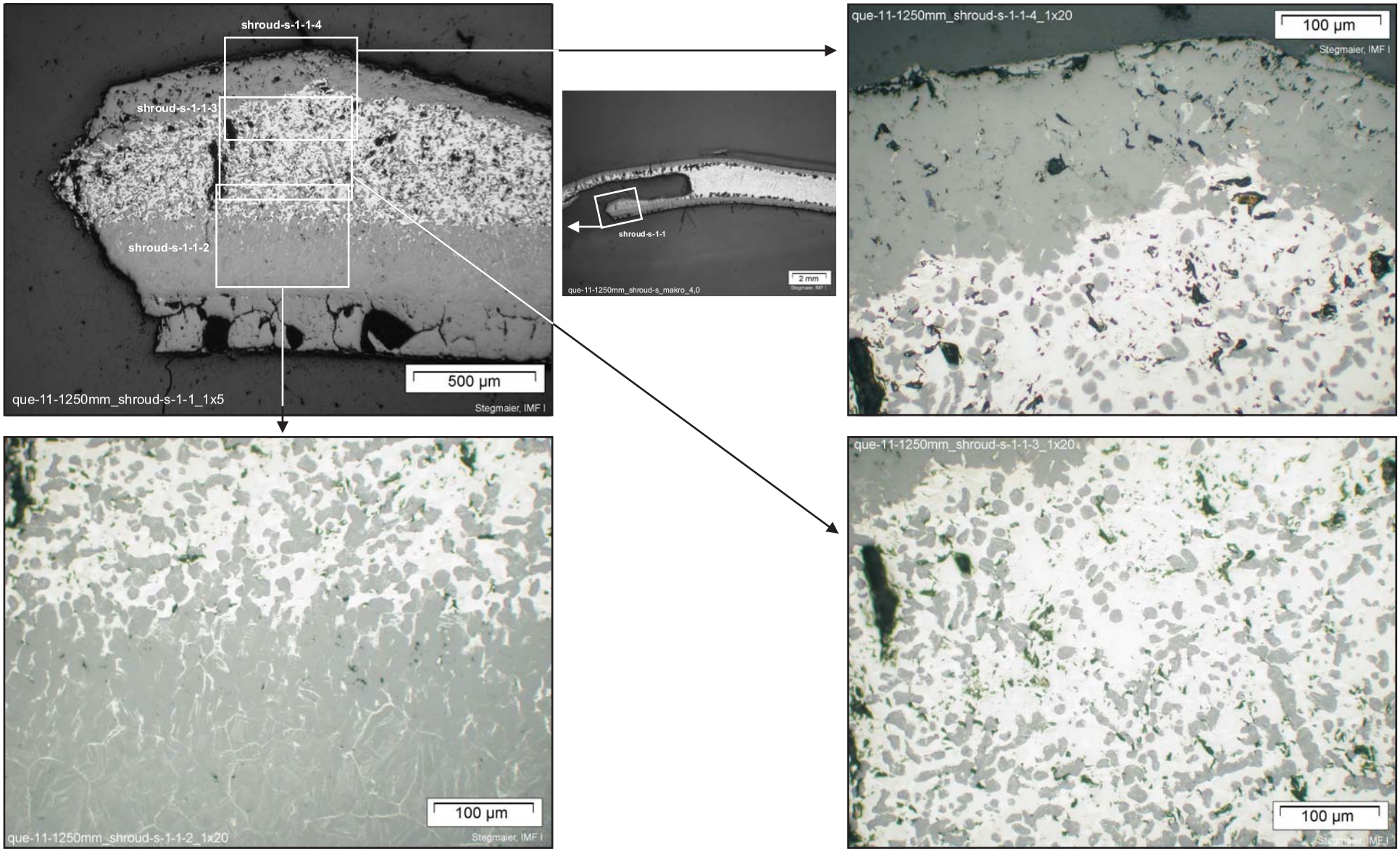

Fig. 83: QUE-11_shroud 1250 mm; oxidation state of partially molten shroud at S direction

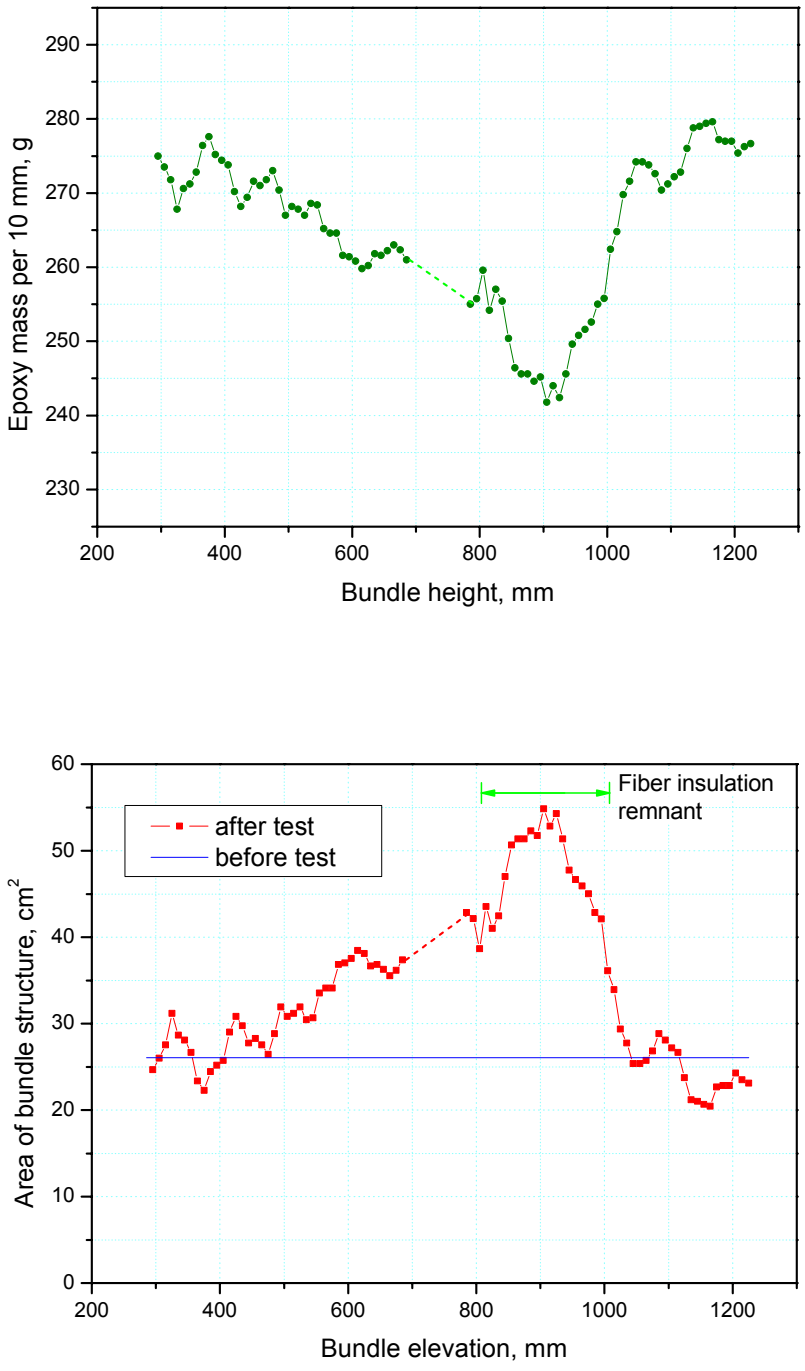

Fig. 84: QUENCH-11; Results of filling the bundle with epoxy resin top, and axial distribution of the area of bundle material, calculated by using the bundle fill-up data, together with the area of the non-oxidized bundle materials (rods, corner rods, shroud) of 26,07 mm² (blue line), bottom.

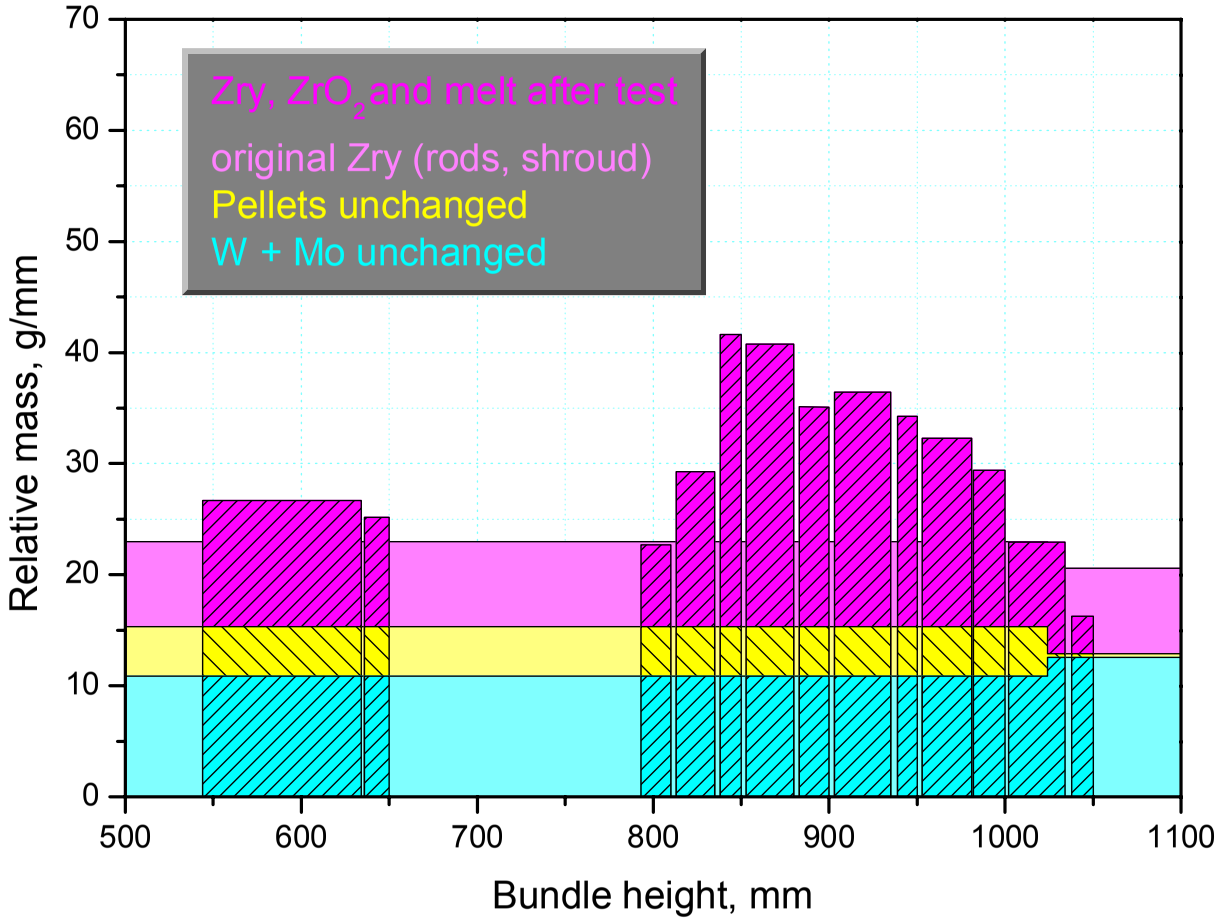

Fig. 85: QUENCH-11; Posttest axial mass distribution of bundle material based on epoxy data and sample weights compared to the pretest status.

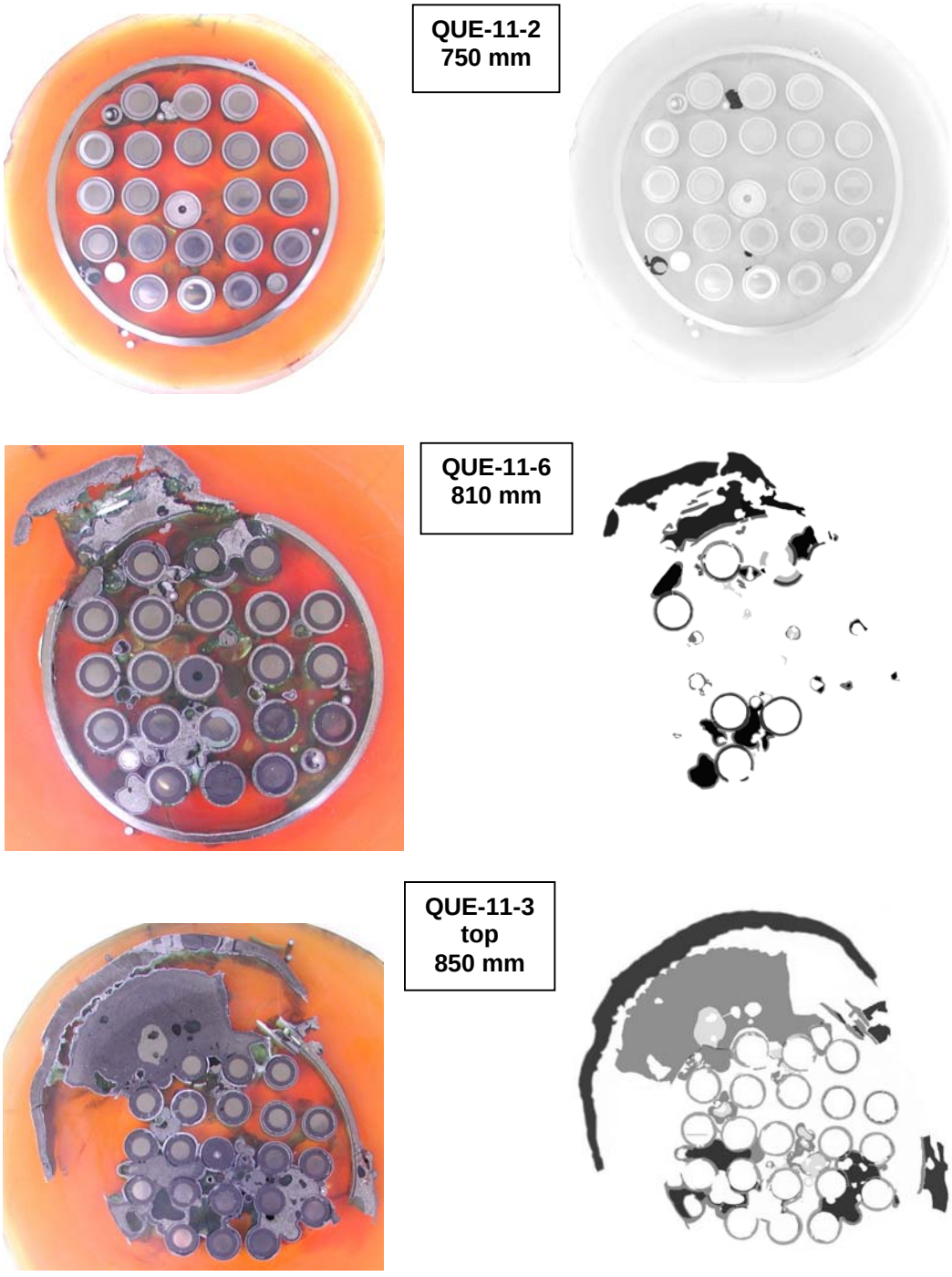

Fig. 86: QUENCH-11; Image analysis of cross sections at 750-850 mm with color macro and reduced gray scale images for quantification of melt distribution. Those structures not shown in the gray scale images are either calculated (unchanged pellets, heaters, rods) or not taken into account (shroud 900 mm and above.) For quantification results see table 16.

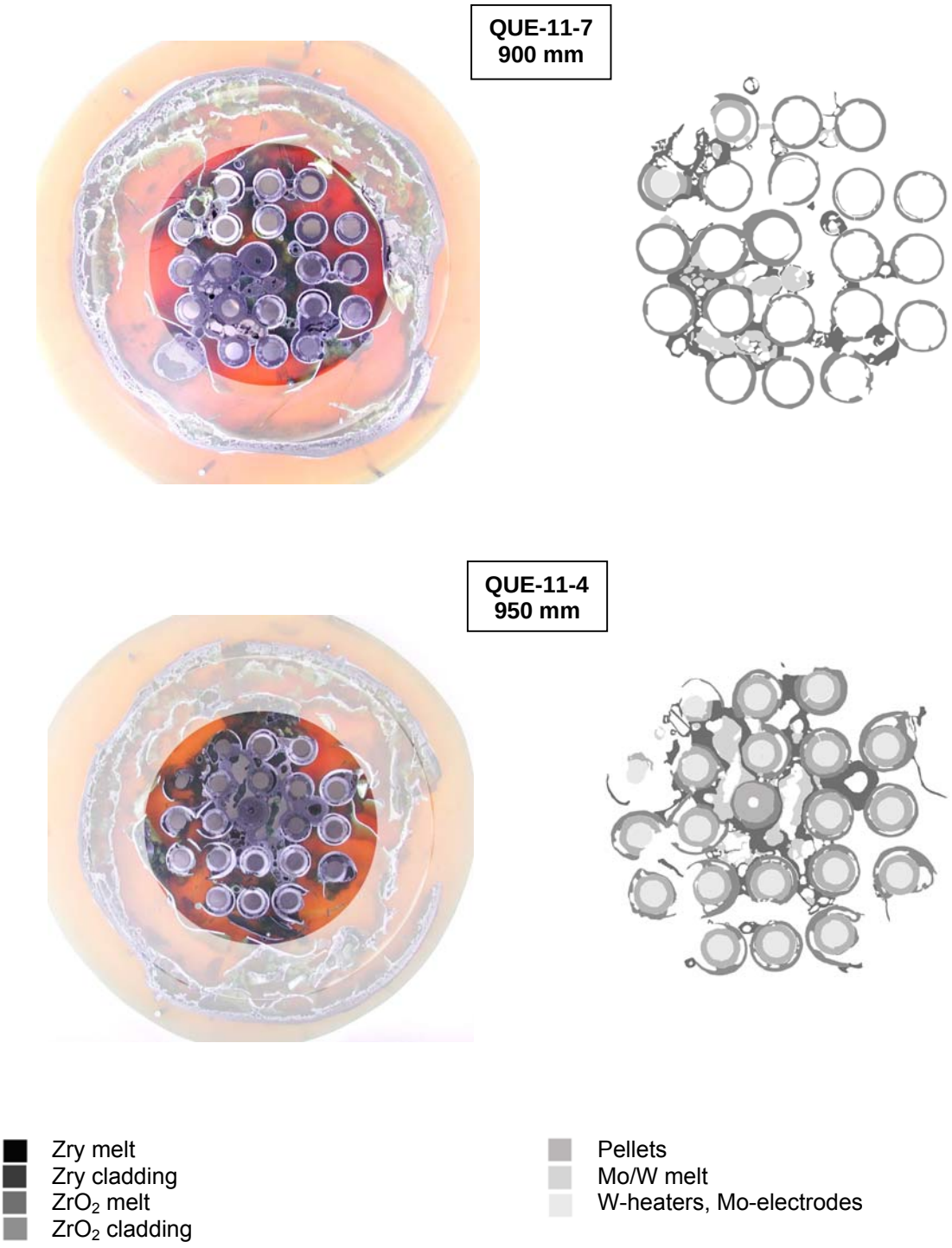

Fig. 87: QUENCH-11; Image analysis of cross sections at 900-950 mm with color macro and reduced gray scale images for quantification of melt distribution. Those structures not shown in the gray scale images are either calculated (unchanged pellets, heaters, rods) or not taken into account (shroud 900 mm and above.) For quantification results see table 16.

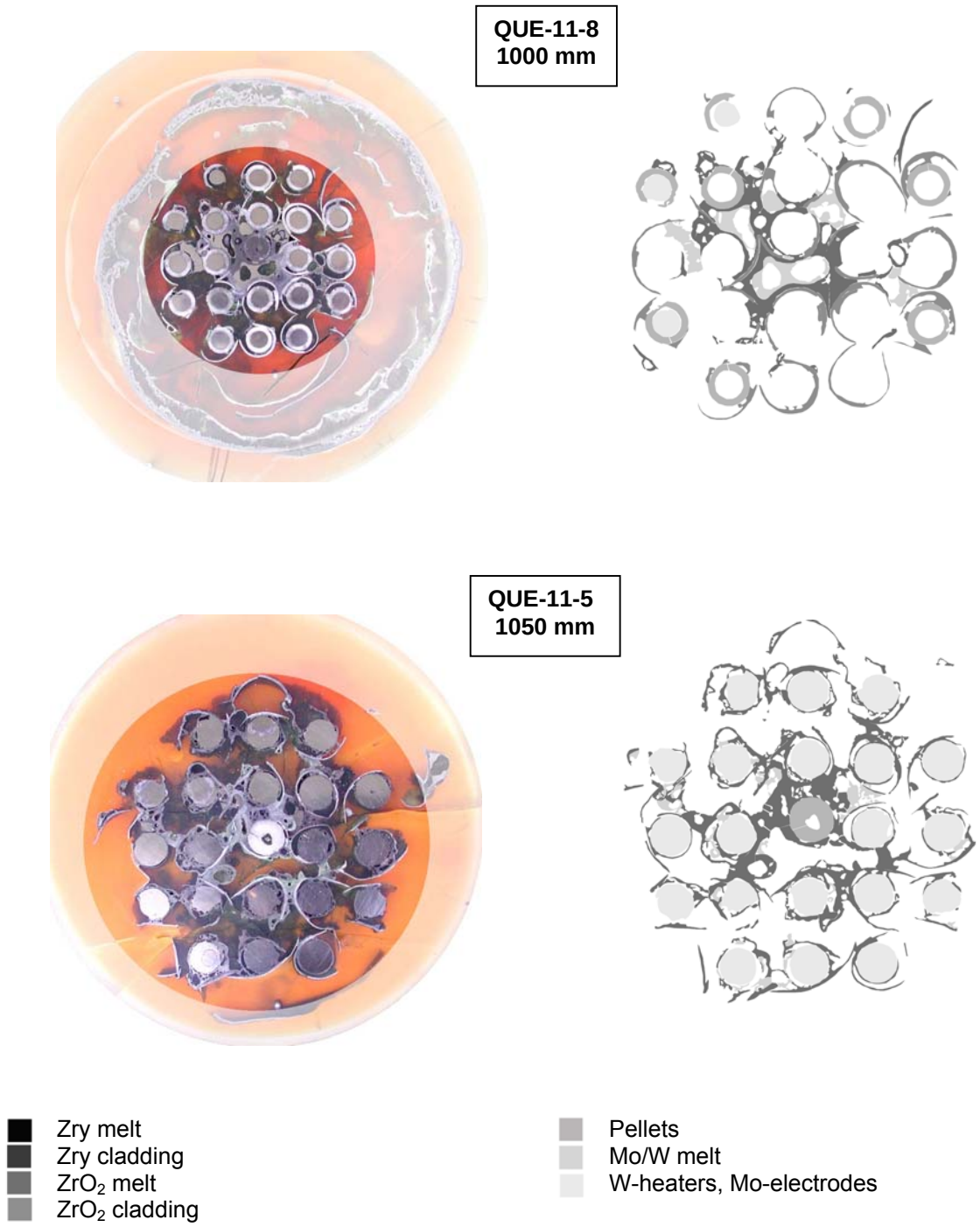

Fig. 88: QUENCH-11; Image analysis of cross sections at 1000-1050 mm with color macro and reduced gray scale images for quantification of melt distribution. Those structures not shown in the gray scale images are either calculated (unchanged pellets, heaters, rods) or not taken into account (shroud 900 mm and above.) For quantification results see table 16.

QUE-11-6
810 mm

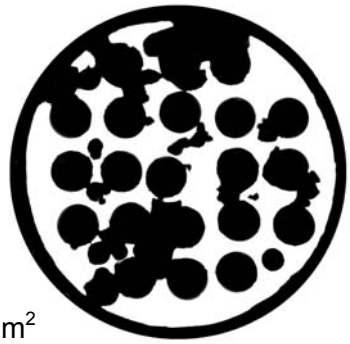

□ 2240 mm^2

QUE-11-3
850 mm
with photo mount

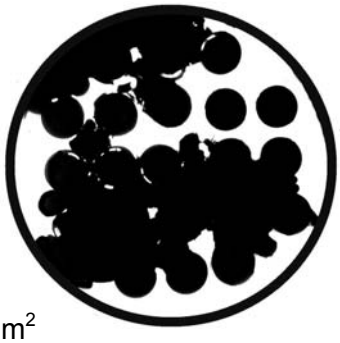

□ 1420 mm^2

QUE-11-3
850 mm

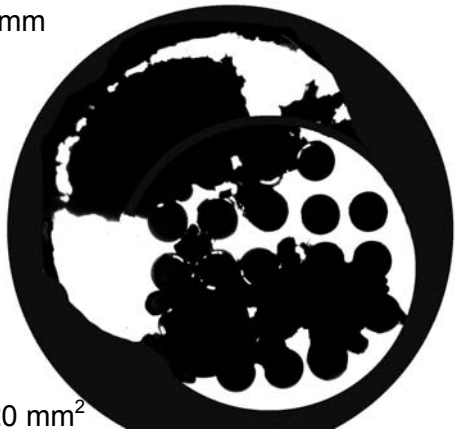

□ 2520 mm^2

QUE-11-7
900 mm
with photo mount

□ 1450 mm^2

QUE-11-7
900 mm

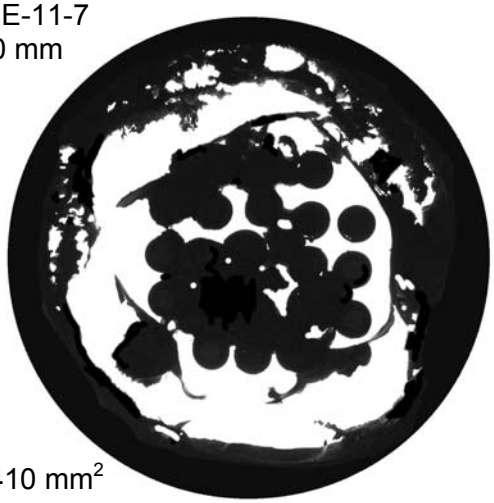

□ 4410 mm^2

Fig. 89: QUENCH-11; Analysis of remaining fluid channels at 810-900 mm elevations by reduction of translucence photographs to b/w images with and without a photo mount with a diameter of 80 mm, i.e. the original shroud diameter.

QUE-11-4
950 mm
with photo mount

□ 1320 mm^2

QUE-11-4
950 mm

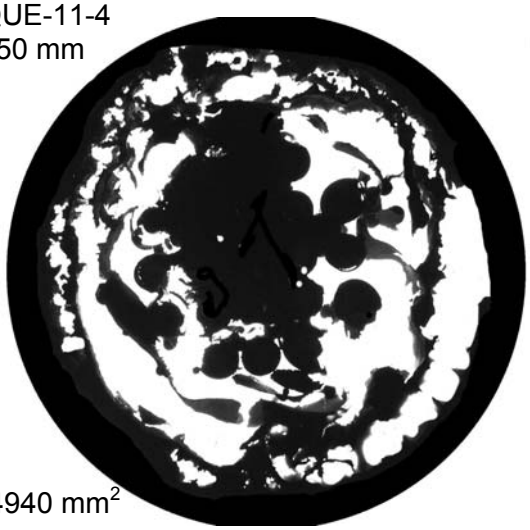

□ 4940 mm^2

QUE-11-8
1000 mm
with photo
mount

□ 1580 mm^2

QUE-11-8
1000 mm

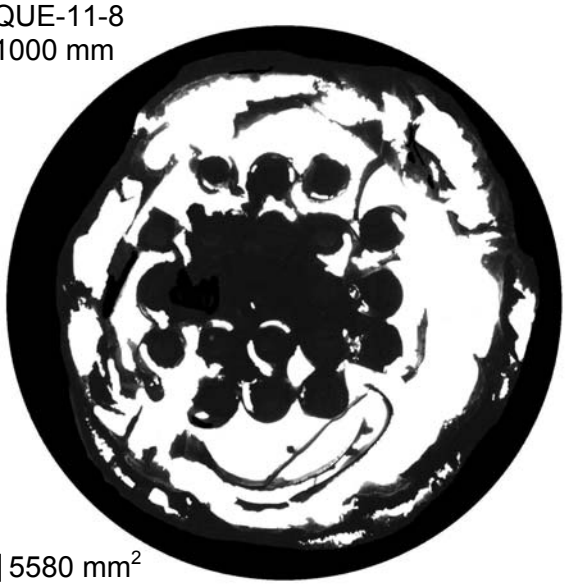

□ 5580 mm^2

QUE-11-5
1150 mm
with photo
mount

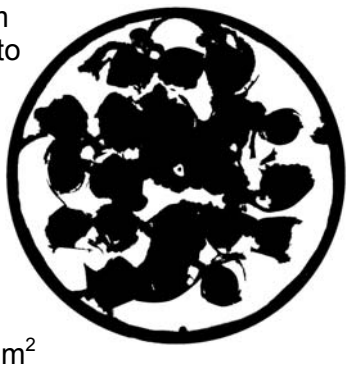

□ 1980 mm^2

Fig. 90: QUENCH-11; Analysis of remaining fluid channels at 950-1150 mm elevations by reduction of translucence photographs to b/w images with and without a photo mount with a diameter of 80 mm, i.e. the original shroud diameter.

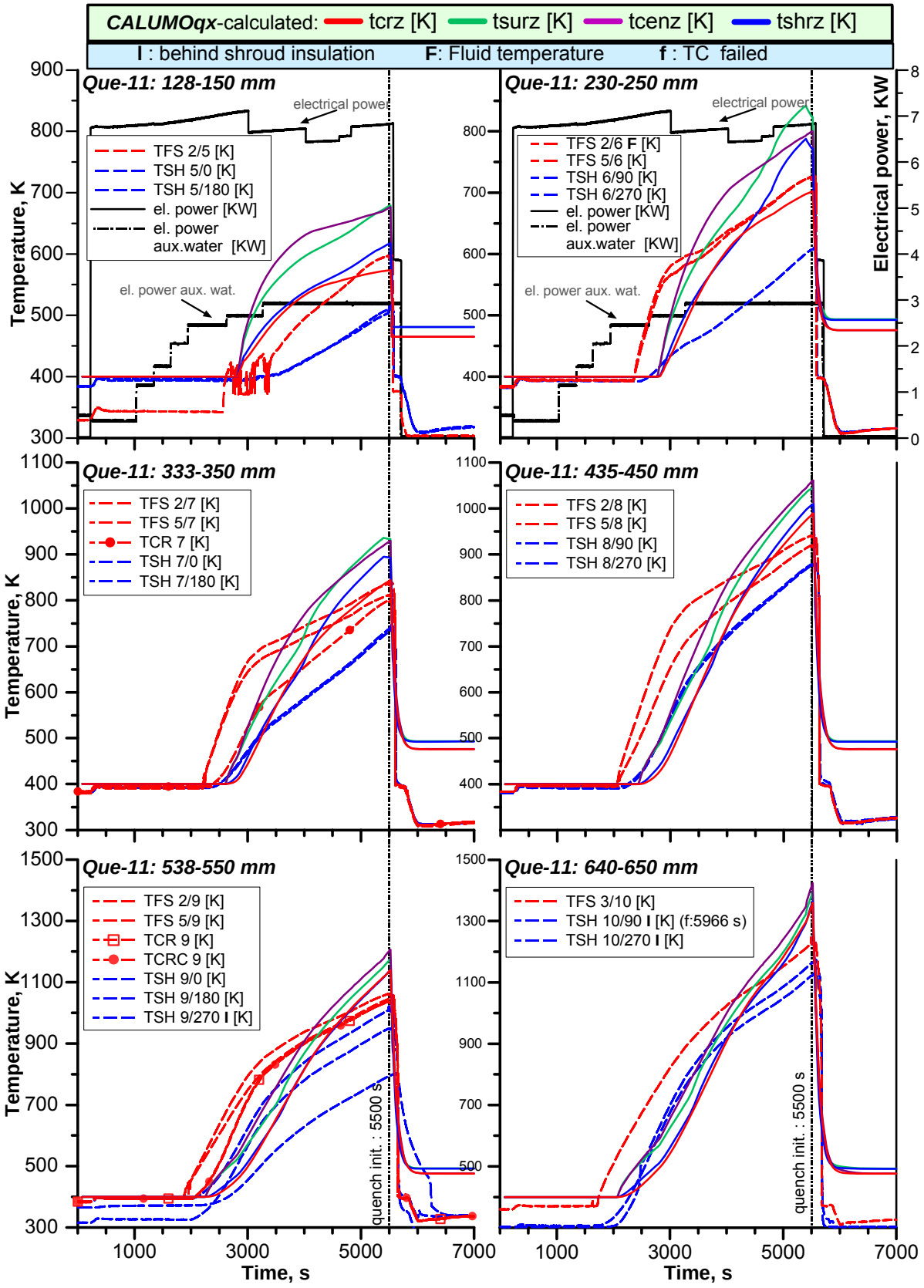

Fig.: 91 Evolution of rod and shroud temperatures of QUENCH-11 at different axial locations, CALUMOqx-calculated data in comparison with experimental values.

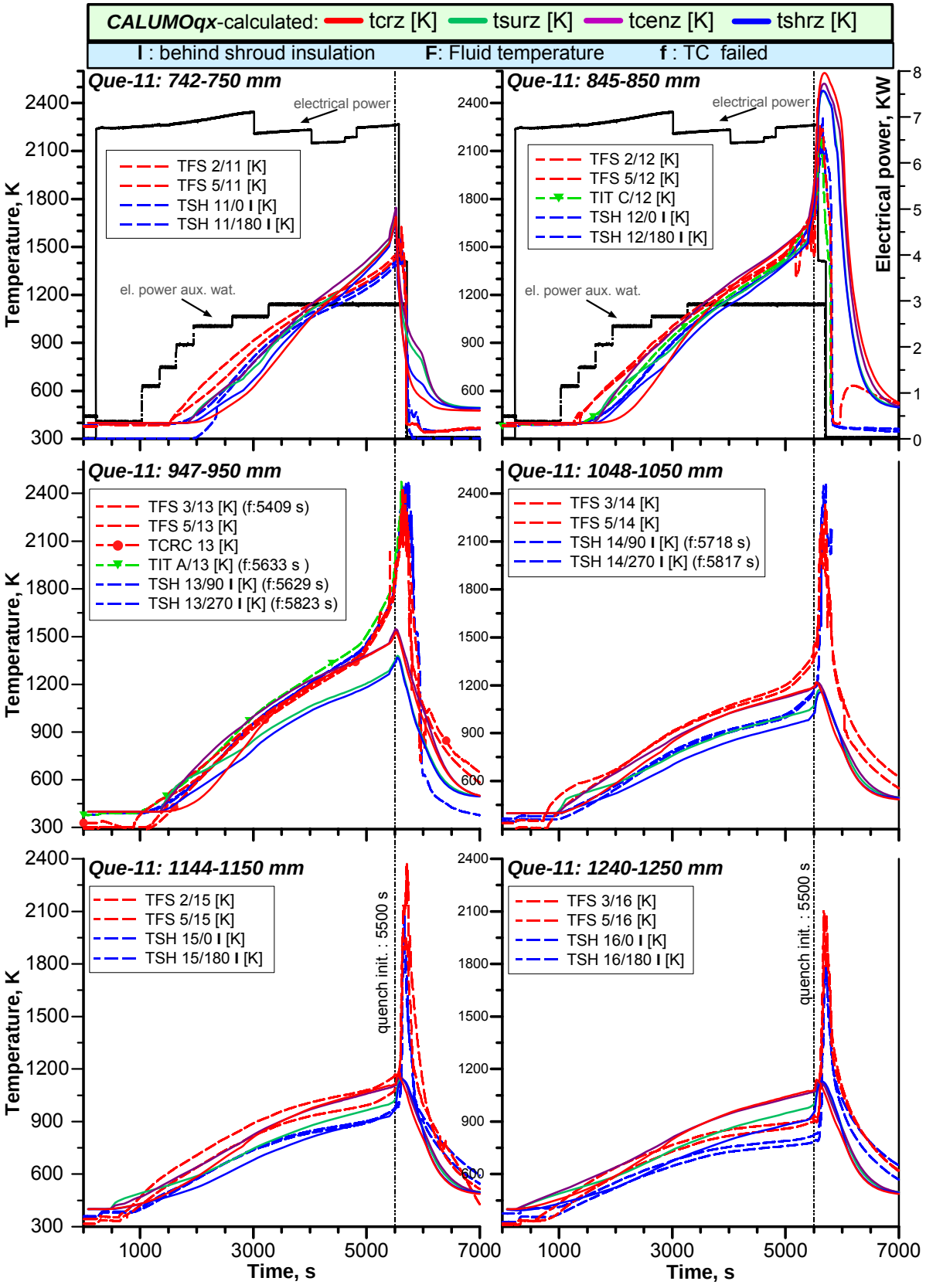

Fig.: 92 Evolution of rod and shroud temperatures of QUENCH-11 at different axial locations, CALUMOqx-calculated data in comparison with experimental values.

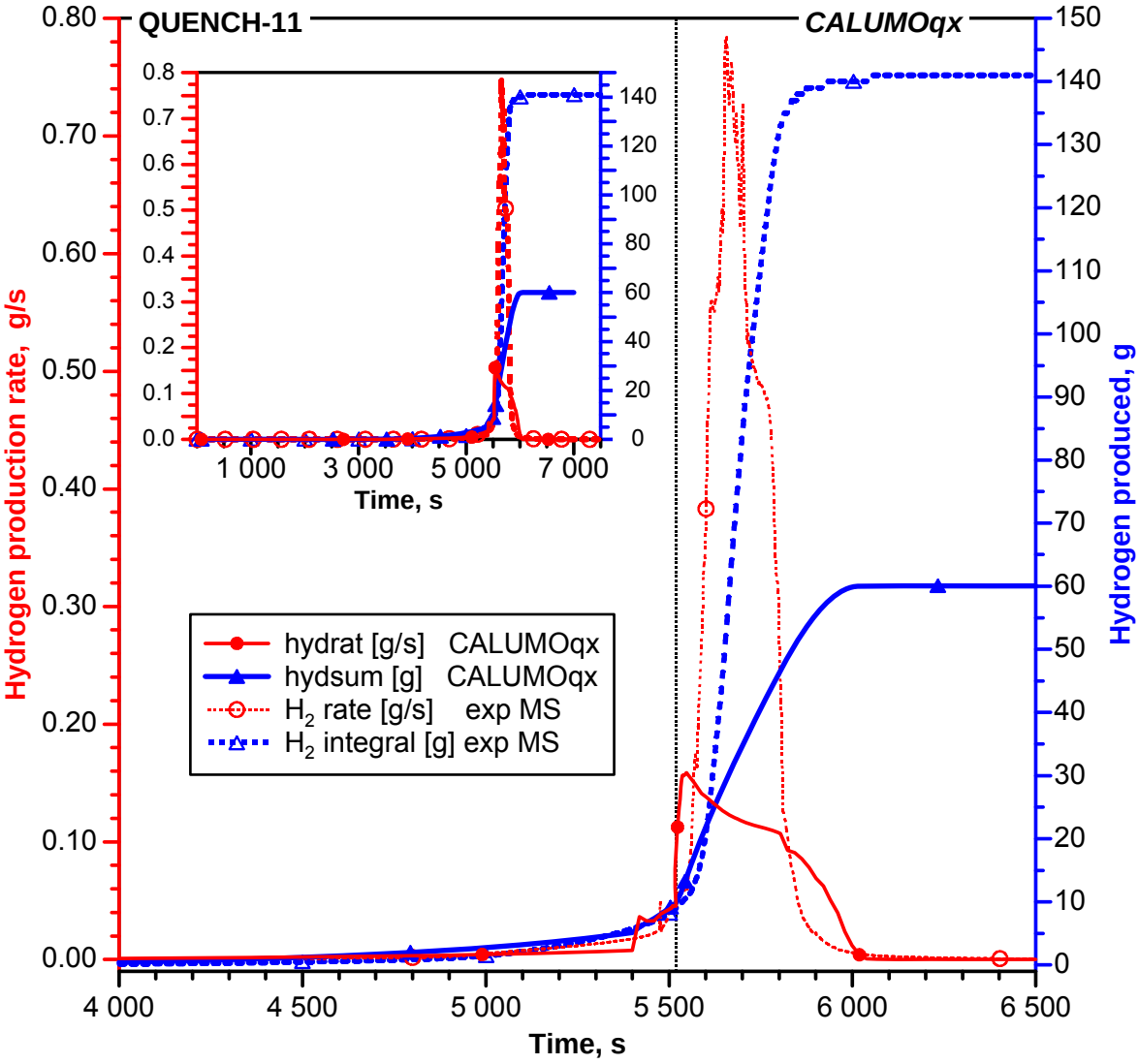

Fig.: 93 Evolution of the hydrogen production rate and the overall produced hydrogen for QUENCH-11 calculated with CALUMOq in comparison with the experimental data.

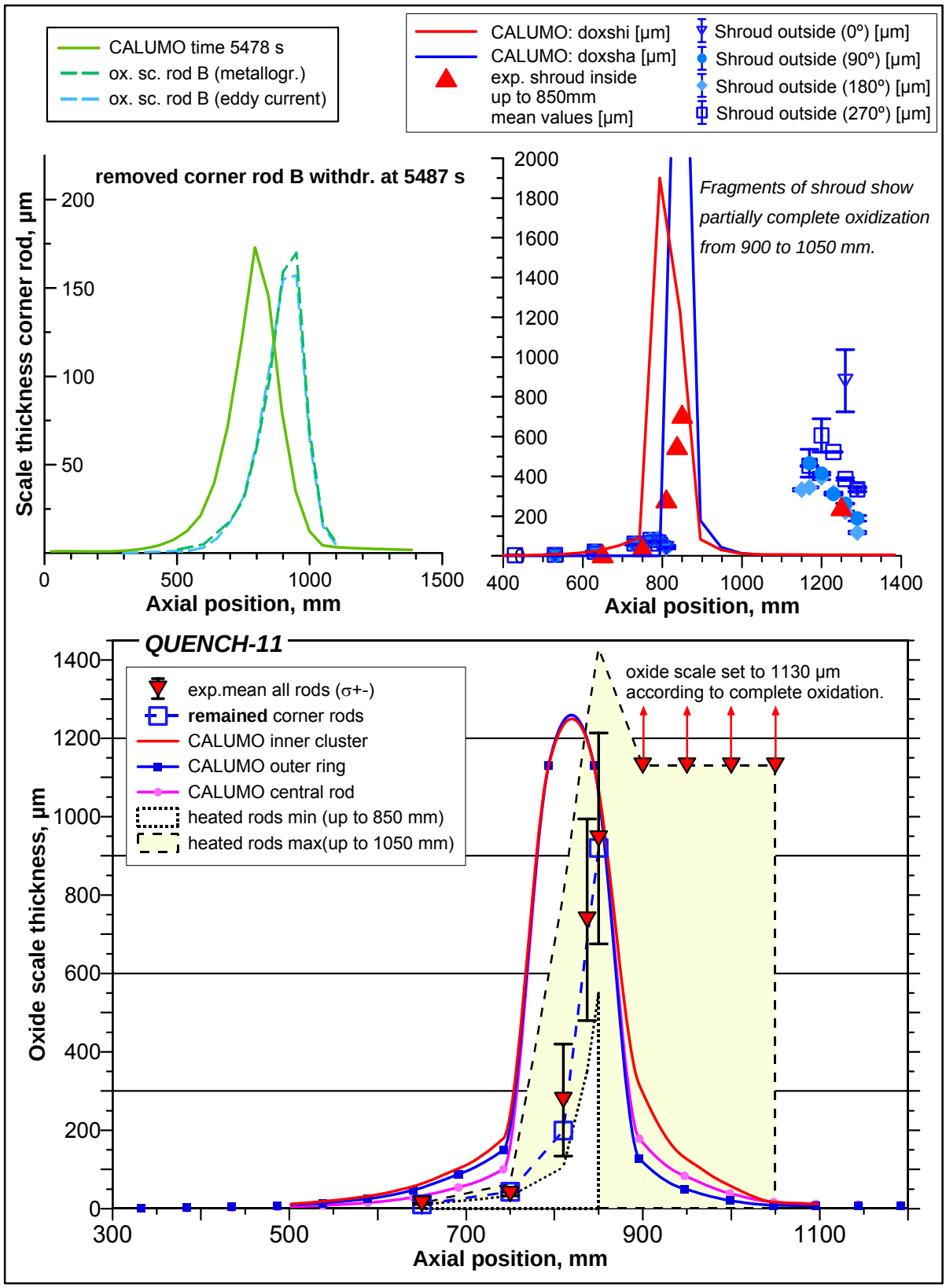

Fig.: 94 Axial distributions of the oxide scale thickness for the removed corner rod B (top, left); at the end of QUENCH-11 for the shroud inside and outside (top, right) and for all rods (bottom).

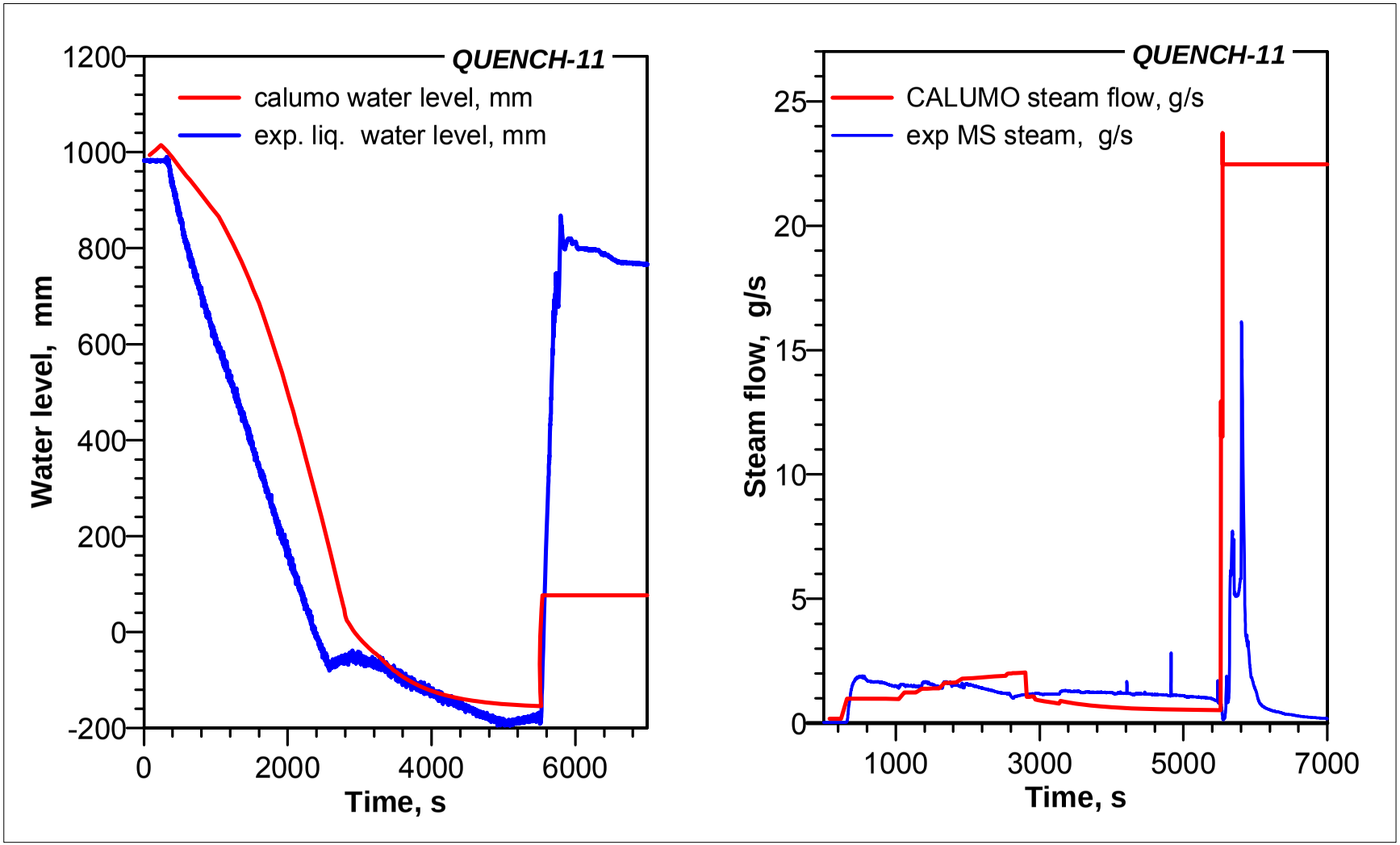

Fig.: 95 Evolution of the water level (left) and the steam flow rate (right) calculated by CALUMOqx in combination with the experimental data.